UNIVERSITY OF BIRMINGHAM

NON-DESTRUCTIVE CHARACTERISATION OF STEEL MICROSTRUCTURES USING ELECTROMAGNETIC SENSORS

By

LEI ZHOU

A thesis submitted to
The University of Birmingham
For the degree of
DOCTOR OF PHILOSOPHY

School of Metallurgy and Materials
College of Engineering and Physical Sciences
The University of Birmingham (UK)
December 2014

Abstract

The properties of steels are controlled by its microstructural parameters, such as grain size, phase balance and precipitates, which are developed during processing or in-service thermal-mechanical exposure. It is desirable to be able to monitor microstructural changes during processing, to allow in-situ feedback control, or to characterize microstructure in steel products in a non-contact and non-destructive manner. Electromagnetic (EM) sensors are sensitive to both changes in magnetic relative permeability and electrical resistivity of the samples, which in steels, vary with composition, microstructure and temperature. In the last decade, EM sensors have been shown to have great potential for assessing the state of the steel microstructures; including monitoring the austenite-ferrite phase transformation, and detecting decarburisation in steel rod both on-line and off-line. However, the influence of key microstructural parameters on the EM signal is not yet fully understood. To extend the potential applications of the sensor, it is important to determine the sensitivity of, and understand the relation to, each individual microstructural factor. This thesis presents an extensive study in this area.

Firstly, the EM sensor output was modelled using the Finite Element (FE) based commercial software; COMSOL MultiPhysics. The sensitivity of the sensor output (real inductance) to changes in relative permeability and electrical resistivity were modelled separately. The latter has much lower impact to the signal due to the narrow range of the electrical resistivity values of structural steels. It was found that, at low frequency (below approx. 100 Hz), the real inductance of the sensor output is

independent of the electrical resistivity but dependent on the relative permeability of the sample. It has been found that the relative permeability determined for steel samples using the EM sensor is very similar to the initial permeability value obtained from hysteresis loop measurements due to the very low field applied by the sensors. A fitting method was developed for cylindrical shaped EM sensor to determine the relative permeability values of the steel sample by fitting the modeled real inductance with the experimental measured one through Comsol LiveLink for Matlab. Therefore the EM sensor can be used to determine relative permeability values of different steel microstructures, which can be compared with the results measured by other methods and are independent of sensor design.

Secondly, the effect of single microstructural parameter changes in steels on the relative permeability and hence the sensor output was studied. It was shown that there is an increase in the relative permeability value when the ferrite grain size increases from 13 to 64 μm in a 0.17 wt% C steel. In addition, a Hall–Petch type relationship between the relative permeability values and the ferrite grain size has been found. The relationship between magnetic domain structures, obtained using Bitter method, and grain size, with closure domains formed near the grain boundaries, explains the phenomenon of effective pinning of the grain boundaries on magnetic domain movement and hence the Hall–Petch type effect for relative permeability. Results obtained for a pure iron sample with large grain size showed that the relative permeability did not increase further when the grain size becomes very large (155 to 223 μm). The domain structure findings suggest that this may be due to the largest grain size sample showing a multi-magnetic domain structure per ferrite grain compared to a single domain per grain for the smaller grain sizes. Pearlitic microstructures, representative of these seen in wire steels were

studies and it was found that the relative permeability/low frequency real inductance increased almost linearly with pearlite interlamellar spacing (in the range of 52-106 nm) increase. This is believed to be due to the reduced pinning effect on the magnetic domain wall movement in the samples with a larger pearlite interlamellar spacing, due to the fine scale of the microstructure direct observation of the magnetic domains was not possible. A case study of EM sensor measurement of pearlite interlamellar spacing in tyre bead steel wire samples shown the linear trend between the low frequency (plateau region) real inductance and pearlite interlamellar spacing is still stand in the pearlite interlamellar spacing range of 142-202 nm. The EM sensor technique has shown potential to determine the pearlite interlamellar spacing of the tyre wire steels. Martensitic steel microstructures were also assessed and it was found that the relative permeability values decreased with an increase in carbon content in the as quenched martensite. After tempering, the relative permeability values become higher, increasing with an increasing tempering temperature (for the same tempering time).

The effect of phase balance, in ferrite-second phase microstructures, on the relative permeability and hence the sensor output was studied using C-Mn steels (ferrite + pearlite) and dual phase (DP) grades (ferrite + martensite/bainite/tempered martensite). It was shown that, with an increase in pearlite content (0-90%), the relative permeability and hence inductance value decreases. The relative permeability increased almost linearly with the ferrite fraction in the range of 35-72% in the DP steels. A 2D FE COMSOL model was used, that allowed the steel microstructures to be included, to predict the relative permeability and showed good agreement with the experimental results. These results indicated that the EM approach can be used to non-destructively measure the ferrite fraction in ferrite – pearlite/martensite microstructures.

Finally, the research outcomes were applied to investigate the possibility of using the EM sensor to predict the microstructure, and hence strength, of commercial DP steel grades. It was found that the low frequency inductance EM sensor reading could be used to distinguish each of the grades, showing approximately linear trend of increasing low frequency inductance value with increasing ferrite content. There is also a trend of decreasing low frequency inductance value with increasing tensile strength for the DP samples. Therefore, it has been shown that the EM sensor has great potential to estimate the phase balance and tensile strength of the DP steels.

List of publications

- L. Zhou, J. Liu, X. J. Hao, M. Strangwood, A.J. Peyton, and C. L. Davis, "Quantification of the phase fraction in steel using an electromagnetic sensor" NDT & E Int 67 (2014) 31-35

- L. Zhou, J. Liu, X.J. Hao, M. Strangwood, W. Yin, A. Peyton, C.L. Davis "The role of microstructure such as phase balance and pearlite lamellar spacing to EM sensor signal" International conference on NDE of steel, Jamshedpur, Dec 2011

- L. Zhou, M. Strangwood, C. L. Davis, A. J Peyton, S.V. Parker, A.W.F. Smith, K. Boos 'Non-destructive monitoring of phase fraction and tensile properties of dual-phase steels by an electro-magnetic sensor" 9th Int conference on Rolling, organised by AIM, June 10-12th 2013, Venice, Italy

- J. Liu, X.J. Hao, L. Zhou, M. Strangwood, C.L. Davis, A.J. Peyton, Measurement of microstructure changes in 9Cr-1Mo and 2.25Cr-1Mo steels using an electromagnetic sensor, Scripta Mat 66 (2012) 367–370

- W. Yin, J. Liu, N. Karimian, X. J. Hao, L. Zhou, A. J. Peyton, M. Strangwood, C. L. Davis, Measurement of Electromagnetic Properties of Power Station Steels, NDT & E Int 51 (2012) 135-141

- S Balamurugan, T. Bhattacharyya, D. Gudhae, L Zhou, C L Davis, A Peyton & S. Chandra, 'Prediction of interlamellar pearlite spacing of tyre bead wires after patenting using electromagnetic techniques', Insight, Volume 55, Issue 3, March 2013, Pages 132-135

- J. Liu, L. Zhou, X.J. Hao, W. Yin, N. Karamian, M. Strangwood, A. Peyton, P. Morris, C.L. Davis "Non-destructive Evaluation of Power-Generation Steel Microstructure Changes using Electromagnetic Sensors" International conference on NDE of steel, Jamshedpur, Dec 2011

- W. Yin, J. Liu, N. Karimian, X. J. Hao, L. Zhou, A. J. Peyton, M. Strangwood, C. L. Davis, "Measurement of EM properties of power generation steels", IEEE International Instrumentation and Measurement Technology Conference, Graz, Austria, 13-16 May 2012

Acknowledgements

I would like to take this opportunity to express my appreciation to everyone who have helped me during my PhD study. Firstly, my sincere thanks go to Prof Claire Davis, and Dr Martin Strangwood, my supervisors, who gave me the opportunity to undertake this project and taught me useful research skills. It was a great honour to work with Claire, who constantly guided the direction of my project, as well as providing much support and encouragement. I learnt a lot from her and developed a lot of confidence in my research area. I would particularly like to thank Martin for his academic guidance, demonstration of the experimental procedure and analysis skills through the course of this work. I feel very lucky to have both of them as my supervisors. Without their valuable help, this thesis would have been impossible.

I would also like to acknowledge my industrial supervisors, Dr Sally Parker and Dr Peter Morris, as well as the many people at Tata Steels for supplying me with the steel samples and giving me valuable suggestions.

I am grateful to Dr Xinjiang Hao and Dr Jun Liu for their help with EM theory and Finite element modelling. Special thanks also go to Prof Anthony Peyton and his research group at the University of Manchester for their valuable advice and discussions related to EM sensor measurements.

I also wish to express my thanks to the United Kingdom Engineering and Physical Sciences Research Council (EPSRC) for their financial support for this research.

Thanks must also go to all of my colleagues at the University of Birmingham: Carl, Rachel, Xi, JP, George, Mark, Daniel, Fei, and Mo, for always creating a great environment and making my PhD a hugely enjoyable experience.

Finally, I would like to thank my parents for sending me aboard to study for nearly ten years now and always supporting my decisions. Most of all, to my fiancee Jiangling Li, thank you for your support. I couldn't have done it without you.

Table of contents

List of figures

List of tables

1 Introduction

1.1 Background

Steel is one of the most widely used engineering materials due to its excellent physical/mechanical properties, abundance in natural resources and relatively low cost to process. The properties of steels are controlled by its microstructural parameters, such as grain size, phase balance and precipitates, which are developed during processing or in-service thermal-mechanical exposure [1].

The conventional microstructure characterisation methods such as optical microscopy, dilatometry, scanning electron microscopy (SEM) and transmission electron microscopy (TEM) are generally carried out using small samples removed from the component or material of interest, as the methods are destructive and time consuming. In order to ensure that steel components have the microstructure, and hence properties, required for a given application, it is desirable to be able to measure these characteristics non-destructively and preferably in a non-contact manner. Electromagnetic (EM) sensors are sensitive to both changes in relative permeability and electrical resistivity of the samples, which in steels, vary with composition, microstructure and temperature. Therefore, the sensors have great potential for assessing the state of the steel microstructure during production or in-service.

In the last decade, multi-frequency EM sensors have been shown to be able to monitor the austenite-ferrite phase transformation in steel [2-4], and are currently being trialled

on-line during steel processing [1, 5]. They have also been shown to be able to detect decarburisation in steel rod both on-line and off-line [6-8]. However, the influence of key microstructural parameters on the EM signal is not yet fully understood. To extend the potential applications of the sensor, it is important to determine the sensitivity of, and understand the relation to, each individual microstructural factor.

1.2 Aim of the project

Therefore the aim of the project is to study the fundamental effects of different microstructure parameters on the electrical and magnetic properties of steels and hence how they affect EM sensor signals. This includes:

- Measuring the EM sensor signal for steel samples where one microstrucutral parameter is varied and using this data to determine the fundamental effect of microstructure parameters such as ferrite grain size, precipitation, phase type/balance, and pearlite interlamellar spacing on the relative permeability, and hence EM signal.

- Modelling the EM sensor and simple sample geometry using a finite element (FE) model, and using the model to predict the relative permeability value of a steel sample by fitting the modelled output with experimentally measured values.

- Incorporate ‘ideal’ microstructures into the FE model to simulate the effect of changing microstructural parameters (such as phase fraction and distribution) on the relative permeability.

- Predicting the relative permeability values for a given steel microstructure, for example using optical or scanning electron micrograph data, though FEM modelling and comparing these values with experimental measured results.

- Applying the research outcome to a commercial steel grade (dual phase steels) to determine if the EM sensor could be used as a non-destructive technique to measure microstructure and, through correlations to mechanical properties, strength.

2 Methods of steel microstructure characterisation

2.1 Conventional methods of steel microstructure characterisation

2.1.1 Optical microscopy

Optical microscopy is one of the most commonly used methods in steel microstructure characterisation. Metallographic samples are required to be carefully ground and polished to a mirror-like finish (1 micron or ¼ micron surface finish) followed by chemical etching if necessary (some microstructure features such as inclusions can be examined on the unetched surface). The microstructure is then examined with a light microscope, where the contrast in the image results from the different reflectivity of the different regions of microstructure. The more chemical active regions to the etchant will dissolve faster than the other areas hence reflect the light differently [9]. Optical micrographs can be used to identify/quantify microstructure parameters such as phase type, phase fraction, grain size/distribution, and precipitates (above approximately 0.2 micron in size due to the resolution limits of optical microscopy). Examples of an optical macrograph of a stainless steel weld, showing grain size in the order of a few millimetres, and an optical micrograph of a high nitrogen containing austenitic stainless steel sample, showing the average austenite grain size of 2.5 μm, are given in Figure 2.1 and 2.2 respectively.

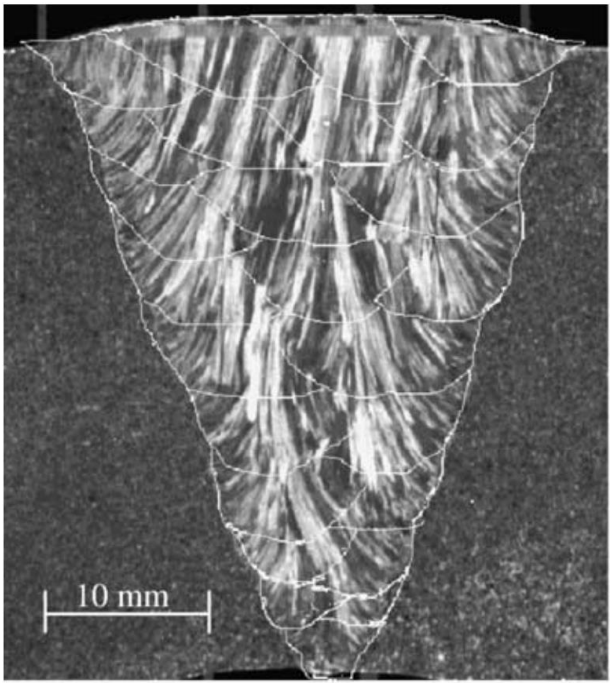

Figure 2.1: Optical macrograph of a stainless 316 weld [10]

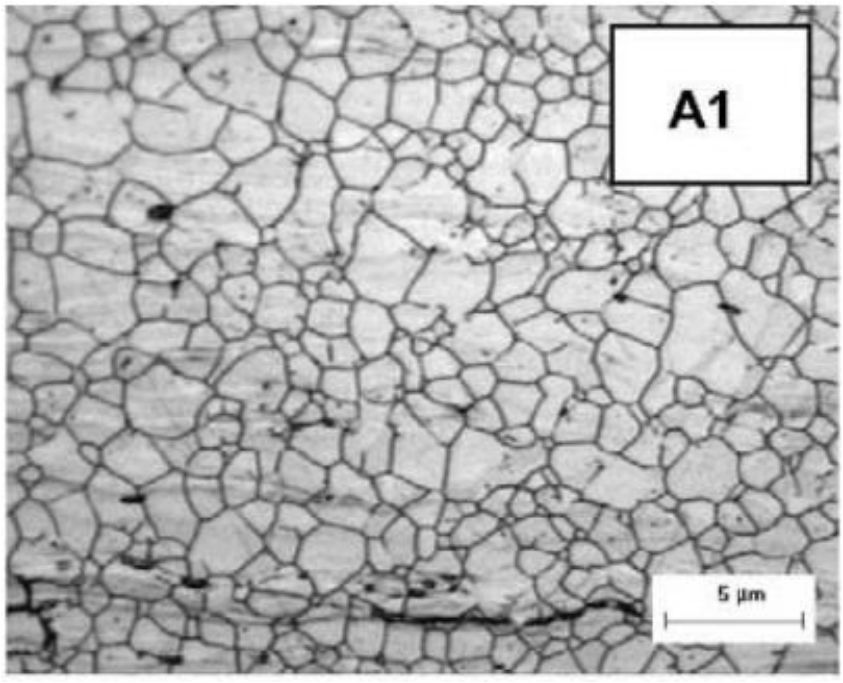

Figure 2.2: Optical micrograph of a high nitrogen containing austenitic stainless steel sample [11].

Optical microscopy is normally carried out in laboratory environment, however, in-situ observation is also possible via portable microscopes and this can be used for e.g. power plant inspection [12]. Replicas can also be used for observations of in-situ components. A replica, which is usually made of plastic thin film, is used to duplicate the microstructure from the surface of the material, particularly where that surface is difficult to reach for inspection. The surface examined has to be prepared in the same way as normal metallography samples (i.e. grinding/polishing and etching). Then the replica can be examined using optical microscopy [13]. The resolution of an optical microscope is limited by the wavelength of visible light. Therefore, some microstructure features (less than approximately 0.2 micron) are too fine to be observed.

2.1.2 Electron microscopy

Electron microscopy can be used to examine the microstructures with much higher resolution resulting from the focused high energy electron beam. The two most common types of electron microscope are scanning electron microscope (SEM) and transmission electron microscope (TEM), which use the reflection and transmission beam modes respectively. Electron microscopes can reach resolutions at the nanometer (nm) scale, making them a powerful technique to characterise the fine details of a steel microstructure, such as martensite/bainite laths, pearlite lamallaes, small precipitates and dislocation structures [14]. SEM also has great depth of field, which is useful when characterising non flat surfaces such as fracture surfaces. Accessory equipment such as energy dispersive spectrometers (EDS) and wavelength dispersive spectrometer (WDS) can be added to an electron microscope for surface composition analysis and electron backscatter diffraction analysis (EBSD) for texture measurement [14].

Most of the SEM and TEM systems are housed in stable (no electrical or mechanical interference) buildings and are relative expensive. Some portable SEM systems are available now [15], but small size samples (a few centimetres) are required. The sample size for TEM analysis is normally required to be a 3mm disc which is prepared to 100-150nm thickness before ion beam thinning or electro-polishing to give a region of approximately 30-40nm thickness that is 'transparent' to the electron beam. The preparation of TEM samples can be challenging and time consuming. Therefore, electron microscopy is a destructive technique for large steel components, and only the local microstructure is assessed.

2.1.3 Thermal analysis

Another way to assess the microstructure of steels is to use an indirect method, such as thermal analysis techniques, which are based on recording physical and/or chemical changes occurring in the material as a function of temperature. The most popular thermal analysis techniques used for steel microstructure characterisation (often phase transformation) are dilatometry and differential scanning calorimetry (DSC) [16]. Dilatometry works by detecting volume changes with temperature during phase transformation. The basic data generated are in the form of curves of dimension against time and/or temperature. An example of dilatometry results for austenitisation of a 0.13 wt% C micro alloyed steel (heated at 0.05 ℃ per second) is shown in Figure 2.3 [17], where the transformation temperatures are indicated by the volume change. Dilatometry has been used for quantifying the austenite to ferrite/pearlite transformation [18, 19] and reaustenisation from a microstructure of bainite - retained austenite [20], ferrite – carbides [21] and ferrite – pearlite [17, 22]. In addition, dilatometry has been used to generate continuous cooling transformation (CCT) and

time-temperature transformation (TTT) curves [23-25], which are very powerful tools to the steel industry. Analysis of the dilatometry data often involves semi-empirical methods, for example careful deconvolution to the measured volume changes are required [22].

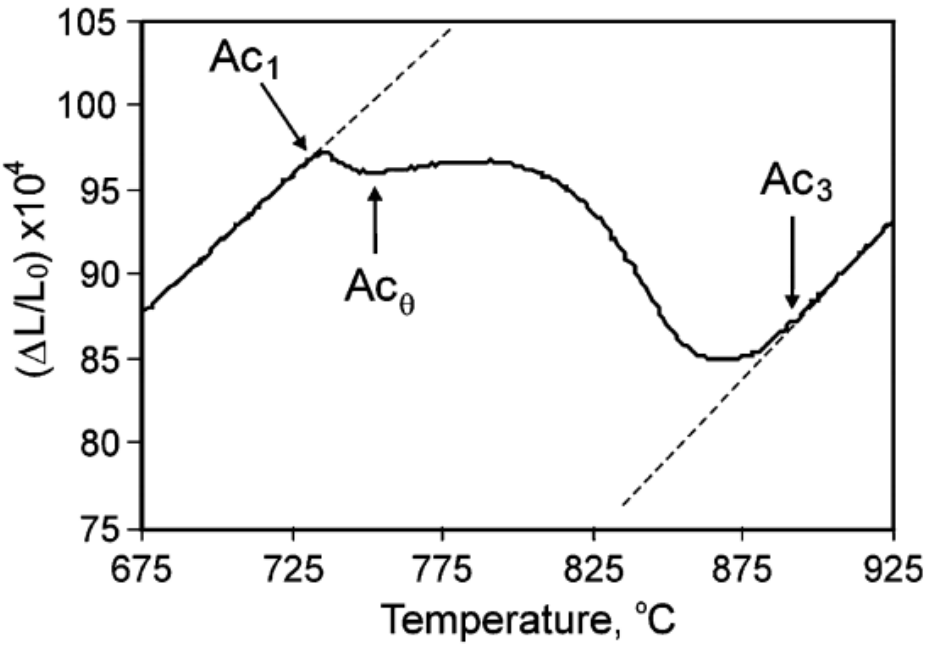

Figure 2.3: An example of dilatometry results for austenitisation of a 0.13 wt% C micro alloyed steel (heated at 0.05 ℃ per second). Austenite formation start (Ac1) and end (Ac3) temperatures and the pearlite dissolution finishing temperature (Ac_θ) are indicared in the Figure [17]

DSC works in a similar way to dilatometry, but instead of measuring the length or volume change the difference between a test sample and a reference sample (of known microstructure) in the amount of heat required to increase their temperature is measured. An example of dilatometry results for a normalised and tempered 9Cr alloyed steel sample during heating (up to 1253 K) and cooling cycles is shown in Figure 2.4, where the transformation temperatures are indicated by the heat change [26]. DSC can also be

used for monitoring phase transformation [26-28], precipitation [29-32], recrystallisation and recovery [33-35] process in steels.

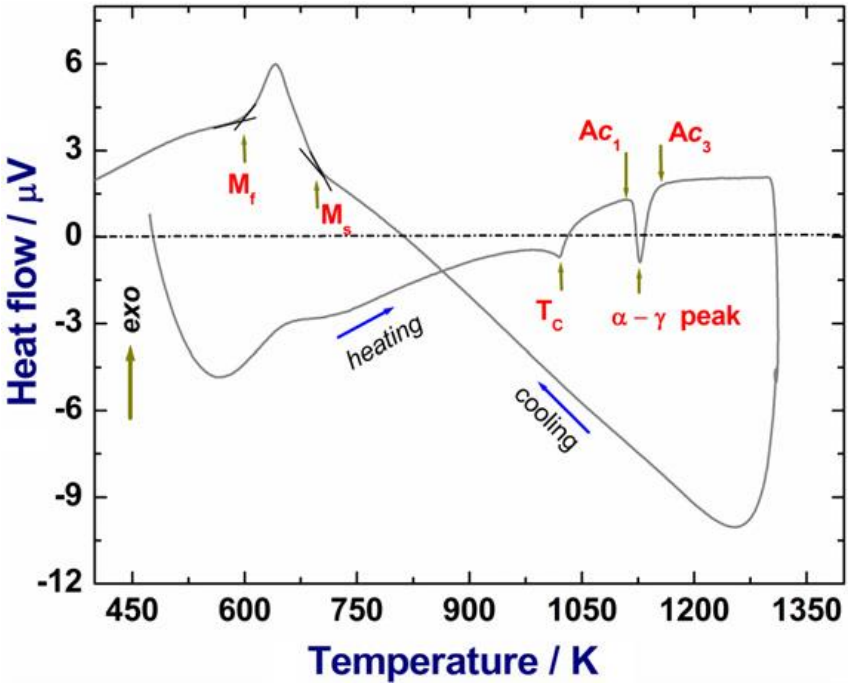

Figure 2.4: An example of DSC results for a normalised and tempered 9Cr alloyed steel sample during heating (up to 1253 K) and cooling cycles. Austenite formation start (Ac1) and end (Ac3) temperatures, martensite formation start (M_s) and end (M_f) temperatures, Curie temperature and the peak for ferrite – austensite transformation(α – γ peak) are indicared in the Figure [26].

2.1.4 X-ray

X-rays are short wavelength (0.01 to 10nm) high energy electromagnetic waves. The low wavelength allows them to penetrate solids with partial absorption during transmission. When X-rays interact with a sample, a portion of the beam will be scattered by the elections in the material. A schematic diagram of X-ray diffraction by planes of atoms is given in Figure 2.5 [9].

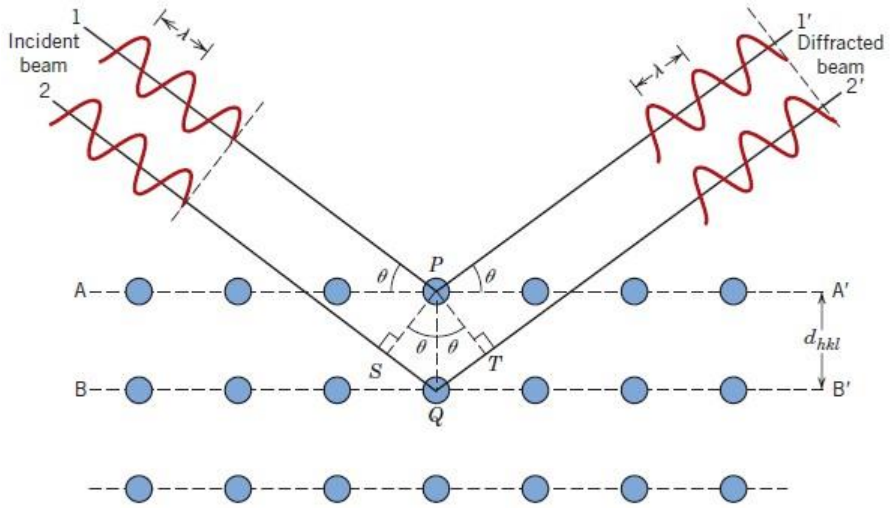

Figure 2.5: Schematic diagram of x-ray diffraction by planes of atoms [9]

Bragg's law (equation 2.1) gives an expression that relates the X-ray wavelength to interatomic spacing and angle of diffraction [9].

$$n\lambda = 2d_{hkl}sin\theta \qquad \text{Equation 2.1}$$

Where n is the order of wavelength (may be any integer), λ is the wavelength, d_{hkl} is interplanar spacing and θ is the angle of incident beam to the targeted solid.

The X-ray diffraction technique can be used to measure steel crystallographic texture [36, 37] precipitates [38-41] and the microstructural phase balance [38, 42-49]. The technique is indirect, for phase fraction it will average over the target area and therefore not give spatial information (which can be obtained from direct observations such as optical metallography). Most analytical X-ray diffraction measurement systems are lab based, where small samples (normally smaller than a 10mm side length cube) are used. The penetration depth of X-rays in laboratory systems is generally very small (tens of microns). However, there are some high energy X-ray systems and industrial systems

than can examine thicker samples. Suwanpinij et al. [50] measured the change in phase fraction during the annealing process of a deformed TRIP steels using in-situ high energy X-ray diffraction in a dilatometer that was installed in the synchrotron beamline. The X-rays used in their study can penetrate through the sample thickness (5mm), however this approach can only be used in the synchrotron which is expensive and not appropriate for industrial application. Also, transmission X-ray systems has been developed for in-situ texture measurement in a rolling strip mill [51, 52]. The technique use high energy X-ray (energy of 60 up to 100 keV) that allows the penetration through the steel strip thickness of 2.5 to 5 mm. It was reported that the device allows the measurement in the industrial production environment of a strip rolling plant as the X-rays are largely unaffected by steam and dust.

2.2 Ultrasonic methods

2.2.1 Introduction

Ultrasonic waves are high frequency sound waves that is above about 20 k Hz (frequency too high to be audible by the human ear). The features of the wave such as velocity, attenuation and analysis of backscattered signals can be used to study the material dimensions, composition, microstructure and elastic properties [53, 54]. The ultrasonic technique (UT) is one of the most widely used non-destructive evaluation (NDE) methods today, it has been shown to be flexible, robust and has little environmental or health risks. The ultrasonic waves used in measurement are usually generated by a piezoelectric, electromagnetic or laser type transducer. The typical frequency range of ultrasonic waves in NDE applications is from 50k Hz to several GHz [53].

2.2.2 Pulse echo and pulse transmission method

The pulse echo method is the simplest and most commonly used approach in UT testing. The method is based on transmission of an ultrasonic wave, which is generated by a piezoelectric transducer, into the material to be tested at a pre-chosen frequency. The reflections of the waves are then detected by an oscilloscope and the transit time after single or multi reflections is measured. When the material being tested has a high attenuation coefficient, the amplitude of echo waves may not be sufficient for evaluation, then the pulse transmission method is applied [55]. In this method, two probes are located in line on opposite sides of the samples, one acting as the transmitting and the other as the receiving probe.

Gur and Tuncer investigated the effect of microstructure phase type on ultrasonic velocity using a lab based direct contact pulse echo measurement system on heat treated AISI 4140 (0.4 wt% C steel with additions of Cr and Mo) and AISI 5140 steels (similar composition to AISI 4140, with less Cr and no Mo and lower strength) [56]. Samples of each steel grade were austenitised at 850 ℃, to minimise any effect of differences in initial texture and grain size, and then quenched/isothermally heat treated to generate microstructures with different phase type/balance. The velocity of both the longitudinal and transverse waves measured in both steel grades was found to be lowest for a martensite microstructure, then bainite, followed by fine pearlite-ferrite and highest in coarse pearlite-ferrite (shown in Figure 2.6). The differences in velocity were believed to be due to the different elastic moduli of the phases, which are affected by lattice distortion and misorientation [56]. Freitas et al. also reported an increase of velocity from the hardest phase (martensite) to the softest phase (ferrite) in AISI 1045 steel (a plain 0.4-0.5 wt% C grade), whilst the opposite trend was found for the ultrasonic attenuation in their lab based measurements [57].

Some lab based studies have examined the correlation between the grain size and ultrasonic velocity. Vary reported that the ultrasonic velocity decreases with decreasing grain size in maraging steels and in a Ti alloy [58]. Palanichamy et al. found a mostly linear decreasing relationship between ultrasonic velocity and grain size in austenite stainless steel (stainless 316) [59]. It was reported that the decrease in velocity with increase in grain size is attributed to the increased resonance interaction between the ultrasonic waves and grains. This is in agreement with the theoretical study carried out by Hirsekorn [60]. In this theory, the ultrasonic velocity of plane longitudinal and transverse waves in polycrystal materials can be considered as the product of the wave-

number and grain diameter. Ultrasonic velocity and attenuation have been shown to correlate well with the amount of deformation in the forging process of cast steels due to grain size and dislocation density changes [61]. Vasudevan and Palanichamy did interrupted ultrasonic velocity tests during aging of a Ti-modified austenitic stainless steel; the recovery, recrystallization and completion of the recrystallization stages were identified due to the dislocation density and texture changes [62]. Vargas-Arista et al. reported that the ultrasonic attenuation increases due to increases in the precipitation density and size in welded joints of API 5L X52 pipeline steels.

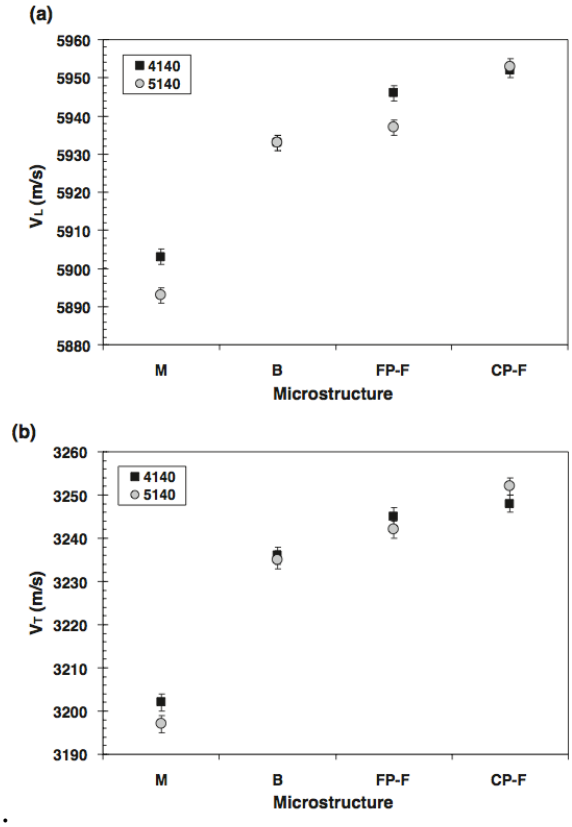

Figure 2.6: Microstructure and sound velocity of heat treated AISI 4140 and AISI 5140 samples: (a) Longitudinal wave (f=20 MHz), (b) Transversal wave (f = 5 MHz) (M: Martensite, B: Bainite, FP–F: Fine pearlite–ferrite, CP–F: Coarse pearlite–ferrite) [56].

The major disadvantages of the traditional pulse echo method are: (a) they require the transducer to be in contact with the sample surface and (b) the piezoelectric type transducer normally does not function at high temperature (above 327 ℃) for in-situ monitoring during steel processing stages or heat treatment [63].

2.2.3 Laser ultrasonic

Laser ultrasonic methods are a relatively recent technique that are based on generating and detecting ultrasonic waves by a pulsed laser, which provides a number of advantages such as non-contact measurement (operates at a distance of up to several meters), remote control, wide range of frequency and works relatively well at high temperature [55, 64-67].

Hutchinson et al. used laser ultrasonic techniques to monitor the recrystallisation process in stainless steel 316 and interstitial free (IF) steels [68]. A linear decrease in wave velocity, as a result of increased recrystallisation fraction, was observed for the austenitic stainless steel (shown in Figure 2.7). The authors stated that the change of wave velocity is due to a uniform change in texture during the recrystallisation process as the velocity of ultrasonic waves is only affected by elastic properties which is dependent on the crystallographic texture, whist attenuation of the waves is dependent on the grain size. However, the wave velocity showed no change in value during the first half of recrystallisation, and then increased with a further increase in recrystallisation fraction for the IF steel (shown in Figure 2.8). The authors stated that this was due to a different and more complex change in texture occurring in the IF steel compared to the austenitic stainless steel. This relationship for the IF steel is in agreement with the results from Pandey's work [69].

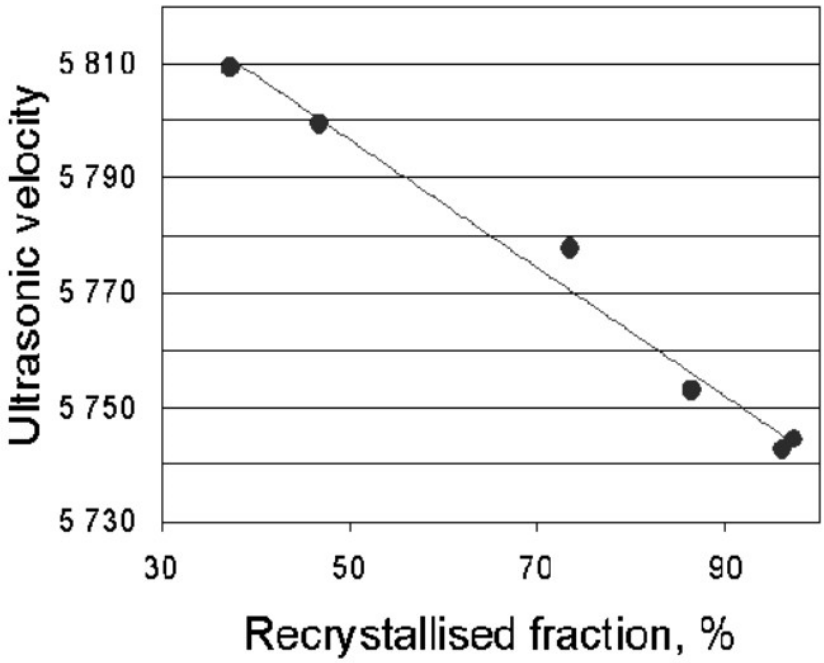

Figure 2.7: Variation in ultrasonic velocity as a function of recrystallised fraction in cold rolled 316 stainless steel [68].

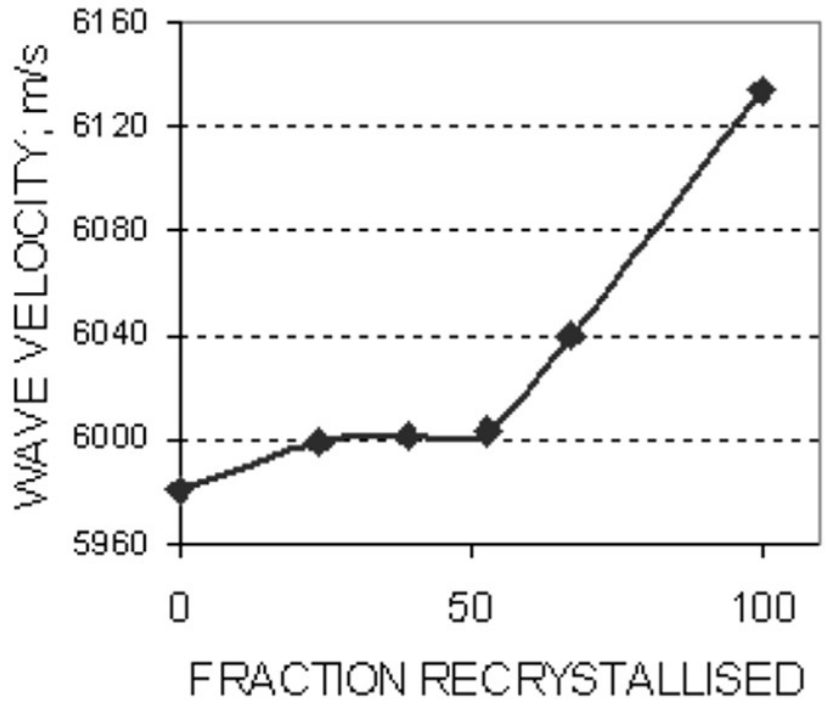

Figure 2.8: Development of ultrasonic velocity with recrystallised fraction in IF steel [68].

A few studies on austenite-ferrite/pearlite transformation have been carried out using the laser ultrasonic technique at elevated temperatures [64, 67, 70-73]. Kruger et al. studied the effect of austenite decomposition on ultrasonic velocity in low carbon steels in-situ in a Gleeble 3500 thermomechanical simulator using the laser ultrasonic method [70]. The ultrasonic velocity was found to decrease almost linearly with temperature but there was a change in slope during the austenite decomposition (shown in Figure 2.9). The dependence of velocity on temperature in the austenite phase was found to be insensitive to the carbon content in solid solution in the steel. Steel samples with different carbon content can be clearly distinguished from the slope of the velocity with temperature in the austenite decomposition period and starting temperature for the decomposition process. The percentage of decomposition estimated by the rule of mixtures showed good agreement with dilatometry measurements in the Gleeble simulator system. [70]. Hutchinson et al. reported online trails on the use of laser ultrasonic measurement on the moving hot strip. The authors stated that the ultrasonic signal is good, and austenite to ferrite transformation state could be determined by analyse the velocity of the waves [74].

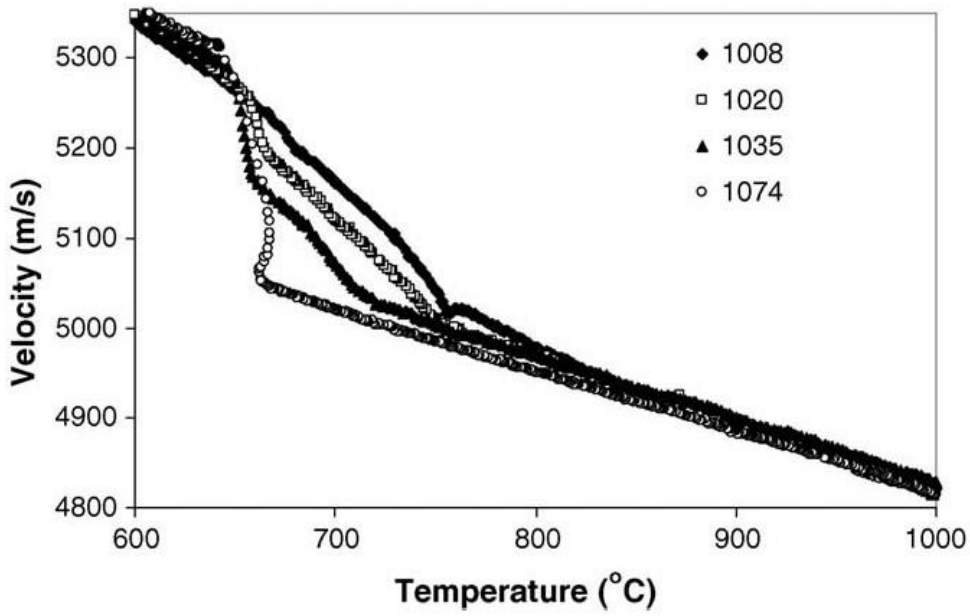

Figure 2.9: Ultrasonic velocity for different carbon content steels measured during cooling over the temperature range where austenite decomposition into ferrite+pearlite occurs. (Carbon content: 0.08 wt% C in 1008, 0.2 wt% C in 1020, 0.35 wt% C in 1035 and 0.74 wt% C in 1074)[70]

2.3 Electromagnetic methods

2.3.1 EM sensors

Electromagnetic (EM) sensors (sometimes referred to as eddy current sensors) operate on the basis of detecting changes in relative permeability and electrical resistivity in the target materials. This type of NDT approach has several advantages including being non contact, having a fast response and is relatively inexpensive setup [53]. EM sensors consist of exciting coils and sensing coils. Many different sensor designs and operating frequency ranges have been used to suit different applications. For example, a cylindrical EM sensor was used for assessing lab based rod samples [6], while a H shaped (or U shaped) sensor was used for plate or strip type samples [75]. A schematic diagram of a cylindrical EM sensor is shown in Figure 2.10 [76]. In this case, the exciting coil is driven by an impendence analyser that generates an ac current with constant voltage and sweeps though a frequency range of 10 to 1M Hz. The sensing coils detect the resulting field and the real and/or imaginary part of the inductance for the different frequencies is recorded.

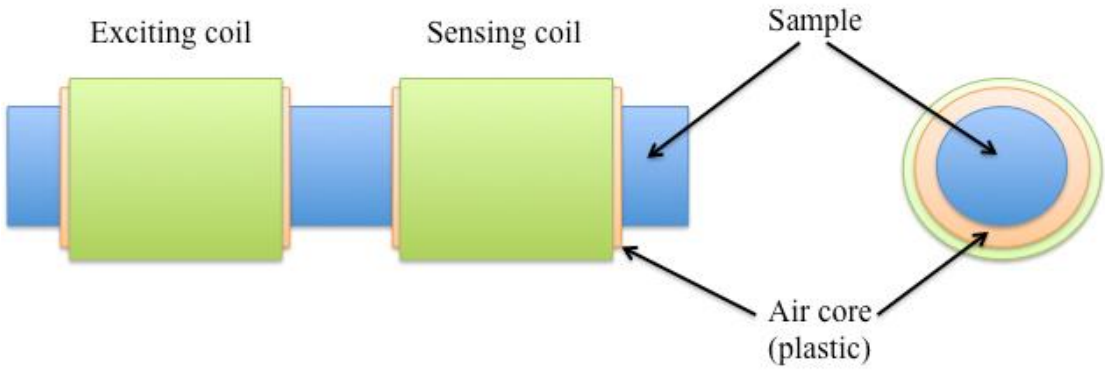

Figure 2.10：Schematic diagram of a cylindrical shaped EM sensor [76].

At low frequency, the exciting coil tends to magnetise the sample, which increases the coil inductance. Here, the magnitude of the eddy currents is low and the electromagnetic field can penetrate deeper into the sample. The mutual inductance of the sensing coil is predominantly affected by the magnetic permeability of the sample.

As the frequency is increased, the eddy currents, which oppose the driving current become more dominant (skin effect) and the coil mutual inductance decreases. The mutual inductance is affected by both the electrical resistivity and magnetic permeability of the sample. The sampling depth is reduced due to the resistance to the electromagnetic field penetration caused by the eddy currents. Therefore, samples with different electrical resistivity and magnetic permeability can be distinguished by the different magnitude and shape of the inductance vs frequency curves.

An example of a typical multi-frequency EM senor output is shown in Figure 2.11. At low frequencies (less than approximately 100 Hz) the real inductance is independent of frequency and is influenced by the relative permeability of the target sample. As the frequency increases the real inductance decreases until at high frequencies (in this case approximately 1000 Hz) eddy currents dominate and little difference between the samples is observed. Figure 2.11 shows that the power plant steel T22 in different heat treatment conditions can be clearly distinguished by the sensor output at low frequencies [77].

In the last decade, multi-frequency EM sensors have been shown to be able to monitor the austenite-ferrite phase transformation in steel [2-4], and are currently being trialled on-line during steel processing [1, 5]. They have also been shown to be able to detect

decarburisation in steel rod both on-line and off-line [6-8]. Other successful examples of measuring microstructures by lab based eddy current sensors include measuring pearlite fraction in cast iron [78], pearlite interlamellar spacing in tyre wire steel [76, 79] and martensite fraction in dual-phase steels [80]. Details of how steel microstructures affect EM properties hence the sensor signal are discussed in sections 3.7 in Chapter 3.

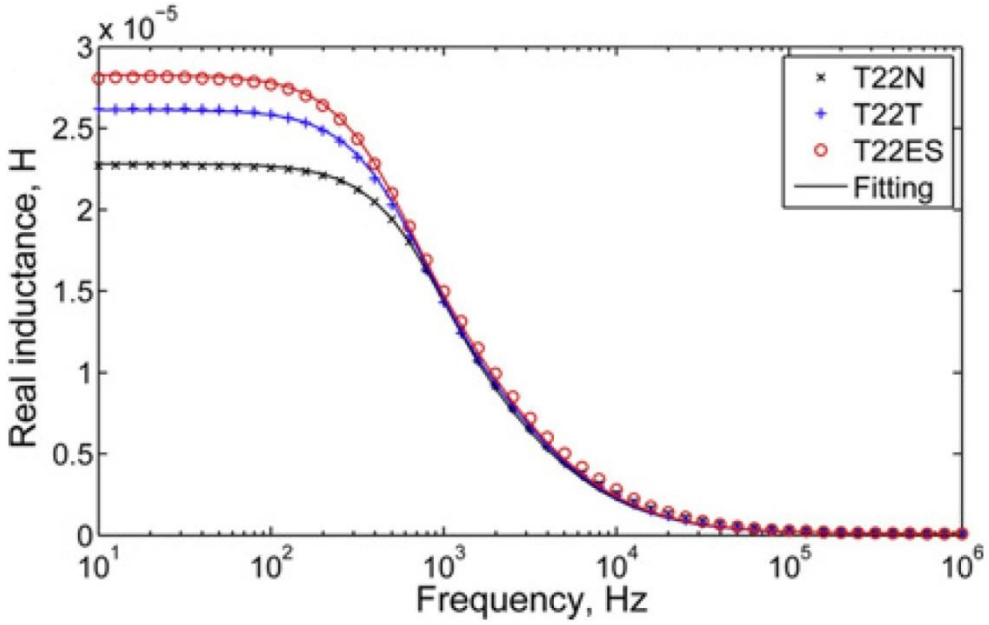

Figure 2.11： An example of the typical multi-frequency EM senor output (in this case power plant steel T22 in different heat treatment conditions are distinguished, where N is the normalised condition, T the normalised and tempered condition and ES the ex-service condition) [77].

Some researchers have attempted to link the mechanical properties directly with sensor outputs [80-83]. Konoplyuk et al. measured the empirical correlations between the mechanical properties (including hardness, tensile strength and elongation) and a lab-based sensor output, at an optimum frequency of 50 kHz, in FCD 450–600 grades cast

iron (according to the Japanese standard) with a changing ferrite-pearlite phase balance [78]. The sensor output values were found to decrease linearly with hardness (shown in Figure 2.12) and tensile strength (shown in Figure 2.13), whilst increase linearly with elongation (shown in Figure 2.14). The correlation coefficients R of these relationships were found to be high and close to each other (-0.88, -0.84 and 0.83 for hardness, tensile strength, and elongation respectively). However, the fundamental relation between the microstructure parameter and magnetic permeability / electrical resistivity was not given in this study [78].

Ghanei et al. studied the relationship between the mechanical properties (including hardness, tensile strength, yield strength and elongation) and normalised impedance values at an optimum frequency of 250 Hz in heat-treated dual phase steel with changing ferrite – martensite phase balance, measured by a lab-based eddy current sensor [80]. The optimum frequency has been determined by applying a regression analysis and choosing the best correlation coefficient between the impedance and the harmonic with a frequency range from 100 Hz to 1000 Hz. The normalised impedance values were found to decrease with hardness (shown in Figure 2.15), tensile strength, and yield strength but increase with elongation (shown in Figure 2.16). The correlation coefficients after applying a second order polynomial fitting were found to be very high (R^2 values were determined to be 0.8987, 0.9346, 0.9271 and 0.8546 for hardness, tensile strength, yield strength and elongation respectively). The authors state that the impedance value at the optimum frequency (250 Hz) is affected by both the magnetic permeability and electrical resistivity of the sample. The fundamental explanations of the effect of martensite fraction on magnetic permeability / electrical resistivity were not given [80-83].

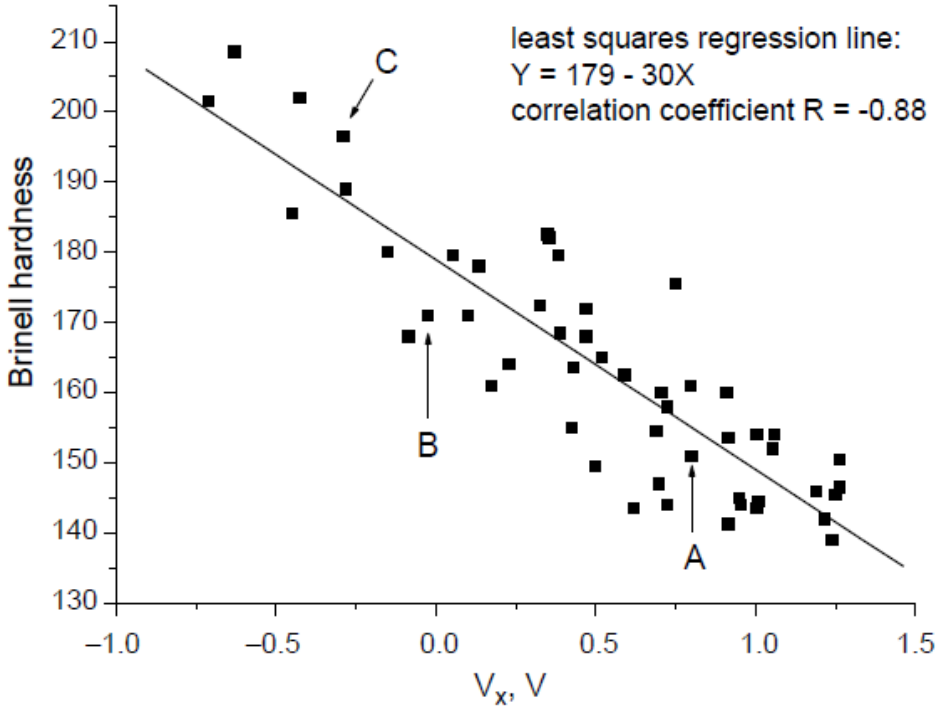

Figure 2.12: Brinell hardness changes with sensor output for cast iron samples [78].

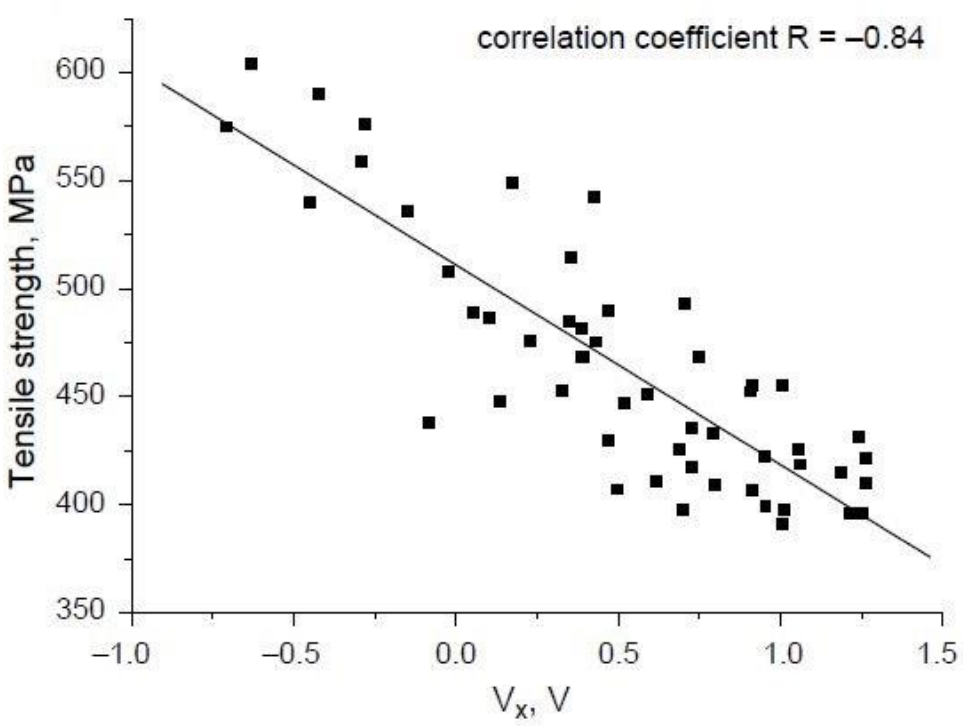

Figure 2.13: Tensile strength changes with sensor output for cast iron samples [78].

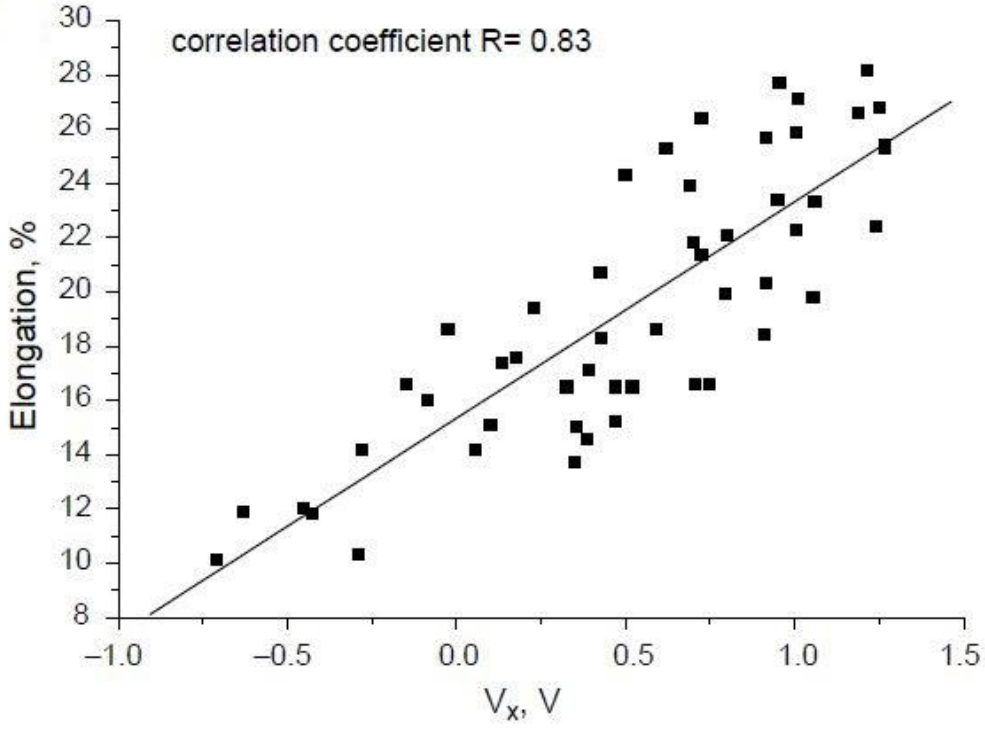

Figure 2.14: Elongation changes with sensor output for cast iron samples [78].

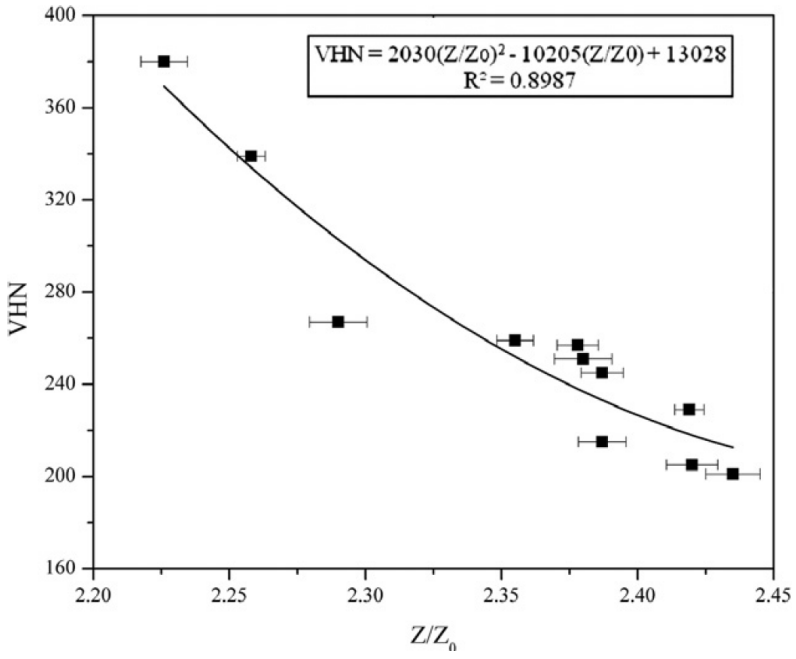

Figure 2.15: Vickers's hardness changes with normalised impedance (250 Hz) for heat treated dual phase steels [80].

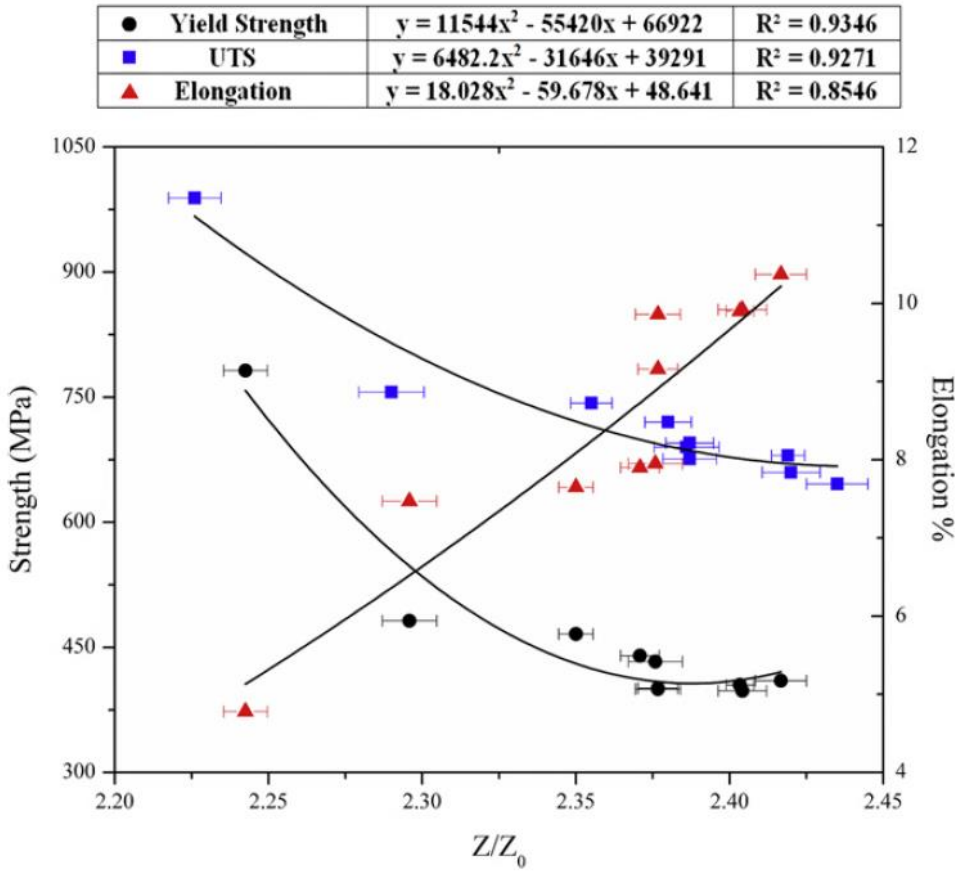

Figure 2.16: Tensile strength, yield strength and elongation changes with normalised impedance (250 Hz) for heat treated dual phase steels [80].

2.3.2 Hysteresis loops

Magnetic inductive parameters, such as initial permeability, maximum permeability, differential permeability, remanence, and coercivity, derived from hysteresis loops, have been used in the literature to correlate to the microstructure of steels as a non-destructive testing method. Details of what these parameter mean and how steel microstructures affect these parameters are discussed in sections 3.6 and 3.7 in Chapter 3 respectively. An example of hysteresis loops (with minor magnetisation curves being shown with the major loop) of a 99.99% pure iron, and a 0.45 wt% C steel are shown in Figure 2.17 [84]. These show that the hysteresis loop shape and related properties

such as the coercivity and remanence change with carbon content. Generally the steel becomes more difficult (require higher applying magnetic field) to achieve fully magnetised state as the carbon content increases.

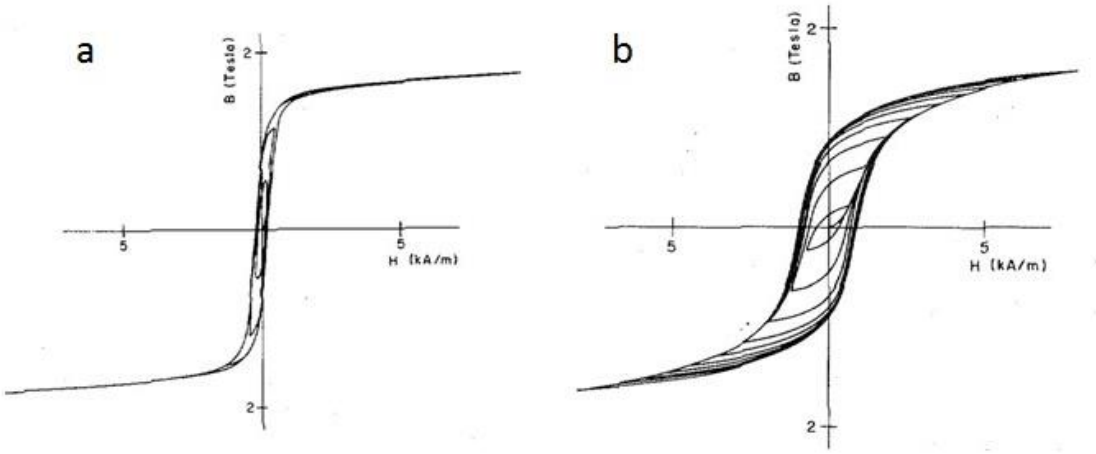

Figure 2.17: Hysteresis loops for sample of a) 99.99% pure iron and b) 0.45 wt-%C steel [84]

The equipment used for the generation of hysteresis parameters normally requires the sample and the pick-up coil to be surrounded by a magnetising coil. In many steel processing applications, the steel is either moving quickly or is too hot to place the coils close enough to its surface, therefore, there are some limitations in terms of this technique being applied on-line during the steel manufacturing process [1].

2.3.3 Barkhausen noise

Magnetic Barkhausen noise (MBN) refers to noise-like voltage pulses that occur during the magnetisation process of a polycrystalline ferromagnetic material. A typical MBN signal for a 0.44 wt% C steel (50% pearlite + 50% ferrite microstructure) is shown in Figure 2.18 [85]. The high frequency changes of the noise are due to the discontinuous

movement of magnetic domain walls as they overcome pinning sites. Precipitates [86], dislocation structures [87, 88] and grain boundaries [89, 90] are known to pin magnetic domain walls and therefore changes in these will affect the MBN signal [88].

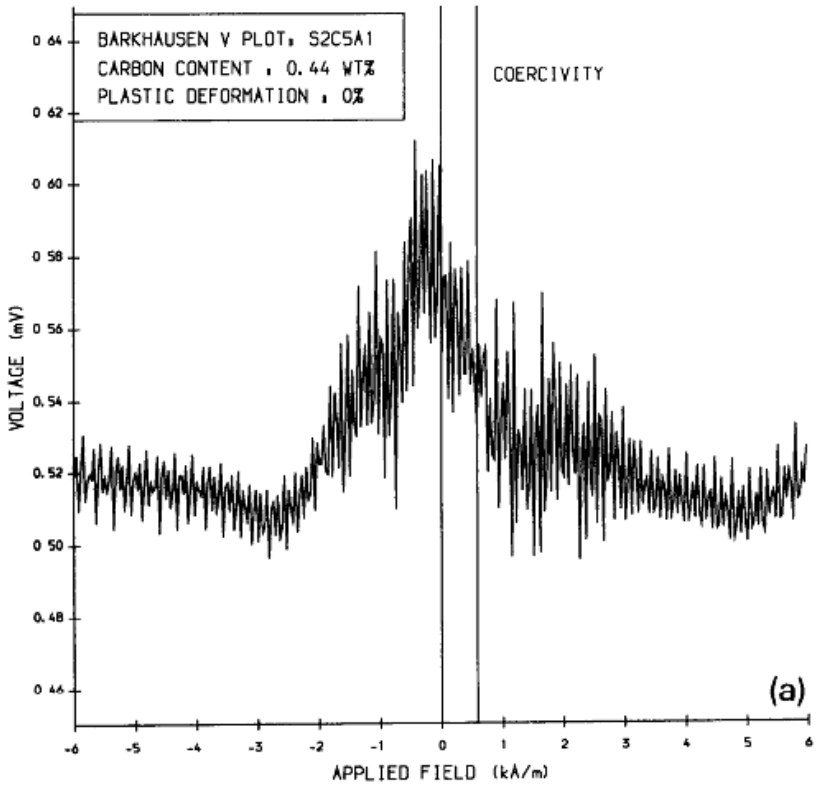

Figure 2.18: A typical MBN signal for a 0.44 wt% C steel (50% pearlite + 50% ferrite microstructure) [85].

Thompson and Tanner measured the MBN signal for plain carbon steels with different pearlite fractions of 20%, 50%, 75% and 100% [91, 92]. The MBN of the 20% pearlite sample showed a central peak as well as an initial peak, the latter one not being observed in the other samples. This was stated to be due to the high ferrite fraction in the 20% pearlite sample leading to much easier irreversible domain wall movement when the magnetic field is reduced from saturation. As the pearlite fraction increased to 50% the amount of pro-eutectoid ferrite is reduced hence the initial peak is lowered and is

difficult to distinguish from the 75% and 100% pearlite samples that only have a central peak in their MBN [91]. Saquet et al. investigated the effect of microstructural phases including ferrite, pearlite, martensite and tempered martensite on the MBN [93]. The MBN results are very different for the different microstructures (shown in Figure 2.19) and it was found that the MBN also showed different signals after tempering of martensite at different temperatures (shown in Figure 2.20).

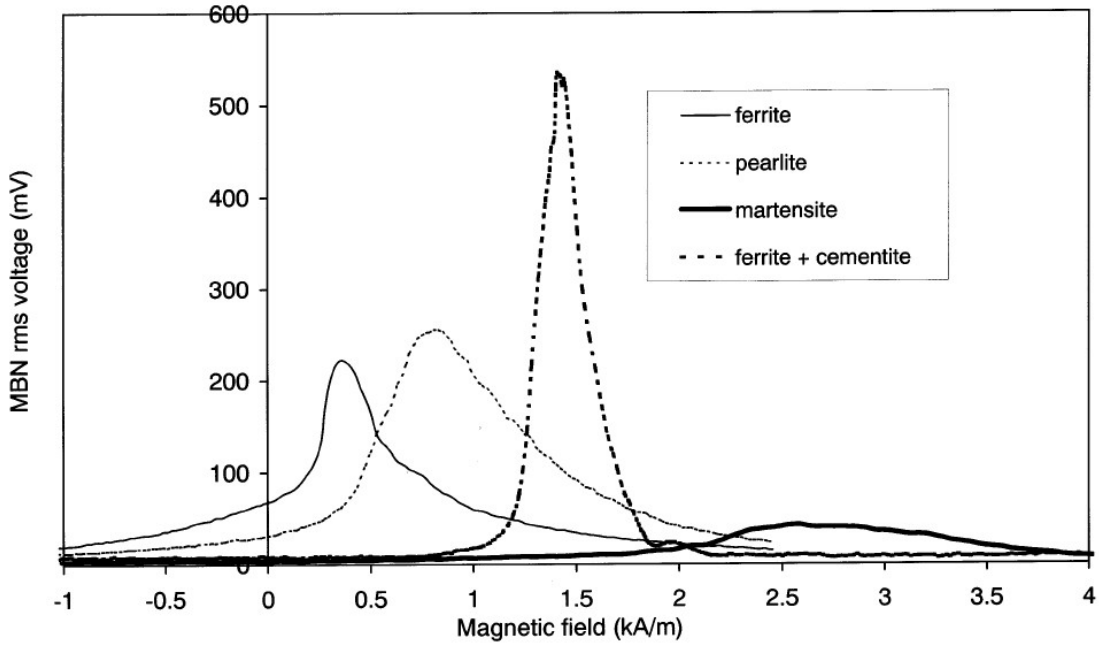

Figure 2.19: MBN curves for ferrite, pearlite, martensite and tempered martensite (ferrite + cementite) (0.55 wt% C)[93].

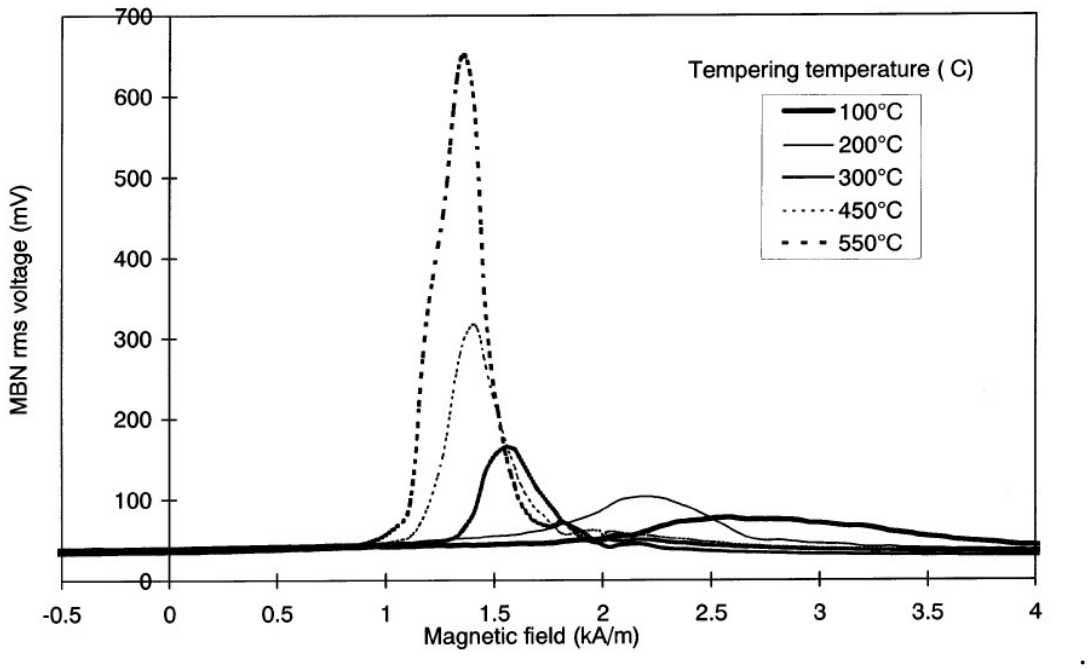

Figure 2.20: MBN curves for martensite (0.55 wt% C) tempered at 100-600 ℃.[93]

Recently, Ghanei et al. measured the MBN signal for heat-treated dual phase steel with a changing ferrite – martensite phase balance [94]. The MBN peak height was found to increase with martensite fraction and the peak position shifted to a higher value of magnetic field (shown in Figure 2.21). This was stated to be due to the fact that more pinning sites against the domain wall movement were produced as the martensite fraction increases. Therefore, a larger field was required for their motion. The peak height and peak position were reported to correlate well with the martensite fraction (shown in Figure 2.22). The R^2 value was measured as 0.9619 and 0.9859 using second order polynomial fitting. In addition, the MBN peak height and peak position were attempted to be correlated to the mechanical properties (including yield strength, tensile strength, and hardness). The peak height and peak position increase with yield strength, tensile strength, and hardness (shown in Figure 2.23). Using second order polynomial fitting, the correlation coefficients were found to be very high ($0.9411 < R^2 < 0.9822$).

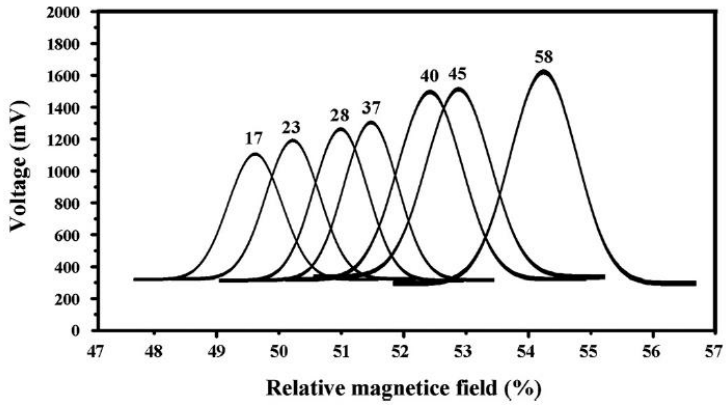

Figure 2.21: MBN peaks for DP steels with different martensite fractions [94].

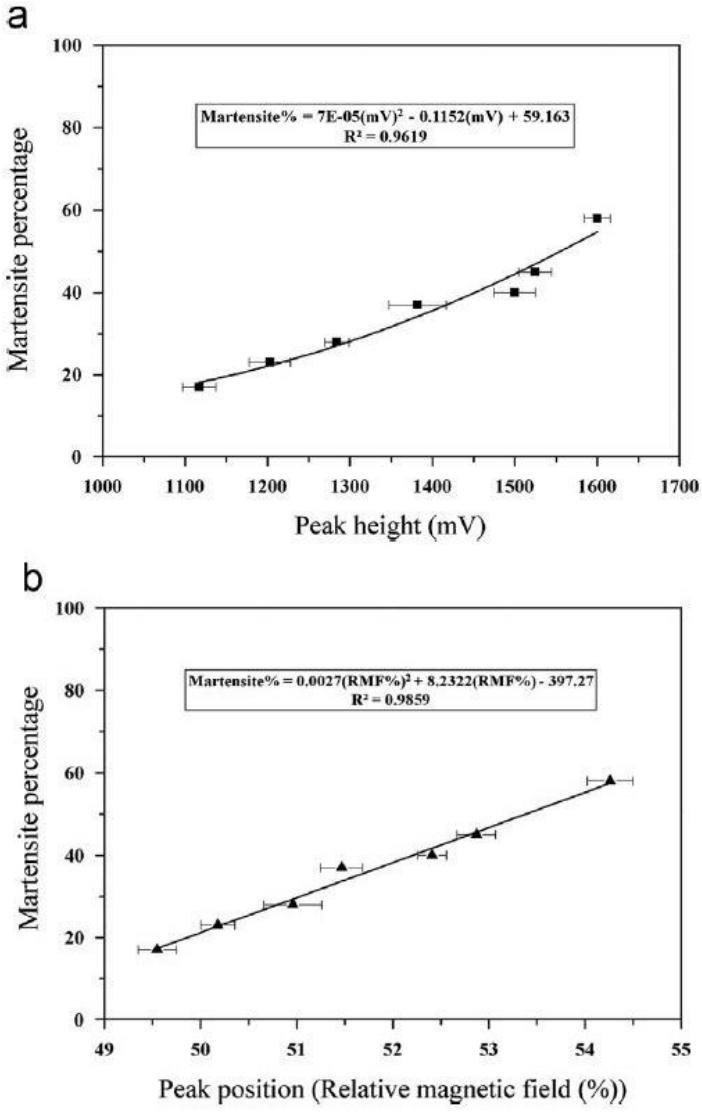

Figure 2.22: MBN peaks a) height and b) position plot with martensite fraction [94].

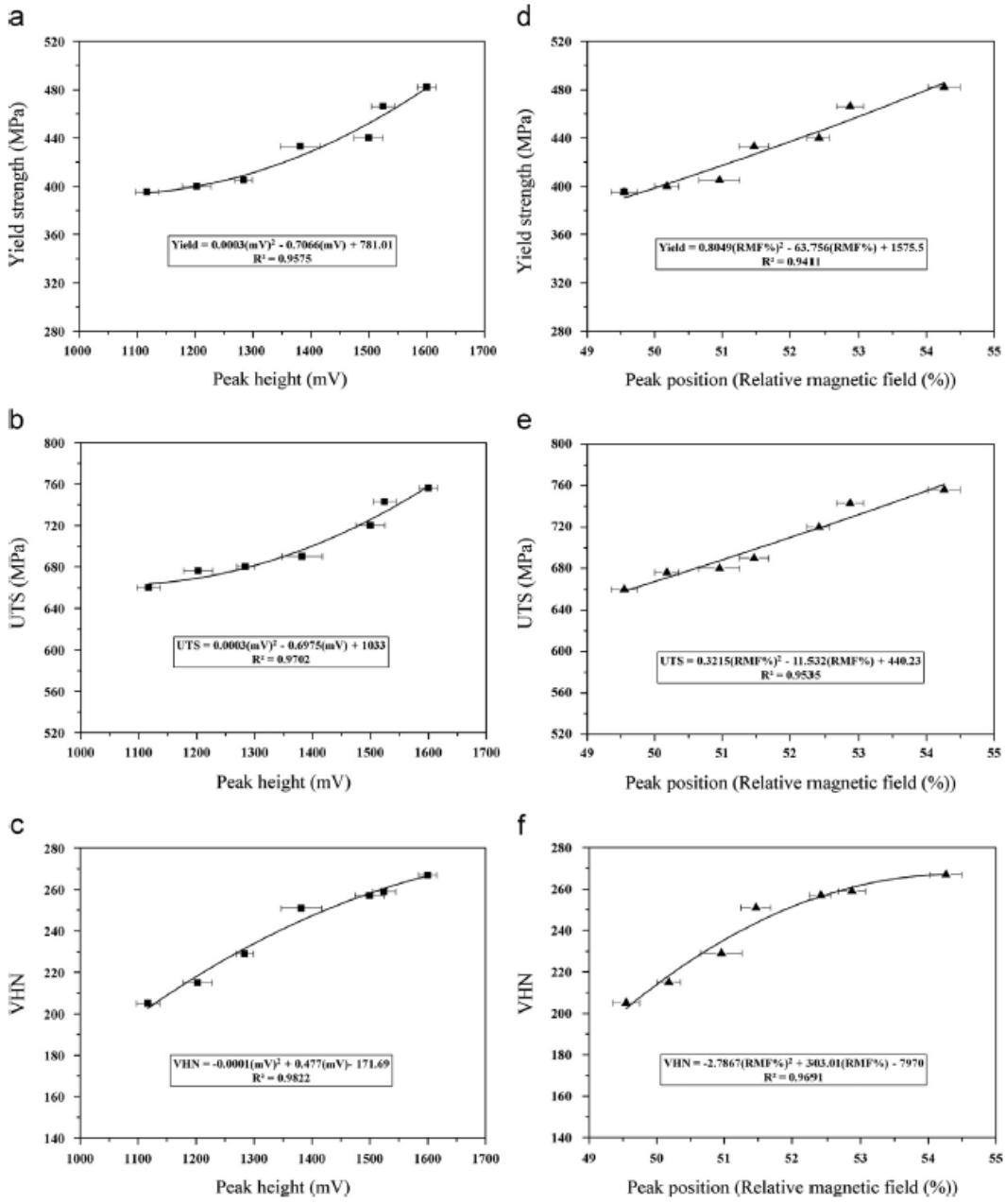

Figure 2.23: Relation of MBN peak height and yield a) yield strength, b) tensile strength (UTS) and c) hardness, and relation of MBN peak position and d) yield strength, e) tensile strength (UTS) and f) hardness [94].

Pal'a and Bydzovsky measured the MBN in non-oriented silicon steels with different grain sizes ranging from 28 to 150 μm [89]. It was reported that the strength of the MBN signal did not show a linear relationship with the grain size due to the two

competing mechanisms. For grain sizes of 28 to 46 μm, the MBN signal increased. This is believed to be due to the increase of correlation domain volume. The correlation domain volume is a term in Titto's model [95] to describe the region inside which the movement of the domain wall are strongly correlated to each other. The model assumes that inside the correlation domain volume, the elementary MBN pulses caused by individual domain wall pinning cluster into large discontinuities that result a higher noise signal. However, with the increase of grain size from 46 to 150 μm, the MBN signal was found to decrease with increasing grain size. This is believed to be due to the decreased number of domains and walls per unit volume, as the size of the domains increase with the size of the grains (in the grain size range of 50 μm - 10 mm) [96]. As a result, there are less domain nucleation and domain wall pinning process, thus the MBN signal decreased with grain size. [89].

Yamaura et al. reported a Hall-Petch type relation between the grain size and MBN power in pure iron samples with grain sizes of 48-179 μm (shown in Figure 2.24) [90]. This was reported to be due to the grain boundaries being preferential sites of domain nucleation and pinning of the domain wall movement. The Barkhausen jump increases with grain boundary density per volume, hence the Hall-Petch relationship was observed [90].

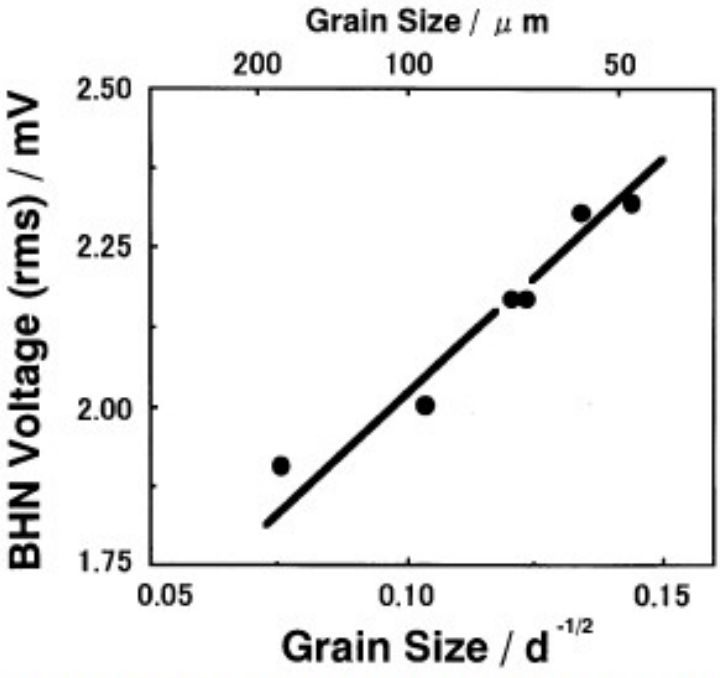

Figure 2.24: Hall-Petch type relation between the grain size and MBN power in pure iron samples with grain size of 48-179 μm [90].

Gurruchaga et al used the MBN technique to monitor recrystallisation during annealing of a cold rolled low carbon steel [97]. It can be seen from Figure 2.25 that the parameters derived from the MBN measurements can be correlated to recrystallised fraction (X_v) and hence be used to monitor recrystallisation.

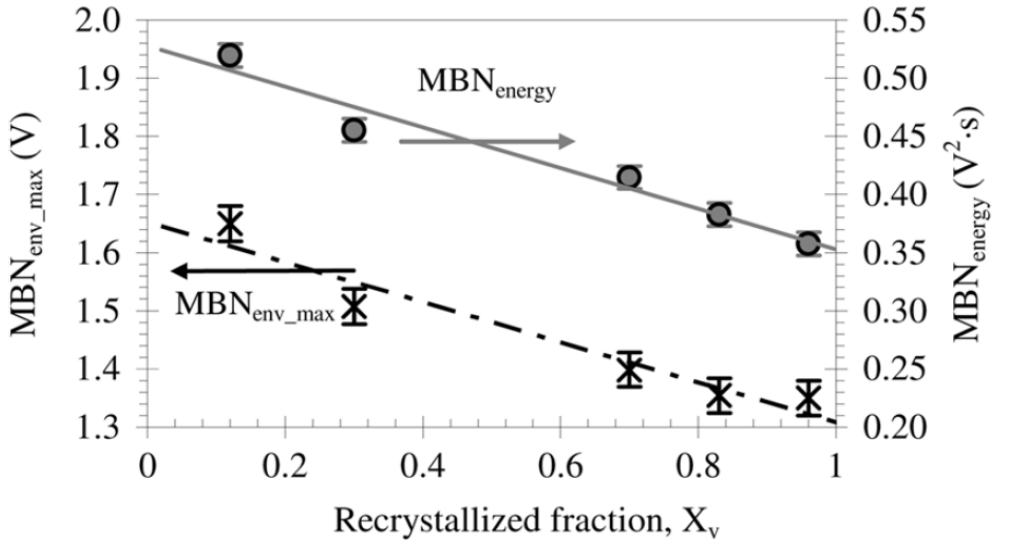

Figure 2.25: Correlation between the amplitude of the peak of the MBN envelope, (MBNenv-max) and the energy of the MBN signal (MBNenergy) with the recrystallised fraction (Xv) for a cold rolled low carbon steel annealed at 575 ℃ [97].

The frequency used in the MBN technique is normally reasonably high (about a few kHz) which results in a strong eddy currents effect and small penetration depth of the signal into the specimen. Therefore, MBN measurements are strongly influenced by near surface microstructure. The MBN measurement system typically has a similar set up as hysteresis loop testing and also requires a Hall probe to be placed on the surface of the samples. This limits its adaptability to on-line measurements, and no measurements have been reported in the literature applying this technique (or hysteresis loop testing) during steel processing.

3 Magnetism and electromagnetic properties of steels

3.1 EM fundamentals

The strength and direction of a magnetic field can be described as endless lines, as shown by Faraday. The total number of lines per unit area is defined as the magnetic flux density (B). During magnetisation, magnetic materials produce a magnetic field in response to the applied field (H). The applied field and the induced magnetic strength are related by a materials parameter of relative permeability (μ_r). B, H and μ_r are related as in equation 3.1 [98]:

$$B = \mu_0 \mu_r H \qquad \text{Equation 3.1}$$

Where B is the magnetic induction in Tesla, $\mu_0$is the magnetic permeability of free space in henry/m, μ_r is the relative permeability of the material, and H is the applied magnetic field strength in A/m.

A magnetic field can be produced either by a permanent magnet or an electrical current. One of the simplest ways of producing a magnetic field is by applying a current to a multi-turn coil. The direction of the field is parallel to the axis of the coil, and the field strength H can be calculated by (equation 3.2) [98]:

$$H = \frac{NI}{l}$$ Equation 3.2

Where N is number of turns, I is the current flow in the coil in ampere, l is the length of the coil in m. Combining equation 3.1 with equation 3.2, the magnetic flux density produced is equal to (equation 3.3) [98]:

$$B = \frac{\mu_0 \mu_r NI}{l}$$ Equation 3.3

The magnetic flux (φ) through a single coil also depends on the angle between the surface of the coil to the magnetic flux lines (θ) (shown in equation 3.4) [99].

$$\varphi = BAcos\theta$$ Equation 3.4

When θ is 0 °, the magnetic flux can be calculated by equation 3.5 [99].

$$\varphi = BA$$ Equation 3.5

When a coil (coil 1), with N_1 turns, is driven by an ac current, an alternating magnetic field is produced. The changes in the magnetic field due to the ac current also generate an induced voltage in the exciting coil. This phenomenon is called self-inductance (L), and can be calculated by equation 3.6 [98].

$$L = \frac{N_1 \varphi}{I}$$ Equation 3.6

Where L is the self-inductance in Wb/Amp, N_1 is the number of turns of the exciting coil, φ is the magnetic flux in Wb and I is the electric current through the exciting coil in Amp.

When another multi-turn coil (coil 2) is placed nearby and is concentric with coil 1, the flux lines produced by coil 1 also pass through the sensing coil (coil 2). The changes in magnetic field due to the ac current will induce a voltage in coil 2. This process is called the mutual inductance (M_L), and is given in equation 3.7 [98]. Combining equations 3.3 and 3.5 with equation 3.7, the mutual inductance can be related to the relative permeability of the samples, and is equal to (equation 3.8) [99]:

$$M_L = \frac{N_2 \varphi}{I} \qquad \text{Equation 3.7}$$

$$M_L = \frac{N_2 \varphi}{I} = \frac{N_2 B A}{I} = \frac{N_1 N_2 \mu_0 \mu_r A}{l} \qquad \text{Equation 3.8}$$

Where M_L is the mutual inductance in Wb/Amp, N_2 is the number of turns of coil 2, φ is the magnetic flux in Wb and I is the electric current through coil 1 in Amp.

If the current in the exciting coil varies with time (t), the induced voltage in the sensing coil is equal to (equation 3.9) [99]:

$$V_{induced} = -M_L \frac{\Delta I}{\Delta t} \qquad \text{Equation 3.9}$$

3.2 Paramagnetism

In magnetic materials atomic dipoles exist as a result of the moving electrons in each atom. The macroscopic magnetic properties are dependent on the orientation and arrangement of these magnetic moments.

In paramagnetic materials, each atom possesses a dipole with a random direction. Therefore, in the absence of an external magnetic field, the total magnetic moment of the material is zero [9]. Paramagnetism occurs when the magnetic dipoles are aligned by rotation due to an external field being applied. As a result, the material has a very small but positive relative permeability and the flux density within the material increases proportionally to the applied field. However, a paramagnetic material does not show any magnetic property when the external field is removed, as thermal motion makes the orientation of the dipoles return to random [98].

3.3 Ferromagnetism

Ferromagnetic materials can similarly be magnetised by an external field and also can retain their magnetic property after the external field is removed. Their relative permeability values are much higher than those of paramagnetic materials [100]. Common ferromagnetic materials are iron, nickel, cobalt and their alloys [98, 100]. These transition metals have unpaired electrons, and since the energy level of their 3s and 3d shells are similar the electron clouds in these shells overlap. This results in an exchange energy which can cause the electrons to align such that their spins are parallel to each other [98]. Therefore, in ferromagnetic materials, local magnetic moments exist before the presence of an applied field. However, the random alignment of the local

moments results in zero overall magnetisation in the absence of any external field. As the magnetic dipoles are free to rotate, by applying an external magnetic field, the magnetic dipole experiences a torque, which tends to align the axis of the dipole with the magnetic field direction. When a certain magnetic field level is reached, all the local magnetic moments are aligned with the external field and form a very stable magnetic structure (even it is not the most energetically favourable state), at this stage the material remains permanently magnetic. The exchange energy is related to the ratio of atomic separation and diameter of the unfilled shell (shown in Figure 3.1) [101]. The exchange energy can be used to explain the temperature effect on magnetic properties: above a critical temperature (the Curie point), changing the distance between the atoms results in the magnetisation of ferromagnetic materials vanishing and the material becomes paramagnetic [102].

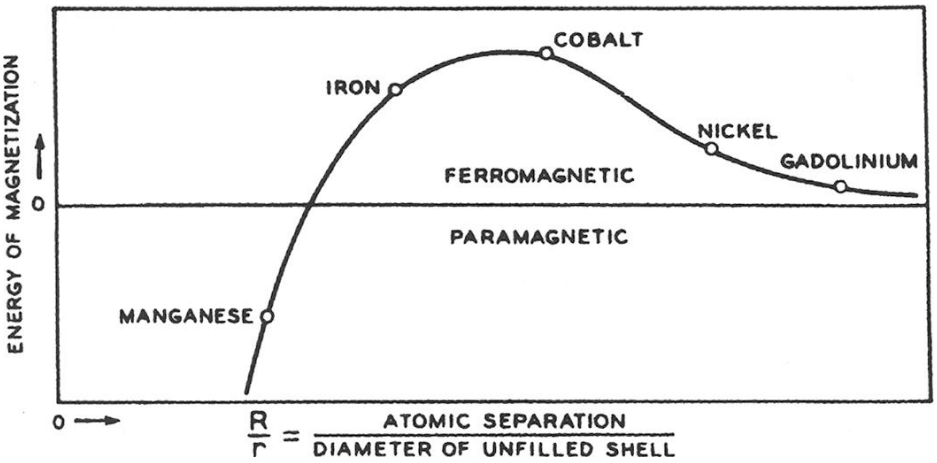

Figure 3.1: Bethe's curve relating the exchange energy of magnetization to the distance between atom centers, for a fixed diameter of active electron shell [101].

3.4 Domains and magnetization process

A uniformly magnetised ferromagnetic sample would have magnetic free poles at the surface, this will generate a magnetic field extending into the space above the surface, which is called the demagnetising field and stores magnetostatic energy. In ferromagnetic materials, magnetic domains exist to reduce the magnetostatic energy. A magnetic domain can be described as a region that has uniform magnetisation where individual magnetic moments are aligned in the same direction. The domain walls, where the magnetic moments direction changes, are the regions separating each domain. The total angle displacement within a domain wall is usually 180 or 90 degrees. A schematic diagram of a 180 ° domain wall structure is shown in Figure 3.2. Although the demagnetising field decreases as the number of domains increases, the domain walls themselves will raise the overall energy of the system as the dipoles within the domain walls are not aligned in the easy magnetisation direction of the material. Therefore, a minimum energy state can be achieved by a specific number of domains in a certain arrangement, which will depend on the size, shape, texture and intrinsic magnetic properties of the material [98]. In cubic crystal structures such as iron, triangular domains can be formed to further minimise the demagnetising field. They are called closure domains as the magnetic flux can close on itself though them. Figure 3.3 shows an example of this configuration with labelled examples of 90° domain walls [100]. The magnetostatic energy in this system is reduced to zero.

The magnetisation of a ferromagnetic material usually involves small domain magnetic moments aligning into larger domains by domain wall motion and/or domain rotation, which makes the material have a greater flux density [103]. Therefore the study of the domain structure is important in understanding the magnetic properties of a material.

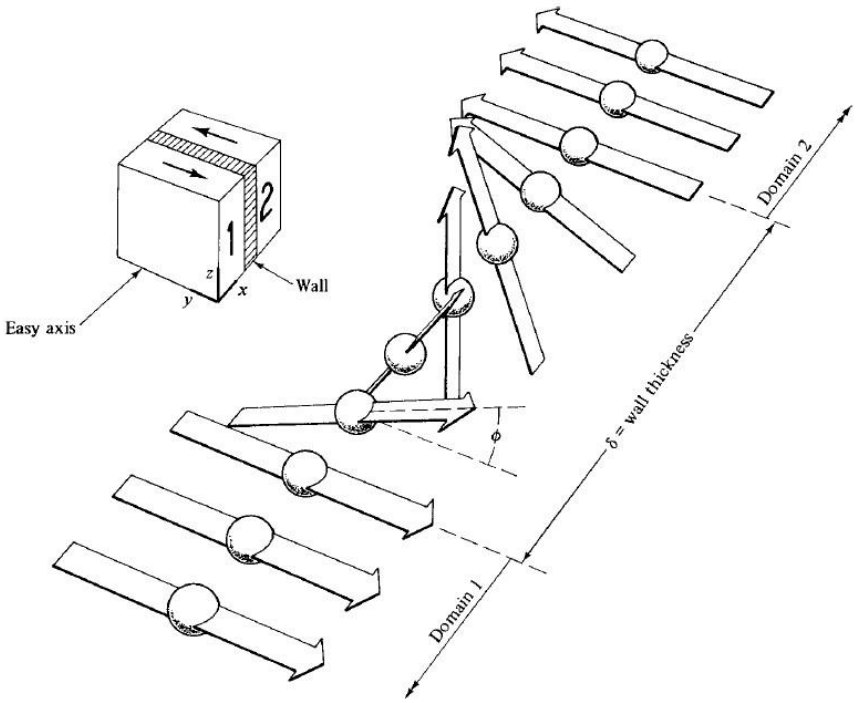

Figure 3.2: Schematic diagram of 180 °domain wall structure [100]

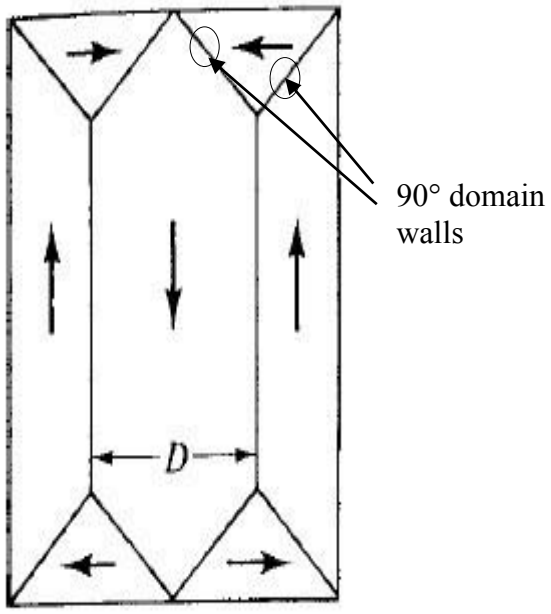

Figure 3.3: Schematic diagram of closure domains in a cubic crystal structure with labelled example of 90° domain walls [100]

3.5 Methods of domain structure observation

In order to observe the domain structure, several techniques can be applied. These include the Bitter method, transmission electron microscopy (TEM), Kerr effect optical microscopy, scanning probe magnetic force microscopy (MFM) and scanning electron microscopy with polarisation analysis [100].

3.5.1 Bitter method

The earliest successful method of domain structure observation was carried out by the Bitter method, which is also called the colloid method [104]. A schematic diagram of the test method is shown in Figure 3.4. The method involves applying Ferrofluid: a liquid suspension of fine (Fe_3O_4) particles (typical size of 10 nm or less) to the polished surface of the sample. The fine particles are attracted to the domain walls, which have a non-uniform magnetic field. When the sample is then examined under an optical microscope [100], the different reflected light from the domain walls distinguish the domain wall from the domain area. A typical domain structure of MnZn ferrite obtained by the Bitter method is shown in Figure 3.5 [105], where examples of domains, domain walls and domain packets are given. In order to improve the resolution of the domain pattern, the dried film method can be used with optical or electron microscopy, in which case only static domain patterns can be recorded.

One of the major disadvantages of the Bitter method is that only surface domain structures can be observed, but this is inherent with all other techniques. Therefore, careful sample preparation must be carried out to eliminate any surface preparation effects [106]. The Bitter method is still a popular method used today due to its simple

set up, fast response and as it is able to show domain wall motion [107-110]. However, the Bitter method cannot be applied when the material has a very low anisotropy constant (less than about 100 J/m^2), where the domain walls are so broad and only have a small attraction force to the magnetic particles. Another disadvantage of the Bitter method is that it can only be applied at a restricted temperature range which depends on the Ferrofluid solution and Curie temperature of the magnetic particles.

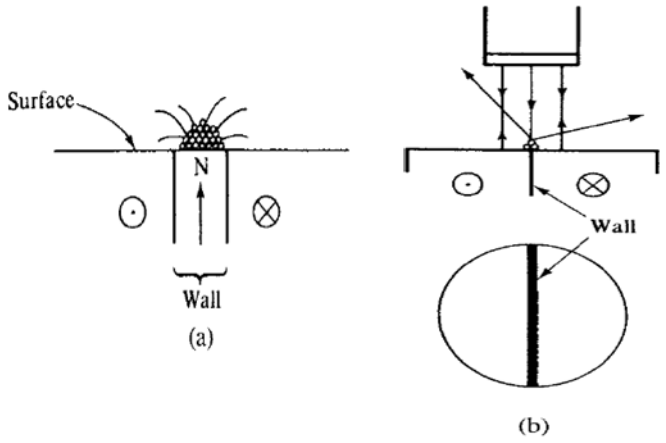

Figure 3.4: Schematic diagram of the Bitter method, image in a) shows the magnetic particles are attracted to the domain wall; and image in b) shows an optical microscope is used to examin the sample surface [100].

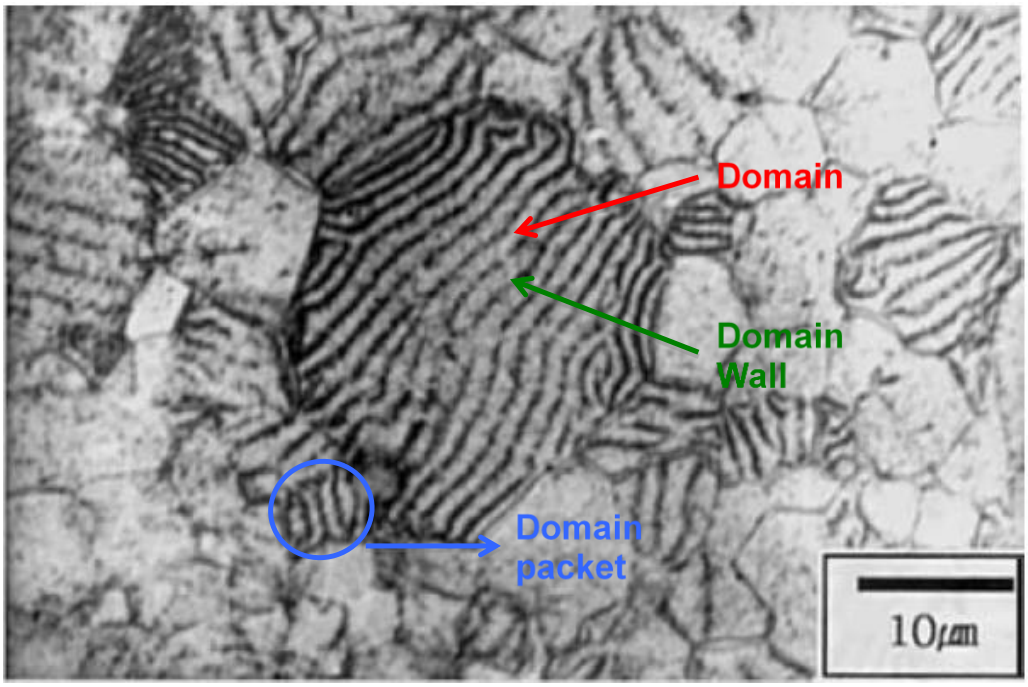

Figure 3.5: A typical domain structure of MnZn ferrite obtain by the Bitter method [105].

3.5.2 Magnetic force microscope

The magnetic force microscopy (MFM) uses a very sharp-pointed tip coated with magnetic material in a scanning probe microscopy system. Sample preparation for MFM is similar to the Bitter method, which also requires a stress free and fine polished surface. The tip can be scanned across a small area with accurate position control in the horizontal and vertical directions by piezoelectric transducers. A measureable force occurs when the tip interacts with any magnetic field gradient resulting from where a domain wall meets the sample surface [100]. The surface magnetic domain structure can be obtained by mapping the force/tip position in the vertical direction in the scanning area. A typical domain structure of duplex stainless steel obtain by the MFM is shown in Figure 3.6 [111].

A MFM tip can measure forces as low as 10−14 nN, with an extremely high resolution as low as 20 nm. MFM has been successfully applied in many research areas [110-114]. For example, Bitasta et al. studied the interactions of domain walls moving in a high purity iron sample with cementite precipitates [110]. Lo used MFM to study the effect of austenite – ferrite phase balance and plastic deformation on domain structures in duplex stainless steel [111].

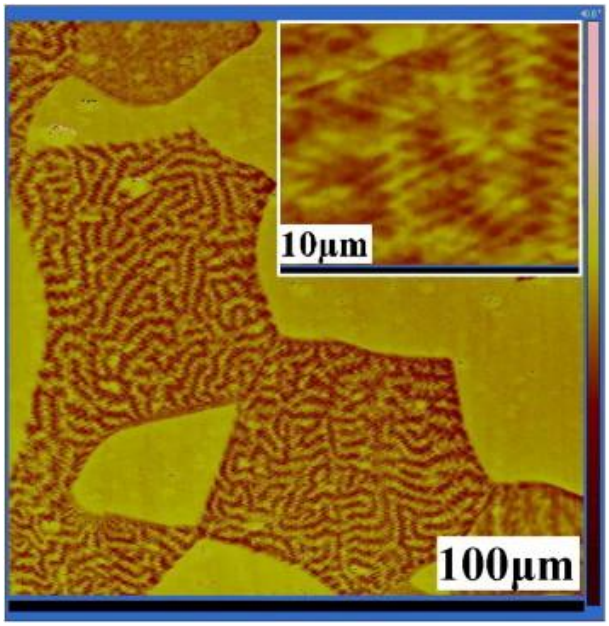

Figure 3.6: Domain structure of duplex stainless steel obtain by MFM showing the domain patterns in the ferritic regions of the microstructure [111]

The disadvantages of MFM are: (a) inaccurate domain patterns can be obtained when domain wall motion is being imaged due to the interaction of the domain walls with the small magnetic field generated from the tip coating materials; and (b) it has a relatively short scanning range (order of a few hundred microns). [100].

3.5.3 Lorentz microscope

The Lorentz microscope is a technique used within a TEM, where electrons pass through the very thin samples (<100nm). The electrons passing through the sample will be deviated by the local magnetic field within the material. The domain walls, which have different orientations at different positions, will show up as dark or light lines on the micrograph when the microscope is slightly under or over focused [100]. An example of the domain structure of an iron foil obtained by the Lorentz microscope is shown in Figure 3.7 [115]. The Lorentz microscope technique has the advantages of obtaining high resolution domain structure (the resolution is the same as for TEM imaging). It has been used for studying the interaction of microstructure features with static domain structures and dynamic domain wall motion in coarse grain pure iron and C-Mn steels [85, 91, 115]. The technique, however, requires a special set up in the TEM and complex sample preparation. As a thin foil sample is used, there is always a debate on whether the domain structure of the thin foil is representative of the bulk material.

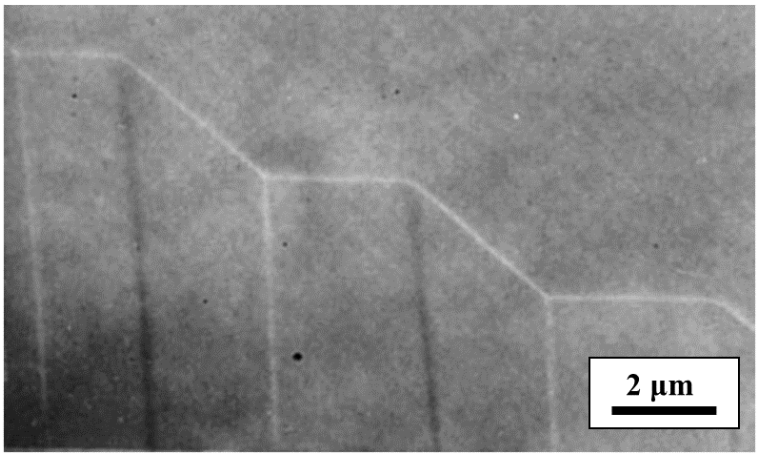

Figure 3.7: Domain structure of a pure iron foil obtained by the Lorentz microscope (Over focus), both the black and white lines are domain walls, the color of the line depends on whether the image is under or over foucsed [115].

3.6 The B-H curve

As described earlier, a magnetic field with flux density (B) can be produced in response to an external applied magnetic field (H). A schematic diagram of a B-H curve (which can also be called a hysteresis loop or magnetization curve) for a ferromagnetic material is shown in Figure 3.8 [9]. For ferromagnetic material, the B field increases non-proportionally with H. The permeability value, which is the slope of the B-H curve, changes with H. In most cases, the slope at H = 0 is called the initial permeability, and the largest slope in the B-H curve is called the maximum permeability.

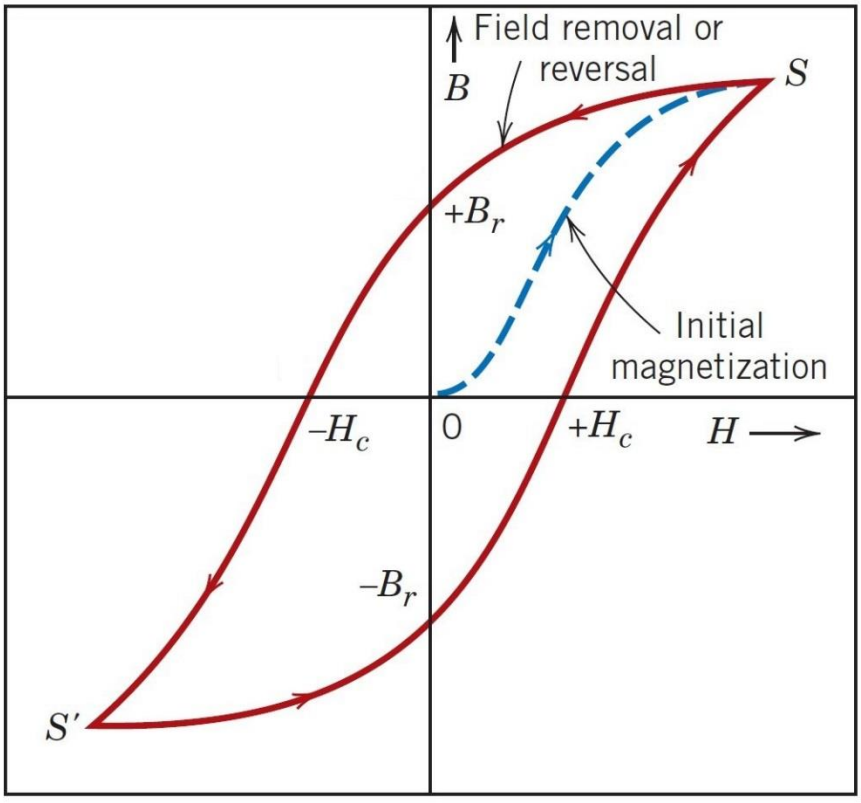

Figure 3.8: Schematic diagram of a B-H curve for a ferromagnetic material, where Hc is coercivity, S is satuartion point, and Br is remanence [9].

As the applied field, H, increases, domains with different magnetisation directions will change their shape and size by domain wall motion and/or domain rotation until saturation at which point they all merge into a single domain, (i.e. all the dipoles are aligned in the same direction as the applied field). If the H field is decreased, by applying a field in the opposite direction, the curve does not fit into the original path (shown in Figure 3.8). At zero H field, the materials still remain magnetised, and the residual B field is called the remanence (B_r). In order to demagnetise the material an opposite H field of magnitude H_c must be applied. The value of H_C is called the coercivity or coercive force [98].

3.7 Effect of steel microstructure on magnetic properties

The relationship between steel microstructural parameters and magnetic permeability is complex and subject to ongoing research. A significant amount of research has been carried out on electrical steel [36, 116-134]. It has been reported that alloy composition, grain size, texture, impurities, inclusions, precipitates, and thickness of the electrical steel sheet can affect the magnetic properties of electrical steel, among which texture and grain size are considered the most important microstructure parameters [118]. However, there is less research published in this area with regard to structural steel [6, 8, 76, 77, 79, 85, 91, 135-146]. In this section, the effect of microstructure parameters (focused on structural steel) on the magnetic properties are discussed.

3.7.1 Ferrite grain size

The magnetic properties of steel are related to its domain structures and domain wall movement under an applied field. Hetherington et al. observed the magnetic domain structure in ferrite grains of a fully killed, normalized steel sample [147]. A magnetic domain structure image in ferrite grains is shown in Figure 3.9. It was stated that the grain boundaries have a major influence on the domain configuration and domain wall motion under an applied field. Closure domain structures were found near the ferrite - ferrite grain boundaries (closure domains are labelled with yellow arrows and grain boundaries are labelled with red dash lines in Figure 3.9). It was reported that a substantial amount of domain wall motion took place in the ferrite grains at an applied field below 0.5 kA/m and examples of changes in the domain wall orientation were observed when the walls crossed the grain boundary [147].

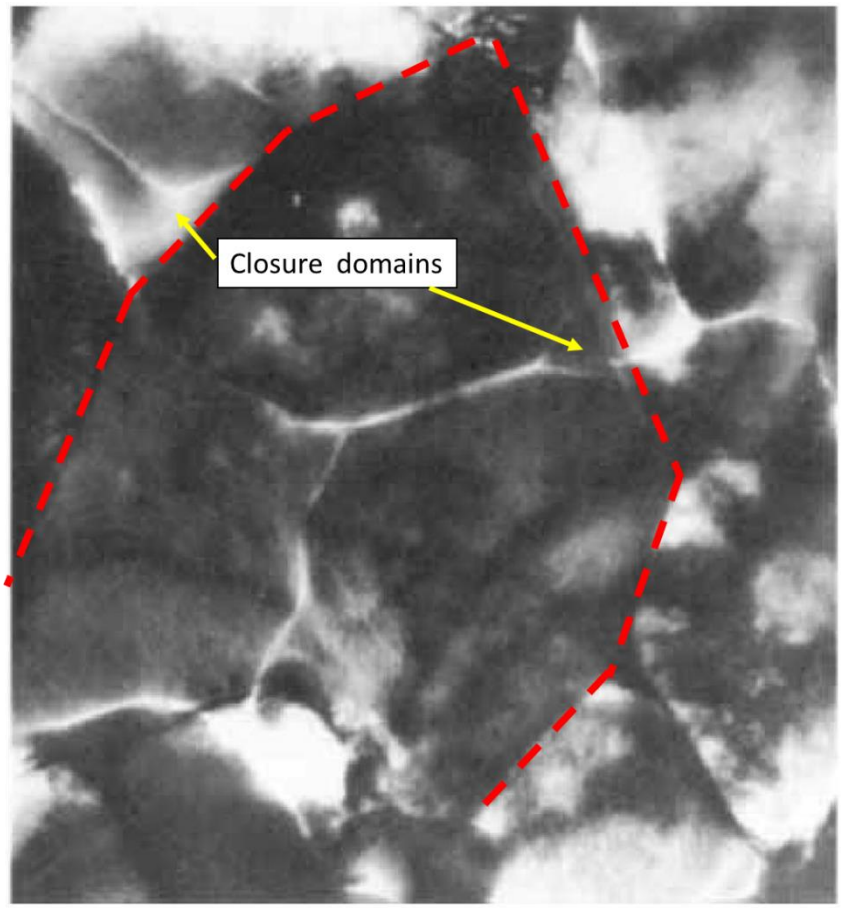

Figure 3.9: Magnetic domain structure of ferrite grains for a fully killed, normalized steel sample, observed using a high voltage Lorentz electrical microscope. Closure domains are labelled with yellow arrows and grain boundaries are labelled with red dash lines [147].

Thompson and Tanner studied the magnetic domain structures in a 0.17 and a 0.44 wt % C steel sample with an applied field using a high voltage Lorentz electrical microscope [91]. An example of magnetic domain structure of the 0.17 wt% C steel sample with no applied field is shown in Figure 3.10 [91]. It can be seen that the domains of opposite orientation are clearly shown as lighter and darker areas, running from the top right to the bottom left of the Figure. The domain structure is difficult to see inside the pearlite grains in this Figure. As can be seen in Figure 3.10, there are also closure domains

forming at the ferrite – pearlite grain boundary. It has been observed that the 90 ° domains walls, which are forming the closure domains, are most distorted and therefore hinder the 180 ° domain walls motion at an applied field. In addition, it was stated that the easy direction of magnetisation (defined by the crystal orientations of ferrite grain) is changing at the ferrite – ferrite grain boundaries, which is also an important factor in determining the domain wall energy when the wall crosses over from one grain to another. The authors concluded that, for low carbon steel with a ferrite phase-dominated microstructure, the effect on the ferrite – ferrite boundaries and the ferrite – pearlite boundaries must be considered and the magnetic properties are affected by grain size.

A 0.17 wt% C steel sample, heat treated at 860 ℃ followed by air cooling, was compared with a furnace cooled one in order to study the effect of ferrite grain size on the magnetic properties [91]. It has been reported that the sample with a smaller grain size has lower initial and maximum permeability, whilst the coercivity and the field at maximum permeability were higher [91]. This is in agreement with Ranjan et al. [148], who found the same trend in decarburised steel with a variation in ferrite grain size from 72 – 115 μm. It was noted that the initial permeability values measured in the decarburised steel samples, however, are approximately a factor of 20 higher than structural steel. This is due to the difference in carbon content (which was measured to be less than 0.005 wt%) and grain size [148]. A linear relationship between coercivity and inverse grain size has been reported in ferrite – pearlite steel [136, 147].

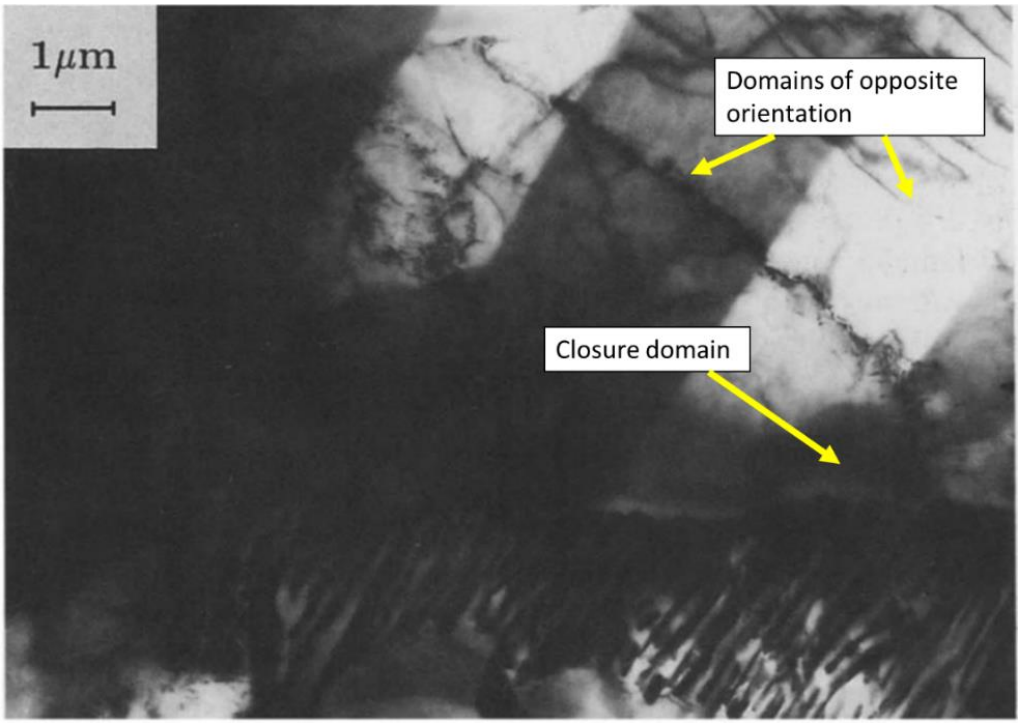

Figure 3.10: Magnetic domain structure for a 0.17 wt% C steels sample, observed using a high voltage Lorentz electrical microscope [91].

3.7.2 Pearlite

An example of the domain structure inside a pearlite grain in a 0.44 wt% C steel sample is shown in Figure 3.11 [91]. It can be seen that there is a more complex structure of the domain walls running both along and across the pearlite lamellaes compared with the domain structure in ferrite grain (Figure 3.10) [92]. A higher magnification image of domain structure in the pearlite grain is shown in Figure 3.12a, where three domain walls can be clearly observed running across the pearlite lamellaes. It can be seen that the domain walls are not straight and that their orientation is altered by each of the lamellaes. This also agrees with Beale et al., who observed a similar domain structure in heat treated C – Mn steel [149]. In addition, the author states that many of the domain walls were found to be ended with closure domains which are formed at the lamellaes, inclusions and highly dislocated areas [91]. Therefore, there are many more pinning

sites for domain wall motion inside the pearlite grain compared with ferrite. It has been reported that permeability decreases (as a result of the more effective domain wall motion pinning effect) with an increase in cementite lamellae thickness and a decrease in interlamellar spacing [91]. In addition, the probability of closure domains forming at the cementite – ferrite boundaries within the pearlite grains increases with the thickness of the cementite lamellae [92]. The initial permeability value of 56 was measured for a 0.87 wt% C steel sample with a fully pearlitic microstructure [91].

The magnetic domain structure of the same area as Figure 3.12a under an applied field of 4.1 kA/m is shown in Figure 3.12b. It can be seen that the domain that aligns with the magnetic field has grown by moving the 180 ° domain wall. It is noted that the required magnetic field strength for domain wall motion in pearlite (4.1 kA/m) is significantly higher than that required in the ferrite microstructure (0.5 kA/m) [147].

Jiles reported that the domain wall pinning effect of cementites in spheroidised pearlite are far weaker compared with cementite lamellaes in the lamellar pearlite [150]. Therefore, the effect of spherodised pearlite in ferrite – pearlite steel was shown to be less efficient at decreasing the initial and maximum permeability, and increasing coercivity compared with the lamellar pearlite [150]. The initial permeability value of a 0.0065 wt% C steel sample with fully ferritic microstructure was measured to be 350 [150].

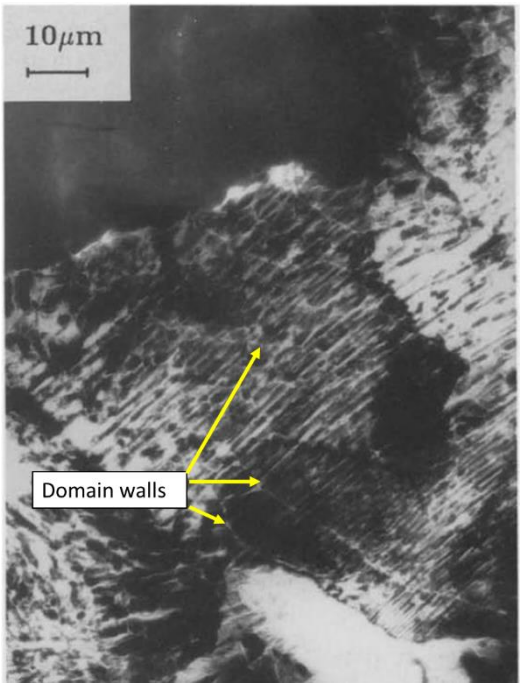

Figure 3.11: Magnetic domain structure for a 0.44 wt% C steels sample, observed using a high voltage Lorentz electrical microscope [91].

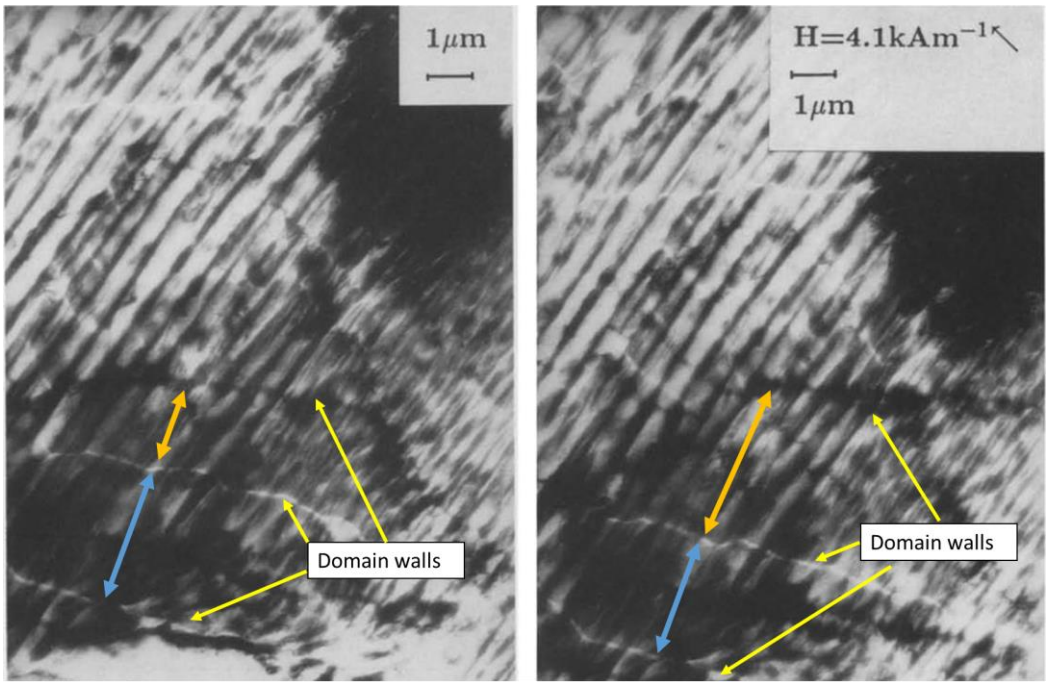

Figure 3.12: Magnetic domain structure inside a pearlite grain for a 0.44 wt% C steels sample a) without and b) with an applied magnetic field of 4.1 kA/m, observed using a high voltage Lorentz electrical microscope [91].

3.7.3 Martensite, bainite, tempered martensite and tempered bainite

Saquet et al. measured the B-H loops for plain carbon steel with different phases including ferrite (in a 0.1 wt% C steel), pearlite (in a 0.8 wt% C steel), martensite and tempered martensite (in a 0.55 wt% C steel) [93]. The B-H curves can be clearly distinguished for each microstructural phase (shown in Figure 3.13). The correlation between the microstructure phases and each of the magnetic property parameters was not discussed in this study. However it can be seen in Figure 3.13 that the coercivity of these samples shows an increasing order of ferrite < pearlite < tempered martensite < martensite, whereas the remanence shows an increasing order of pearlite < ferrite ≤ martensite < tempered martensite.

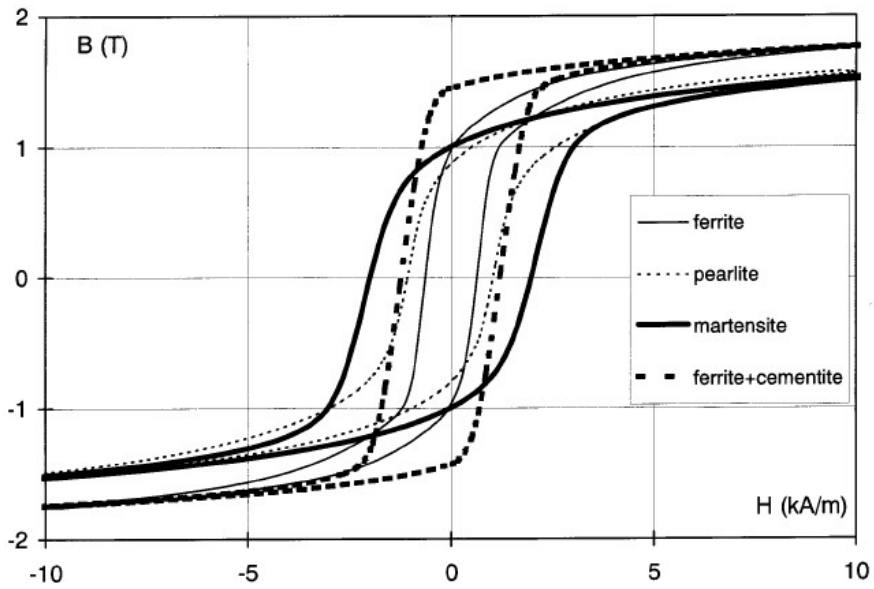

Figure 3.13: B-H curves for ferrite, pearlite, martensite and annealed martensite [93].

Liu et al. used a multi frequency cylindrical-shaped EM sensor to measure the microstructure states in power generation steel of P9 (9Cr–1Mo) and T22 (2.25Cr–1Mo) [138, 144]. The EM sensor output for the P9 and T22 samples at normalised, normalised

and tempered, and long service exposure states are shown in Figures 3.14a and 3.14b respectively. It can be seen that the different microstructural states can be distinguished by the EM sensor output. The relative permeability values were predicted by an FE sensor output fitting method (similar to the fitting method described in section 5.4 in chapter 5). The predicted relative permeability value for a normalised P9 sample, with a microstructure of predominately martensite mixed with some bainite, is 37. After tempering at 760 ℃ for 1 hour, the relative permeability value of the tempered martensite/bainite microstructure was increased to 66. This is believed to be due to the decrease in the dislocation density in the strained martensite laths of the normalised P9, and the increase in lath size. It was stated that the effect of the precipitation of carbides is minor, as the carbides are located at the grain/lath boundaries which already act as major pinning sites for domain wall motion [144]. The long service exposure states (after approximately 11 years at 520 ℃) microstructure of the P9 sample consist of equiaxed ferrite with large carbides distributed within ferrite grains or on grain boundaries, and the relative permeability value was increased to 133. This was attributed to the effect of the coarsening of the ferrite lath widths which reduces the number of planar pinning features, and the coarsening of the carbide precipitates. Therefore the mean free path of pinning points to domain wall motion was increased whilst the number of pinning pointed was reduced [138].

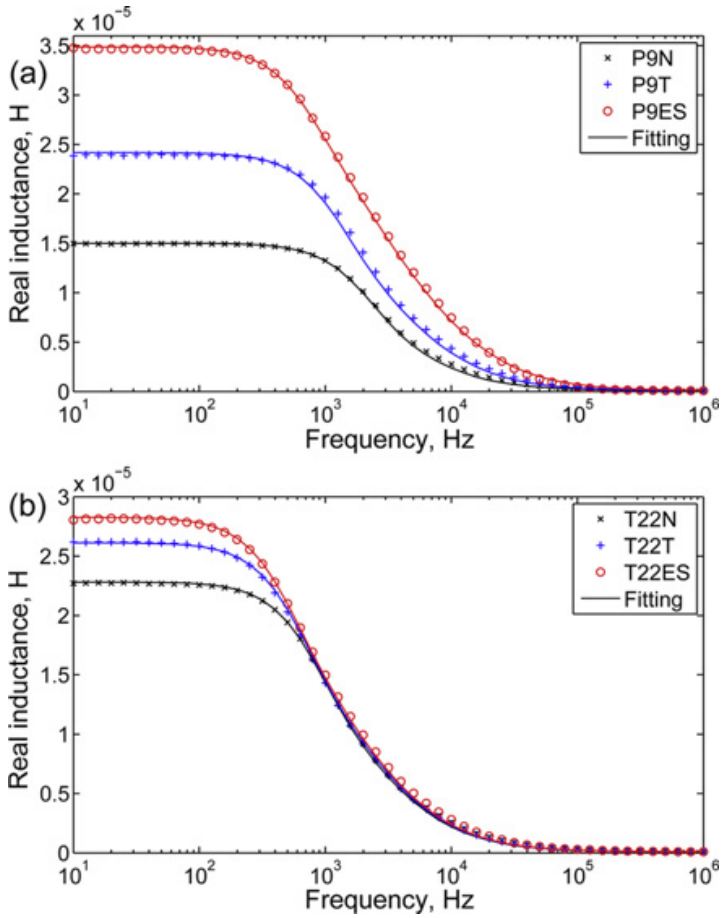

Figure 3.14: EM sensor output: real inductance plot with frequency for a) P9 and b) T22 samples, at as normalised (N), normalised and tempered (T), and long service exposure (ES) states.

For the normalised T22 sample with a microstructure of bainite lath width, some pro-eutectoid ferrite was predicted to have a higher relative permeability value (66 compared to 37) than for the normalised P9 sample. This was believed to be due to the greater bainite lath width, and pro-eutectoid ferrite grain size compared with the martensite lath in the normalised P9 sample. After tempering of the T22 sample at 720 ℃ for 1.5 hours, the change in the relative permeability value compared with the normalised state was very small (75 compared to 66), which is believed to be due to the fact that many of the carbides in the tempered state are too small and have little pinning

effect on the domain wall motion. The relative permeability is still dominated by the lath size of the bainite and grain size of the pro-eutectoid ferrite. The long service exposure T22 (after approximately 11 years at 520 ℃) has a microstructure that consists of equiaxed ferrite with large carbides distributed within ferrite grains or on grain boundaries. After long service exposure, the carbides were coarsened and became effective pinning points for domain wall motion; hence, the inter particle spacing determines the mean free path of the domain wall motion. The relative permeability value of T22 in the long service exposure state was predicted to be 86 [138, 144]. It was concluded that the relative permeability values for both the P9 and T22 sample is determined by the mean free path of domain wall motion. A power law relationship between the relative permeability and the mean free path for domain wall motion at an exponent of -1.03 was reported (shown in Figure 3.15) [138].

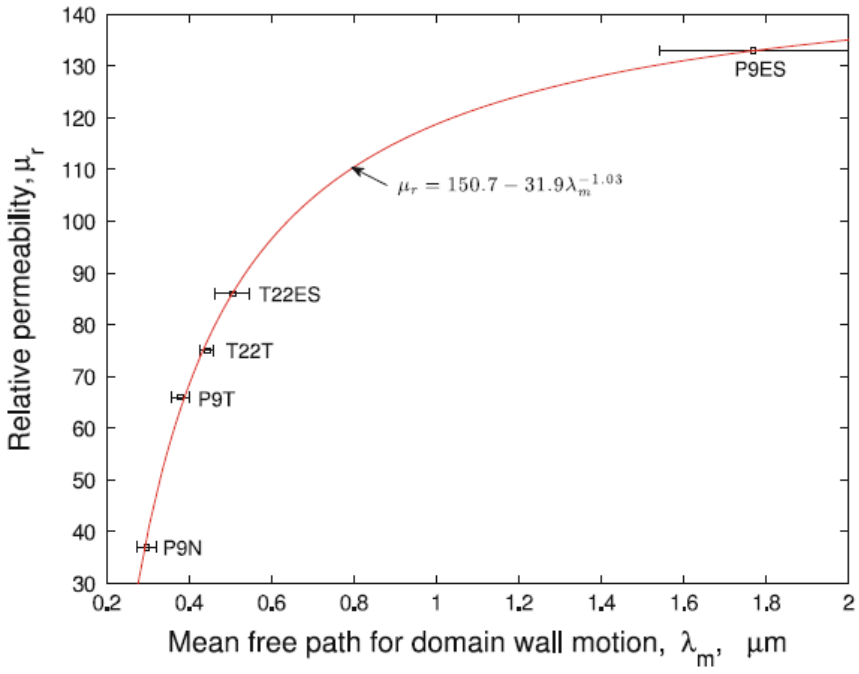

Figure 3.15: Relationship between the relative permeability and the mean free path for domain wall motion, showing a power law relationship at an exponent of -1.03 [138].

3.7.4 Phase balance

Thompson et al. [91] studied the magnetic properties of ferrite-pearlite steel as a function of carbon content. The maximum relative permeability, initial permeability, and remanence were found to decrease with increased carbon content, whilst coercivity and an applied field to achieve maximum permeability have shown the opposite effect (shown in Figure 3.16 – 3.18). This is because the fraction of the pearlite phase, which has a lower initial and maximum permeability than ferrite, increases with carbon content. It can be seen from Figures 3.16 - 3.18 that the effect of carbon content on maximum relative permeability, initial permeability, and remanence are shown to be greater for carbon content from 0.17 – 0.44 wt% than for 0.44 -0.87 wt %. This is believed to be due to the microstructures of the 0.44 – 0.87 wt % C steel samples mainly consist of the pearlite phase, where the domain wall motion has to occur when a magnetic field is applied. Therefore, the magnetic properties (maximum relative permeability, initial permeability, and remanence) of these samples were dominated by the pearlite phase. In contrast, during the initial magnetisation for the 0.17 wt % C steel, the majority of the low field domain wall movement was happening within the ferrite grains instead of the pearlite grains, at which the domain wall motion does not occur until a higher field is applied. Therefore, the magnetic properties of the 0.17 wt % C steel is dominated by the ferrite phase, which has far higher permeability values [91].

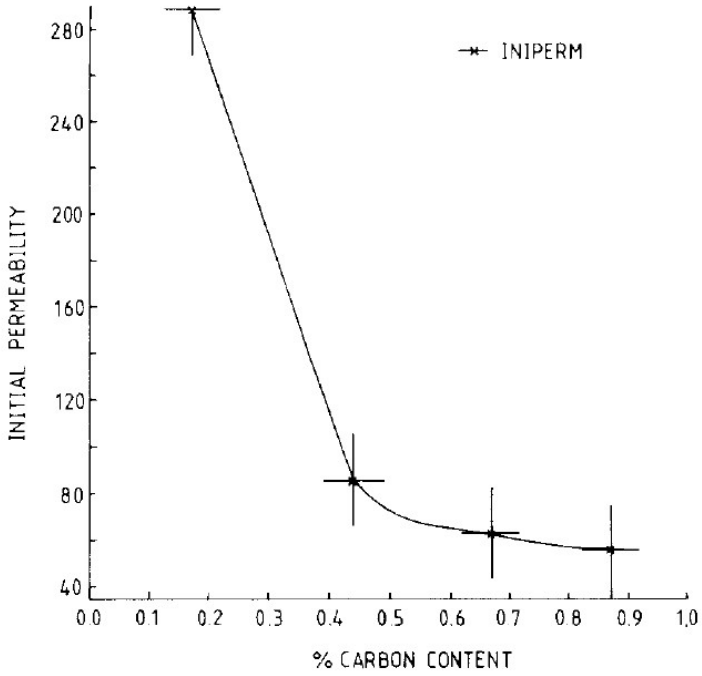

Figure 3.16: Plot of initial permeability with carbon content in ferrite + pearlite steels [91].

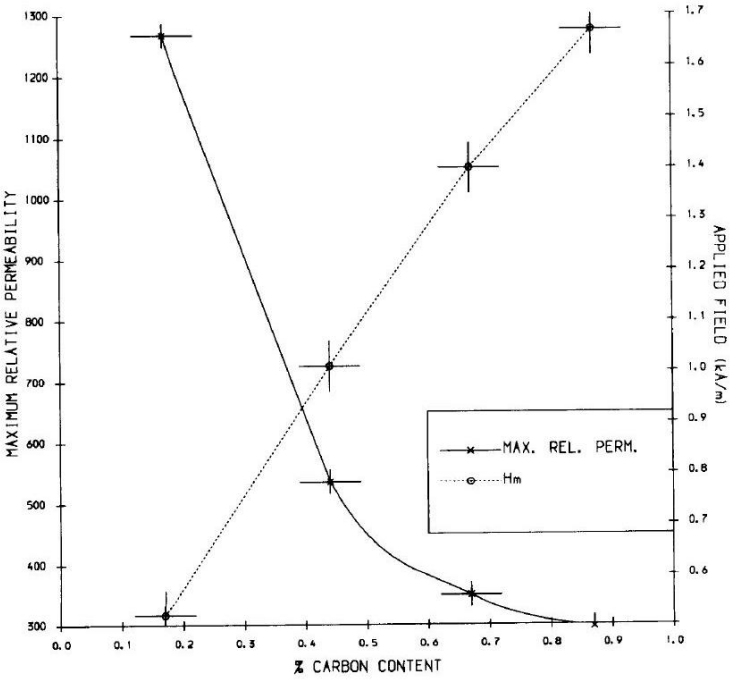

Figure 3.17: Plot of maximum relative permeability and applied field at which this occurs with carbon content in ferrite + pearlite steels [91].

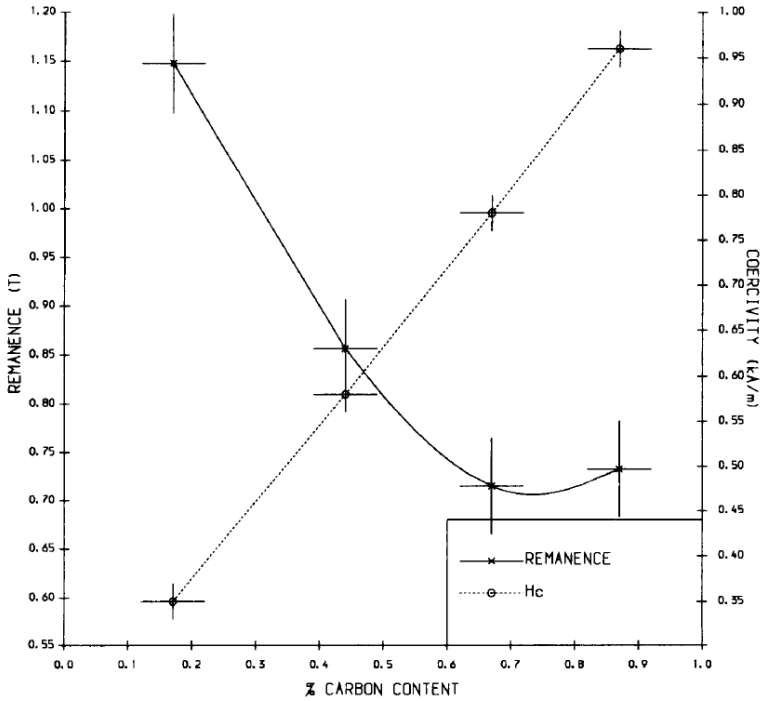

Figure 3.18: Plot of remanence and coecivity with carbon content in ferrite + pearlite steels [91].

In addition, it has also been reported that the initial and maximum relative permeability decreases with an increase in the plastic strain due to the increased pinning sites of domain wall motion at the dislocation tangles resulting from the deformation process [135]. The plot of the initial and maximum permeability change with the plastic strain is given in Figures 3.19 and 3.20 respectively [85, 92], which show that the pinning effect of dislocations become less effective when the dislocation density in the steel becomes saturated.

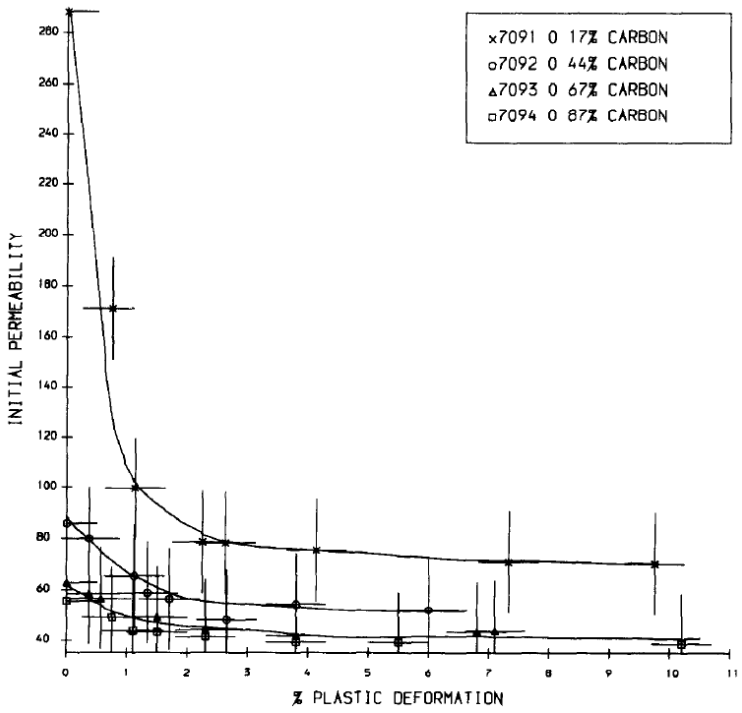

Figure 3.19: Plot of initial permeability with plastic deformation in ferrite + pearlite steels

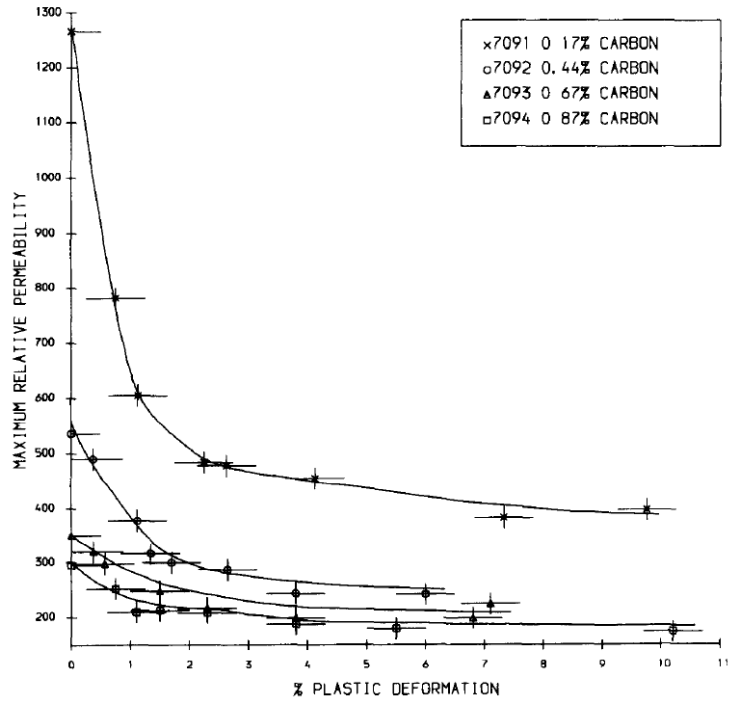

Figure 3.20: Plot of maximum permeability with plastic deformation in ferrite + pearlite steels [85]

Hao et al. [8] used multi frequency EM sensors to measure the ferrite fraction from 0% to 100% in austenite-ferrite dual phase steel microstructures (produced using hot isotatic pressing from stainless steel powders). It was reported that the real inductance at low frequency (10Hz), which is related to the relative permeability of the samples, increased with the ferrite percentage (shown in Figure 3.21). Measurements were carried out using different sensor designs (an air cored cylindrical sensor and a ferrite core H-shaped sensor) in order to study the sensitivity to the different ranges of ferrite fractions. In addition, it was found that a different sensor output parameter (zero crossing frequency) is more sensitive to the changes in the samples with low ferrite fractions [8].

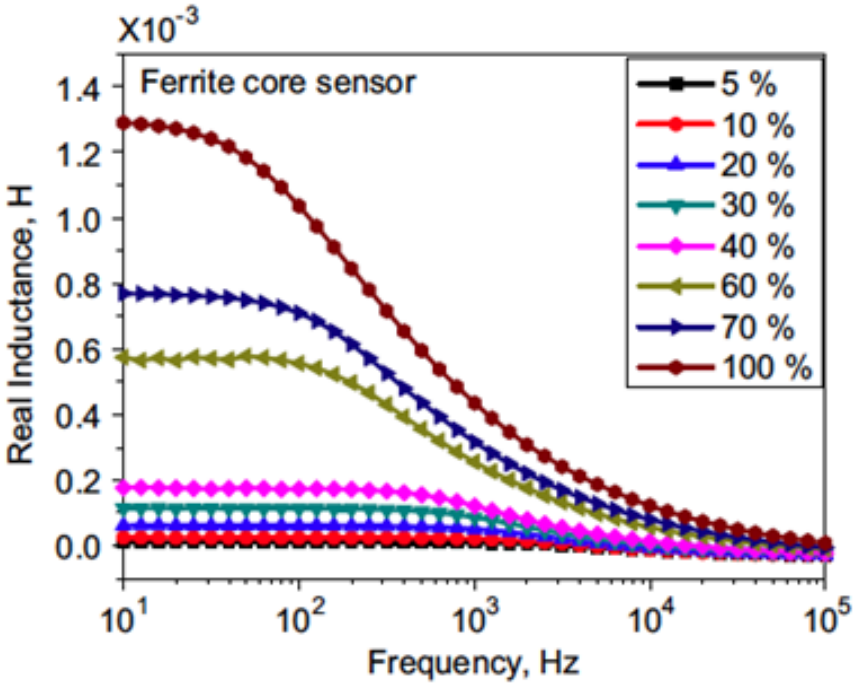

Figure 3.21: Real inductance versus frequency at ferrite fraction of 5%-100% in ferrite + austenite steels [8].

Yin et al. [151] used a MultiPhysics FEMLAB model to fit the sensor measurements with relative permeability values (shown in Figure 3.22). In this case, the relative permeability values only increase significantly when there was more than about 35% ferrite present in the sample, which was related to the point at which the ferrite grains provided connected pathways through the sample to allow the magnetic flux to pass through.

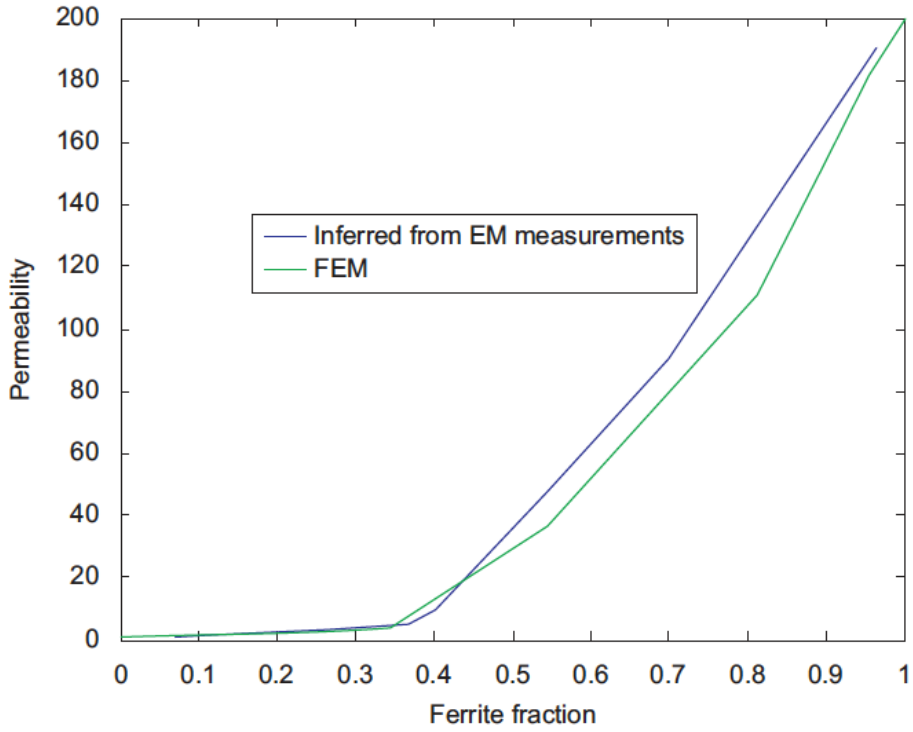

Figure 3.22: FEM and EM measurements of the ferrite fraction and permeability relation [151].

In order to estimate the effective electrical or magnetic property of a material with a microstructure consisting of two phases with contrasting properties, power law models have been popularly used [8, 152-154]. The power law model predicts the effective permeability as:

$$\mu_e{}^{\beta} = (1-f)\mu_1{}^{\beta} + f\mu_2{}^{\beta} \qquad \text{Equation 3.10}$$

Where μ_1 and μ_2 are the relative permeability values of the first and second phase respectively, f is the fraction of the second phase, and β is a dimensionless parameter.

Examples of the power law are the Birchak formula (β = 1/2) [154] and the Looyenga formula (β = 1/3) [153] for predicting the dielectric constant of mixtures. Hao et al. developed a FE microstructure model to predict the relative permeability based on actual microstructures [8]. It can be seen in Figure 3.23 that the model showed good agreement with measured results over the whole range of ferrite fractions for austenite/ferrite microstructures. However, the power-law model with β = 1/2 did not give a good fit, whilst β = 1/3 only gave good agreement with measured results at ferrite fractions above 40% (samples with ferrite fractions below 40% would require a much smaller β value to provide a good fit) [8]. In addition, the FE microstructure model can also consider the effect of second phase morphology, such as a banded microstructure which has been found to be significant in some extreme cases in which a high degree of banding existed [8].

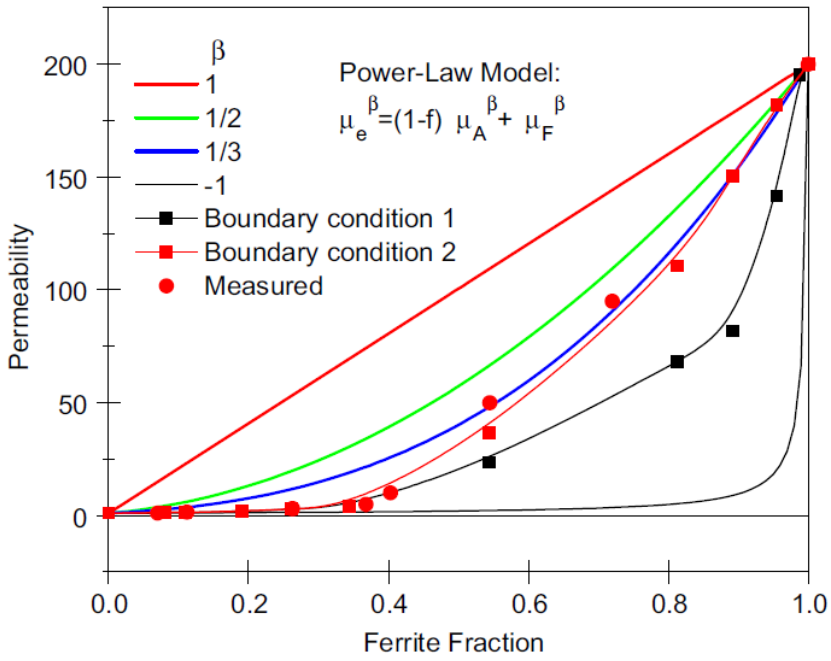

Figure 3.23: Relationship between effective permeability and ferrite fraction in austenite – ferrite microstructure. The FE modelled results (with real microstructure input) were compared with the experimental measured and power law modelled results [8].

3.7.5 Summary

In summary, it can be seen that several reports have identified the role of certain phase types/balance and grain sizes in the magnetic properties of steel. However, there is a lack of systematic study on the role of different microstructural features on the initial relative permeability, which is important as EM sensors operate at very low field strengths (details will be given in section 5.1 in Chapter 5), and hence the EM signals. For example, the role of grain size, pearlite interlamellar spacing, carbon content in the martensite and ferrite - martensite phase balance were not systematically studied under a well-defined experimental control.

In addition, the FE microstructure modelling method, which has been proven to be accurate in predicting the austenite – ferrite phase balance, has not been tested for predicting the effective relative permeability of the ferrite - pearlite and ferrite - martensite phase balance.

3.8 Effect of steel microstructure on electrical resistivity

The EM sensor signal is dependent on both the magnetic and electrical properties of steel. Therefore it is important to understand how microstructure might affect the electrical properties.

When electrons are conducted through a perfect metal crystal with no thermal effect, there should be no scattering of the electrons and the resistivity is zero. However, 'defects', including impurities, grain boundaries, dislocations from plastic deformation and thermal vibrations, can scatter electrons in metals; increasing the number density of defects causes an increase in the resistivity [9]. This is described as Matthiessen's rule (equation 3.10 and equation 3.11) [9]:

$$\rho_{total} = \rho_T + \rho_i + \rho_d \qquad \text{Equation 3.10}$$

$$\rho_T = \rho_0 + aT \qquad \text{Equation 3.11}$$

Where ρ_{total} is the resistivity of the material, $\rho_T, \rho_i, and\ \rho_d$ are the contributions from thermal, impurity and deformation effects respectively, ρ_0 is the residual resistivity, a is a constant and T is the temperature.

The resistivity of a material is related to its composition and microstructural parameters. These include alloying elements in solid solution, phase balance, precipitates, grain size and stress/strain. D. Ludwigso et al. has reported that steel resistivity can be estimated from the solid solution content of different elements, represented in equation 3.12 [155]. Figure 3.24 shows the influence of various elements on electrical resistivity [155].

Other research carried out by A. Norbury reported a slightly different relationship which includes the effect of carbon in solid solution (shown in equation 3.13) [156].

$$\textit{Resistivity of Steel (n}\Omega\textit{m)} = 101 + 117Si + 62Mn + 56Cr + 30Ni + 39Cu + 143P - 104S \quad \text{Equation 3.12}$$

$$\textit{Resistivity of Steel (n}\Omega\textit{m)} = \textit{Resistivity of pure iron} + 340C + 146N + 135Si + 50Mn + 54Cr + 15Ni + 40\,Cu + 34Mo \quad \text{Equation 3.13}$$

Where, the alloying elements in the equations denote the amount in wt% in solid solution.

Different microstructural phases in steels may have different resistivity values. For example, the resistivity of ferrite is about 130 nΩm, whereas the resistivity of pearlite is about 180 nΩm [157]. A mixture of two phases can be estimated by applying the rule of mixtures using the known resistivity of each phase [102].

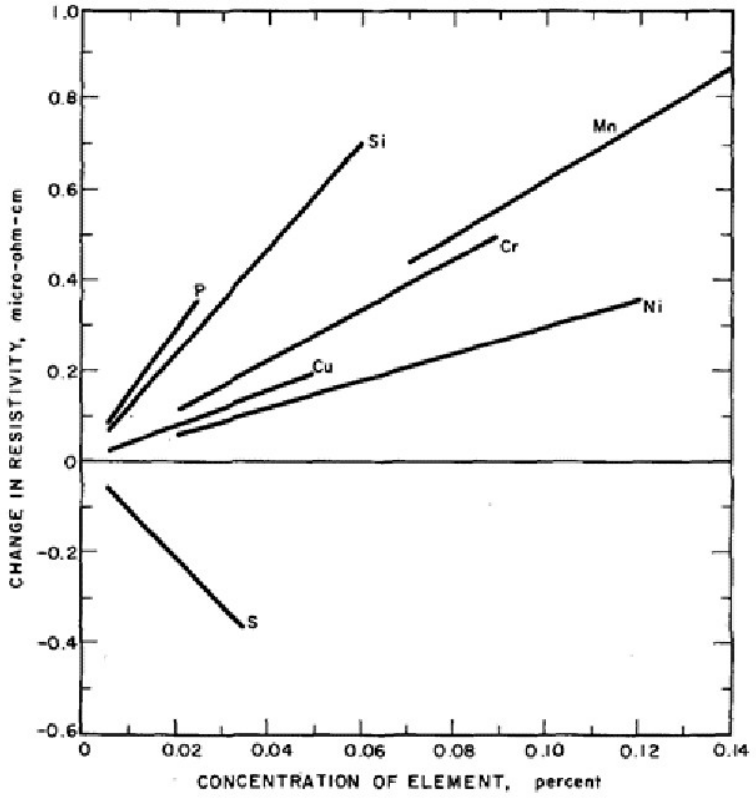

Figure 3.24: Influence of various elements (in solid solution) on the electrical resistivity [155].

Resistivity can also change during the process of precipitation due to removal of elements in solid solution, or the dissolution of precipitates to put alloying elements into solid solution [158-160]. Mohanty et al. [158] reported that tempering of a HSLA-100 steel at 450 ℃, 500 ℃ and 550 ℃ causes a maximum 5.5% decrease in resistivity values. Continuous measurements of resistivity have been used to quantitatively estimate precipitation in a copper bearing steel [161]. In another report Chaudhuri et al. [159] measured the resistivity of Ti and Nb + Ti containing HSLA steel at different temperatures up to 500 ℃; the change in slope of the resistivity versus temperature curve indicated the onset of precipitation within the temperature range of 270-400 ℃. Park et al. [160] examined the dissolution temperature of Nb(C,N) precipitates using

resistivity. The resistivity increased with solution treatment temperature up to 1200 ℃ due to the dissolution of Nb particles into solid solution, indicating the dissolution temperature was 1200 ℃.

Stress and strain can also affect the resistivity values. Chaudhuri et al. reported that there is an approx. 2.5% decrease in resistivity in the initial stage of heat treatment of a steel wire at 800 ℃, due to the combination of stress relief and dissolution of second phase.

4 Materials and experimental procedure

4.1 Materials and heat treatment

4.1.1 C-Mn steels

Melting grade (pure) iron and C-Mn steels with different carbon contents, both provided by Tata Steel UK, have been used in this project. The chemical compositions of the steels used are given in Table 4.1. The form of the samples and their thermal history/heat treatment conditions are given in Table 4.2.

Table 4.1: Chemical composition for the C-Mn steel samples, all in wt%.

Sample	C	Si	Mn	S	P	Cu
0.17C	0.17	0.28	0.80	0.03	0.01	0.09
0.38C	0.38	0.26	0.75	0.03	0.02	0.12
0.53C	0.53	0.29	0.72	0.01	0.02	0.09
0.80C	0.80	0.20	0.96	0.03	0.02	0.02

In order to study the effect of ferrite grain size on the EM sensor readings, the 0.17 wt% C steel sample was heat treated at 890, 1000, 1100 and 1200 ℃ for 1 hour followed by furnace cooling, to achieve near-equilibrium conditions and therefore the same ferrite-pearlite phase balance. In addition, a pure iron sample was normalised at 930 ℃ and air cooled, for 5 cycles, to reduce the ferrite grain size, and another pure iron sample

was austenitised at 1300 ℃ for 2 hours followed by furnace cooling to increase the ferrite grain size.

The C-Mn steels were used to study the effect of ferrite – pearlite phase balance, carbon level in as-quenched martensite and tempered martensite phase on the EM sensor readings. 0.17 wt% C, 0.38 wt% C, 0.53 wt% C and 0.80 wt% C steel samples were heat treated at 910 ℃ for 1 hour followed by a water quench to create a as quenched martensitic structure. After that, a water quenched 0.80 wt% C steel samples was quenched in liquid nitrogen in order to transform the retained austenite to martensite. 0.38 wt% C and 0.80 wt% C martensite samples were also tempered at 280 ℃ and 450 ℃ for one hour to study the effect of tempering on the magnetic permeability values and the EM sensor readings.

Table 4.2: C-Mn steel samples and their heat treatment conditions

Sample	**Thermal history/heat treatment conditions**
Fe	Pure iron sample normalised at 930 ℃ followed by air cooling for 5 cycles
Fe - 1300	Pure iron sample austenitised at 1300 ℃ for 2 hours followed by furnace cooling
0.17C	As received hot rolled bar sample
0.17C-890	0.17C sample austenitised at 890 ℃ for 1 hour followed by furnace cooling
0.17C-1000	0.17C sample austenitised at 1000 ℃ for 1 hour followed by furnace cooling

0.17C-1100	0.17C sample austenitised at 1100 ℃ for 1 hour followed by furnace cooling
0.17C-1200	0.17C sample austenitised at 1200 ℃ for 1 hour followed by furnace cooling
0.17C-Q	0.17C sample austenitised at 910 ℃ for 1 hour followed by water quenching
0.38C	As received hot rolled bar sample
0.38C-Q	0.38C sample austenitised at 910 ℃ for 1 hour followed by water quenching
0.38C-QT280	0.38C-Q sample tempered at 280 ℃ for 1 hour
0.38C-QT450	0.38C-Q sample tempered at 450 ℃ for 1 hour
0.53C	As received hot rolled bar sample
0.53C-Q	0.53C sample austenitised at 910 ℃ for 1 hour followed by water quenching
0.80C	As received rail track steel grade 260 (hot rolled, stress free)
0.80C-Q	0.80C sample austenitised at 910 ℃ for 1 hour followed by water quenching
0.80C-LQ	0.80C-Q sample quenched in liquid nitrogen
0.80C-QT280	0.80C-Q sample tempered at 280 ℃ for 1 hour
0.80C-QT450	0.80C-Q sample tempered at 450 ℃ for 1 hour

4.1.2 Pearlitic steels

Pearlitic steel (termed PW steel) wire samples were supplied by Tata Steel (UK) with different heat treatment conditions (variation in austenitisation temperature, cooling rate, and salt bath heat treatment temperatures). Three nominally identical samples (measuring 4.95 mm in diameter ×200mm in length) for each heat treatment condition were provided. The ferrite fraction, pearlite interlamellar spacing, cementites lath thickness and tensile strength of these samples were measured and supplied by Tata Steel (UK).

In addition, a case study was carried out using another grade of tyre bead steel wire samples (termed TW steel), supplied by Tata Steel (India). The samples were austenitised at 1100 ℃ followed by salt bath heat treatment at 590 ℃, 600 ℃, 610 ℃, 620 ℃ and 630 ℃ for 6 minutes. Three nominally identical samples (measuring 3 mm in diameter ×200mm in length) for each heat treatment condition were provided. The pearlite interlamellar spacing of these isothermally transformed samples was measured by Tata Steel (India) using the intercept method. It is worth mentioning that all of the TW wire samples are slightly curved in as a received condition.

The chemical composition of the PW and TW steel wire samples is given in Table 4.3. The heat treatment conditions of the PW and TW steel wire samples are given in Table 4.4 and 4.5 respectively.

Table 4.3: Chemical composition for the PW and TW steel wire samples, all in wt%.

Sample	C	Si	Mn	S	P
PW steel	0.81	0.21	0.52	0.005	0.01
TW steel	0.67	0.20	0.66	0.01	0.02

Table 4.4: Heat treatment conditions of PW steel wire samples

Sample	Austenitisation Temperature (°C)	Cooling rate (°C/s)	Salt bath Temperature (°C)	Maximum transformation temperature (°C)
PW-A	900	11	N/A	666
PW-B	900	22	N/A	646
PW-C	900	28	N/A	636
PW-D	1000	11	N/A	653
PW-E	1000	22	N/A	630
PW-F	1000	28	N/A	623
PW-G	900	132	450	552
PW-H	900	100	500	620
PW-I	900	52	550	646
PW-J	1000	72	450	591

PW-K	1000	68	500	614
PW-L	1000	34	550	632

Table 4.5: TW steel wire samples and their heat treatment conditions

Sample	Descriptions/heat treatment conditions
TW-590	TW steel wire sample austenitised at 1100 ℃ followed by salt bath heat treatment at 590 ℃ for 6 minutes.
TW-600	TW steel wire sample austenitised at 1100 ℃ followed by salt bath heat treatment at 600 ℃ for 6 minutes.
TW-610	TW steel wire sample austenitised at 1100 ℃ followed by salt bath heat treatment at 610 ℃ for 6 minutes.
TW-620	TW steel wire sample austenitised at 1100 ℃ followed by salt bath heat treatment at 620 ℃ for 6 minutes.
TW-630	TW steel wire sample austenitised at 1100 ℃ followed by salt bath heat treatment at 630 ℃ for 6 minutes.

4.1.3 Dual phase steels

In order to study the EM response of ferrite – martensite phase balance, dual phase (DP) steels were used. A lab grade dual phase steel (DPL600) with carbon content of about 0.17 wt% was supplied by Tata Steel (UK) in different intercritical annealing heat treatment states (full compositions of the lab and commercial DP steels have not been included for commercial reasons). These samples were heat treated for 1 hour at a different temperature ranging from 650 to 800 ℃ in 50 ℃ steps followed by water

quenching. As a result, a fraction of the microstructure was re-austenitised and transformed to martensite during the quenching process.

A case study using EM measurement for commercial DP and CP strip steels was carried out. For this work different grades of commercial DP and CP strip steels samples (measuring approximately 400mm ×200mm ×2mm) were supplied by Tata Steel. The steels contained 0.1-0.2 wt% C and 1.5 – 2.2 wt% Mn, the amount of these elements generally increasing with increasing strength. Additions of Nb and Ti are also used to achieve strength levels of DP800 and above. The DP600GI and DP800GI grades have, nominally, the same composition as the DP600 and DP800 grades respectively and were supplied with a galvanised layer approximately 50μm thick. DP1000A and DP1000B grades achieve similar mechanical properties by using different chemical compositions and manufacturing processes. The form of the dual phase steel samples and their thermal history/heat treatment conditions are given in Table 4.6.

The yield and tensile strength were measured, by Tata Steel, in the transverse direction for the DP600, DP600GI and DP1000B grades and the longitudinal direction for the DP800, DP800GI, DP1000A and CP1000 grades.

Table 4.6: Dual phase steel samples and their heat treatment conditions

Sample	Descriptions/heat treatment conditions
DPL600-650	DPL600 strip steel (1mm thickness) intercritical annealed at 650 ℃ for 1 hour followed by water quench
DPL600-675	DPL600 strip steel (1mm thickness) intercritical annealed at 675 ℃ for 1 hour followed by water quench

DPL600-700	DPL600 strip steel (1mm thickness) intercritical annealed at 700 ℃ for 1 hour followed by water quench
DPL600-725	DPL600 strip steel (1mm thickness) intercritical annealed at 725 ℃ for 1 hour followed by water quench
DPL600-750	DPL600 strip steel (1mm thickness) intercritical annealed at 750 ℃ for 1 hour followed by water quench
DPL600-800	DPL600 strip steel (1mm thickness) intercritical annealed at 800 ℃ for 1 hour followed by water quench
DP600	As received strip steel sample (1mm thickness)
DP600GI	As received strip steel sample with Zn coating (1mm thickness)
DP800	As received strip steel sample (1mm thickness)
DP800GI	As received strip steel sample with Zn coating (1mm thickness)
DP1000A	As received strip steel sample (1mm thickness)
DP1000B	As received strip steel sample (1mm thickness)
CP1000	As received strip steel sample (1mm thickness)

4.2 Microscopy and image analysis

Sectioned samples were mounted in conductive Bakelite, ground and fine polished to an OPS finish and etched in 2% Nital. The optical microstructure was characterised using a Zeiss optical microscope. Ferrite/pearlite phase balance and ferrite grain size (equivalent circle diameter) of the samples were analysed using "Image J" image

analyser software. Typically ten images were analysed for phase balance and 1000 grains quantified to give grain size distributions.

In order to distinguish and quantify the second phases, SEM micrographs were obtained using a JEOL7000 SEM. The ferrite, bainite/tempered martensite and martensite phases were manually distinguished based on the contrast within the grains (bainite and tempered martensite have higher contrast whilst martensite has low contrast, as shown in Figure 4.1) and the percentage of each phase present was quantified using "Image J" image analysis software. Typically ten SEM images were analysed for phase balance quantification.

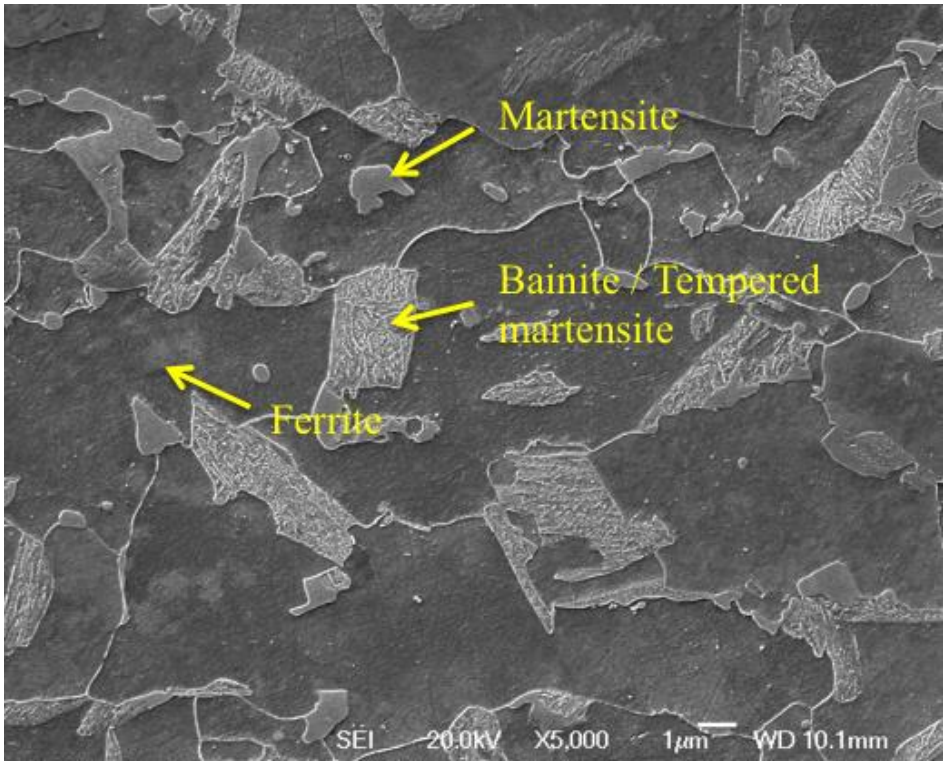

Figure 4.1: SEM image of a DP600 sample showing the different phases identified in the microstructure.

4.3 Magnetic domain observation

The magnetic domain structure was obtained by the Bitter method for pure iron and low carbon steel samples. Samples were firstly mounted in conductive Bakelite, ground and fine polished to 1 μm finish. Then a drop of (~ 1 ml) ferrofluid (purchased from Ferrofluid Ltd with average particle size of 10 nm) was applied to the polished surface using a measuring pipette and the sample was examined using a Zeiss optical microscope. A micro hardness indent grid was used as a reference map to correlate the domain structure with the ferrite microstructure, obtained following cleaning the surface to remove the ferrofluid then etching with Nital, in the same area.

4.4 Hardness and electrical resistivity measurement

Hardness was measured on polished samples by Vickers micro hardness measurement with a 500g load. Each hardness value was determined by taking the average of five measurements spaced at least three hardness diameters apart to avoid overlapping stress fields.

Electrical resistivity measurements were performed on cylindrical samples measuring 4.95 mm diameter and 50 mm length using a conventional four point DC method with a Cropico microhommeter which has a resolution of 0.1 microhms over a 30 milliohm range. Each resistivity value was determined by taking the average of ten measurements.

4.5 EM sensor measurement

4.5.1 Cylindrical sensor

The cylindrical EM sensor used in this project has exciting and sensing coils that are air-cored. Each coil has an inner diameter of 7.95mm, 0.2mm height, 10.5mm length and 56 turns. The coils were driven by an impedance analyser (Solartron 1250) at frequencies from 10 Hz to 65000Hz, and the real inductance values were taken.

Samples for cylindrical EM sensor measurements (cylindrical shape with 4.95mm diameter and 50mm length) were machined from the C-Mn grade as-received or the heat-treated samples. Each C-Mn sample was examined with three repeat tests at the same locations.

Pearlitic steel wire samples (including both TW and PW grades) were place into cylindrical EM sensor in as received condition. In this case, the EM sensor was place in centre (in terms of length of the wire samples) of the wire sample to avoid any edge effect (length of sample 200 mm is larger than the sensor 50 mm). Each sample was examined with eight repeat tests at the same locations.

4.5.2 U-shaped sensor

The EM measurements for strip steels (dual phase and complex phase steels) were carried out using a U-shape EM sensor (measuring 20×9×2mm). The sensor has one generating coil (100 turns) and two sensing coils (60 turns). An impedance analyser (Solartron 1250) was connected to the sensor supplying a 3V ac current at 100Hz. The

real inductance values were recorded. Measurements were made with the sensor oriented parallel and perpendicular to the rolling direction of the steel strip samples with zero lift-off. Each sample was examined with eight repeat tests at different locations. The average inductance values and standard deviation were calculated.

4.6 FE modelling of relative permeability with real microstructures

The relative permeability values for steels with different phase balance were modelled from their microstructures using a previously developed FE model using COMSOL MultiPhysics software. The model is described in ref [8]. Optical and SEM micrographs (about 8 images for each sample) were processed into black–white binary images using Image J software (Figure 4.1a - 4.1b). The binary image is then imported into FE model using the built-in "image import function" in COMSOL, where the relative magnetic permeability values were manually assigned to each phase type. The relative permeability of ferrite, pearlite, martensite and tempered martensite was set as 330, 59, 55 and 97 respectively (predicted values for single phase steels, details of how these values were obtained is given in Chapter 5). An example of image processing for modelling on an actual microstructure is shown in Figure 4.2. The model microstructure sample was subjected to a uniform horizontal magnetic field by setting the top and bottom boundaries of the sample with a magnetic potential of 1 and 0, respectively. The left and right boundaries of the sample were set as electric insulation (magnetic field normal to boundary) to eliminate the demagnetising field. An example of modelled results of magnetic flux density distribution with indicated boundary conditions of the model is shown in Figure 4.3. The relative permeability was calculated by equation 4.1:

$$\mu_r = \frac{B_{ave}}{\mu_0 H_{ave}} \qquad \text{Equation 4.1}$$

Where μ_r is the relative permeability of the sample, μ_0 is the permeability of free space, H_{ave} is the average magnetic field inside the sample, and B_{ave} is the average flux

density inside the sample. H_{ave} and B_{ave} were obtained from the output of the FE model which included geometry calculations of the sample.

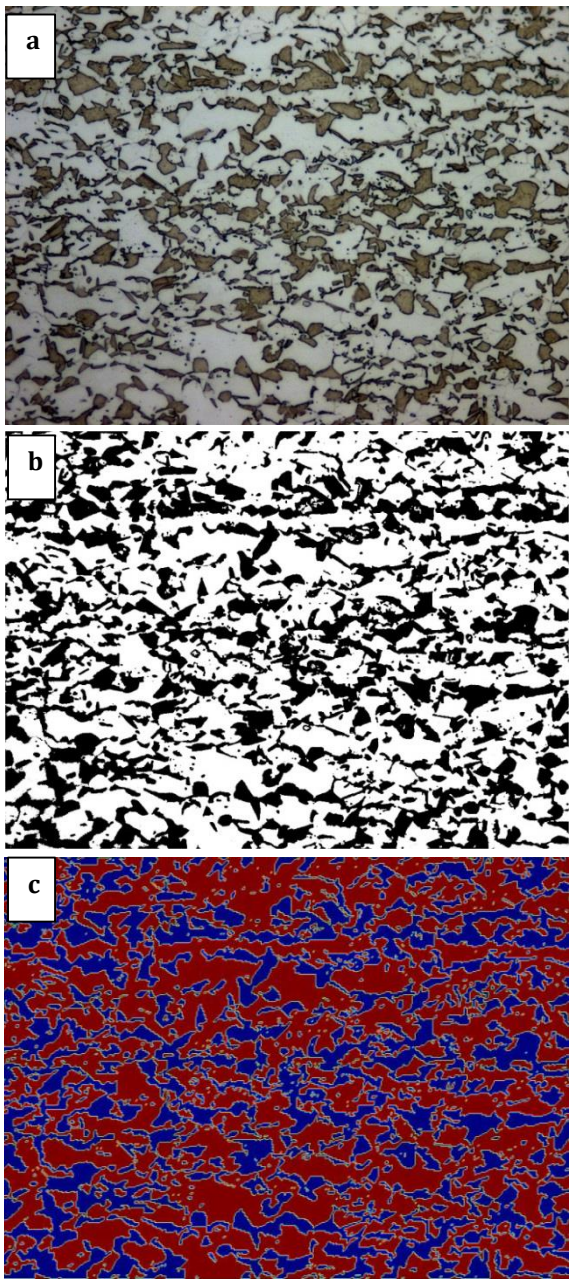

Figure 4.2: Image processing for modelling on actual microstructures: (a) an optical micrograph of a DP steel sample; (b) processed black–white image of (a); (c) the relative magnetic permeability of ferrite phase (330, red) and martensite phase (55, blue).

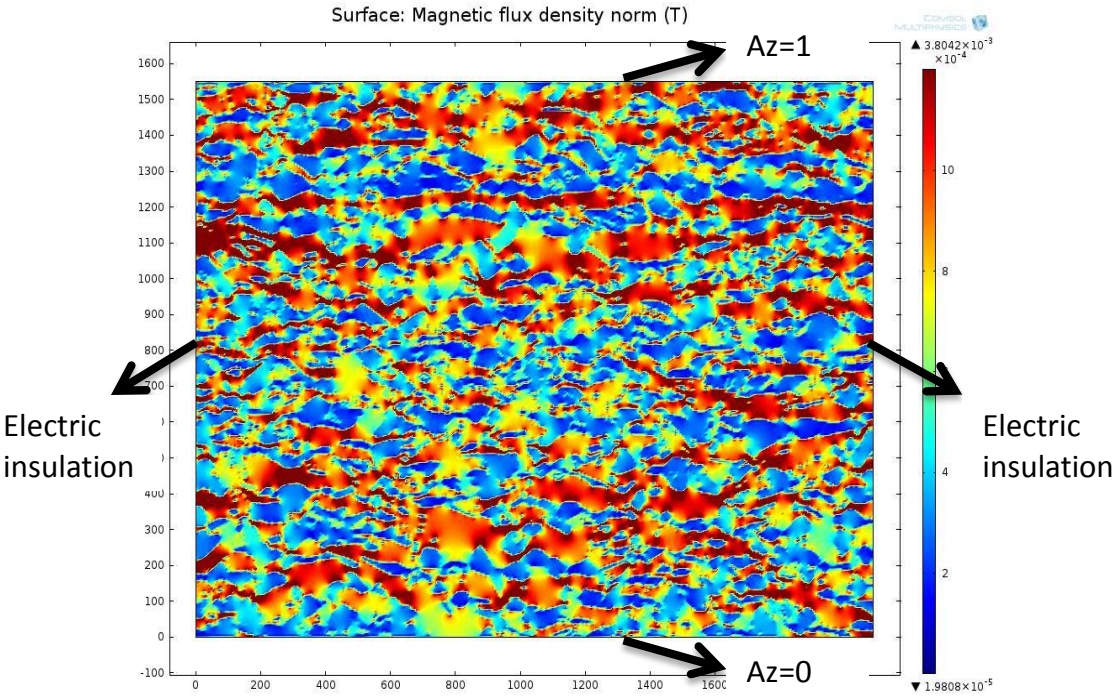

Figure 4.3: An example of modelled results of magnetic field distribution from the micrograph shown in Figure 4.1. The applied magnetic field is in the horizontal direction to the image, boundary conditions are indicated.

5 Modelling of the EM sensor output using FE method

5.1 EM sensor output model settings

The EM sensor signal is affected by both the magnetic and electrical properties of the materials under inspection. Therefore, it is important to understand the effect and the significance of changes in each material's property on the EM sensor signal. In this chapter, this is studied using a two-dimensional (2D) axial symmetry FE sensor output model developed using COMSOL software, described below.

The model is similar to that reported in ref [7]. The geometry and coil details of the sensor-sample were set to be the same as the experimental cylindrical sensor set up used in this project, described in Chapter 4.6.1. The geometry of the sensor and sample in the model is shown in Figure 5.1 and a three dimension (3D) view of the 2D model is presented in Figure 5.2. The model geometry consists of an air block, an exciting coil, a sensing coil and the sample. The exterior boundaries were set as magnetic insulation and the interior boundaries were set as continuity (as system default setting which allow the magnetic flux to penetrate through the selected boundary). Extra fine physics controlled mesh (defined in the COMSOL software) was applied to the entire sensor geometry with refined (defined in the COMSOL software) mesh to the sample geometry. The complete mesh of the model consists of 14782 domain elements and 758 boundary elements. A screen shot of the model showing the refined mesh elements near the coils is given in Figure 5.3.

An AC voltage of 3V was applied to the exciting coil in the model with a sweeping frequency of 10-65000 Hz. Total number of 51 frequency data points (logarithmically spaced) from 10 Hz to 65000 Hz were calculated in each model. The real inductance values of the sensing coil were derived from the model output. A typical sensor output of real inductance plotted with frequency (logarithmic scale) calculated from the model for a sample that has relative permeability value of 200 and electrical resistivity value of 210 nΩm (typical permeability and resistivity values for ferritic steels [8, 76]) is given in Figure 5.4. The shape of the sensor output plot agrees with that reported in the literature using the similar sensor setup [8, 162]. An explanation of the curve shape has been given in section 2.3.1 in Chapter 2.

The 2D plot of modelled magnetic flux density and flux line distribution in a sample (with permeability = 200, resistivity = 210 nΩm) at 10 Hz and 65000 Hz are presented in Figure 5.5 and 5.6 respectively. It can be seen that the magnetic flux at frequency of 10 Hz can penetrate into the sample with much greater depth than at the high frequency of 65000 Hz due to the skin effect, described in section 2.3.1.

The average applied magnetic field to the sample, calculated from the model, is 7.4007 A/m. As it can be seen from Figure 2.12 in section 2.3.2 in Chapter 2, the magnetic field applied to achieve saturation is about 5 kA/m and 7 kA/m for a 99.99% pure iron and a 0.45 wt% C steel sample respectively. Therefore, applied magnetic field to the sample in the EM sensor corresponds to a very low applied field (approx. 0.15% or 0.11% of a saturation field for a 99.99% pure iron sample and a 0.45 wt% C steel sample respectively) in the hysteresis loop measurement for steels. Therefore the relative permeability value, which dominates the low frequency inductance (approx. below

100Hz) of this sensor output, is expected to be very similar to the initial permeability value measured with hysteresis loop measurements. For example, the results in section 7.2.3 in Chapter 7 shown that the relative permeability values, determined by fitting the experimental EM sensor results with the FE model, for a 0.80 wt% C steel which contains single-phase pearlite is 58.6. This value agrees well (within 6%) with Thompson et al. [91], who reported that the initial relative permeability of fully pearlitic phase (in a 0.87 wt.% C steel) is 56.

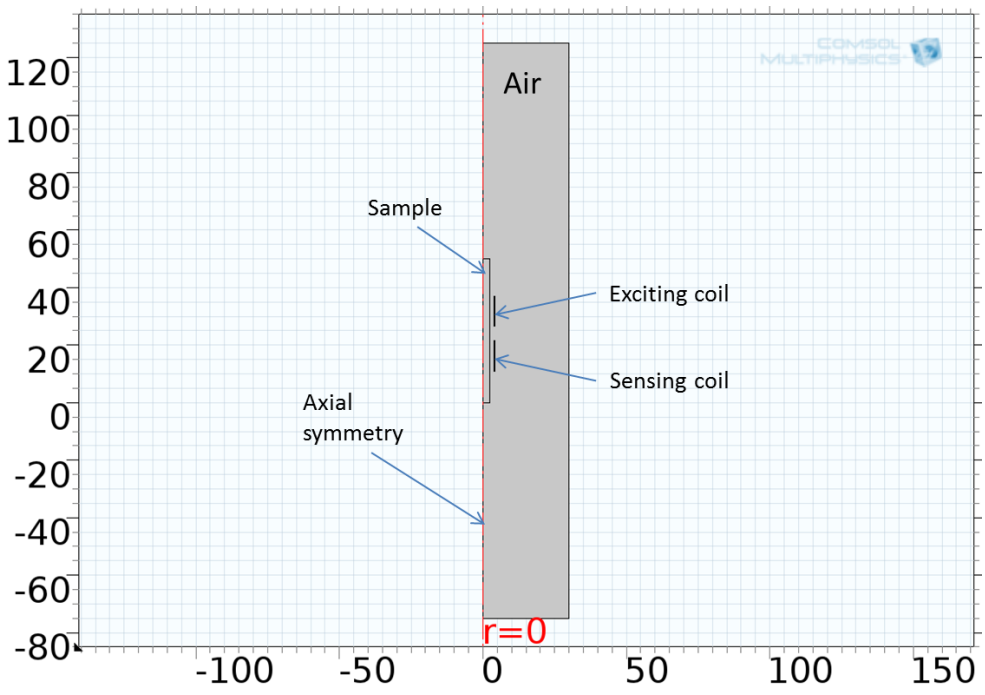

Figure 5.1: Geometry setup of the sensor and sample in the 2D axial symmetry sensor output model

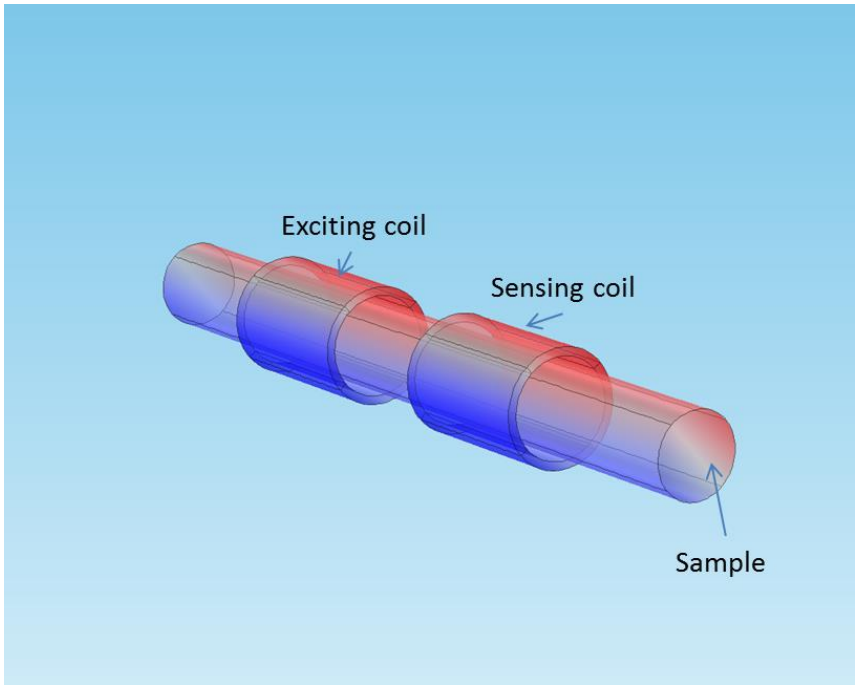

Figure 5.2: 3D view of the 2D sensor output model.

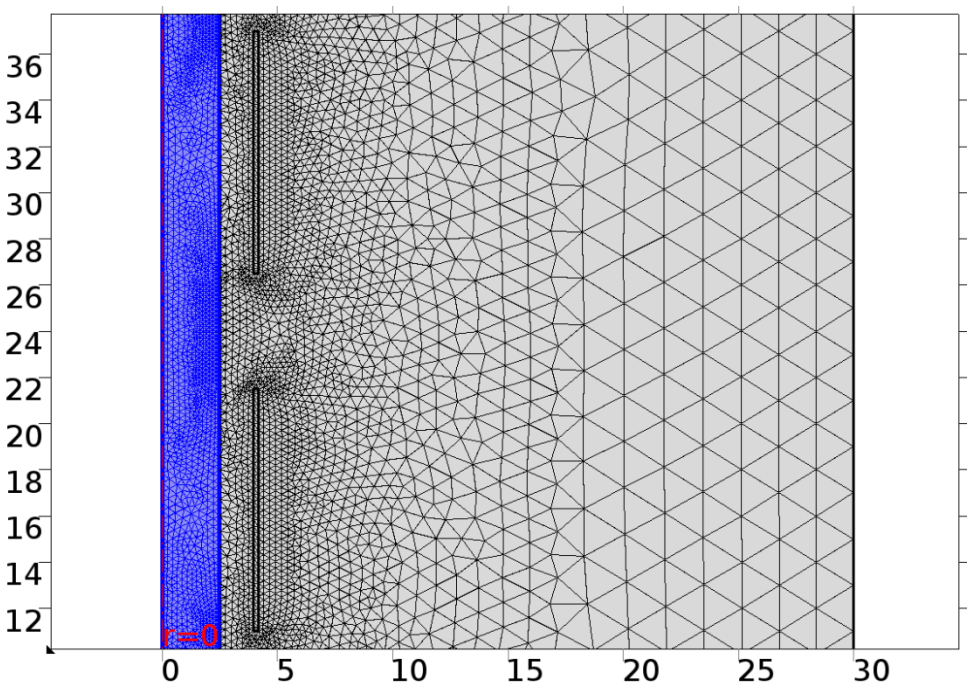

Figure 5.3: Meshing view of the 2D sensor output model, axes are geometry coordinates in millimetres.

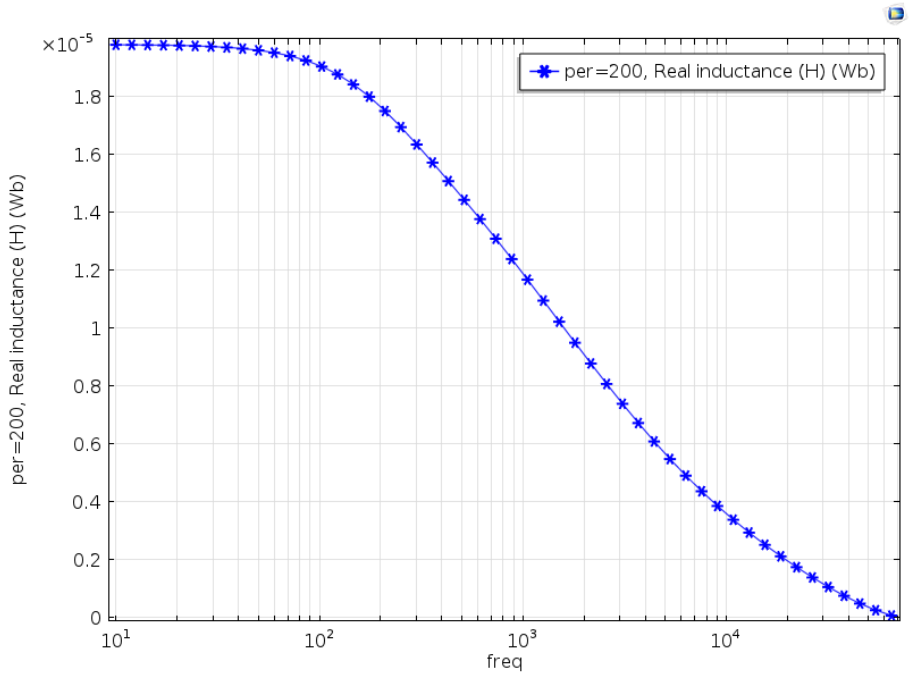

Figure 5.4: Modelled sensor output: real inductance plot with frequency (logarithmic scale) of a sample with properties of: Permeabiltiy = 200 and resistivity = 210 nΩm.

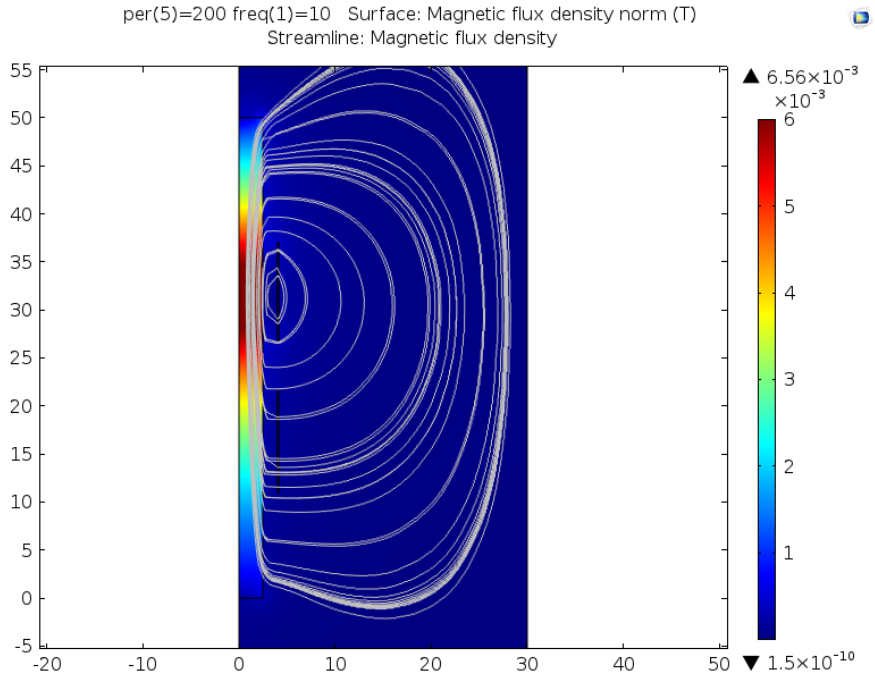

Figure 5.5: 2D plot of modelled magnetic flux density of a sample (Permeabiltiy = 200, resistivity =210 nΩm) at 10Hz

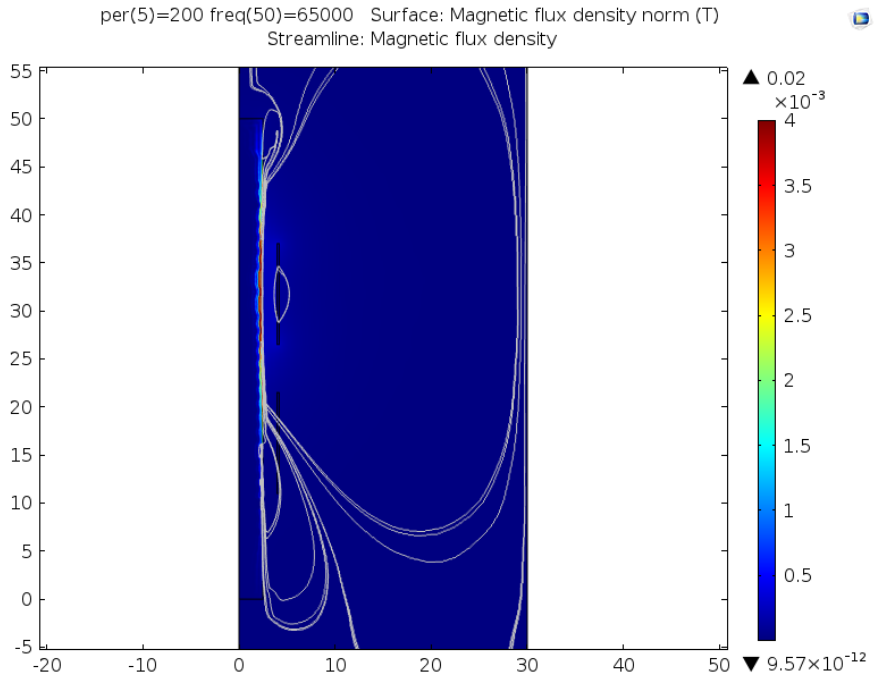

Figure 5.6: 2D plot of modelled magnetic flux density of a sample (Permeabiltiy =200) at 65000Hz

5.2 Sensitivity of EM sensor to changing relative permeability

EM sensor output for samples with the same electrical resistivity (210 nΩm) but changing relative permeability value in the range of 1-350 (relative initial permeability range for structural steel, initial permeability value of 1, 56, and 350), as been reported for fully austenitic, pearlitic and ferritic microstructures respectively [91, 100, 150]), are modelled.

The modelled real inductance plot with frequency (logarithmic scale) for different relative permeability values is given in Figure 5.7. It can be seen that the real inductance at low frequency (below approx. 100 Hz) increases with the relative permeability values. This is because, at low frequency, the sensor attempts to magnetise the sample, so the strength of the generated magnetic flux from the sample increases with relative permeability (details of how inductance is related to the relative permeability of the samples are provided in section 3.1 in Chapter 3). Relative permeability has a dominant effect for steel on the low frequency inductance.

The relationship between the modelled real inductance value at 10 Hz and relative permeability of the sample is given in Figure 5.8. It can be seen that the real inductance at low frequency in this specific sensor design is more sensitive to the lower relative permeability range than the higher ones.

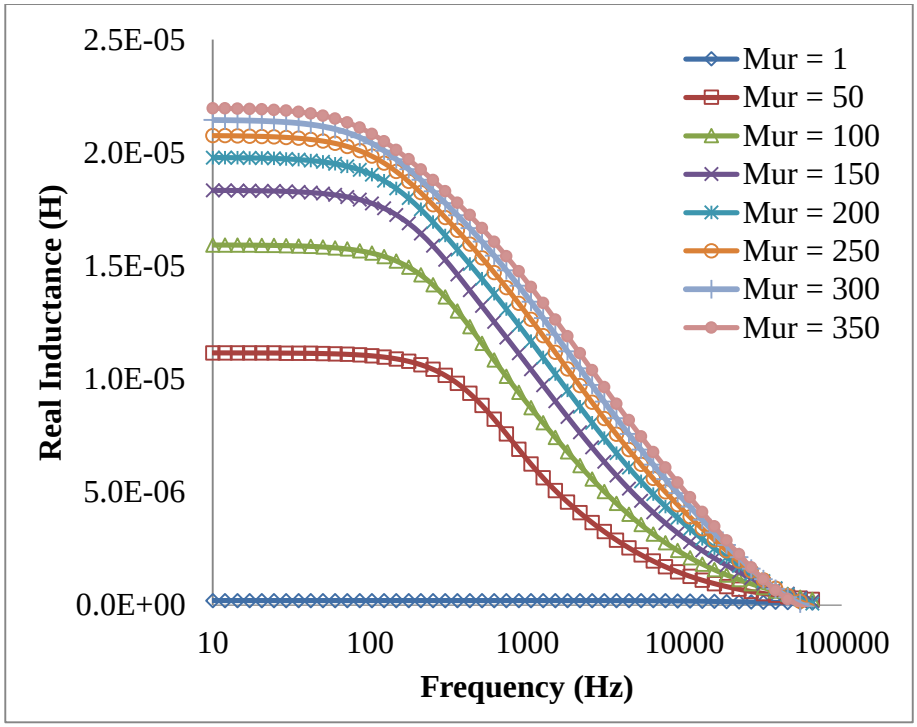

Figure 5.7: Modelling results of real inductance changes with frequency for samples with same electrical resistivity but changing relative permeability.

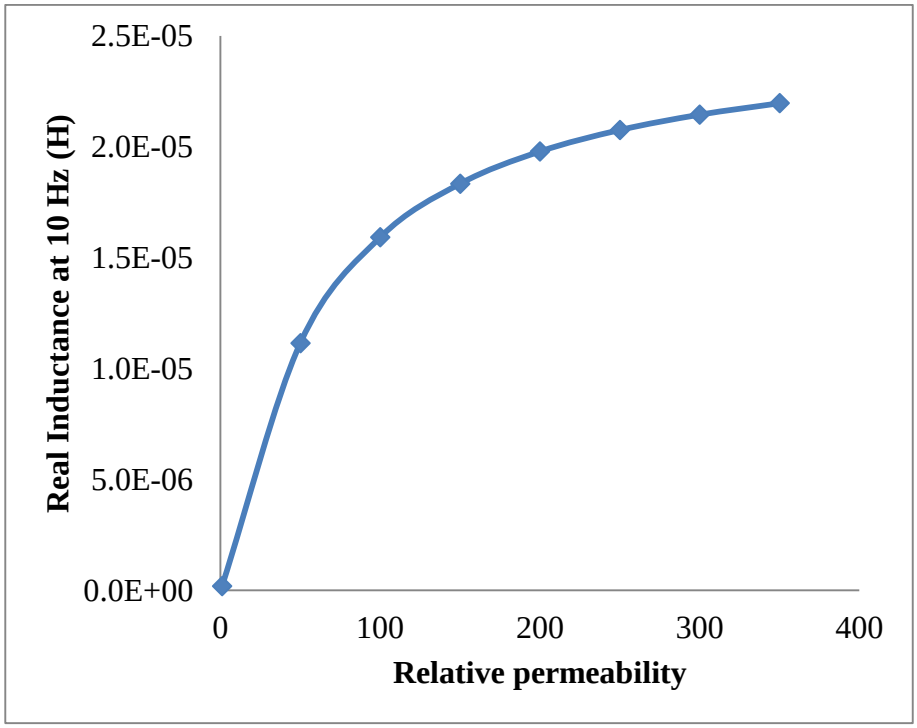

Figure 5.8: Relationship between modelled real inductance at 10 Hz and relative permeability of the sample.

5.3 Sensitivity of EM sensor to changing electrical resistivity

As discussed in Chapter 3.8, the electrical resistivity is affected by the steel microstructure and chemistry. The effect of changing electrical resistivity on the sensor output was studied with the FE sensor output model. A board range of electrical resistivity has reported (95 – 120 nΩm for iron, 130 - 289 nΩm for structural steels and 250 - 780 nΩm for alloyed and stainless steels) [157, 163]. The typical resistivity value range for structural steels examined in this project is 210 - 250 nΩm and 105 nΩm of a pure iron sample (results are presented in Chapter 6 and 7). The EM sensor output for samples with the same relative permeability value of 200 and 1, selected as a typically high and low relative permeability value respectively, but with changing electrical resistivity in the range of 210-250 nΩm are modelled.

The modelled real inductance plot with frequency (logarithmic scale) for same relative permeability value of 200 but different electrical resistivity values is given in Figure 5.9. An expanded version of Figure 5.9 focusing on showing the frequency range of 500-5000 Hz (which has the highest sensitivity to electrical resistivity change) is given in Figure 5.10. It can be see that the effect of changing of electrical resistivity in the range of structural steels (210-250 nΩm) on the sensor output is very small (maximum difference of 5.6% in real inductance at any frequency). The real inductance value measured below 100 Hz is insensitive to the change in electrical resistivity values.

The modeled sample with an electrical resistivity value of pure iron (105 nΩm) shows a clearly different shape in its real inductance versus frequency plot than the other samples. This is due to a significant eddy current effect occurring at a much lower frequency (20 Hz) than in other samples (100 Hz). The real inductance at frequencies

below 20 Hz is independent of any change in electrical resistivity value and has the same value as the other samples as this is controlled by the relative permeability.

A plot of real inductance with frequency (logarithmic scale) for same relative permeability value of 1 but different electrical resistivity values is shown in Figure 5.11. in compare with the higher relative permeability (200) results, the real inductance value remain insensitive to the change in electrical resistivity values until up to 1000 Hz. Therefore the effect on plateau low frequency inductance is not significant to changes in electrical resistivity values regardless of high or low relative permeability value.

In summary, the model results for the EM sensor output show that changes in resistivity can be ignored if the plateau low frequency inductance value is considered, where changes in relative permeability dominate the signal. Equally, in order to determine the effect of microstructure on the relative permeability of steel, the low frequency inductance value in the plateau region can be measured.

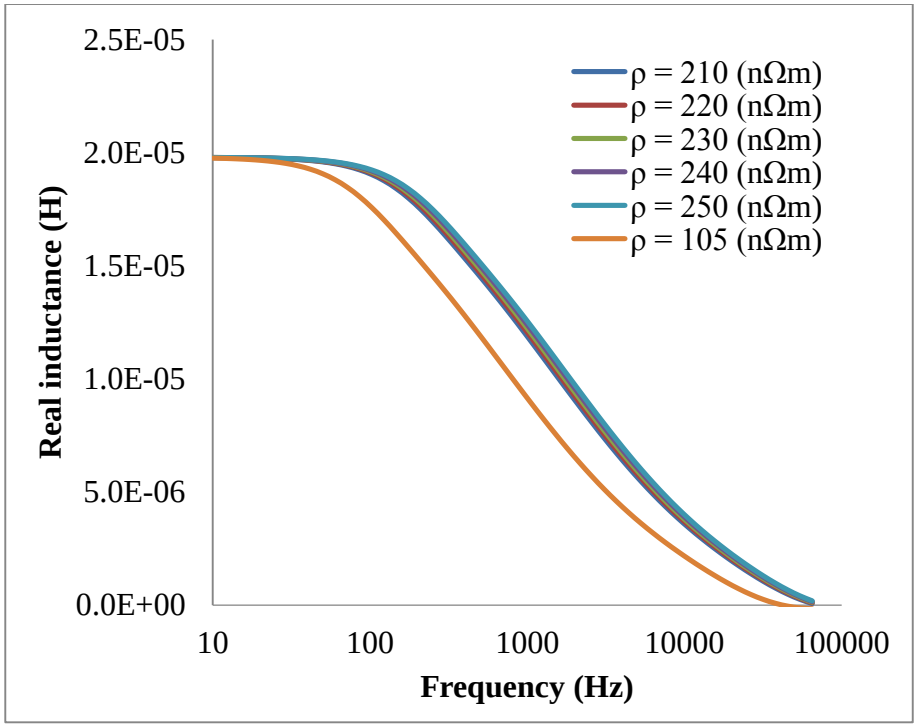

Figure 5.9: Modelling results of real inductance changes with frequency for samples with same relative permeability (200) but changing electrical resistivity.

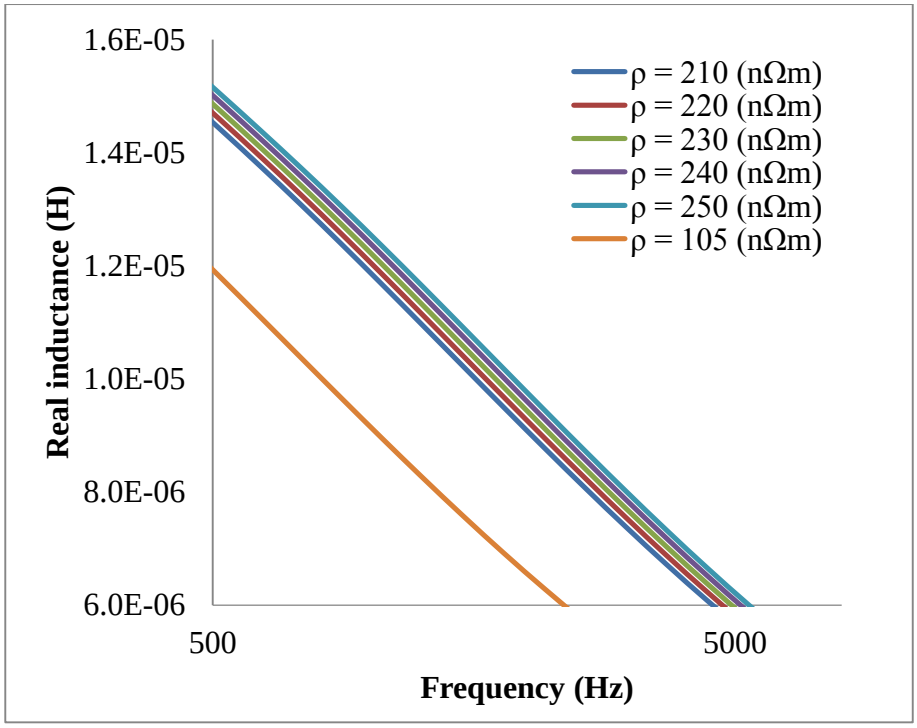

Figure 5.10: An expanded version of Figure 5.5 focusing on showing the frequency range of 500-5000 Hz.

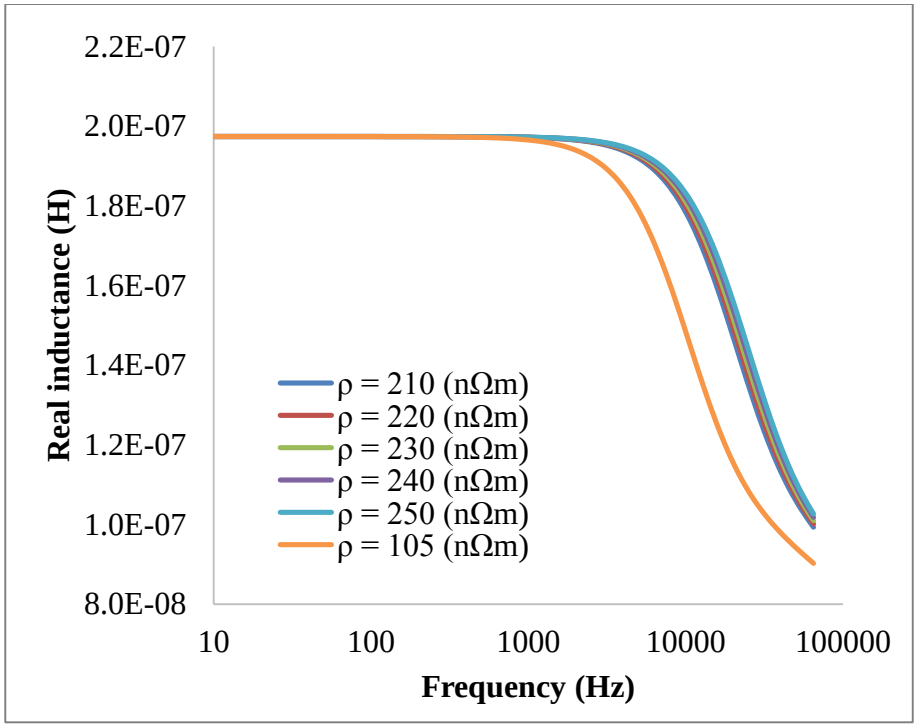

Figure 5.11: Modelling results of real inductance changes with frequency for samples with same relative permeability (1) but changing electrical resistivity.

5.4 Prediction the relative permeability values for the experimental EM measurement

The EM sensor output signal is dependent on both the electromagnetic properties sample and sensor design. In order to study the effect of microstructure parameter on the EM properties of the material, which is regardless of sensor design, it is important to be able to measure the electromagnetic properties of the sample from the sensor output. In this case, conclusions drawn from one study can be also applied to another even where a different sensor design is used.

A method has been developed to fit the 2D FE sensor model output to the experimental measured values using the cylindrical sensor described in section 4.5.1 in Chapter 4. The relative permeability values can be determined by fitting the modelled real (as in not imaginary) inductance with the experimental measured real ones, based on a nonlinear least square method in Comsol LiveLink for Matlab. The resistivity values of the samples were taken from the experimental measurements separately and used as an input in the FE model. The fitting was also carried out for both the relative permeability and electrical resistivity (in the case of electrical resistivity is not measured). In order to improve the accuracy of the fit, a total of 51 frequency data points (logarithmically spaced) across the full frequency range of 10 Hz to 65000 Hz were fitted.

Close fits (less than 1% error) between the modelled and measured real inductance for all the samples have been achieved in this project. An example of the FE model fitted sensor output result is plotted with the experimental measured ones for a 0.17 wt% C steel with average grain size of 63 μm is given in Figure 5.12. The relative permeability predicted for this sample is 210.

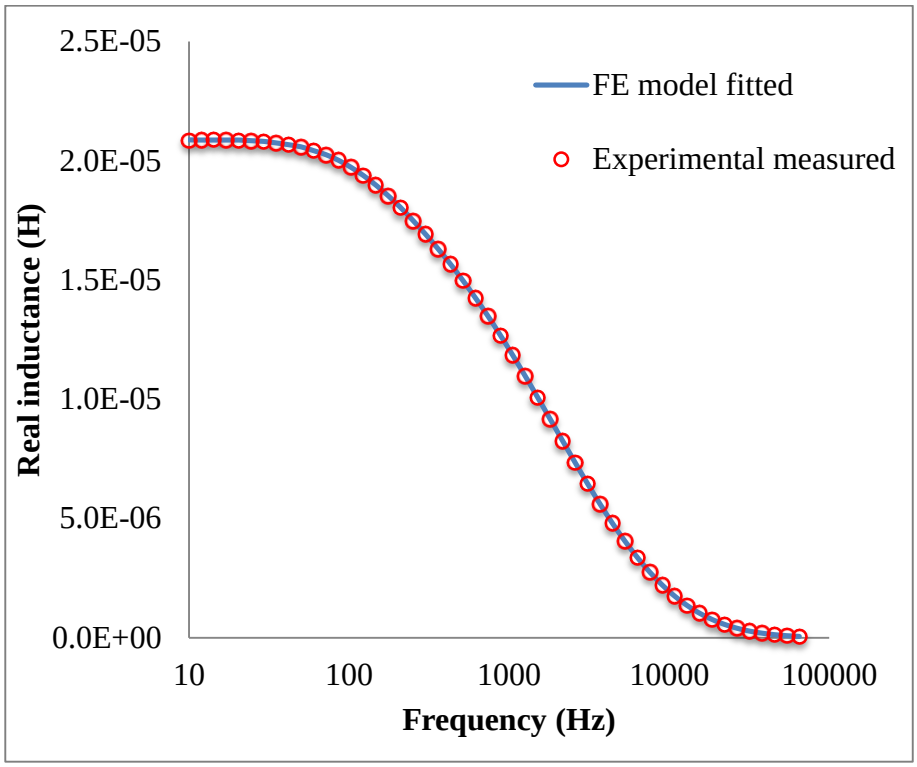

Figure 5.12: Plot of FE model fitted sensor output result with the experimental measured ones, for a 0.17 wt% C steel with average grain size of 63 µm.

6 EM detection of change in single microstructure parameters

6.1 Ferrite grain size for heat treated 0.17 wt% C steel samples

In structural steels, ferrite grain size is a well-known microstructure parameter which can have significant impact on mechanical properties such as yield strength (Hall-Petch) and toughness [9]. Previous research also suggested that magnetic properties are related to ferrite grain size, as the magnetic domain structure and domain wall motion are affected by grain boundaries [85, 89-92, 95, 136, 147, 149]. In this section, heat treated 0.17 wt% C steel and pure iron samples were used to study the effect of grain size on relative permeability values and hence the EM sensor signals, with the study of magnetic domain structures observed using Bitter method.

6.1.1 Microstructure characterization

The optical microstructures of the 0.17C steel samples, annealed at 890, 1000, 1100, and 1200 ℃ for 1 hour followed by furnace cooling, at ×100 magnification, are shown in Figures 6.1-6.4 respectively. The micrographs show a ferrite + pearlite microstructure with a random distribution of pearlite. It can be seen that the ferrite grain shape is almost equiaxed and that the ferrite grain size increases with an increase in annealing temperature. Table 6.1 shows a summary of the average ferrite grain size (d) (equivalent circle diameter), ferrite fraction, and the measured electrical resistivity, with standard deviation values. There is little difference in ferrite fraction (within 2%)

and electrical resistivity values between the samples, due to the use of isothermal heat treatments and the identical steel chemical composition.

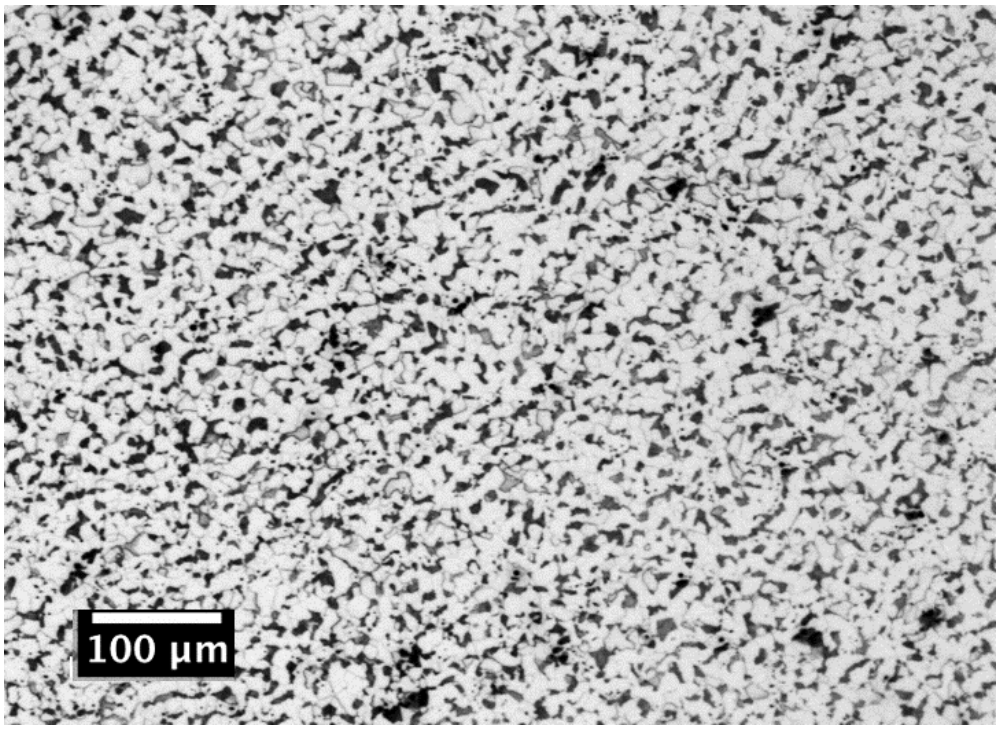

Figure 6.1: Optical microstructure of 0.17C-890 sample, at ×100 magnification.

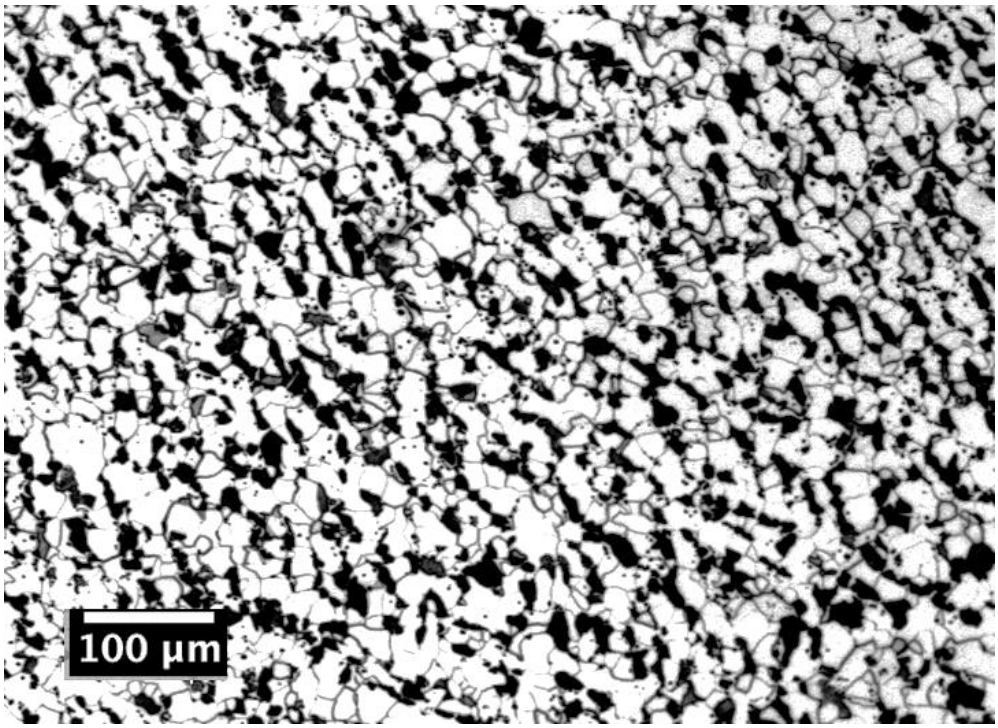

Figure 6.2: Optical microstructure of 0.17C-1000 sample, at ×100 magnification..

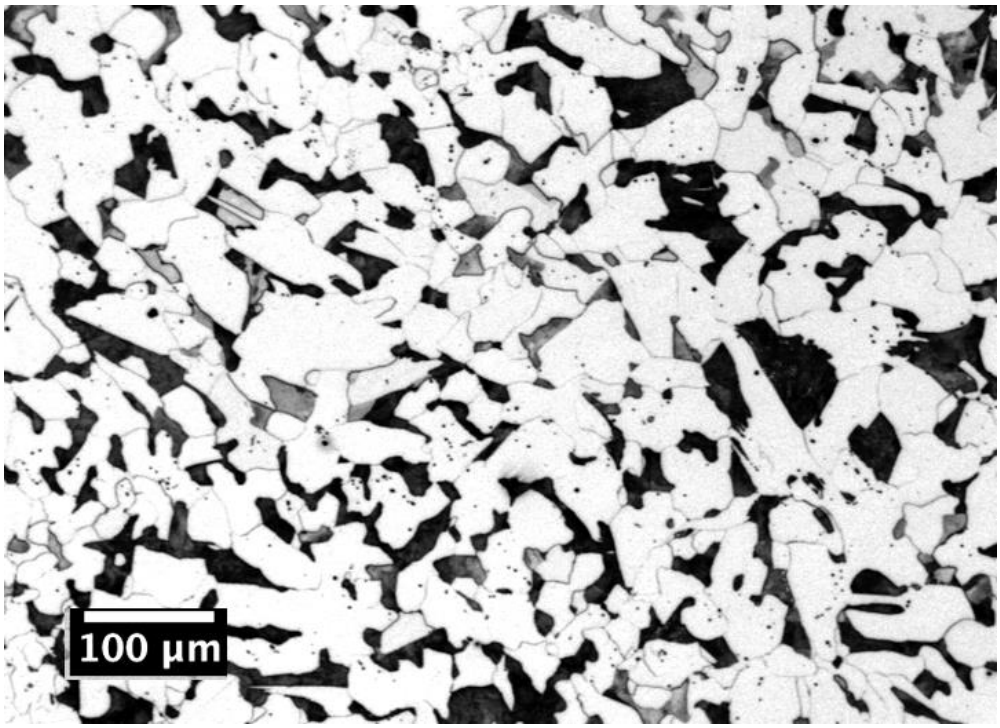

Figure 6.3: Optical microstructure of 0.17C-1100 sample, at ×100 magnification.

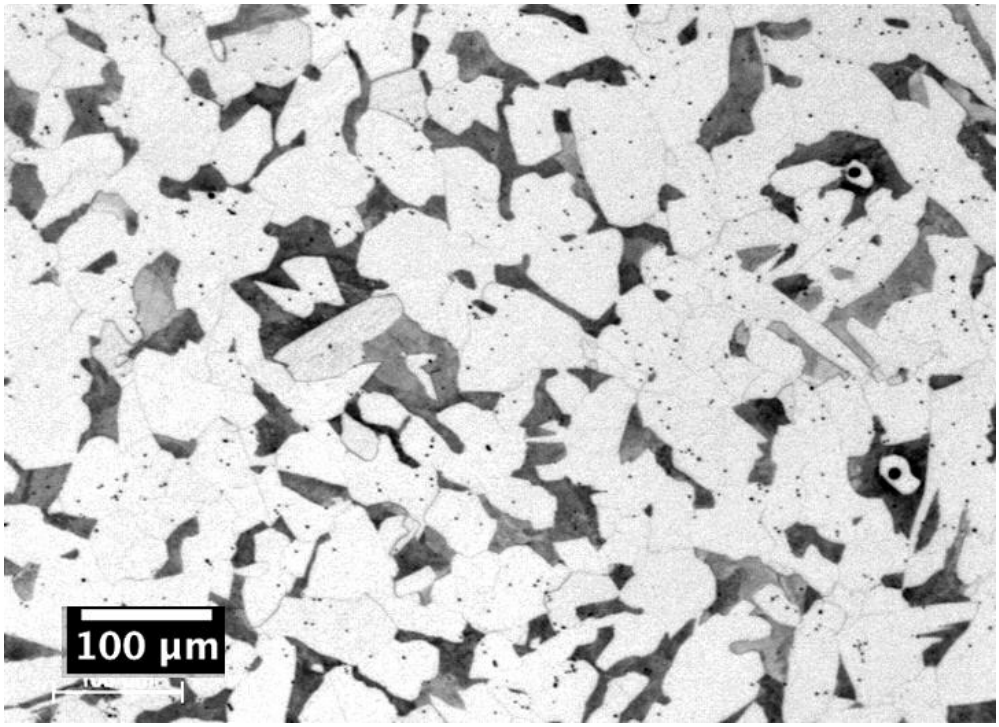

Figure 6.4: Optical microstructure of 0.17C-1200 sample, at ×100 magnification.

Table 6.1: Summary of the ferrite grain size, ferrite fraction and resistivity values of the 0.17C-890, 0.17C-1000, 0.17C-1100, and 0.17C-1200 steel samples.

Austenising temperature (°C)	**Average ferrite grain size (µm)**	**Ferrite fraction %**	**Resistivity (n.Ω.m)**
890	13 ± 5.8	66.8± 1.1	209± 0.1
1000	20 ± 8.3	67.6± 0.8	210± 0.2
1100	51 ± 23.3	67.6± 1.8	209± 0.2
1200	63 ± 27.2	68.3± 2.3	209± 0.1

6.1.2 EM sensor results

The measured real inductance versus frequency (logarithmic scale) results for the 0.17C steel samples with the same ferrite fraction but different ferrite grain size, using the cylindrical EM sensor are shown in Figure 6.5. An expanded version of Figure 6.5, focusing on showing the low frequency range, is given in Figure 6.6. It can be seen from Figure 6.5 and 6.6 that the sensor output (real inductance changes with frequency) can clearly distinguish the samples with the different grain size but same ferrite fraction. The real inductance values at low frequencies (below approximately 100 Hz), which are dominated by the relative permeability of the samples, increase with an increase in the average ferrite grain size. Repeatability tests have been carried out, the results of EM sensor output shown that the difference between the samples is significant and distinguishable from each other.

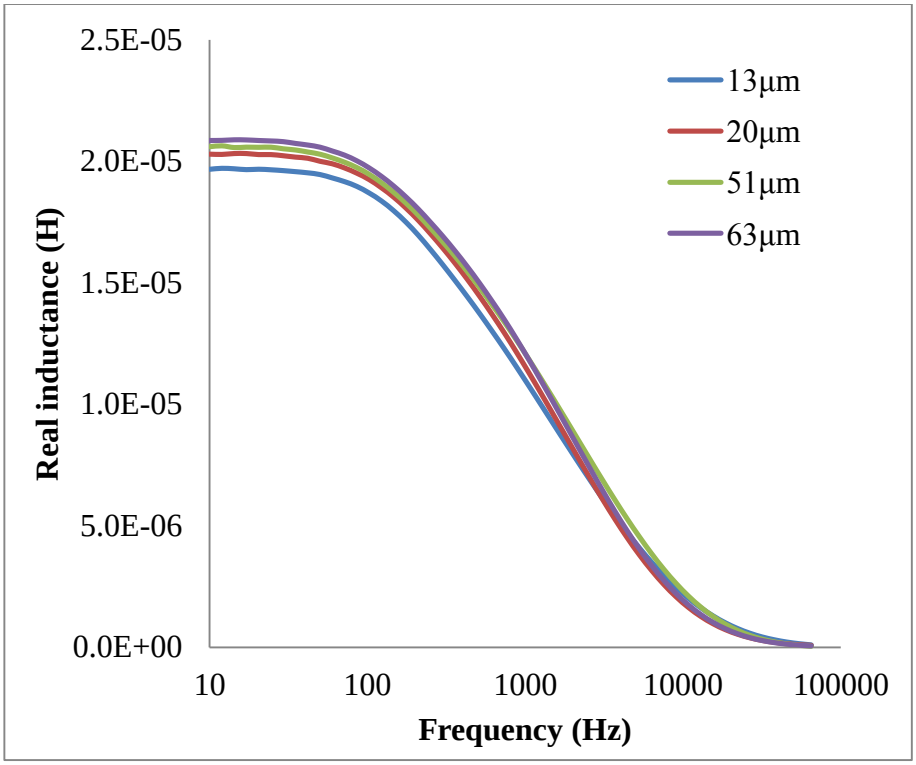

Figure 6.5: Real inductance changes with frequency for 0.17wt% C steel sample with ferrite grain size of 13, 20, 51 and 64µm.

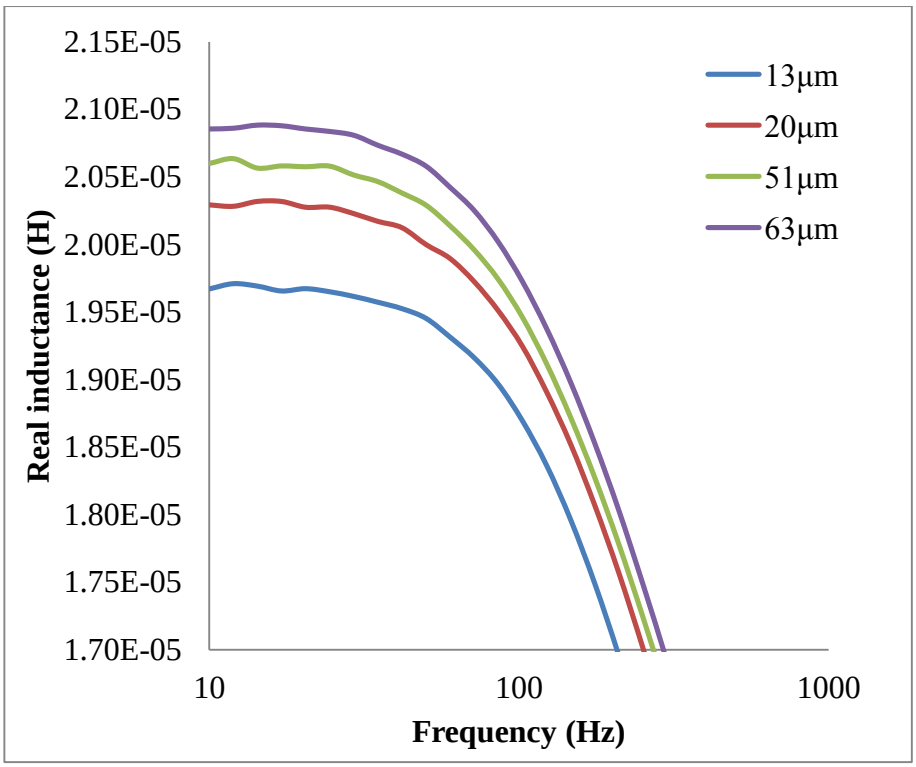

Figure 6.6: An expanded version of Figure 6.5 focusing on showing the low frequency range.

6.1.3 Magnetic domain structures

The EM sensor output signal (real inductance values at below approximately 100 Hz), is dominated by the relative permeability of the sample which is related to its magnetic domain structure. Therefore, the magnetic domain structures are observed to see how the domain structure is related to the grain size.

An example of the magnetic domain structure for the 0.17wt%C-1200 steel sample overlaid on the microstructure is shown in Figure 6.7. It can be seen from Figure 6.7 that there is a clear magnetic domain pattern apparent in most of the ferrite grains. In steel, the easy magnetisation direction is along the <100> crystallographic direction; as the 0.17C steel samples were hot rolled and then heat treated, they will have a random crystallographic texture. Therefore, on the 2D metallographic section, some of the ferrite grains will be oriented with easy directions in the plane. Hence, the domain structure will be clearly visible in such locations, although some of the ferrite grains will be oriented in a non-easy direction and will only show an unclear pattern. As adjacent grains usually have different crystal orientations, a domain packet, in which the 180 °domain wall orientations are similar to each other, is formed in each grain.

It can be seen from Figure 6.9 that closure domains (highlighted with red circles) are also present and are mainly located near the domain packet boundaries (i.e. the grain boundaries) to reduce the free pole density at the domain packet boundaries; hence the magnetostatic energy. These are more clearly seen in grains where the 180 ° domain walls are parallel (i.e. grains with crystallographic orientations such that the easy directions are in the metallographic plane). Such observation is in agreement with

Hetherington et al. and Cullity who also find closure domains forming at the grain boundaries in a ferritic microstructure [147].

When a small magnetic field is applied (e.g. by an EM sensor), the domains which are the most parallel to the applied field grow first by the movement of the 180 ° domain walls. This process will force the 90 ° domain wall (forming the closure domains), located at the end of the 180 ° domain walls, to bend. In this case, the normal components of the local magnetisation vector across these 90 ° domain walls will no longer be continuous, resulting in free poles being formed at the walls; hence the magnetostatic energy rises [100]. Therefore, the 180 ° domain wall motion is restricted by the closure domains located at the grain boundaries (i.e. effectively pinning the grain boundaries to the domain wall motion).

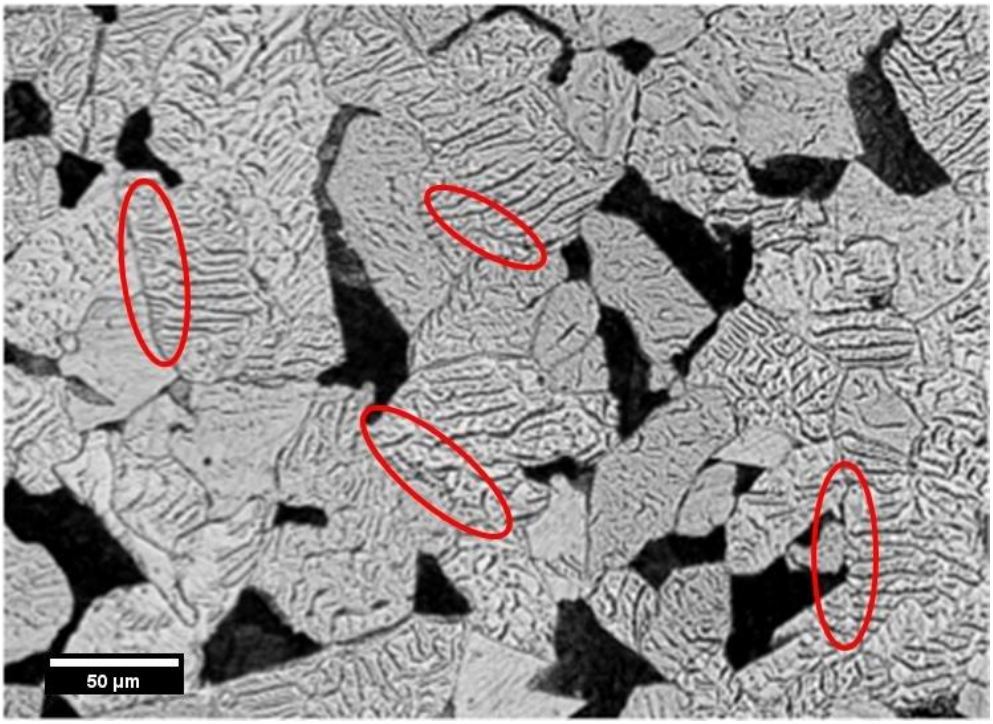

Figure 6.7: Magnetic domain structure of the 0.17wt%C-1200 steel sample overlaid on the steel microstructure, at ×200 magnification. The red ovals indicate the presence of closure domains.

6.1.4 Effect of ferrite grain size on relative permeability in 0.17 wt%C steel

The relative permeability values for the samples with different grain sizes were determined by fitting the experimental EM sensor measurement using the FE sensor output model described in section 5.4 in Chapter 5. Close fits (within 0.1% error) between the modelled and measured real inductance for all of the samples have been achieved. The relative permeability values are plotted against the ferrite grain size in Figure 6.8. It can be seen that there is an increase in the relative permeability value as the ferrite grain size increases from 13 to 64 μm. This agrees with Thompson et al. and Ranjan et al., who reported an increase in initial permeability with ferrite grain size in the 0.17 wt% C steel and decarburised steel samples [91, 148].

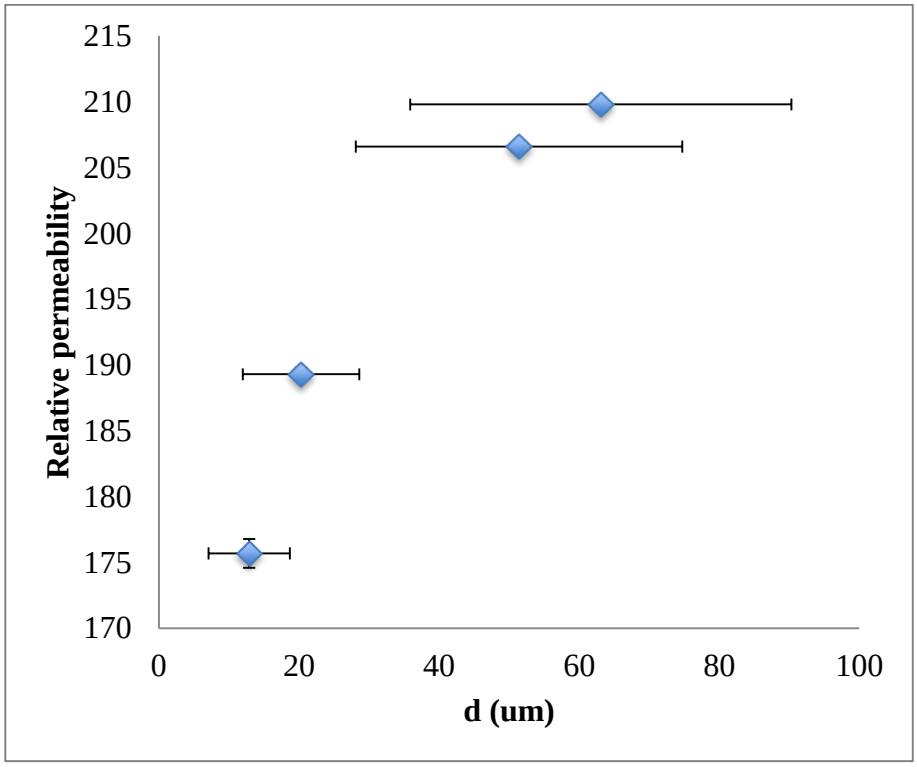

Figure 6.8: Predicted relative permeability for 0.17wt% C steel sample with ferrite grain size of 13, 20, 51 and 64μm.

As discussed in section 5.1 in Chapter 5, the relative permeability predicted from the EM sensor output relates to the initial permeability, which is related to the ease of the reversible movement of the magnetic domains walls [100], which in turn is related to the grain size (as discussed in section 6.1.3 in Chapter 6). Such a relationship is similar to that reported for yield strength prediction in steel, i.e. the Hall-Petch relationship, where the yield strength is related to the initial dislocation movement, and the ease of movement of the dislocation is related to the grain size [9]. It is worth mentioning that the Hall-Petch relationship is applied to cases where grain boundaries dominate the properties (i.e. the absence of precipitates, multi-phases, etc.).

Figure 6.9 shows that there is a Hall–Petch type relationship between the relative permeability values and the grain size (i.e. relative permeability being related to the inverse square root of the grain size), which suggests that there is an effective pinning effect of grain boundaries on magnetic domain wall movements. A Hall-Petch type relationship between the MBN power and the grain size was previously reported in pure iron samples with grain sizes of 48-179 μm [90]. However, such a relationship was attributed to the fact that the grain boundaries were acting as preferential sites of domain nucleation and pinning points of the domain wall movement across the grain boundary which correspond to a far higher field strength than that at which the EM sensor was applied. In addition, an empirically-based, inverse relationship between coercivity and grain size has been reported in ferrite – pearlite steel [136, 147]. However, the Hall-Petch type relationship between the initial permeability and ferrite grain size was reported previously.

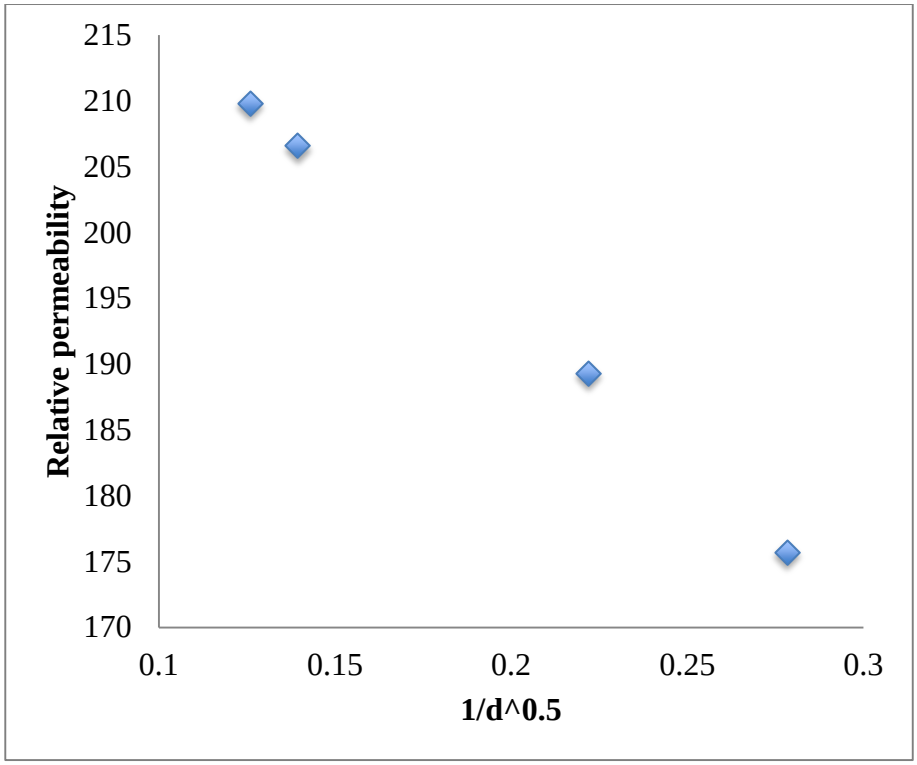

Figure 6.9: Hall-Petch type relation between the grain size (d) and relative permeability in 0.17wt%C steel samples with grain size of 13-64 μm.

6.1.5 Effect of ferrite grain size on relative permeability in pure iron

In order to determine if the relationship between relative permeability and ferrite grain size determined for grain sizes in the range 13-65 μm in the 0.17C samples could be extended to much larger grain size, pure iron samples in the as-received and heat treated, 1300 ℃ for 1 hour (termed Fe and Fe-1300) were used. The microstructures of Fe and Fe-1300 samples are shown in Figure 6.10 and 6.11 respectively. The measured results of the real inductance versus frequency (logarithmic scale) for the Fe and Fe-1300C steel samples using the EM sensor are shown in Figure 6.12. The low frequency real inductance value slightly decreases with the increased average grain size (155 to 223 μm). The relative permeability values are predicted, using the FE model, as 330 and 287 for the Fe and Fe-1300C sample respectively. These results show the opposite trend

(decreasing relative permeability with increasing grain size) compared with the results obtained for the 0.17wt%C steels.

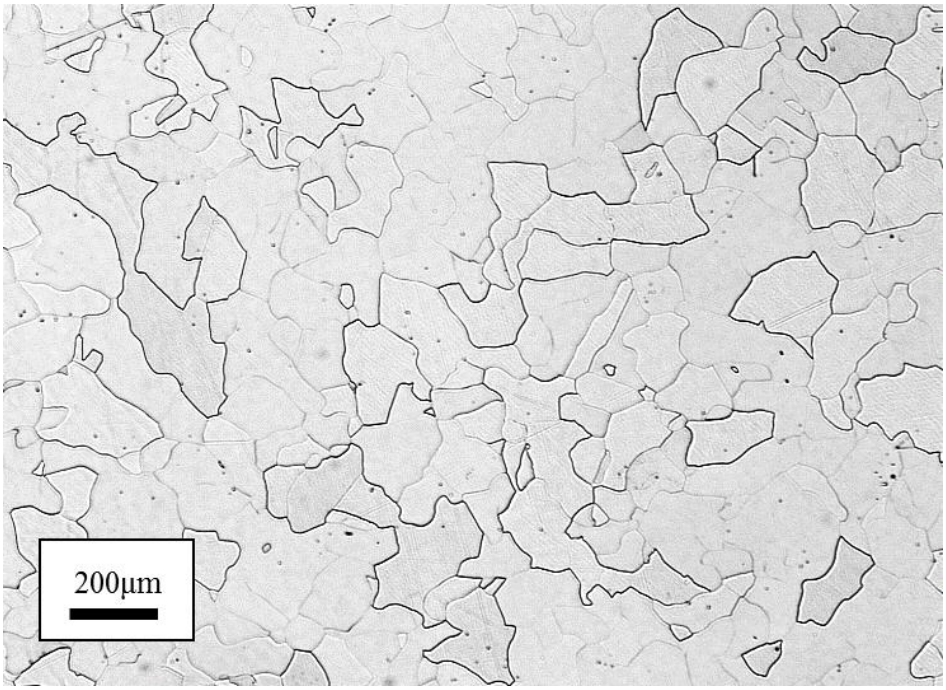

Figure 6.10: Optical microstructure of Fe sample, at ×50 magnification.

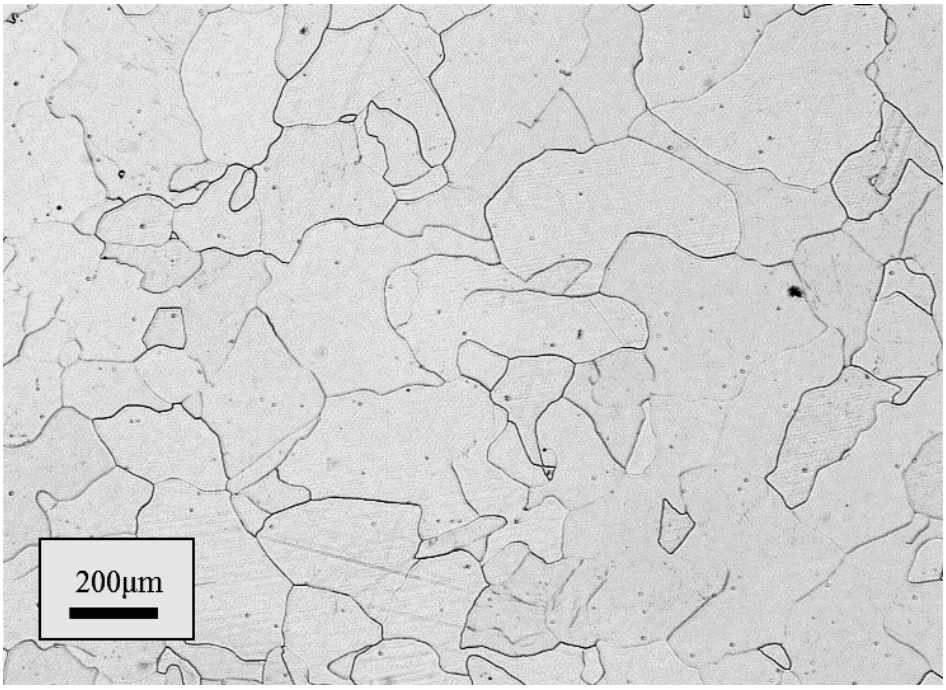

Figure 6.11: Optical microstructure of Fe sample, at ×50 magnification.

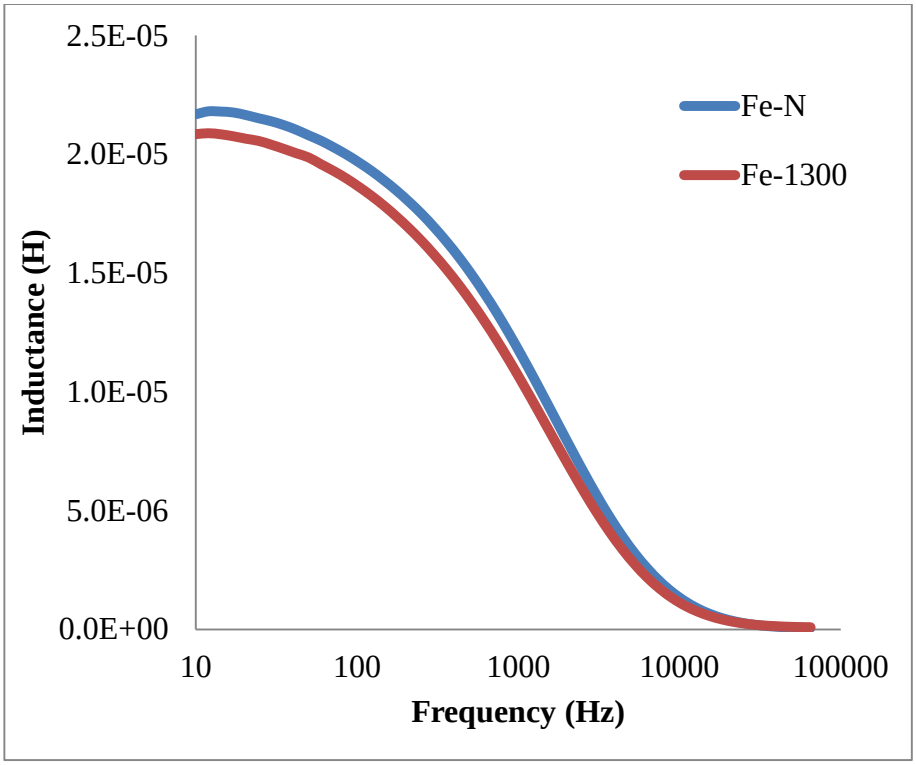

Figure 6.12: Real inductance changes with frequency for Fe (average grain size of 155 μm) and Fe-1300 (average grain size of 223 μm) samples

The magnetic domain structures for the Fe and Fe-1300 samples were observed in order to investigate the reason for the decrease in relative permeability with increase in grain size. The magnetic domain structures of the Fe and Fe-1300 samples obtained by the Bitter method overlaid with the ferrite grain structure (indicated in red) are shown in Figure 6.13 and 6.14 respectively. It can be seen that, in Figure 6.13, each ferrite grain in the Fe sample contains a single domain packet. However, in Figure 6.14 for the Fe-1300 sample, more than one domain packet can be observed per grain. It was observed that the domain packet size is actually smaller in the larger (223 μm) ferrite grain size sample (Fe-1300) compared to the smaller (155 μm) ferrite grain size sample (Fe). Closure domains are usually formed at the end of the 180 °domain walls, at the domain packet boundaries. A higher magnification magnetic domain image (×400

magnification) of Fe-1300 steel sample is given in Figure 6.15. It can be seen that the closure domains in the larger grain size (223 μm) pure iron sample are not only located at the ferrite grain boundaries, but also located within the ferrite grains. Therefore, for the large grain sizes the relative permeability cannot be simply correlated to the average grain size, which explains why the low frequency real inductance value for the pure iron sample does not increase with the ferrite grain size, as the domain size does not increase.

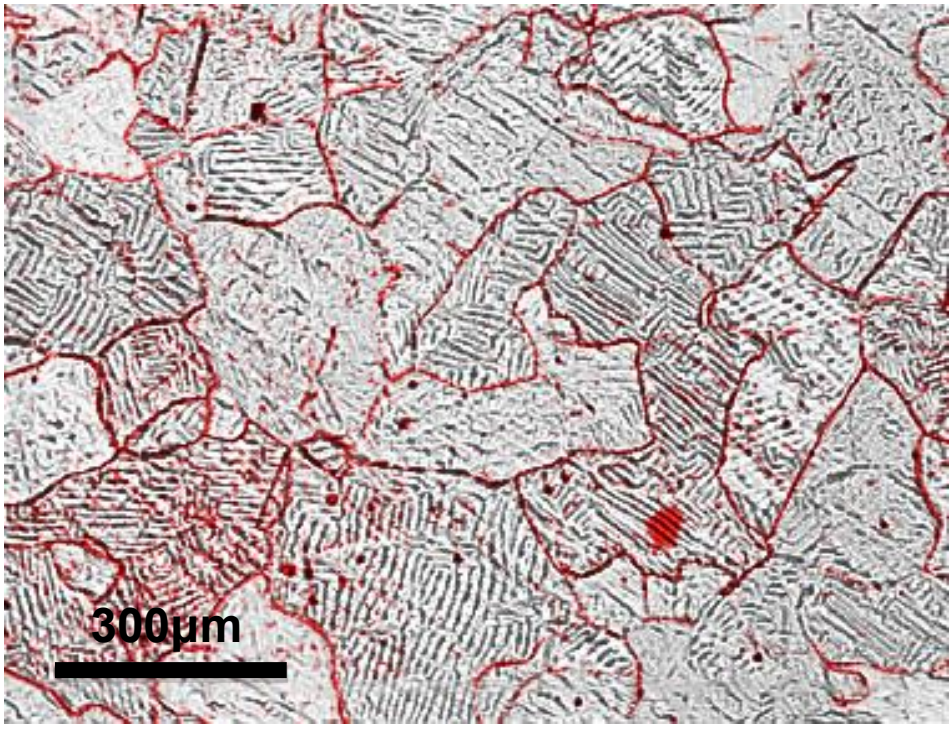

Figure 6.13: Magnetic domain structure for the Fe steel sample overlaid with the ferrite grain structure (shown in red).

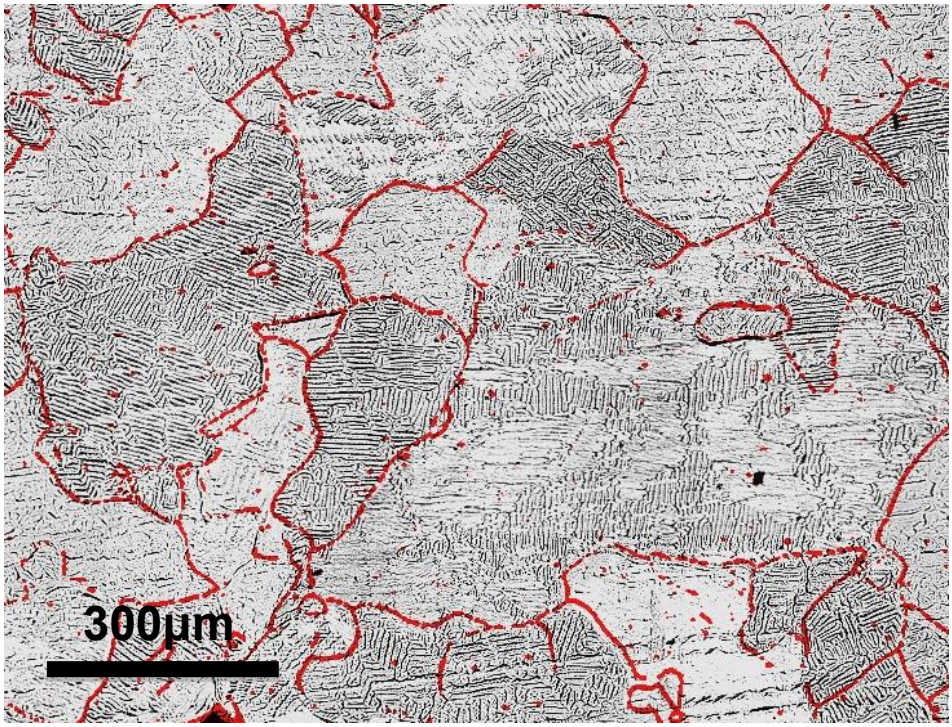

Figure 6.14: Magnetic domain structure of Fe-1300 steel sample overlaid with the ferrite grain structure (in red) showing multiple domain packets per grain.

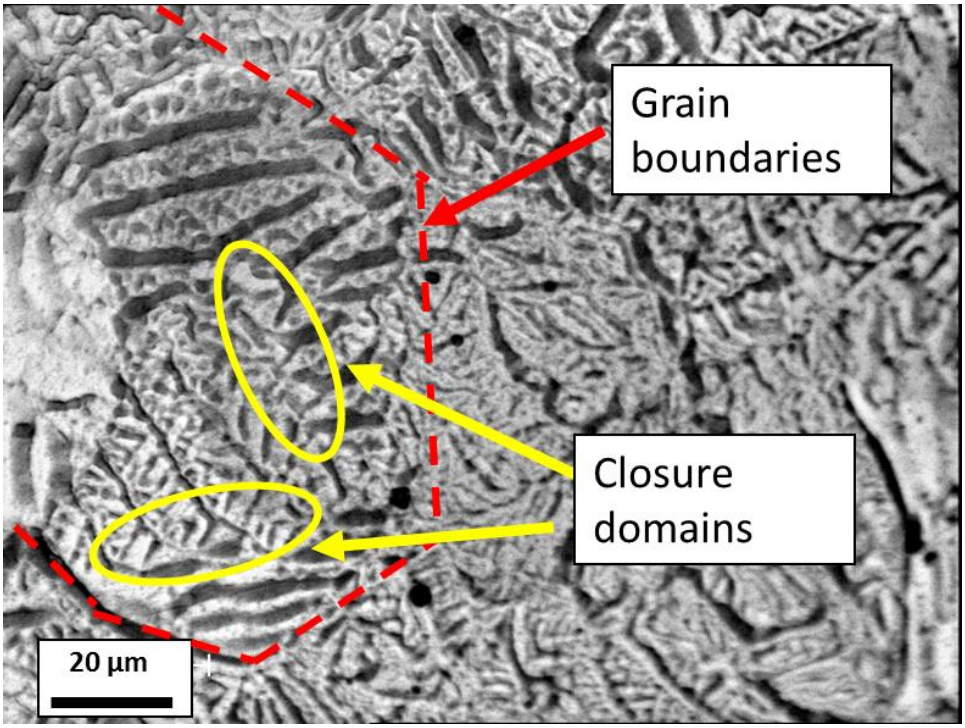

Figure 6.15: High magnification magnetic domain image of Fe-1300 steel sample, showing ferrite grain boundaries (in red) and internal closure domains inside a grain.

6.1.6 Summary

In summary it can be seen that in the 0.17C steel, each ferrite grain contains a single domain packet, and the increase in grain size from 13 µm to 64 µm results in an increase in the domain packet size and hence an increase in the relative permeability. However, when the grain size increases significantly (for the experiments carried out this is for a grain size of 223 µm in a pure iron sample) more than one domain forms in some grains so the effective domain size can decrease with an increase in grain size. Therefore the Hall–Petch type relationship between the relative permeability values and the grain size, as shown in Figure 6.9, is only valid when one 180 ° domain packet forms in a grain, which, for the 0.17C steel studied in this work relates to grain sizes of 13 µm to 64 µm. For the pure iron sample one domain packet was observed in each grain for material with an average grain size of 155 µm suggesting that the Hall-Petch type relationship may be valid to grain sizes of the order of 100-150 µm.

6.2 Pearlite interlamellar spacing for pearlitic steel wire samples

Pearlitic steel has relative high strength and wear resistance and hence wide applications including rails, springs wire and dies [164]. In general, the mechanical properties of pearlitic steels are influenced by a number of microstructure parameters including prior-austenite grain size, pearlite colony size, thickness of the cementite lamellaes and interlamellar spacing, among which, the latter has been considered the most important parameter for strength properties [165, 166]. In this section, PW grade steel samples were used to study the effect of pearlite interlamellar spacing on relative permeability values and hence EM sensor signals.

6.2.1 Microstructure characterization

The ferrite fraction, pearlite interlamellar spacing, and cementites lath thickness of the PW steel wire samples were measured and supplied by Tata Steel (UK). A summary of the microstructure parameters measured in these samples is given in table 6.2. The pearlite fraction of (> 98.8%) has been obtained for all the PW steel samples due to the high carbon content of 0.81 wt%. The identical chemical composition of the samples results in the same volume fraction of cementites in pearlite grains; hence, the cementites' lath thickness increases with pearlite interlamellar spacing. The samples that were austenitised at 1000 ℃ should result in a larger prior austenite grain size than that austenitised at 1000 ℃, which in turn reduces the pearlite transformation temperature [167]. Therefore, as can be seen from table 6.2, by comparing the samples without salt bath heat treatment. (i.e. group of samples from PW-A to PW-F), lower maximum pearlite transformation temperatures were obtained with samples that were austenitised at 1000 ℃ than at 900 ℃ with the same cooling rate. It can be seen from Figure 6.16 that the pearlite

interlamellar spacing increases with the maximum pearlite transformation temperature. This is attributed to the fact that the higher transformation temperature allows faster diffusivity, hence increasing the diffusion distance of the cementites [168]. In the group of samples from PW-G to PW-L (i.e. samples which were salt bath heat treated), the salt bath heat treatment temperature seems to dominate the maximum pearlite transformation temperatures. Therefore, it can be seen from Figure 6.17 that pearlite interlamellar spacing increases with salt bath heat treatment temperature. It was noted that the pearlite interlamellar spacing of the sample PW-K (salt bath heat treated at 500 ℃) did not increase in compare with PW-J (salt bath heat treated at 450 ℃), which was not expected.

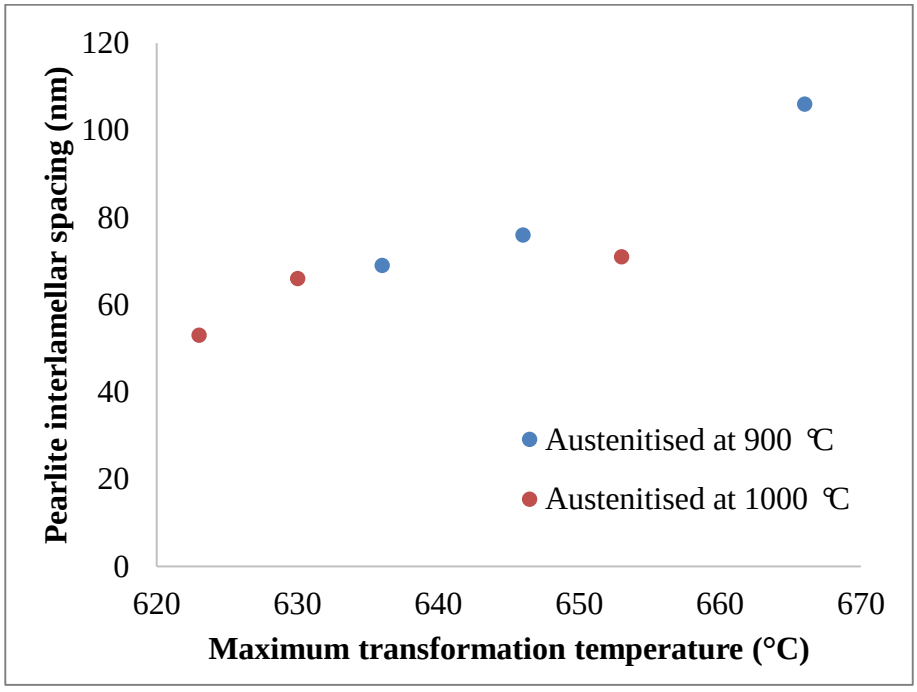

Figure 6.16: Plot of pearlite interlamellar spacing with maximum pearlite transformation temperature for group of samples from PW-A to PW-F.

Table 6.2: Summary of the ferrite fraction, pearlite interlamellar spacing, and cementites lath thickness of the PW steel wire samples, with their heat treatment conditions.

Sample	Austenitisation Temperature (°C)	Cooling rate (°C/s)	Salt bath Temperature (°C)	Maximum transformation temperature (°C)	Pearlite fraction (%)	Interlamellar spacing (nm)	Cementite lath thickness (nm)
PW-A	900	11	N/A	666	99.1	106	15
PW-B	900	22	N/A	646	99.1	76	11
PW-C	900	28	N/A	636	99.1	69	10
PW-D	1000	11	N/A	653	99.3	71	10
PW-E	1000	22	N/A	630	99.5	66	9
PW-F	1000	28	N/A	623	99.3	53	7
PW-G	900	132	450	552	99.1	52	7
PW-H	900	100	500	620	98.8	60	8
PW-I	900	52	550	646	98.8	66	9
PW-J	1000	72	450	591	99.2	55	8
PW-K	1000	68	500	614	98.9	54	8
PW-L	1000	34	550	632	99.1	69	10

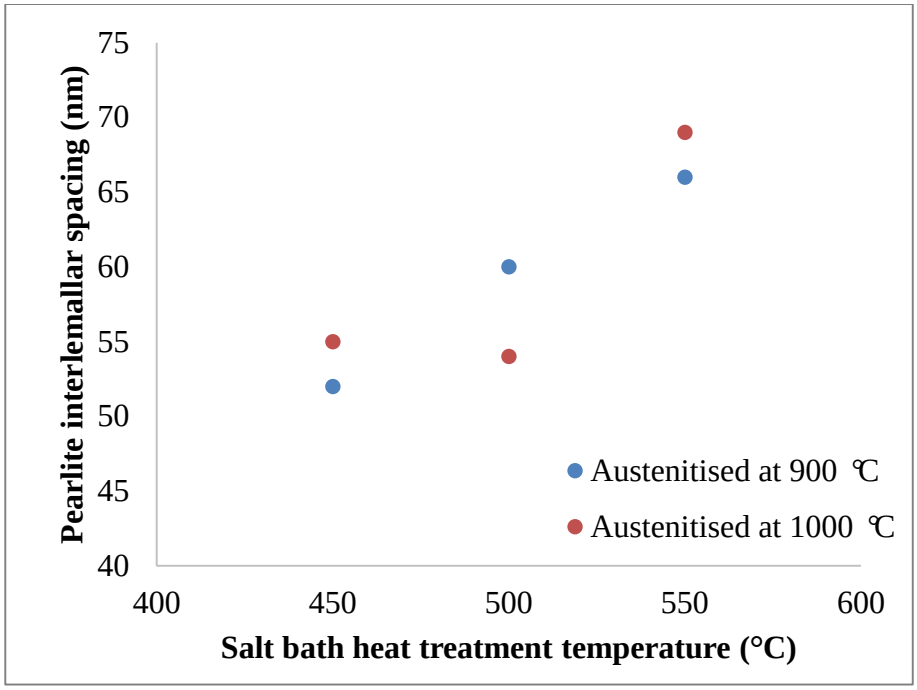

Figure 6.17: Plot of pearlite interlamellar spacing with salt bath heat treatment temperature for group of samples from PW-G to PW-L.

6.2.2 Tensile properties

The tensile strength of the samples was measured and supplied by Tata Steel (UK). It can be seen from Figure 6.18 that tensile strength decreases with increased pearlite interlamellar spacing. It is worth mentioning that the tensile strength value of the sample austenitised at 1000 ℃ with 71nm lamellar spacing is lower than expected. A Hall-Petch type relation between pearlite interlamellar spacing and tensile strength has been observed in the PW-A to PW-L samples (shown in Figure 6.19). This agrees with that reported in ref [164, 166, 169]. It can be seen that the samples which were austenitised at 900 ℃ follow the trend better than that austenitised at 1000 ℃.

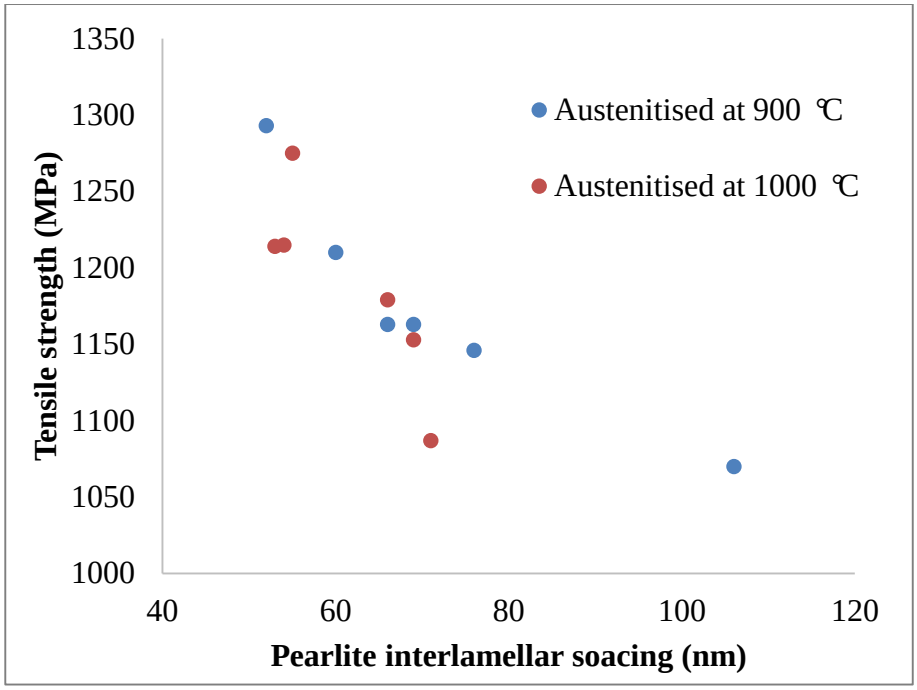

Figure 6.18: Plot of tensile strength with pearlite interlamellar spacing for pearlitic wire steel samples austenitised at 900 ℃ and 1000 ℃.

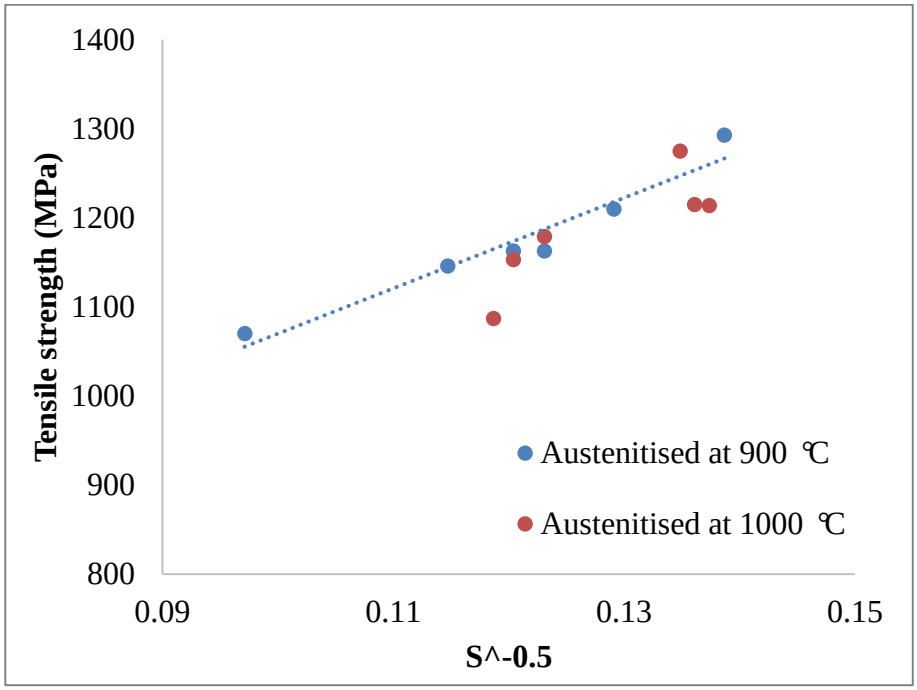

Figure 6.19: Hall-Petch type relation between the pearlite interlamellar spacing (S) and tensile strength for pearlitic wire steel samples austenitised at 900 ℃ and 1000 ℃.

6.2.3 EM sensor results

The measured real inductance versus frequency (logarithmic scale) results for group of samples from PW-A to PW-F (i.e. samples without salt bath heat treatment) using the cylindrical EM sensor are shown in Figure 6.20. It can be seen that the sensor output (real inductance changes with frequency) can clearly distinguish samples with different pearlite interlamellar spacing. The real inductance values at low frequencies (below approximately 100Hz), which are dominated by the relative permeability of the samples, increase with increased pearlite interlamellar spacing. Repeatability tests were carried out, and the results of the EM sensor output show that the difference between these samples is significant and distinguishable from each other.

The measured real inductance versus frequency (logarithmic scale) results for group of samples from PW-G to PW-L are shown in Figure 6.21. It can be seen that the EM signal between the samples which have a pearlite interlamellar spacing of 54-66 could not to be distinguished due to the very small difference in pearlite interlamellar spacing.

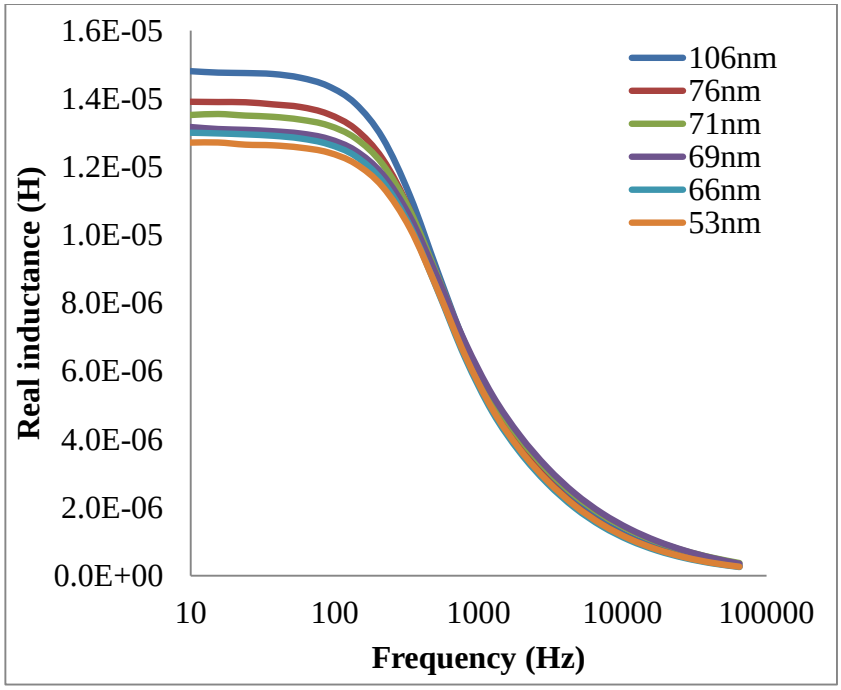

Figure 6.20: Real inductance changes with frequency for PW-A to PW-F steel samples with pearlite interlamellar spacing of 106, 76, 71, 69, 66 and 53nm.

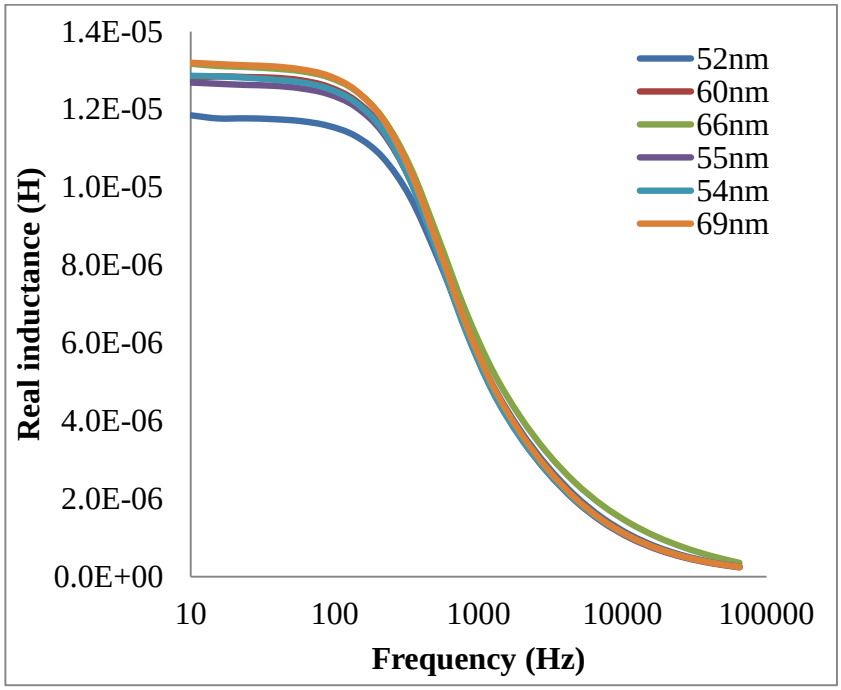

Figure 6.21: Real inductance changes with frequency for PW-A to PW-F salt bath heat treated steel samples with pearlite interlamellar spacing of 52, 60, 66, 55, 54, and 69nm.

6.2.4 Effect of pearlite interlamellar spacing on relative permeability

The relative permeability values for the group of samples from PW-A to PW-L with different pearlite interlamellar spacing were determined by fitting the experimental EM sensor measurement using the FE sensor output model described in section 5.4 in Chapter 5. It can be seen from Figure 6.22 that the relative permeability values increase with increased pearlite lamellar spacing. This is believed to be due to the reduced pinning effect on the magnetic domain wall movement in the samples with larger pearlite interlamellar spacing [91, 92]. Samples austenitised at different temperatures show a slightly different trend. This indicates that the relative permeability values may also be affected by pearlite colony size. The domain walls running across the cementite lamellaes receive less pinning from them (as there is only a small amount of energy change by domain wall motion), but the domain wall motion will be further pinned by the colony boundaries, at which the easy magnetisation direction and hence the domain wall orientation changes.

As can be seen in figure 6.23, the tensile strength values decreases with increasing relative permeability values. The correlation for the 1000 ℃ austenitised samples is weaker than that for the 900 ℃ austenitised samples, which is expected due to the poorer agreement between tensile strength and lamellar spacing.

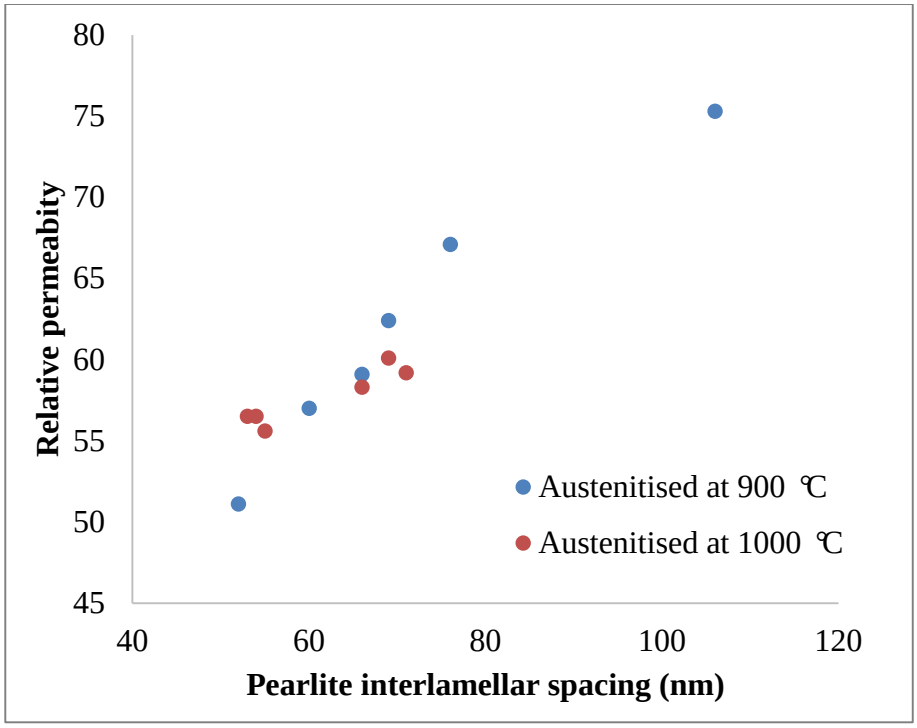

Figure 6.22: Plot of relative permeability against pearlite interlamellar spacing for PW steel samples austenitised at 900 ℃ and 1000 ℃.

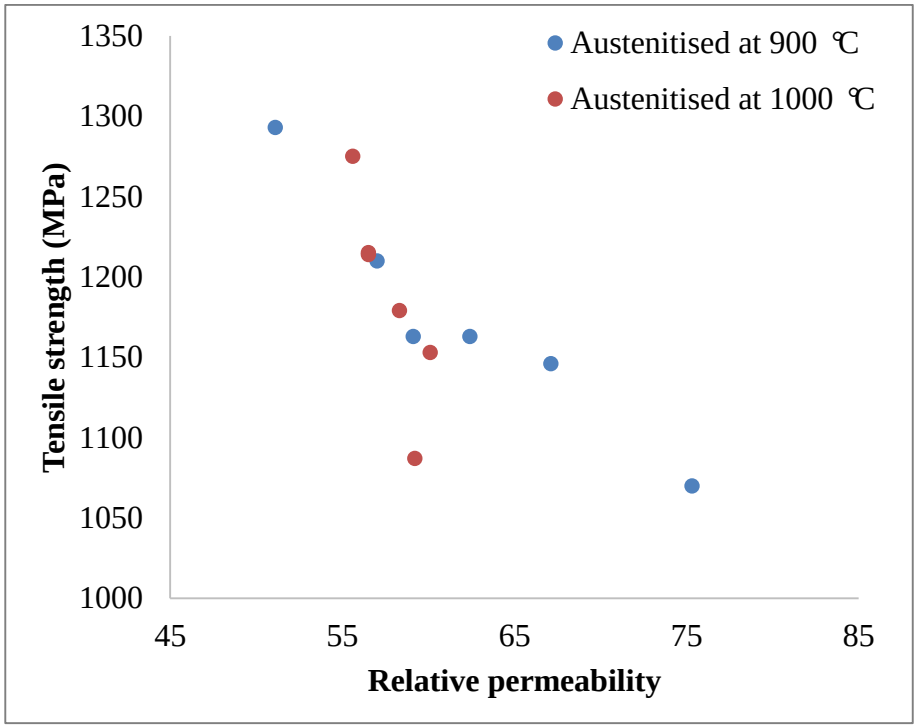

Figure 6.23: Plot of tensile strength against relative permeability for PW steel samples austenitised at 900 ℃ and 1000 ℃.

6.2.5 Summary

The relative permeability and hence low frequency (plateau region) real inductance increased almost linearly with pearlite interlamellar spacing in the range of 52-106 nm in the 0.81 wt%C pearlitic steel wire samples. This is believed to be mainly due to the reduced pinning effect on the magnetic domain wall movement in the samples with larger pearlite interlamellar spacing. Due to the close correlation between the tensile properties and pearlite interlamellar spacing, the EM sensor has shown potential for determining the pearlite interlamellar spacing and tensile properties in fully pearlitic steels samples.

6.3 Case study for EM sensor measurement of tyre bead steel wire samples

High strength tyre bead steel wires are widely used for the reinforcement of most types of tyre. It was reported that the strength properties of the wires are mainly dependent on the pearlite interlamellar spacing [79]. Based on the research outcome obtained earlier (in section 6.2 in Chapter 6), a case study of EM sensor measurement of pearlite interlamellar spacing in tyre bead steel wire samples is presented in this section. Some of the results presented in this section has been published in ref [76].

6.3.1 Microstructure characterization

Typical SEM images of TW-590, TW-600, TW-610, TW-620 and TW-630 steel samples at ×1000 magnification are shown in Figures 6.24-6.28. The SEM micrographs show a mainly pearlitic microstructure with a very small fraction of grain boundary ferrite (measured to be less than 5%) due to the high carbon content (0.65 wt% C). The pearlite interlamellar spacing of these isothermally transformed samples was measured by Tata Steel (India) using the intercept method. Table 6.3 provides a summary of the pearlite interlamellar spacing and electrical resistivity values of these samples. The relationship between the salt bath heat treatment temperature and the pearlite interlamellar spacing is shown in figure 6.29, which shows that pearlite interlamellar spacing increases with salt bath heat treatment temperature. This is attributed to the fact that the higher transformation temperature (resulting from the higher salt bath heat treatment temperature) allows faster diffusivity, hence increasing the diffusion distance of the cementites [168].

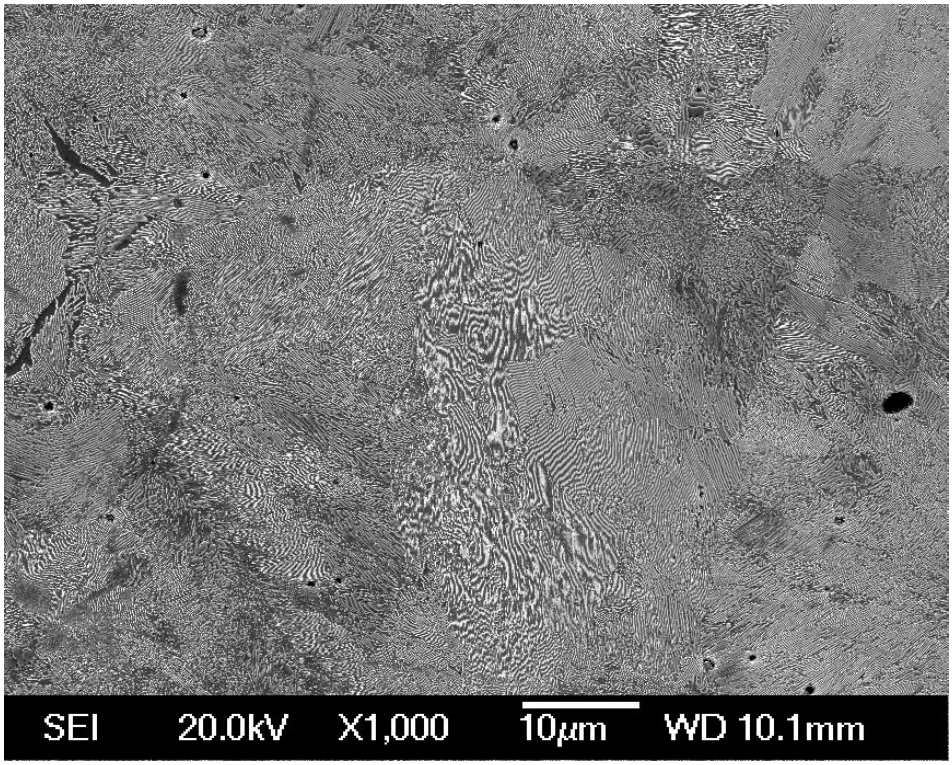

Figure 6.24: Typical SEM image of the TW-590 sample, at ×1000 magnification

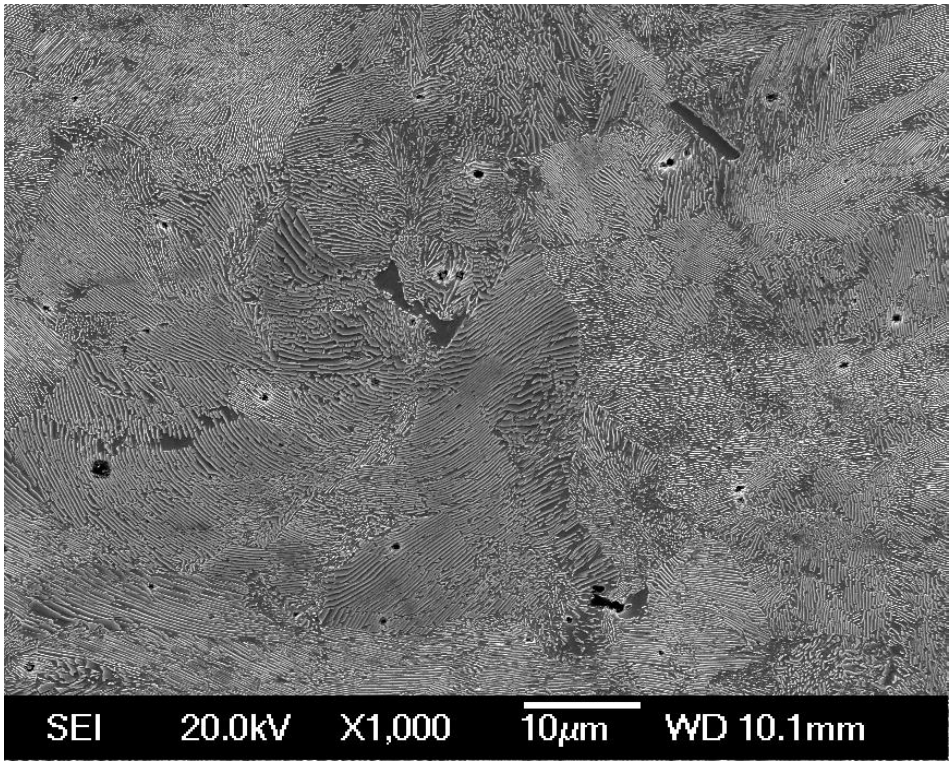

Figure 6.25: Typical SEM image of the TW-600 sample, at ×1000 magnification

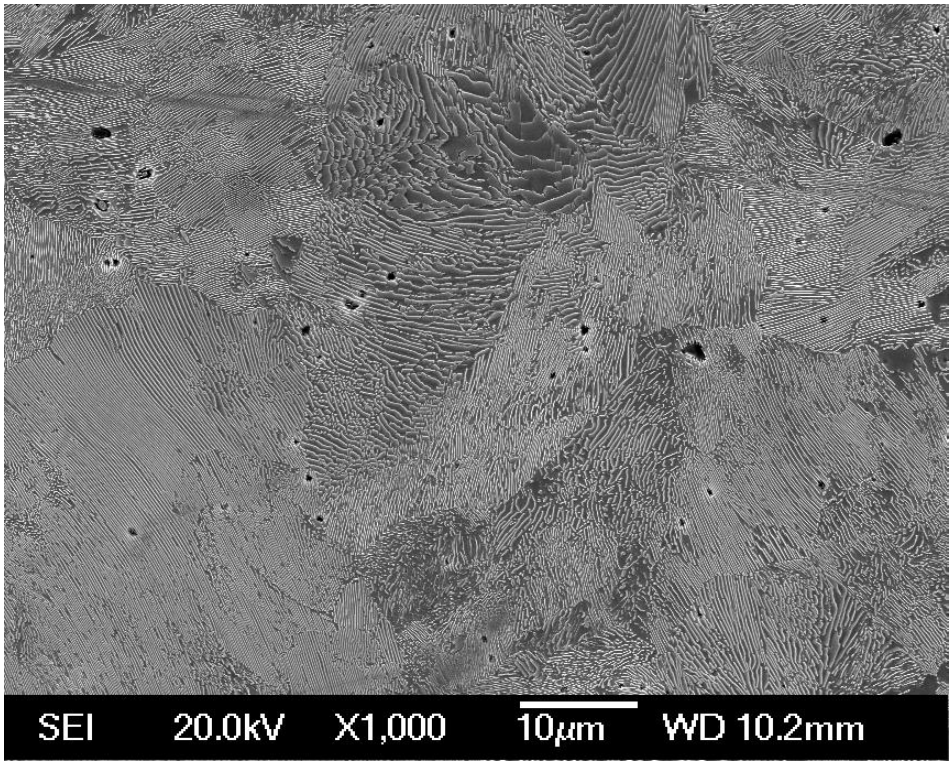

Figure 6.26: Typical SEM image of the TW-610 sample, at ×1000 magnification

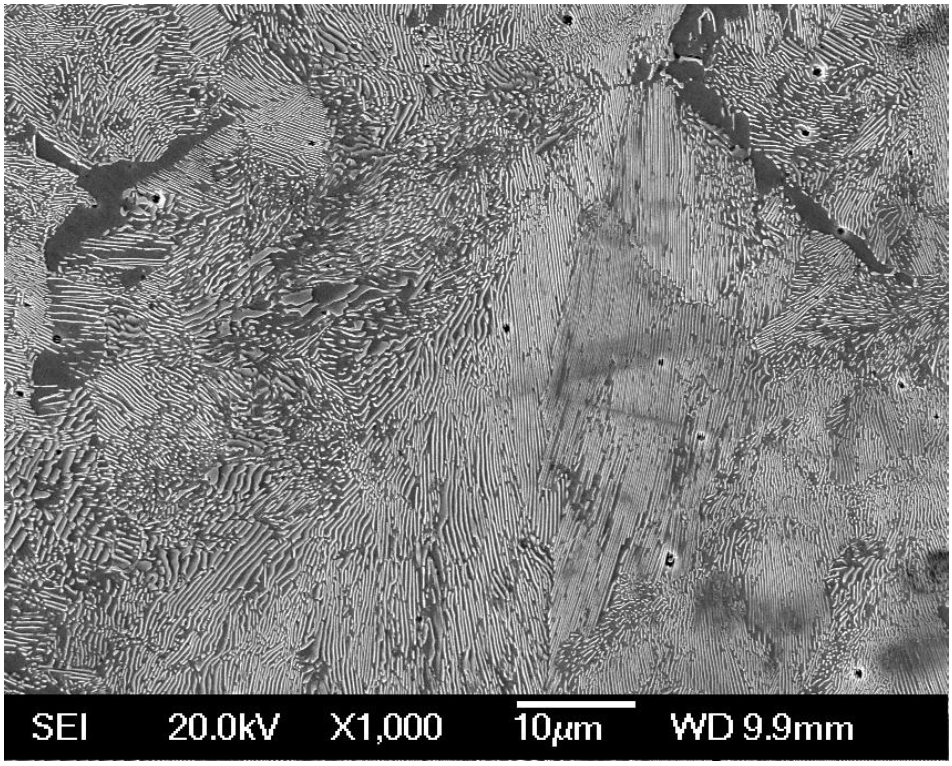

Figure 6.27: Typical SEM image of the TW-620 sample, at ×1000 magnification

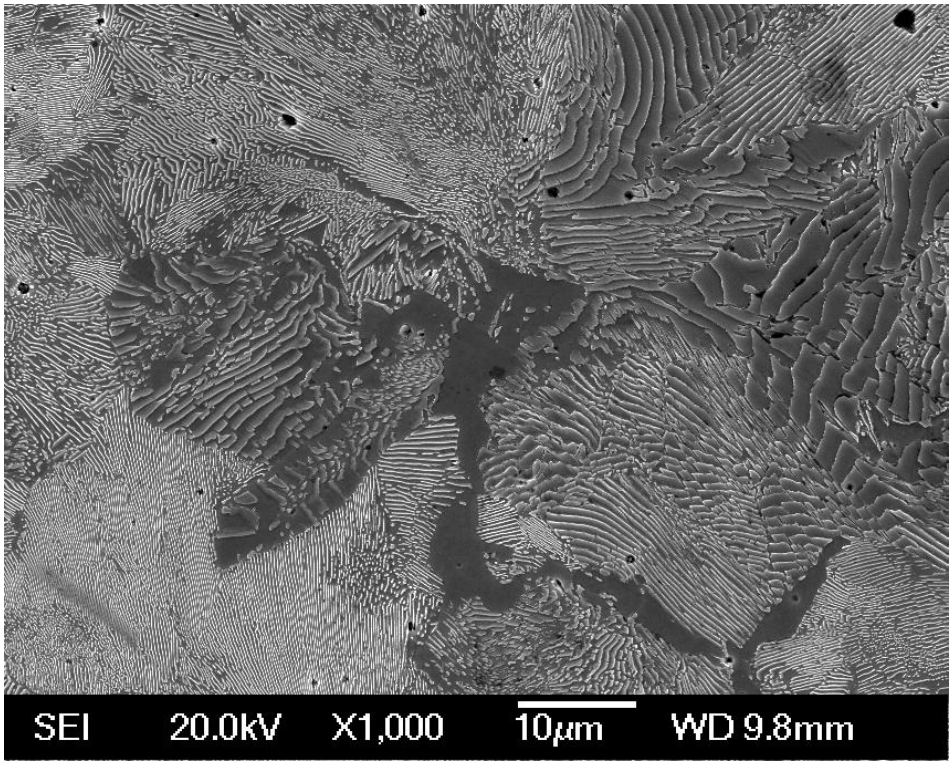

Figure 6.28: Typical SEM image of the TW-630 sample, at ×1000 magnification

Table 6.3: Summary of the pearlite interlamellar spacing and electrical resistivity values of the TW-590, TW-600, TW-610, TW-620 and TW-630 steel samples.

Salt bath heat treatment temperature (°C)	**Average pearlite interlamellar spacing (nm)**	**Average resistivity (n.ohm.m)**
590	142 ± 3.8	202.5
600	148 ± 8.5	205.2
610	182 ± 10.5	199.8
620	187 ± 8.6	199.3
630	202 ± 11.2	203.2

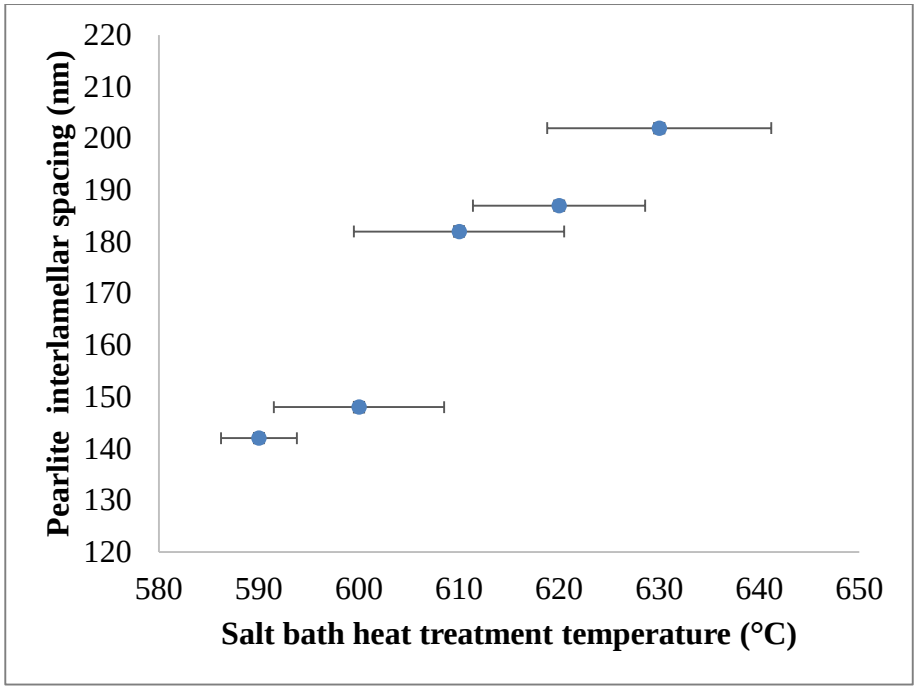

Figure 6.29: Pearlite interlamellar spacing versus salt bath heat treatment temperatures for the TW steel samples.

6.3.2 Electrical resistivity measurements

The resistivity values versus pearlite interlamellar spacing, for the salt bath heat treated steel wire samples, are shown in figure 6.30. The resistivity changes, due to the changes in interlamellar spacing, are small and fall within the experimental scatter. This means that resistivity measurements are insufficiently sensitive to determine the interlamellar spacing.

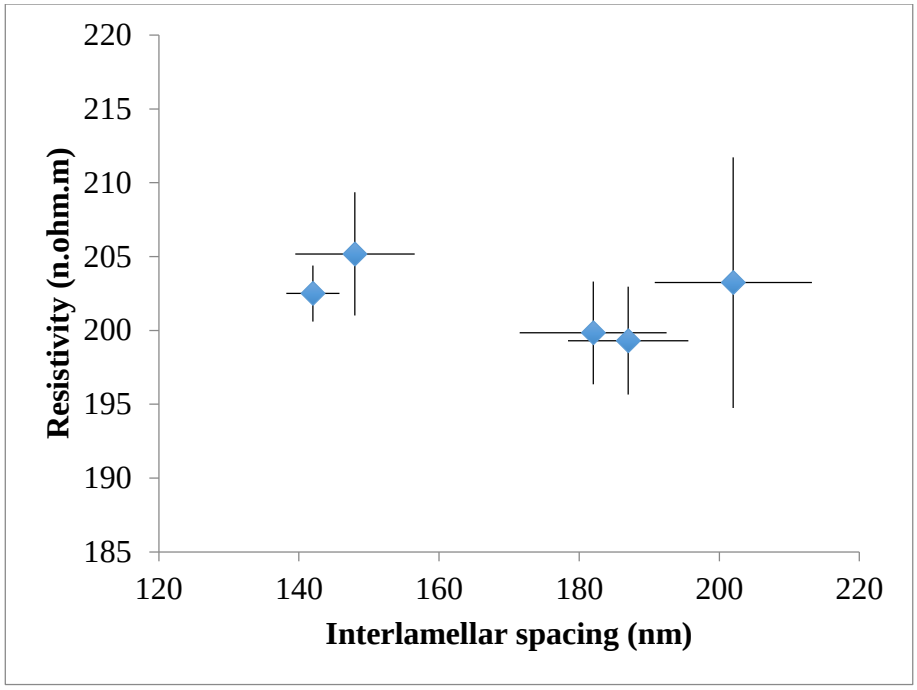

Figure 6.30: Electrical resistivity values versus pearlite interlamellar spacing for the TW steel salt bath heat treated samples.

6.3.3 EM sensor results

The EM sensor measurements were carried out using the cylindrical EM sensor described in section 4.5.1 in Chapter 4. The EM sensor results of real inductance at 100Hz (this frequency was found to be in the plateau region of the real inductance versus frequency curve for all of the pearlitic steel samples; hence, inductance is dominated by relative permeability) versus pearlite interlamellar spacing are shown in figure 6.31. Unlike the resistivity results, the low frequency (100Hz) real inductance, which is dominated by the relative permeability of the sample, gives a very good correlation, showing an increase relationship with pearlite interlamellar spacing. This is believed to be due to the reduced pinning effect on the magnetic domain wall motion in the samples with larger spacing [91, 92].

As mentioned in section 4.1.2 in Chapter 4, the TW steel wire samples are slightly curved; hence, the errors in real inductance value measured for the TW steel samples are slightly larger than those observed for the C-Mn steel samples. The curved sample shape also made the fitting of the FE sensor output model insufficiently accurate (a 2D axial symmetry model could not accomplish the effect of a curved sample) to give robust relative permeability values. Therefore, the relative permeability values of the TW steel samples were not measured. However, it was found that the reproducibility in EM sensor readings between the nominally identical samples is quite good.

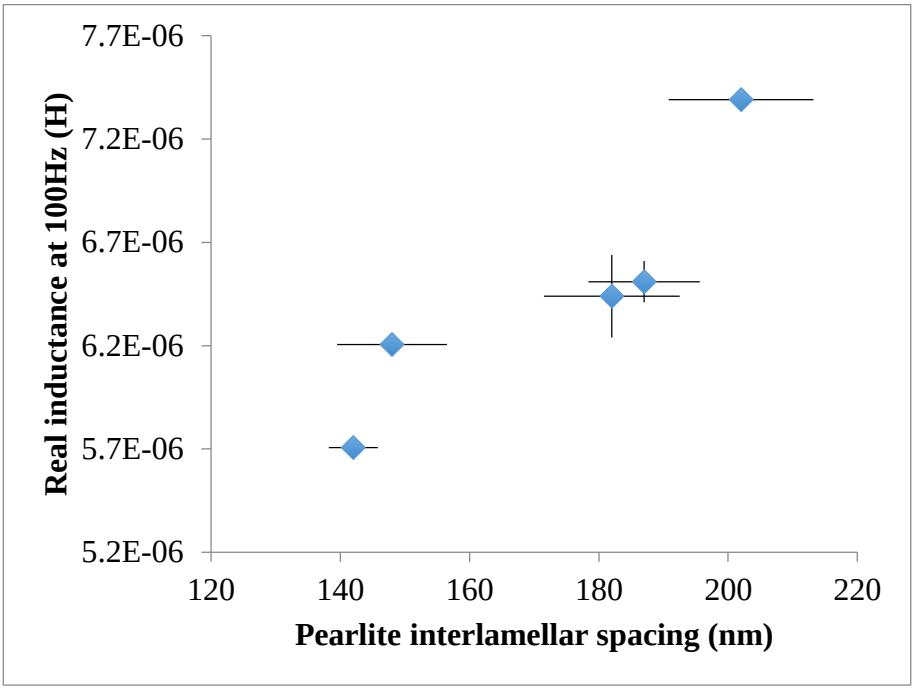

Figure 6.31: Real inductance values at 100Hz versus pearlite interlamellar spacing for the TW steel salt bath heat treated samples.

6.3.4 Summary

In summary, the case study of EM sensor measurement of pearlite interlamellar spacing in commercial tyre bead steel wire samples (fully pearlitic microstructures) shown the

linear trend between the low frequency (plateau region) real inductance and pearlite interlamellar spacing also held in the pearlite interlamellar spacing range of 142-202 nm. The EM sensor technique therefore shows potential to be used as a non-destructive charaterisation technique for determining the pearlite interlamellar spacing of tyre wire steels.

6.4 Martensite and tempered martensite

Martensite in steel is a nonequilibrium phase which can be formed by austenitising and rapid cooling to a relatively low temperature or adding alloying elements. Of the various microstructures that can be generated in steels, martensite is the hardest and strongest but most brittle phase. Carbon content (up to 0.8 wt%) was shown to have very large impact on the hardness of martensite [167]. Tempering heat treatment commonly happened by heating the martensitic steel below the eutectoid temperature (typically 250-650 ℃) and hold for a specific period of time, in order achieve the balance between strength and toughness properties [9, 167]. In this section, the effect of carbon content in the as quenched martensite and tempering temperature in tempered martensite on relative permeability values and hence the EM sensor signals were studied using austenitised and quenched, and quenched and tempered C-Mn steel samples with different carbon content. Some of the results presented in this section has been published in ref [76].

6.4.1 Microstructure characterization

Typical SEM images of the 0.17C-Q, 0.38C-Q, 0.53C-Q, and 0.80C-Q samples at ×4000 magnification are shown in Figures 6.32-6.35. As can be seen a predominantly lath type martensite microstructure was observed in these four samples. The measured average martensite lath size of the samples are given in table 6.4. It can be seen that the martensite lath size decreased with the carbon content in the as quenched martensite samples. This agrees with He et al. [170] who reported the same trend in as quenched martensite for low carbon steels.

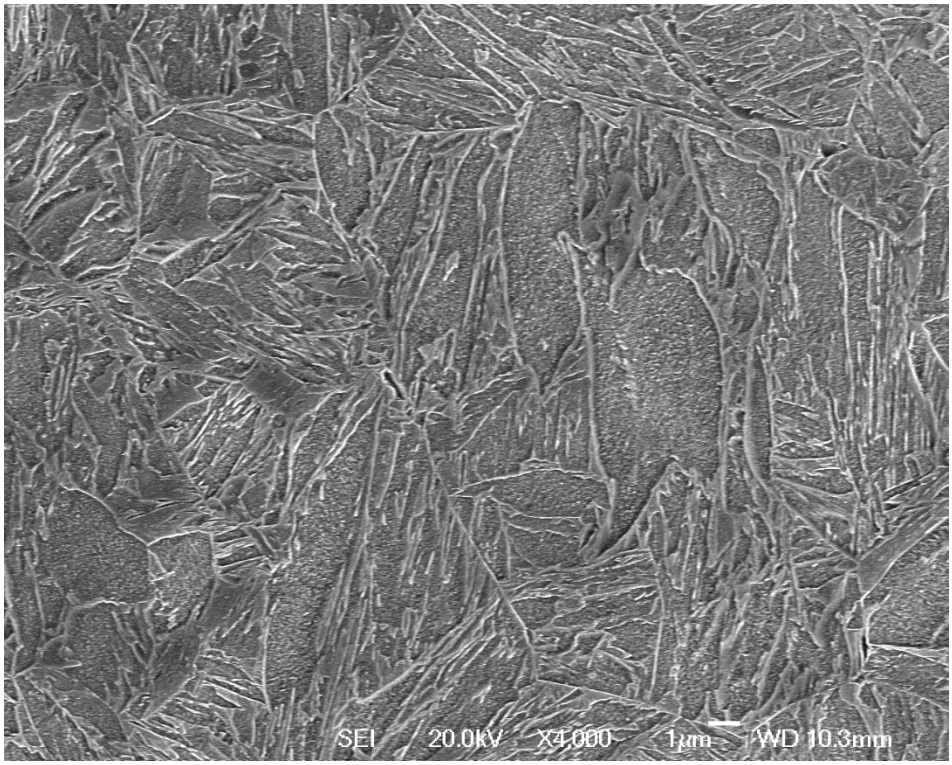

Figure 6.32: SEM image of an 0.17C-Q sample, at ×4000 magnification.

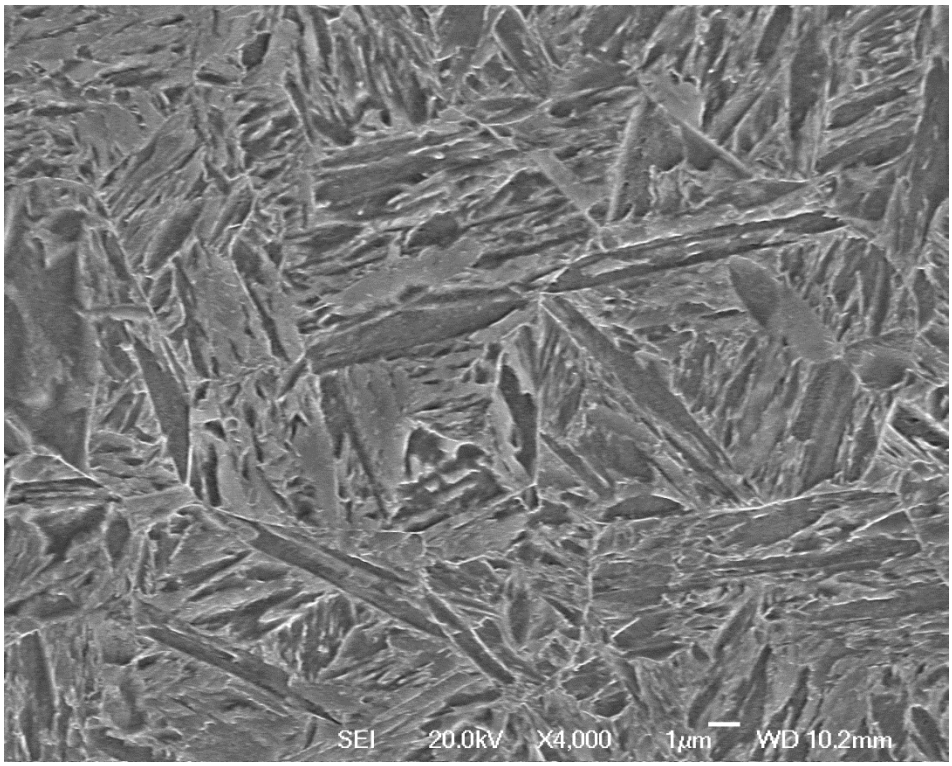

Figure 6.33: SEM image of an 0.38C-Q sample, at ×4000 magnification.

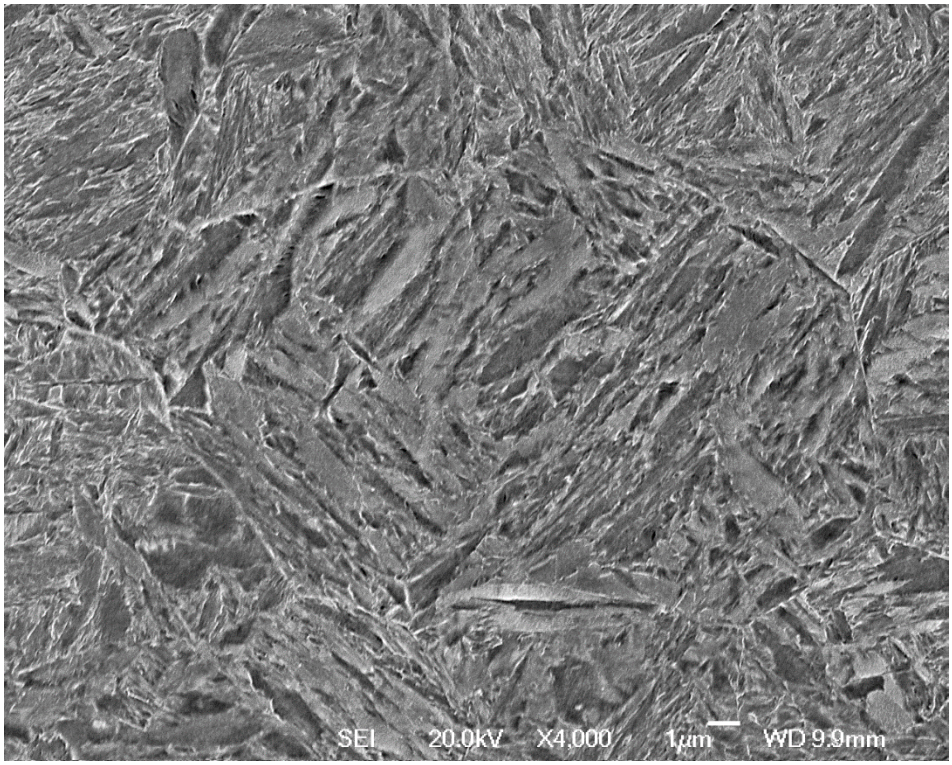

Figure 6.34: SEM image of an 0.53C-Q sample, at ×4000 magnification.

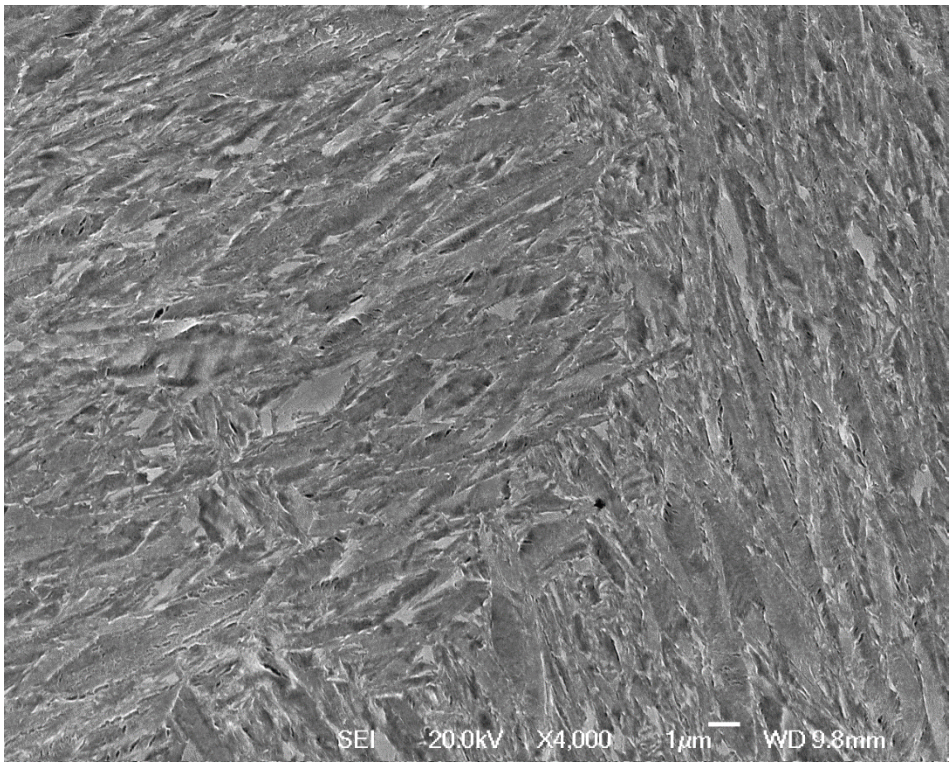

Figure 6.35: SEM image of an 0.80C-Q sample, at ×4000 magnification.

Table 6.4: Martensite lath size for the as quenched martensite samples: 0.17C-Q, 0.38C-Q, 0.53C-Q, and 0.80C-Q

Sample	Martensite lath size (μm)
0.17C-Q	0.57 ± 0.45
0.38C-Q	0.46 ± 0.24
0.53C-Q	0.41 ± 0.16
0.80C-Q	0.36 ± 0.16

6.4.2 Effect of carbon content in as quenched martensite on relative permeability.

The measured real inductance versus frequency (logarithmic scale) results for the 0.17C-Q, 0.38C-Q, 0.53C-Q, and 0.80C-Q samples using the cylindrical EM sensor (described in section 4.5.1 in Chapter 4) are shown in Figure 6.36. It can be seen that the sensor output (real inductance changes with frequency) can clearly distinguish samples with different carbon content. The relative permeability values for the these samples were determined by fitting the experimental EM sensor measurement using the FE sensor output model described in section 5.4 in Chapter 5. The relative permeability values are plotted against the carbon content in as quenched martensite samples in Figure 6.37. It can be seen that relative permeability of the samples and hence the real inductance values at low frequencies (below approximately 100Hz), decrease with increased carbon content in the as quenched martensite. This is believed to be mainly due to the increase in dislocation density and reduction in martensite lath size in the

higher carbon content samples, which in turn decreased the size of mean free path for domain wall motion hence the relative permeability values.

In addition, a higher amount of retained austenite, which is a paramagnetic phase (relative permeability of 1), was expected to be formed in the higher carbon content samples (i.e. 0.53C-Q and 0.80C-Q). A volume fraction of 5 and 10% retained austenite was reported in water quenched 0.6 and 0.8 wt% C steels respectively [167]. In order to determine the significance of retained austenite to the relative permeability values, a 0.80C-LQ sample (a 0.80C-Q further quenched in liquid nitrogen to eliminate the retained austenite) was measured by the cylindrical EM sensor. The relative permeability of the 0.80C-LQ sample was determined to be 37, which is very slightly increased in compare with the relative permeability value of 0.80C-Q sample (36). The effect of retained austenite in the 0.53C-Q on relative permeability is expected to be less significant than 0.80C-Q due to its lower volume fraction of retained austenite. Therefore the effect of retained austenite is minor and can be neglected in compare with the effect of increase in dislocation density and reduction in martensite lath size in these samples.

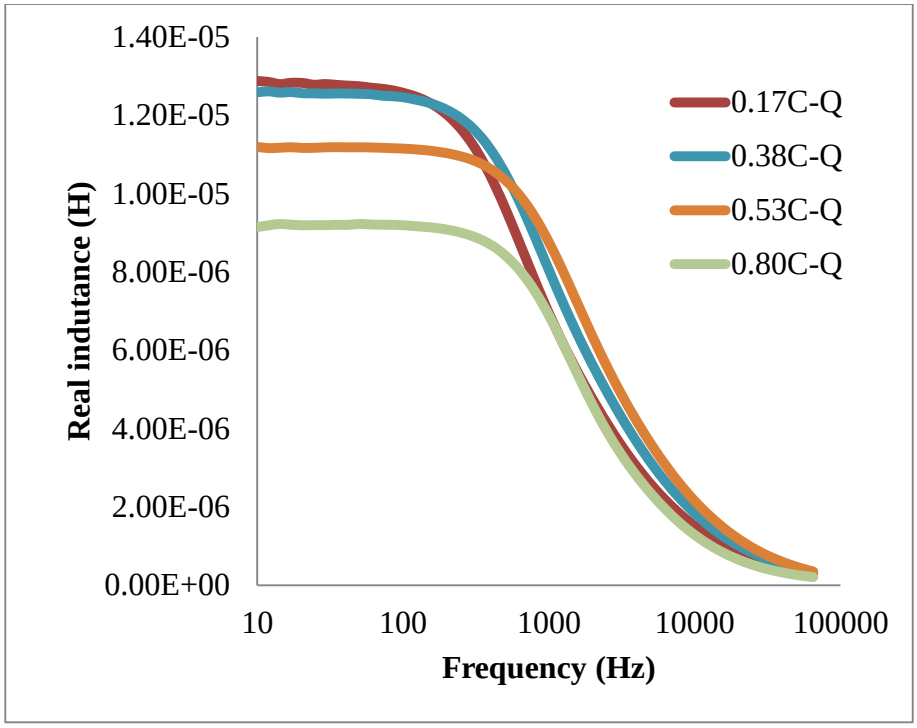

Figure 6.36: Real inductance changes with frequency for as-quenched 0.17C-Q, 0.38C-Q, 0.53C-Q and 0.80C-Q steel samples.

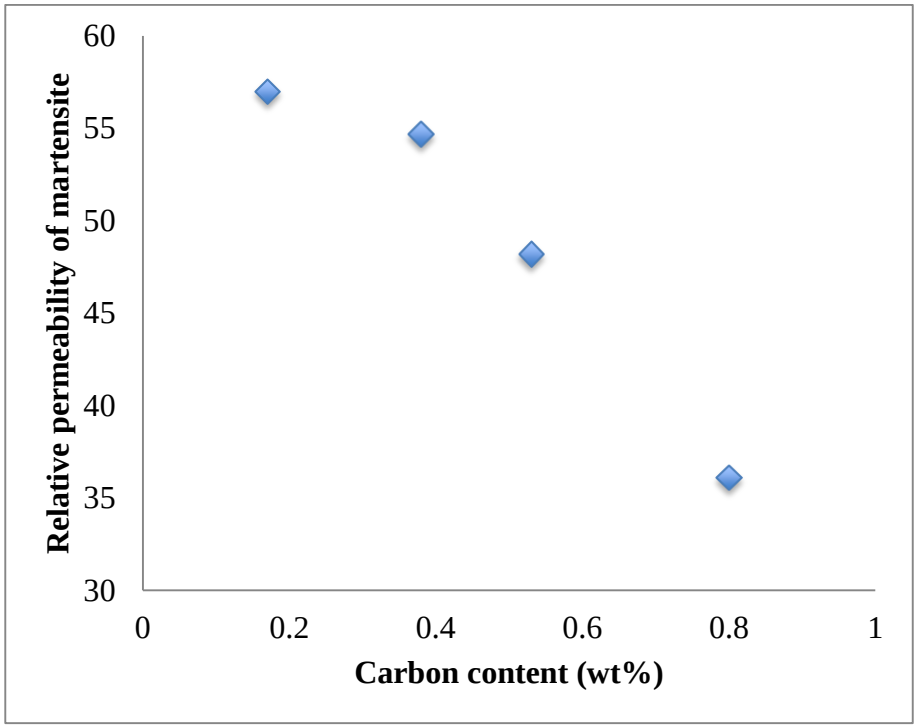

Figure 6.37:Plot of relative permeability against carbon content in as quenched 0.17C-Q, 0.38C-Q, 0.53C-Q and 0.80C-Q steel samples.

6.4.3 Effect of tempering temperature in tempered martensite

The measured real inductance versus frequency (logarithmic scale) results for the as-quenched and quenched and tempered samples for 0.38 and 0.80 wt%C steel using the cylindrical EM sensor (described in section 4.5.1 in Chapter 4) are shown in Figure 6.38 and 6.39 respectively. It can be seen that the heat treatment states of each sample can be distinguished from the EM sensor output.

The relative permeability values (determined by fitting the experimental EM sensor measurement using the FE sensor output model described in section 5.4 in Chapter 5) were plotted with the heat treatment conditions in Figure 6.40. It can be seen that the relative permeability values become higher after tempering. This is mainly due to the effect of decreased dislocation density during the tempering process [167]. The precipitation of carbides should result in a decrease of the relative permeability values as the carbides can provide extra pinning sites for domain wall movement. The results here suggested this was a less dominant effect. It can be seen the relative permeability increased further with an increasing tempering temperature (for the same tempering time). This is believed to be due to the coarsening and spheroidisation of carbides, which increases the mean free path length for domain wall motion.

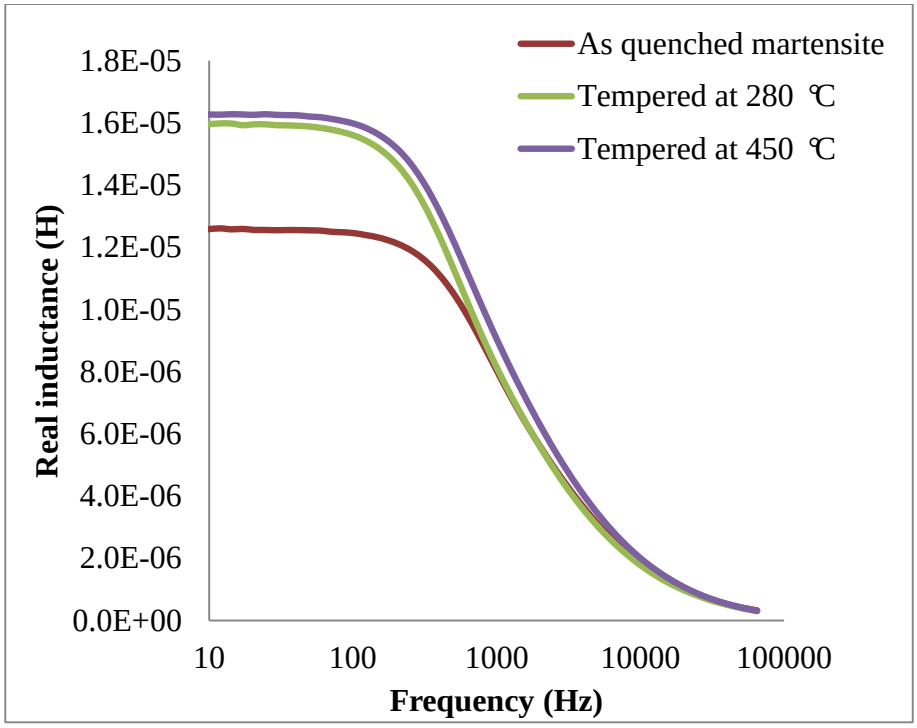

Figure 6.38: Real inductance changes with frequency for as-quenched 0.38C-Q sample, quench and tempered 0.38C-QT280, and 0.38C-QT450 samples.

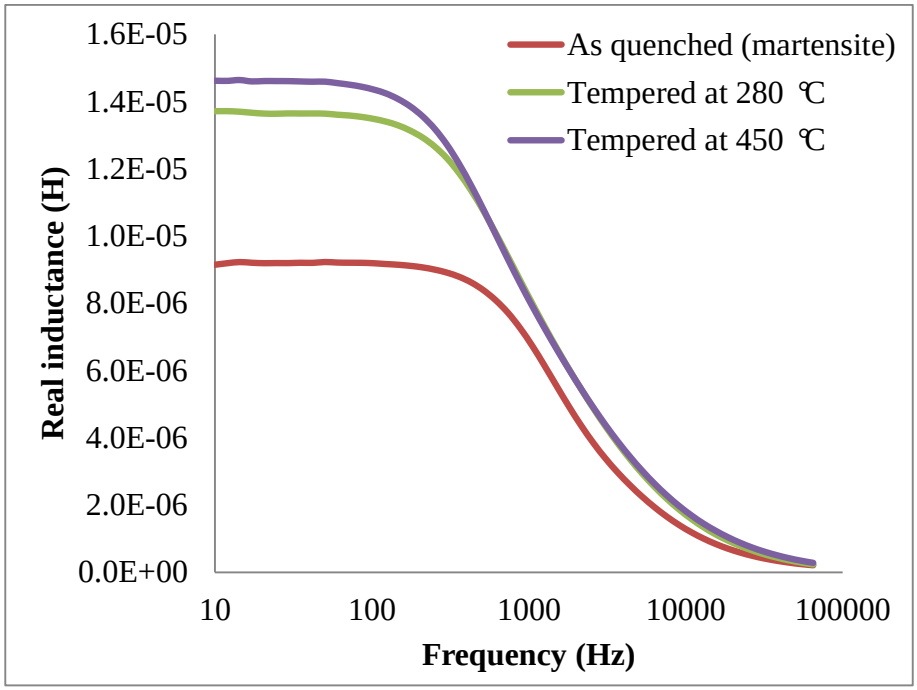

Figure 6.39: Real inductance changes with frequency for as-quenched 0.80C-Q sample, quench and tempered 0.80C-QT280, and 0.80C-QT450 samples.

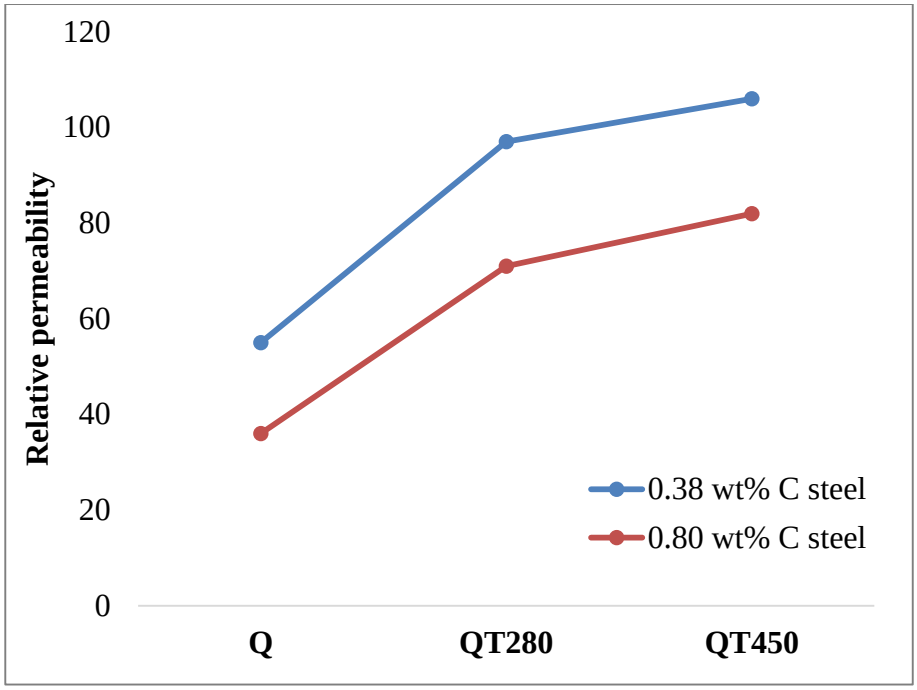

Figure 6.40: The relative permeability of 0.38 and 0.80 wt%C steel plot with heat treatment conditions: Q: as-quenched, QT280:quenched and tempered at 280 ℃ for 1 hour and QT450:quenched and tempered at 450 ℃ for 1 hour

6.4.4 Summary

Martensitic steel microstructures were assessed in C-Mn steel samples, with a range of carbon contents from 0.17 to 0.80 wt%. The relative permeability values, and hence the low frequency (plateau region) real inductance, decreased with an increase in carbon content in the as quenched martensite microstructure. This is believed to be due to the increase in dislocation density and reduction in martensite lath size in the higher carbon content samples, which in turn decreased the size of mean free path for domain wall motion and hence the relative permeability values. After tempering the martensitic structures, the relative permeability values increased due to the effect of decreased dislocation density. The precipitation of carbides, which would be expected to decrease the permeability values (due to providing pinning sites for domain wall movement) was

a less dominant effect. The relative permeability increased with an increasing tempering temperature (for the same tempering time) due to the coarsening and spheroidisation of carbides, which further increases the mean free path length for domain wall motion.

7 EM detection of phase balance

7.1 Ferrite – pearlite phase balance

In this section, the effect of ferrite-pearlite phase balance on the relative permeability and hence the sensor output was studied using C-Mn steels (ferrite + pearlite) with different carbon contents. The results presented in this section has been published in ref [140].

7.1.1 Microstructure, hardness and resistivity results

The optical microstructures of the pure iron, 0.17C, 0.38C, 0.53C and 0.8C as-received samples, all at ×400 magnification, are shown in Figures 7.1-7.5 respectively.

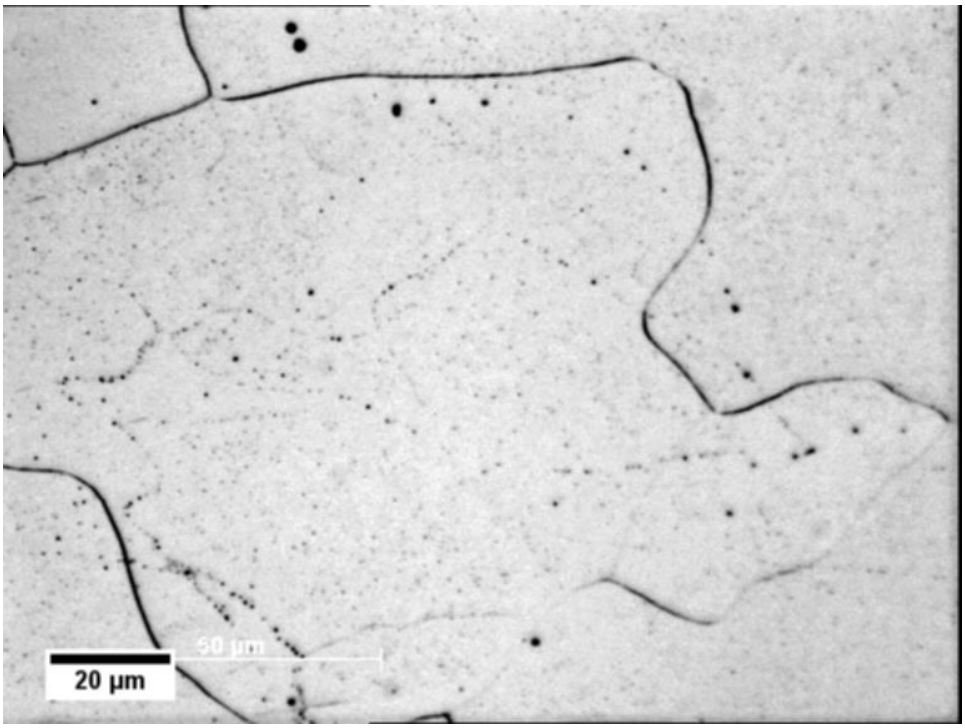

Figure 7.1: Optical microstructure of Fe sample, at ×400 magnification.

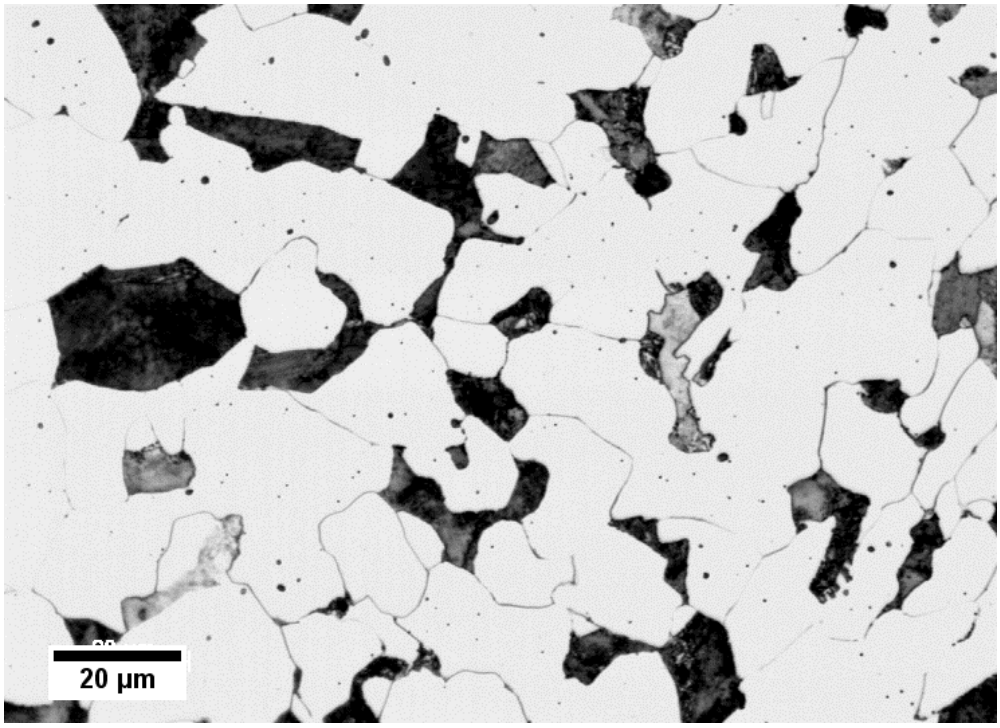

Figure 7.2: Optical microstructure of as-received 0.17C sample, at ×400 magnification.

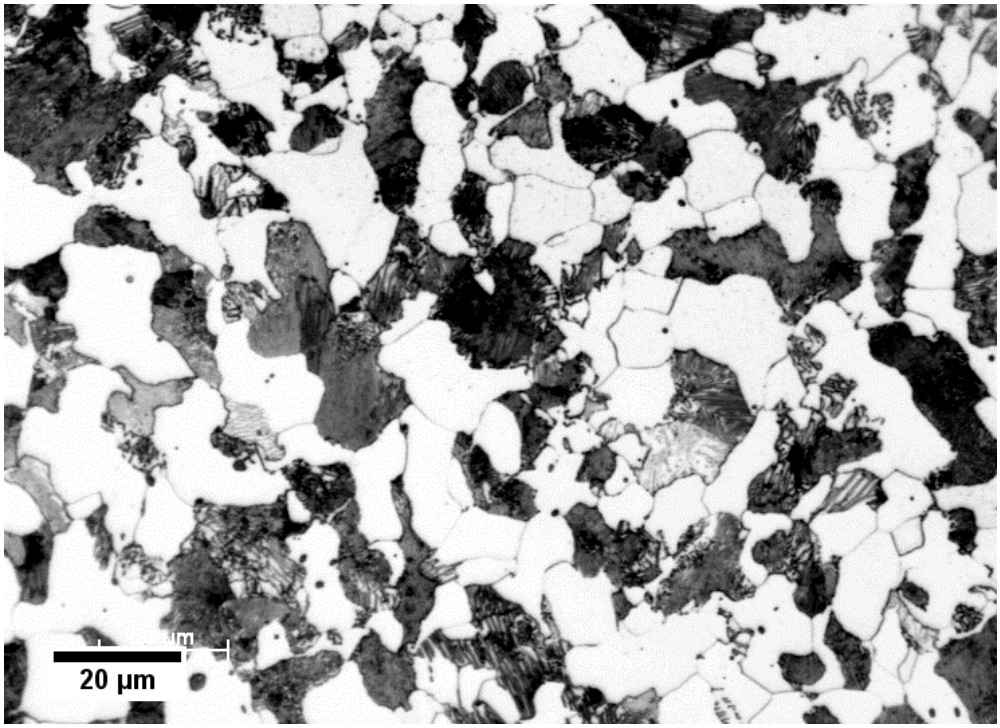

Figure 7.3: Optical microstructure of as-received 0.38C sample, at ×400 magnification.

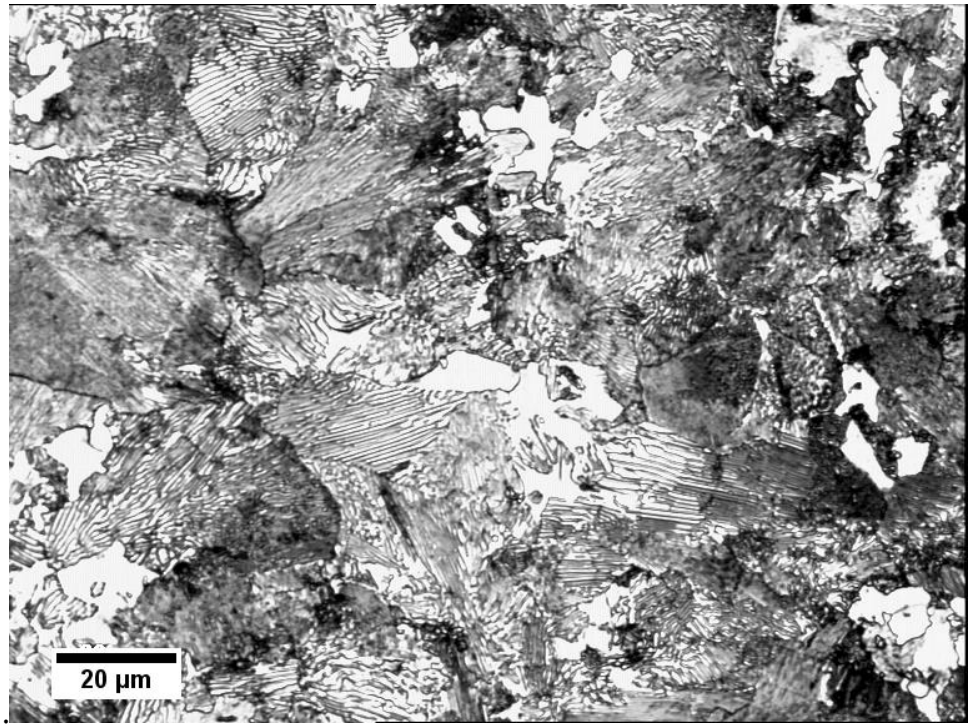

Figure 7.4: Optical microstructure of as-received 0.53C sample, at ×400 magnification.

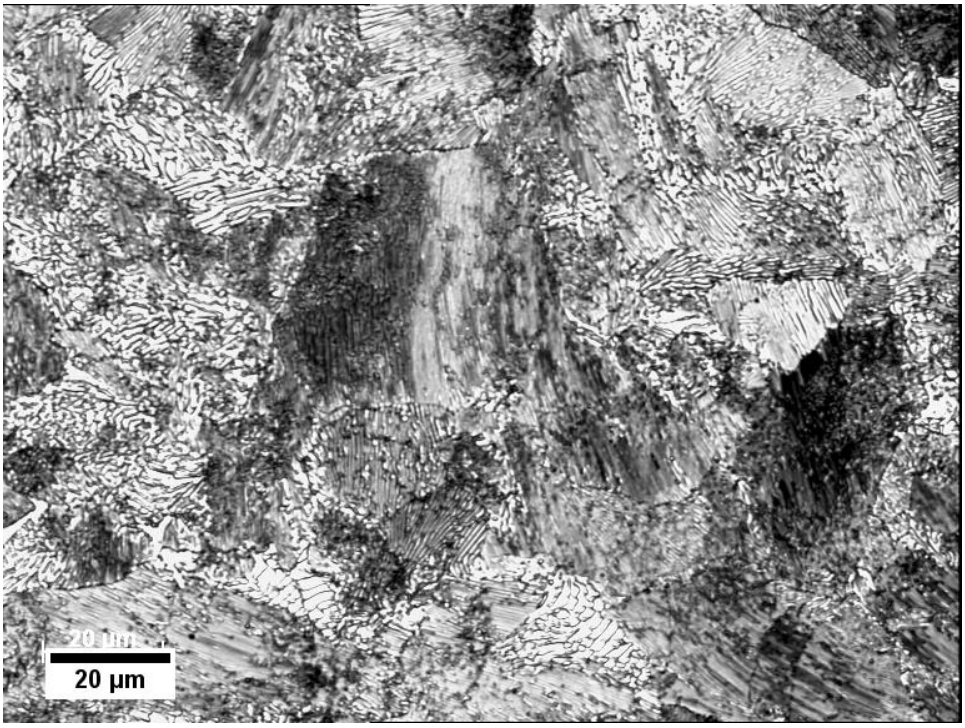

Figure 7.5: Optical microstructure of as-received 0.8C sample, at ×400 magnification.

The pure iron sample microstructure consists of larger (155 µm) ferrite grains, the 0.8C steel microstructure consists of pearlite, whilst the 0.17C, 0.38C and 0.53C steel microstructures consist of both ferrite (lighter) and pearlite (darker). Table 7.1 shows a summary of the average ferrite grain size (equivalent circle diameter), ferrite fraction, hardness and resistivity with standard deviation values. As the carbon content increases, more pearlite is formed (hence the ferrite fraction decreases) and resulting an increase of hardness. The resistivity value of 0.17C, 0.38C, 0.53C and 0.80C sample (ferrite and pearlite or fully pearlitic microstructure) are much higher than that of the pure iron (fully ferritic microstructure) due to the presence of pearlite and alloying elements in these steels, it can also be seen that for these steels the resistivity value increases with carbon content due to the increasing amount of pearlite phase formed. Considering the aim of non-destructive characterisation of steel microstructure then it can be seen that there is a clear measureable difference in resistivity values between the samples. Therefore, resistivity measurement could be used to distinguish them.

Table 7.1: Summary of the microstructure, hardness and resistivity values of the ferrite-pearlite microstructures.

Sample	Average ferrite grain size (µm)	Ferrite%	Hardness (HV)	Resistivity (nΩm)
Fe	155.1 ± 68.1	100	72.8 ± 1.1	104.0 ± 0.3
0.17C	24.5 ± 10.7	72.8 ± 1.8	146.8 ± 0.4	210.9 ± 0.1
0.38C	14.0 ± 5.8	48.9 ± 1.2	171.3 ± 1.3	218.6 ± 0.2
0.53C	8.0 ± 3.7	9.0 ± 0.7	224.7 ± 2.1	230.1 ± 0.2
0.80C	-	0	277.2 ± 3.2	243.7 ± 0.3

7.1.2 EM sensor results for ferrite – pearlite phase balance

The measured real inductance versus frequency (logarithmic scale) results for the as-received pure iron, 0.17C, 0.38C, 0.53C and 0.8C steel samples, using the cylindrical EM sensor are shown in Figure 7.6. At low frequencies (below approximately 100 Hz), the real inductance values, which are dominated by relative permeability, decrease with the increase in carbon content up to 0.53 wt% C due to the formation of pearlite, which has a much lower relative permeability than ferrite [7, 91]. It can be seen that the 0.53C and 0.8C steels show little difference in real inductance value at low frequency despite the former sample containing 9% ferrite whilst the latter contains no ferrite. The reason for this is discussed in the next section (7.1.3). It can be seen in Figure 7.6 that the pure iron sample shows a slightly different real inductance – frequency curve shape; this is due to the higher relative permeability and much lower resistivity (stronger eddy current effect) of the pure iron sample compared to the C-Mn samples, hence the inductance starts to decrease at much lower frequency.

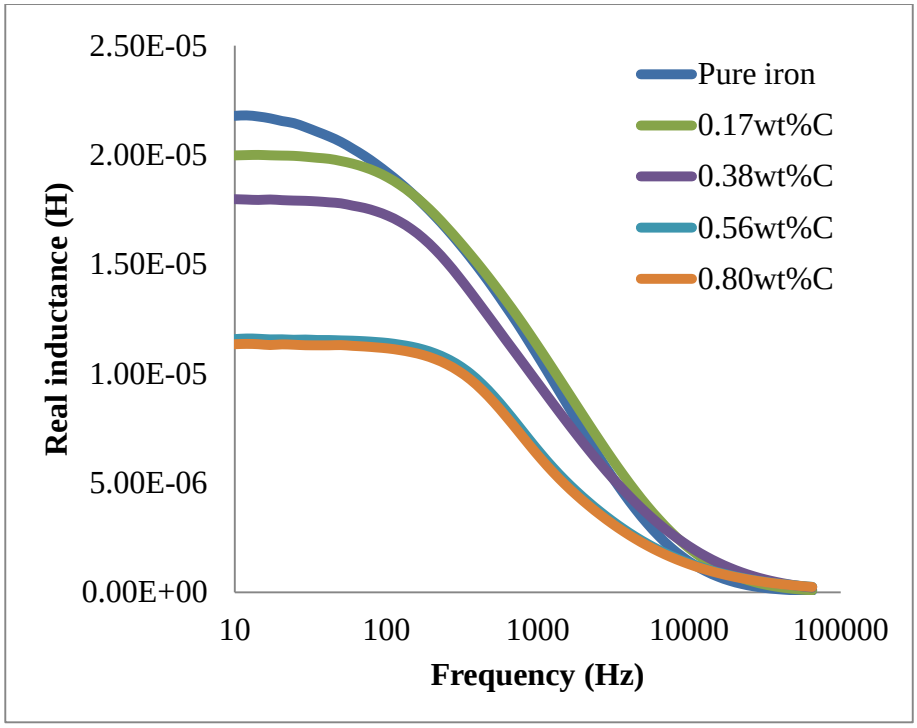

Figure 7.6: Real inductance changes with frequency for pure iron, 0.17C, 0.38C, 0.53C and 0.80C as-received (i.e. ferrite + pearlite) steel samples.

7.1.3 Effect of ferrite-pearlite phase balance on relative permeability

The relative permeability values, calculated from the FE permeability fitting model (described in Chapter 5.4), are plotted against the ferrite fraction in the different steel microstructures in Figure 7.7. It can be seen that there is an increase in the relative permeability value as the ferrite fraction increases. The small difference in relative permeability between the 0.53C and 0.8C steels is believed to be due to the ferrite regions in the 0.53C steel being unconnected (shown in Figure 7.4) and hence not contributing much to the effective permeability of the sample. This is similar to the effect reported by Yin et al. who found that in austenite + ferrite steel samples a low fraction of ferrite (<40%), present as isolated regions due to the powder processing fabrication route used to make the samples, did not result in much increase in permeability for both the measured and FE modelled results (shown in Figure 7.8) [162].

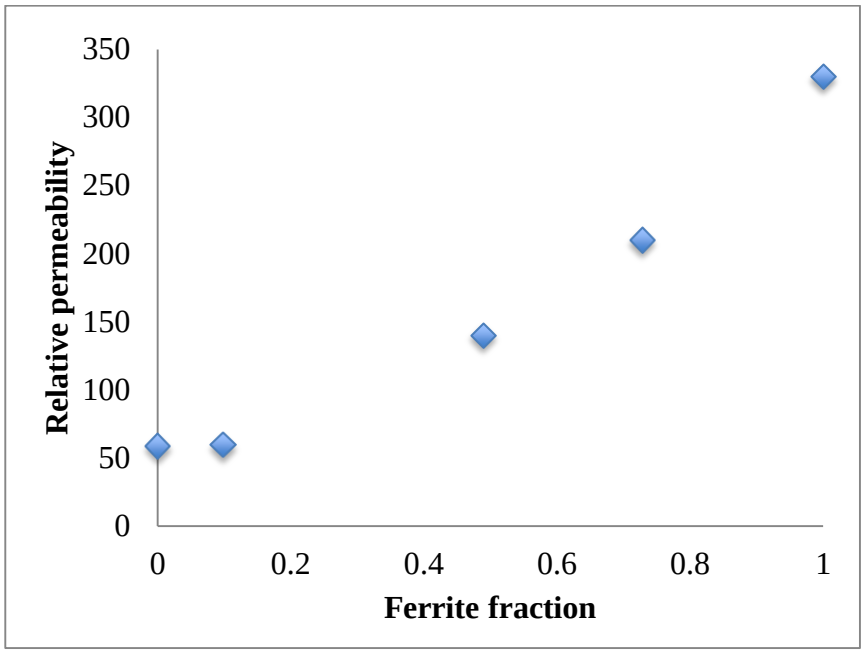

Figure 7.7: Predicted relative permeability for pure iron, 0.17C, 0.38C, 0.53C and 0.8C steel samples plot aginst ferrite fraction.

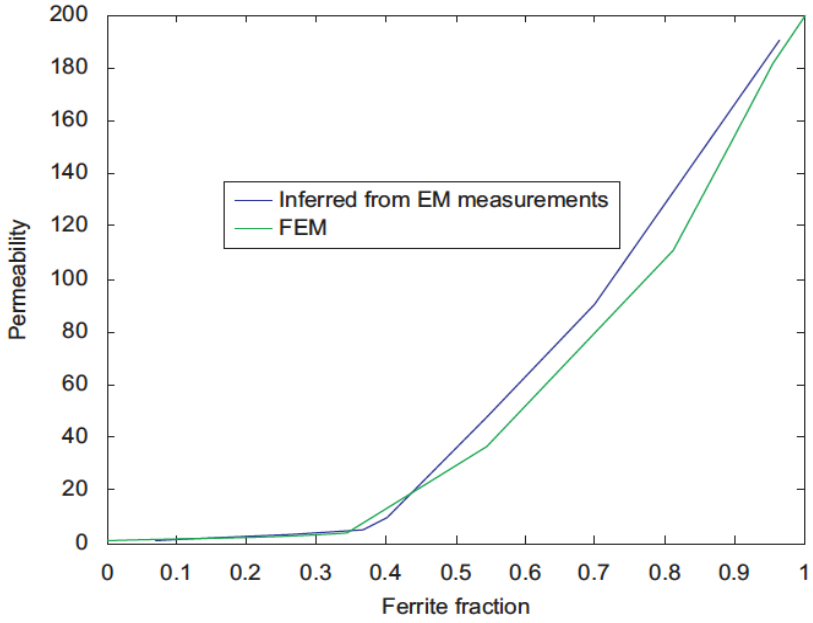

Figure 7.8: FEM and EM measurements of the ferrite fraction and permeability relation for ferrite and austenite microstructures [162].

The relative permeability values, determined by fitting the experimental EM sensor results with the FE model, for single-phase pearlite and ferrite are 58.6 and 330 respectively. The value for pearlite agrees well (within 6%) with Thompson et al. [91], who reported that the initial relative permeability of fully pearlitic phase (in a 0.87 wt.% C steel) is 56. Thompson et al also reported that ferrite with 19.5% pearlite (a predicted phase fraction base on the carbon content) has a relative permeability of 280 whilst Jiles et al. [150] reported the permeability in a very low-carbon steel (0.0065 wt.% C) as being 350±50. As was discussed in section 3.7 in Chapter 3 and Chapter 6, the relative permeability values are also affected by factors such as ferrite grain size, pearlite interlamellar spacing, plastic strain and temperature [91, 100]. For the C-Mn steel samples, room temperature measurements on stress free samples (no applied stress and in a hot rolled or heat treated condition therefore having little/no residual stresses) have been made. In terms of microstructural parameters, pearlite interlamellar spacing does not change significantly between the samples as they were all air cooled; and the effect of ferrite grain size on the relative permeability (difference in relative permeability value is 36 due to grain size change from 13 to 64 μm in 0.17C steel) is much smaller than the effect of ferrite/pearlite phase balance (difference of relative permeability value is 274 due to ferrite fraction change from 0 to 100% in ferrite + pearlite microstructures). Therefore, the variation in phase balance has the dominant effect on the relative permeability values and is considered further here.

7.1.4 Modelling of the relative permeability for ferrite/pearlite phase balance

The relative permeability determined from the experimentally fitted results has been compared with that predicted using the power law models (described in section 3.7.4 in

Chapter 3) and obtained from the FE microstructure model described in section 4.7 in Chapter 4), using a pearlite value of 58 and ferrite value of 330, and are shown in Figure 7.9. It can be seen that the FE modelled permeability value gives the best fit with the experimental data. The power law models, using the β values of 1/2 [153] and 1/3 [154] reported in the literature for prediction of the dielectric constant of mixtures, give higher relative permeability values than the experimental measured ones. A β value of 1/5 was found to give the best fit with the measured values, except for the low ferrite fraction (9%) sample. This β value has not been reported in the literature.

It is apparent that the effect of low ferrite volume fractions on the relative permeability values for ferrite-pearlite is more significant on increasing the relative permeability than previously reported for low ferrite fractions in a ferrite-austenite phase balance, Figure 7.8 [8]. This is because pearlite is a ferromagnetic phase at room temperature, therefore when the ferrite fraction is low (ferrite grains are isolated), the magnetic flux can more readily pass through pearlitic regions between the preferred ferrite regions, whereas the austenite phase is less favourable hence a more complex route between ferrite regions, to minimize passage in austenite, occurs (shown in Figure 7.10). Therefore, the previous results in ref [8] for the shape of the permeability-ferrite fraction relationship in ferrite-austenite cannot be used to predict the relative permeability in a ferrite-pearlite (or other ferromagnetic steel phase such as martensite or bainite), as this will give errors in predicting relative permeability values for low ferrite fractions. Using the modelling approach described above, it is possible to predict the effective permeability of any dual phase (or indeed multi-phase) microstructure provided that each single-phase relative permeability values are known, whereas power law models cannot easily deal with triple phase microstructures.

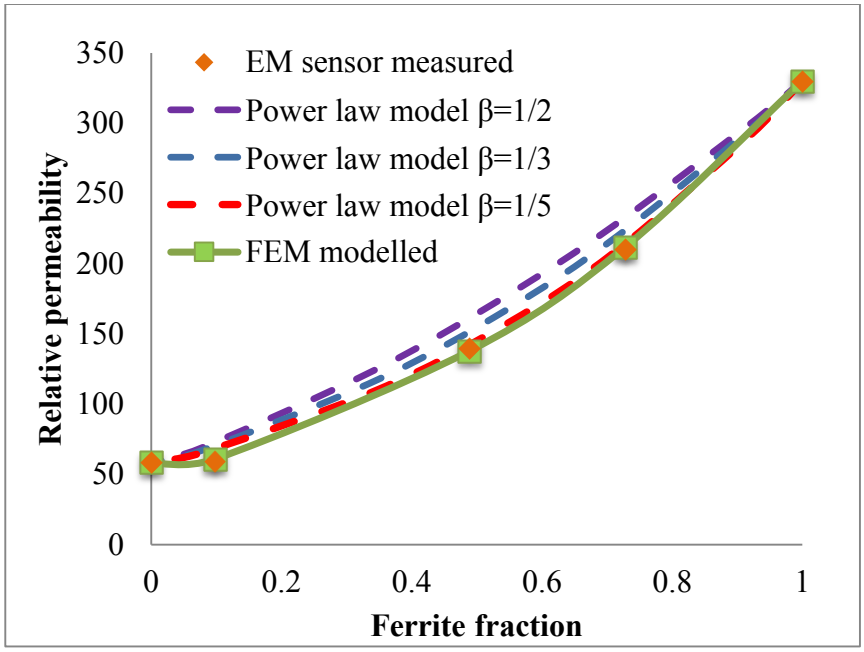

Figure 7.9: Relative permeability change with ferrite fraction, FEM modelled results were compared with the power-law model and the experimental fitted results [140].

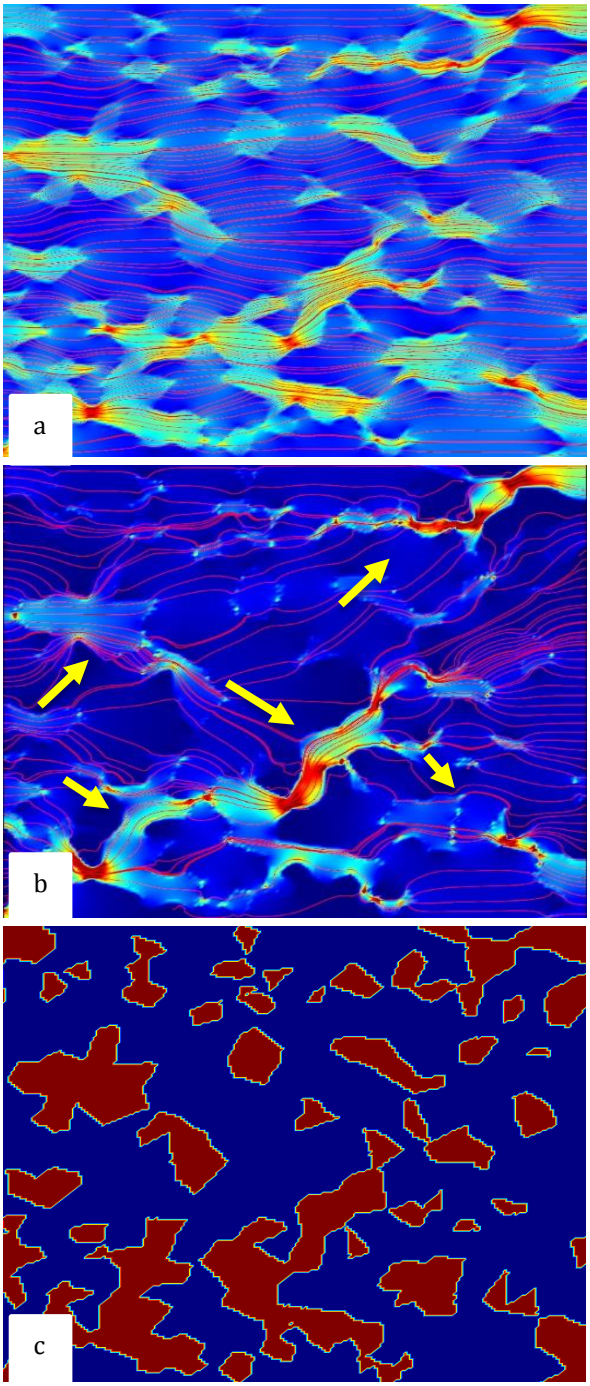

Figure 7.10: FE modelled results of the magnetic flux distribution with 30% ferrite in a) ferrite- pearlite and b) ferrite-austenite phase balance. (Red lines represent the magnetic flux density and red represents the highest flux density regions, whilst blue areas show the lowest flux density; the arrows show clear deviation of the magnetic flux to the ferrite in the ferrite-austenite mix); c) image processed micrograph showing phase distribution of ferrite (red) and pearlite/austenite (blue).

7.1.5 Summary

In this section, the effect of ferrite-pearlite phase on the relative permeability was studied. The results shows that the relative permeability, and hence inductance value, decreases with an increase in pearlite content (0-90%), due to the low permeability of pearlite compared with ferrite. A 2D FE model including microstructure has been shown to match the experimental results, therefore showing the potential of the EM sensor to non-destructively measure the ferrite fraction (up to approximately 90% ferrite) in ferrite/pearlite, or other dual phase, microstructures. The cylindrical sensor was initially used as this provides the 'best case' scenario to determine the relative permeability values (i.e. the materials property) and study their relationship with ferrite fraction in ferrite-pearlite phase balance. Measurements of ferrite-martensite phase balance in laboratory heat-treated dual phase (DP) steels were carried out using a U-shaped sensor to indicate how the approach could be used for more industrially interesting steel grades (presented in the next section – section 7.2 in Chapter 7).

7.2 Ferrite – martensite phase balance

In this section, the ferrite-martensite phase balance of dual phase steel (DPL600) samples in different heat treatment states were studied using a U-shaped EM sensor.

7.2.1 Microstructure results

Optical microstructure images for a DP600 grade steel grade after different heat treatments were provided (about 10 images for each heat treatment) by Tata Steel. An example of the optical microstructures of DPL600-650, DPL600-675, DPL600-700, DPL600-725, DPL600-750 and DPL600-800 samples using a 40× objective are shown in Figures 7.11-7.16 respectively.

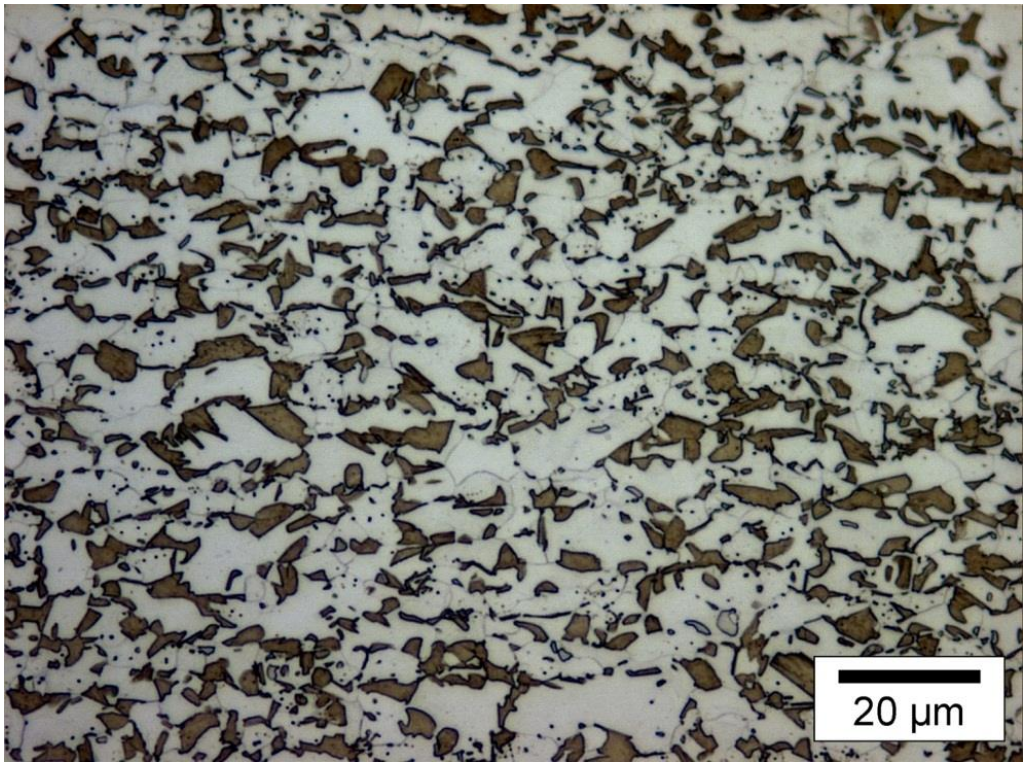

Figure 7.11: Optical microstructure of DPL600-650 sample at ×400 magnification.

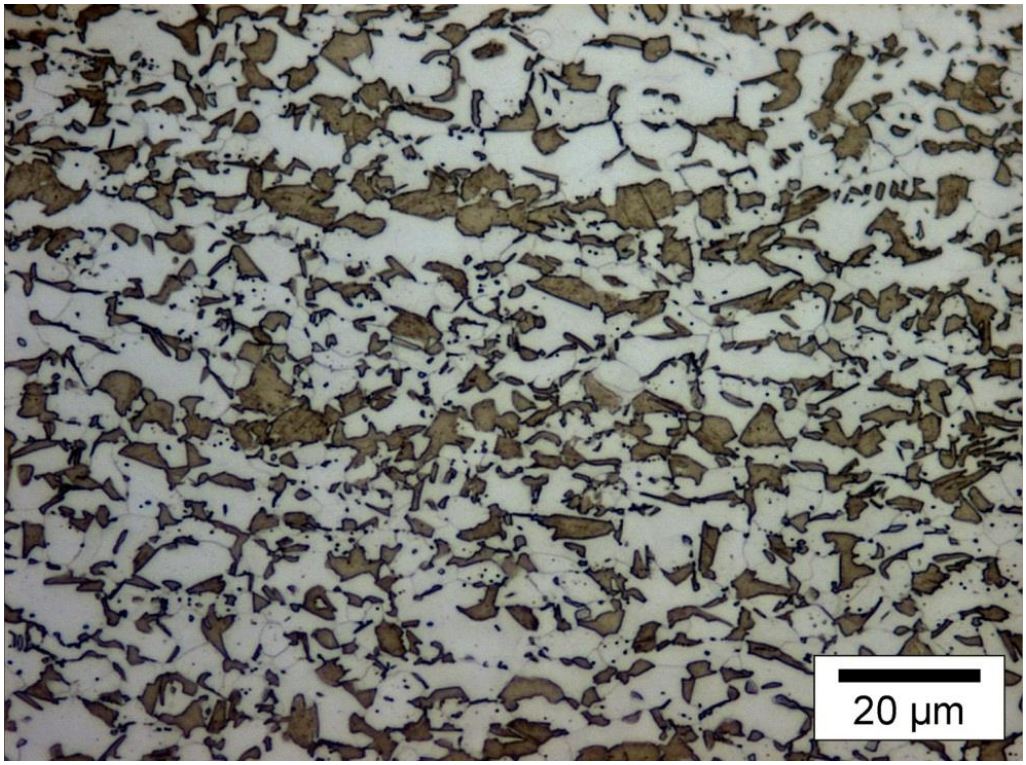

Figure 7.12: Optical microstructure of DPL600-675 sample at ×400 magnification.

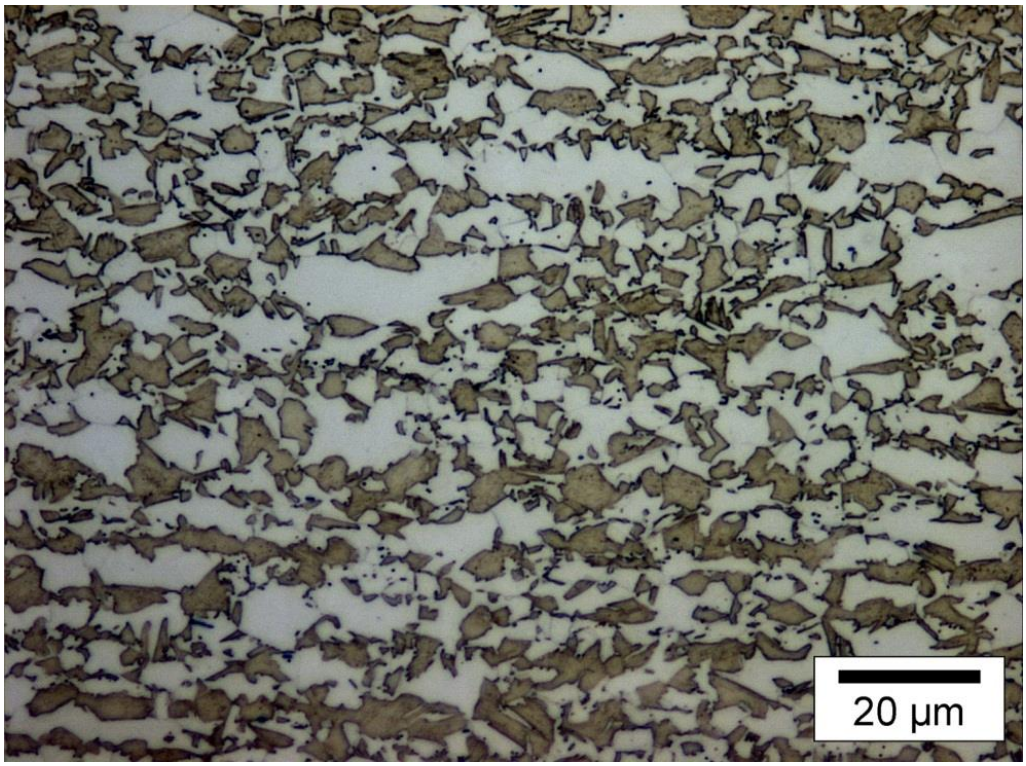

Figure 7.13: Optical microstructure of DPL600-700 sample at ×400 magnification.

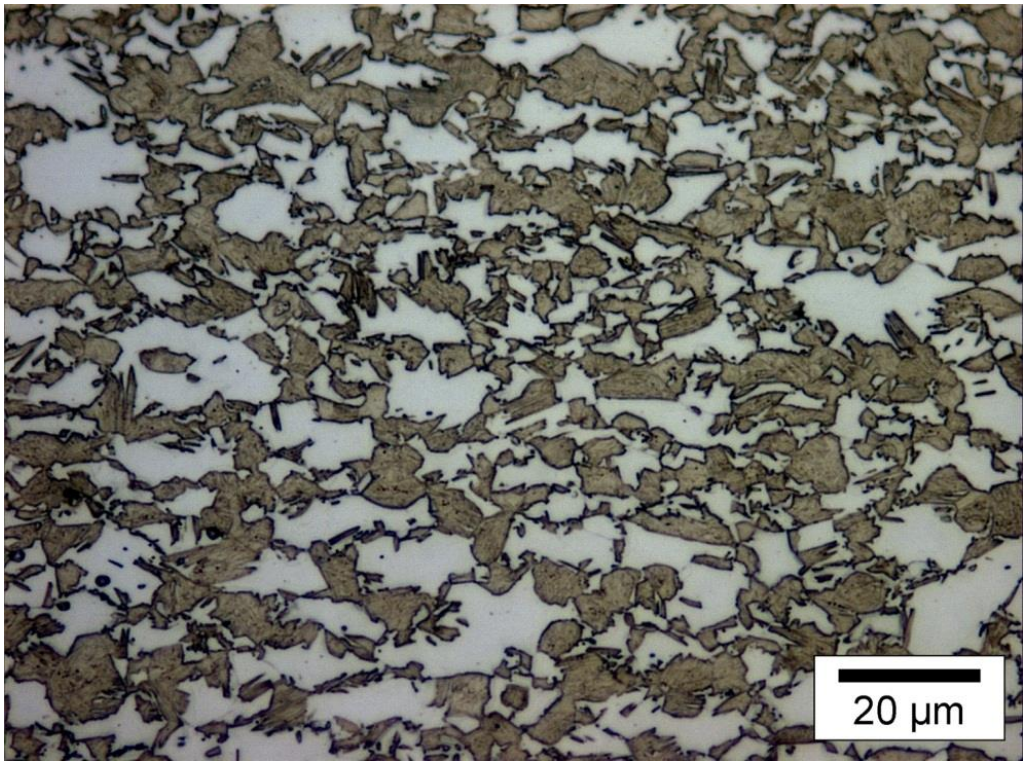

Figure 7.14: Optical microstructure of DPL600-725 sample at ×400 magnification.

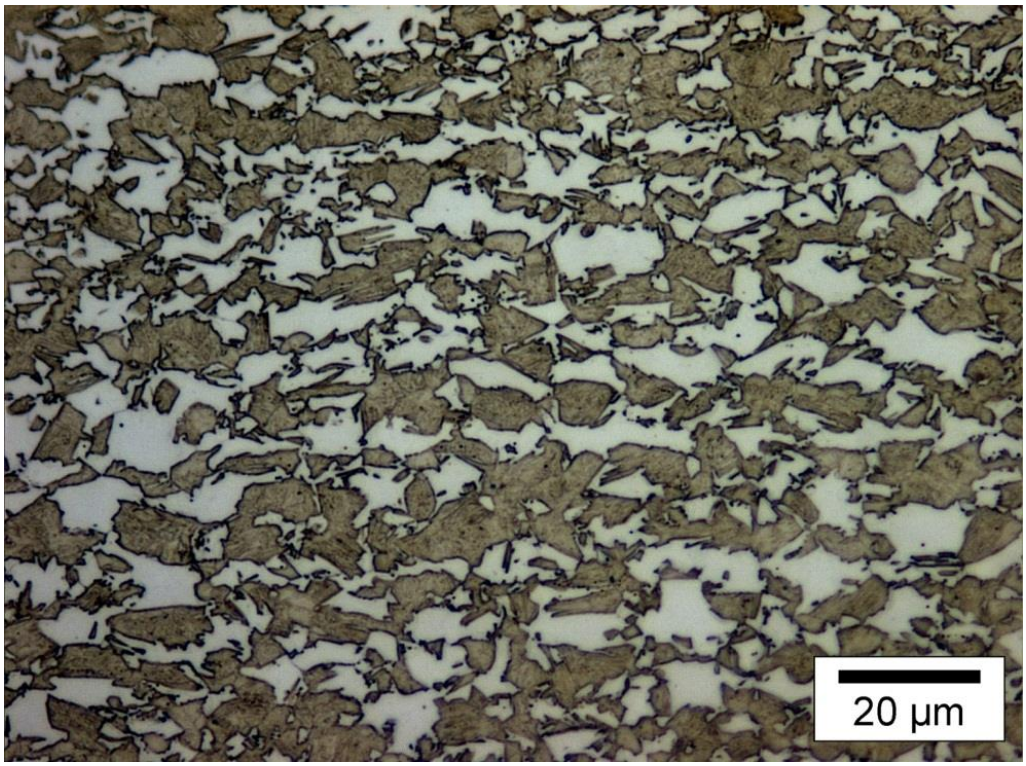

Figure 7.15: Optical microstructure of DPL600-750 sample at ×400 magnification.

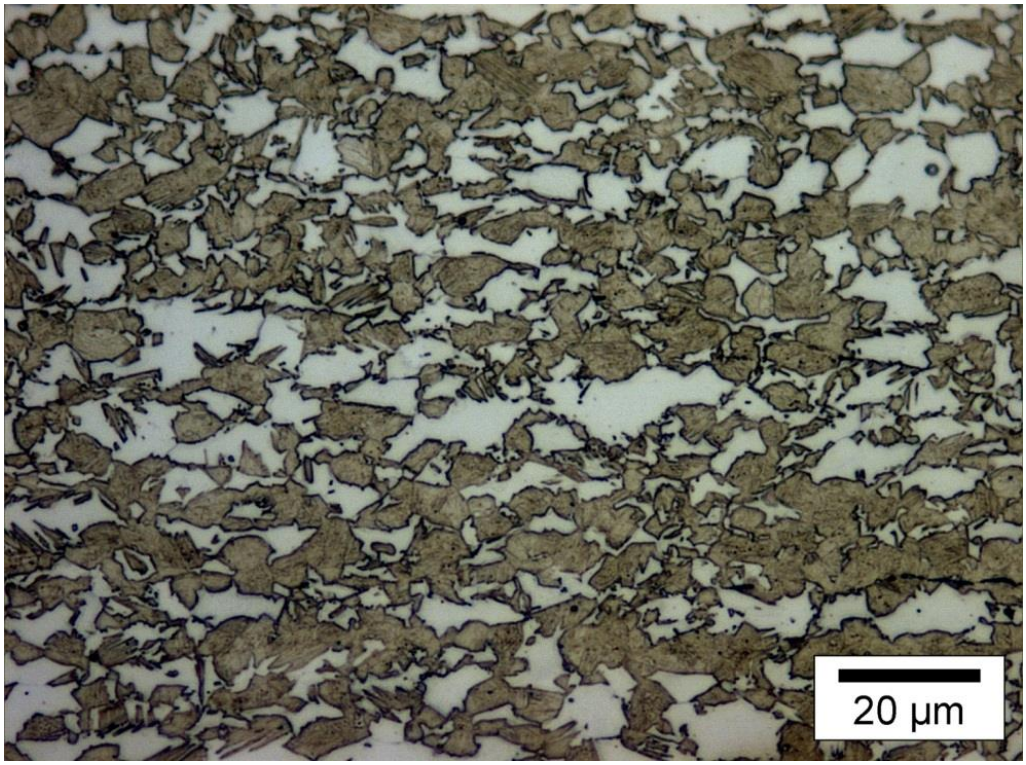

Figure 7.16: Optical microstructure of DPL600-800 sample at ×400 magnification.

The microstructures consist of two phases, which are ferrite (lighter) and martensite (darker). As can be seen from Figure 7.11-7.16, the second phase (martensite) was randomly distributed in the ferrite matrix. The carbon content in martensite after each heat treatment condition is different due to the different ferrite-martensite phase balance with identical steel composition. As discussed in section 6.4 in Chapter 6, the permeability value of martensite will vary with carbon content. The carbon content in the martensite for each heat treatments state was predicted by assuming that the carbon content of the DPL600 steel samples was 0.17wt%, the carbon content of the ferrite was 0.02wt% and all of the rest of the carbon is in the martensite. Table 7.2 provides a summary of the ferrite fraction, carbon content in martensite, and predicted relative permeability value of martensite for each heat treatment parameter according to the results obtained from section 6.3 in Chapter 6.

Table 7.2: Summary of ferrite fraction, carbon content in martensite and permeability of martensite for dual phase steel after different heat treatment.

Sample	Ferrite fraction %	Carbon content in martensite (wt %)	Permeability of martensite
DPL600-650	71.8 ±0.8	0.55	47
DPL600-675	66.6 ±1.23	0.47	51
DPL600-700	51.4 ±1.92	0.33	55
DPL600-725	39.2 ±2.29	0.27	56
DPL600-750	39.8 ±2.41	0.27	56
DPL600-800	34.7 ±1.17	0.25	56

7.2.2 Modelling of the relative permeability for ferrite/martensite phase balance

The results of the relative permeability modelled from the FE microstructure model described in section 4.6 in Chapter 4 change with the ferrite fraction for the dual phase steel after the different heat treatments are given in figure 7.17. The modelled relative permeability values for the dual phase steel samples show large differences (from 115 to 216) between the different heat treatments, corresponding to the different fractions of ferrite present (35-72%).

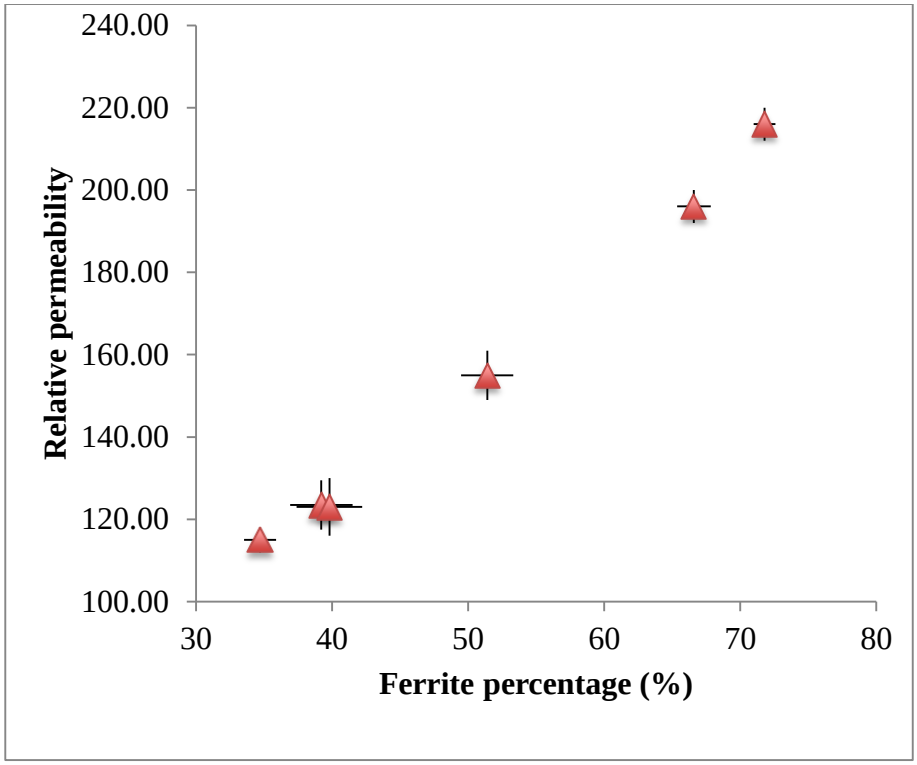

Figure 7.17:Modelled relative permeability values plot against ferrite fraction for ferrite/martensite dual phase steels.

7.2.3 EM sensor results for ferrite – martensite phase balance

The real inductance at a 100Hz plot against the ferrite fraction is shown in Figure 7.18. The real inductance values, which are dominated by relative permeability, increase with the amount of ferrite that has a much higher relative permeability than martensite. This agrees well with the trend between relative permeability and ferrite fraction modelled using real microstructure of these samples (shown in Figure 7.17). The relative permeability values for these samples were not determined, due to the fact that the U-shaped sensor was used, and a 3D FE model has not been developed for this sensor in this project (recommendation has been made in future work section).

The EM sensor results of the samples are consistent and distinguishable. The error bar of the EM sensor measurements on some samples is relatively large. This is due to the fact that a relatively small U-shaped sensor is used for the large strip steel samples which are not perfectly flat. The flatness of the samples will affect the sensor lift-off, which has been proven to be extremely sensitive to the sensor output [8, 143, 152, 171].

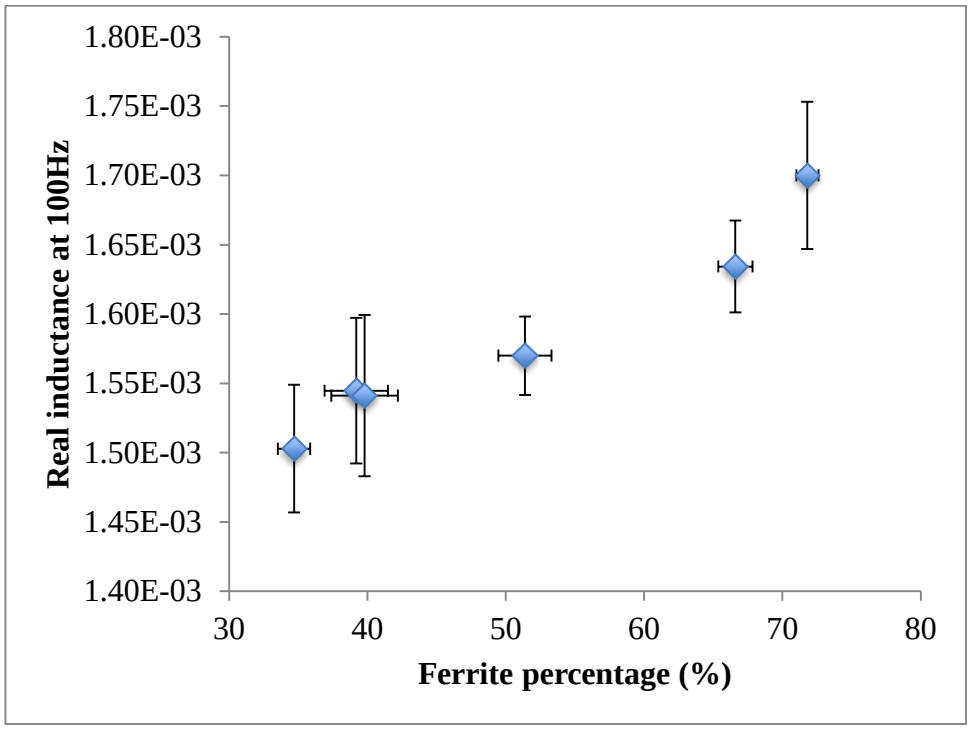

Figure 7.18: Real inductance at 100Hz plot against ferrite fraction for DPL600-650, DPL600-675, DPL600-700, DPL600-725, DPL600-750 and DPL600-800 samples.

7.2.4 Summary

Measurements of ferrite-martensite phase balance in laboratory heat-treated dual phase (DP) steels were carried out using a U-shaped sensor to indicate how the approach could be used for more industrially interesting steel grades (DP steels). The low frequency (plateau region) real inductance value increased almost linearly with the ferrite fraction in the range of 35-72% in these DP steels. The results demonstrated the potential of

using the U-shaped EM sensor to measure the microstructure in these DP steels. A case study was carried out to investigate the possibility of using the U-shaped EM sensor to predict the microstructure, and hence strength, of commercial DP steel grades.

7.3 Case study for EM sensor measurement of commercial DP/CP steels

7.3.1 Introduction

Strip steels with a dual-phase (DP) or complex-phase (CP) microstructure are widely used in the automotive industry. The microstructure of dual phase steels consists of ferrite typically with 20-80% dispersion of second phase (e.g. martensite and / or bainite) islands. The microstructure is produced either by controlling the transformation of austenite after hot rolling or by heat treatment after cold rolling [172]. The amount and type of any second phase plays an important role in determining the mechanical properties. In order to obtain accurate quality control, it is desirable to be able to monitor the mechanical properties of the product non-destructively and this may be achieved by measurement of the phase balance, as there is a direct link between microstructure and strength [173, 174]. The main differences between the commercial grades and lab based heat treated ones (discussed in section 7.2) are: firstly commercial grades achieve phase balance by both chemical compositions and thermal processing; secondly the microstructures obtained in commercial grades steels can have bainite and tempered martensite present instead of just martensite.

In this case study, a U - shaped EM sensor (described in section 4.6.2 in Chapter 4) has been used to measure the different commercial DP and CP steels; DP600, DP800, DP1000 and CP1000 grades. The EM signal has been related to the phase balance in the steels and to the measured tensile strength values. In addition to the experimental measurements, the FE microstructure model, described in section 4.6 in Chapter 4, was used to predict the relative permeability values of commercial DP samples with a range

of ferrite contents using SEM images of the phase balance as input. Some of the results presented in this section has been published in ref [175].

7.3.2 Microstructures

SEM images at ×3000 magnification (about 5 images for each grade) were used to quantify the phase balance of the commercial strip samples. Typical SEM images of each sample are shown in Figures 7.19-7.25 (rolling direction is horizontal to the images and ferrite appears dark). A heavily banded microstructure was seen for the DP800 and DP1000 samples (shown in figure 7.21 and 7.24 respectively). The CP1000 steel appears to have a non-connected ferrite morphology whereas for the DP steels the ferrite appears continuous, albeit this is based on the 2D micrographs.

The phase fraction was quantified using the method described in section 4.1 in Chapter 4. Table 7.3 gives a summary of the average phase fractions in the samples; it can be seen that the second phase observed is predominantly bainite/tempered martensite, although a significant amount of martensite is present in the CP1000 steel. It can be seen from Table 7.3 that the galvanised samples have lower martensite fraction (in particular the DP600GI sample has no martensite in compare with 6.4% martensite seen in the DP600 sample). This is due to the thermal effect of the additional processing treatment during the galvanising (some martensite phase has transformed into tempered martensite).

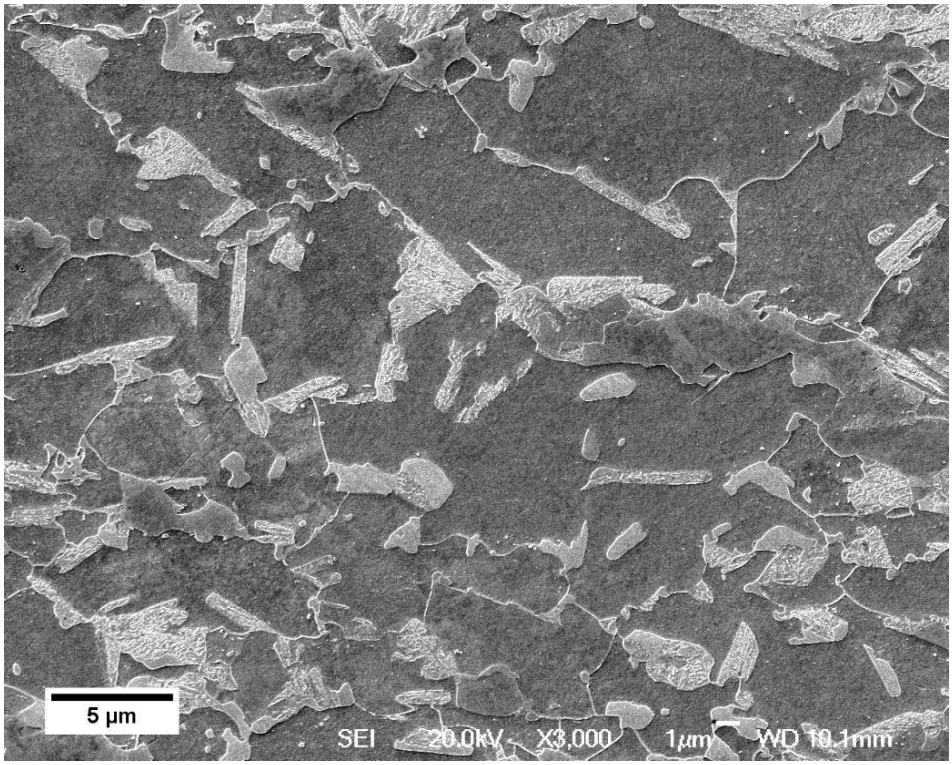

Figure 7.19: Typical SEM image of the DP600 samples

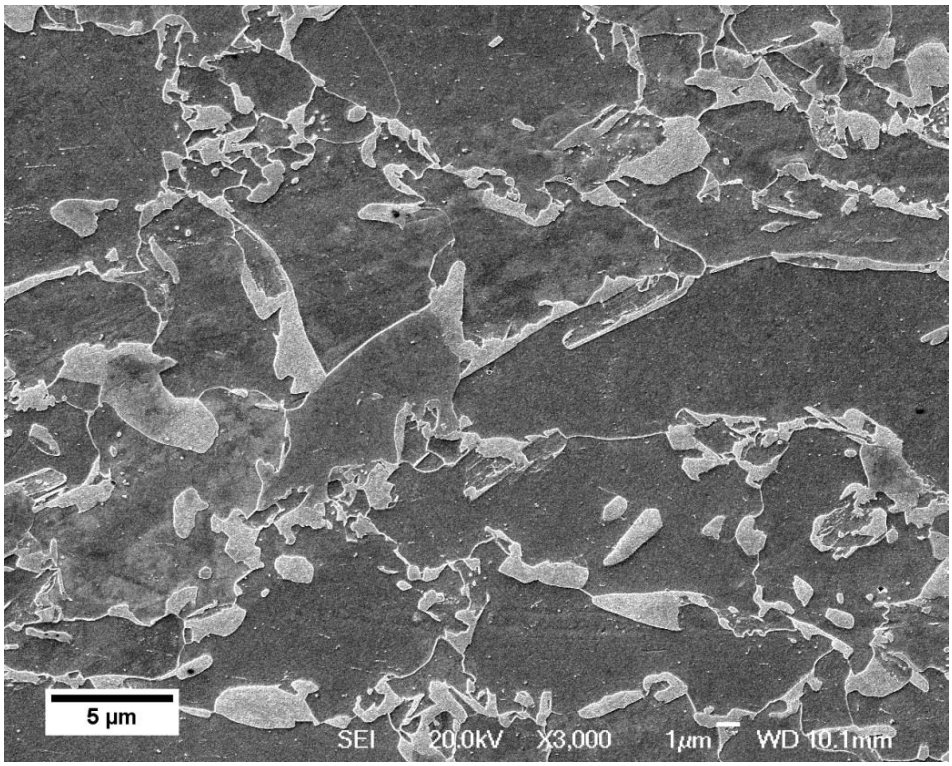

Figure 7.20: Typical SEM image of the DP600GI samples

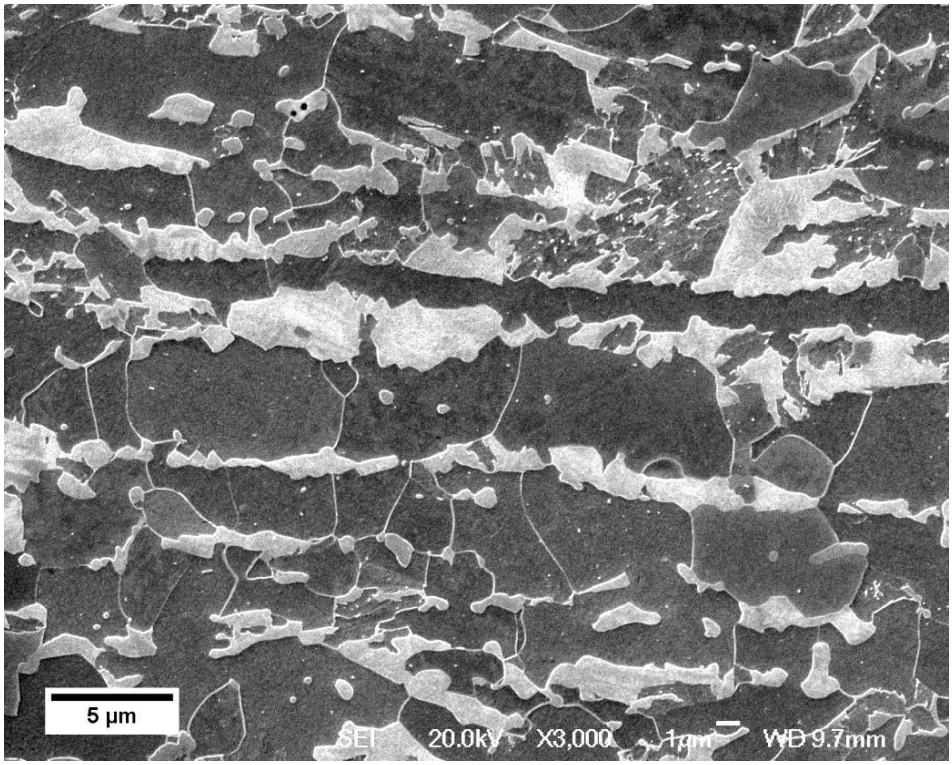

Figure 7.21: Typical SEM image of the DP800 samples.

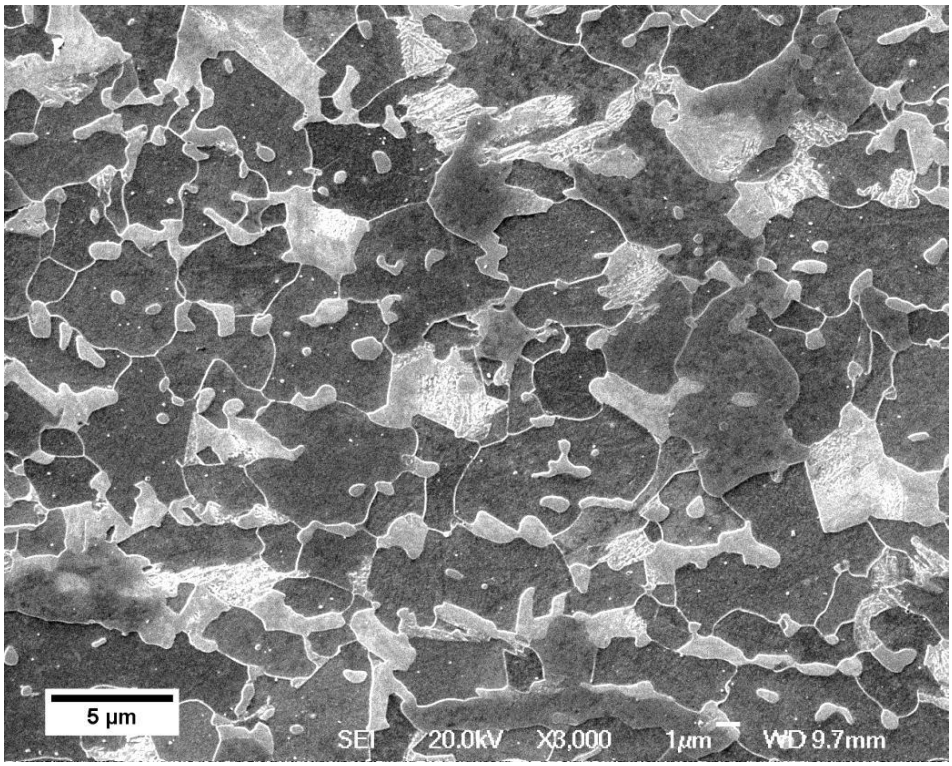

Figure 7.22: Typical SEM image of the DP800GI samples

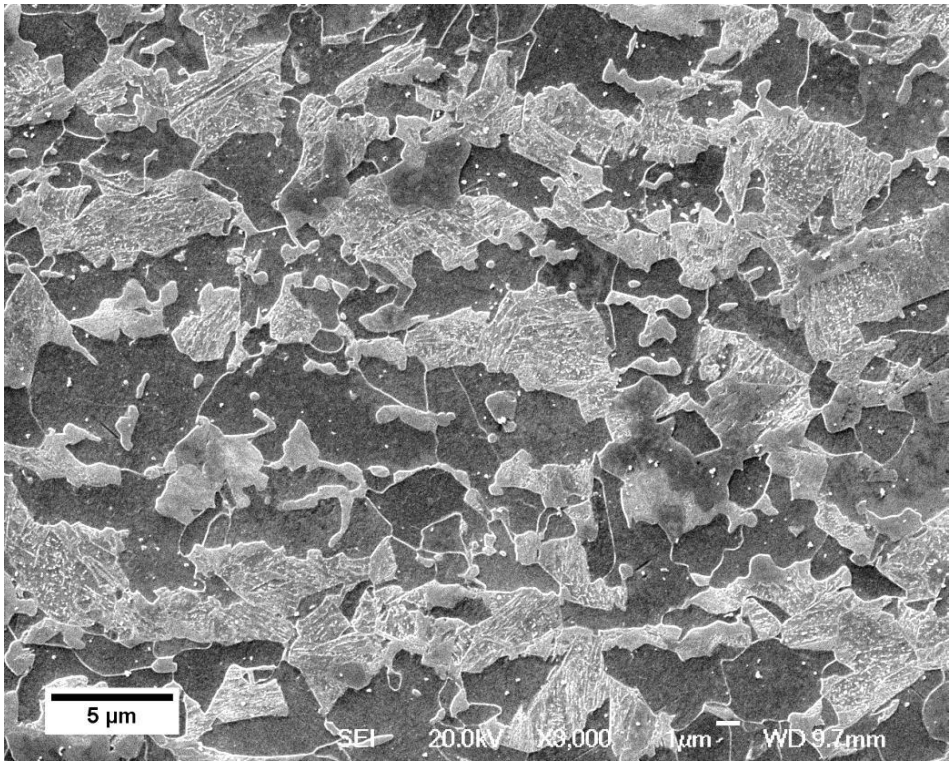

Figure 7.23: Typical SEM image of the DP1000A samples

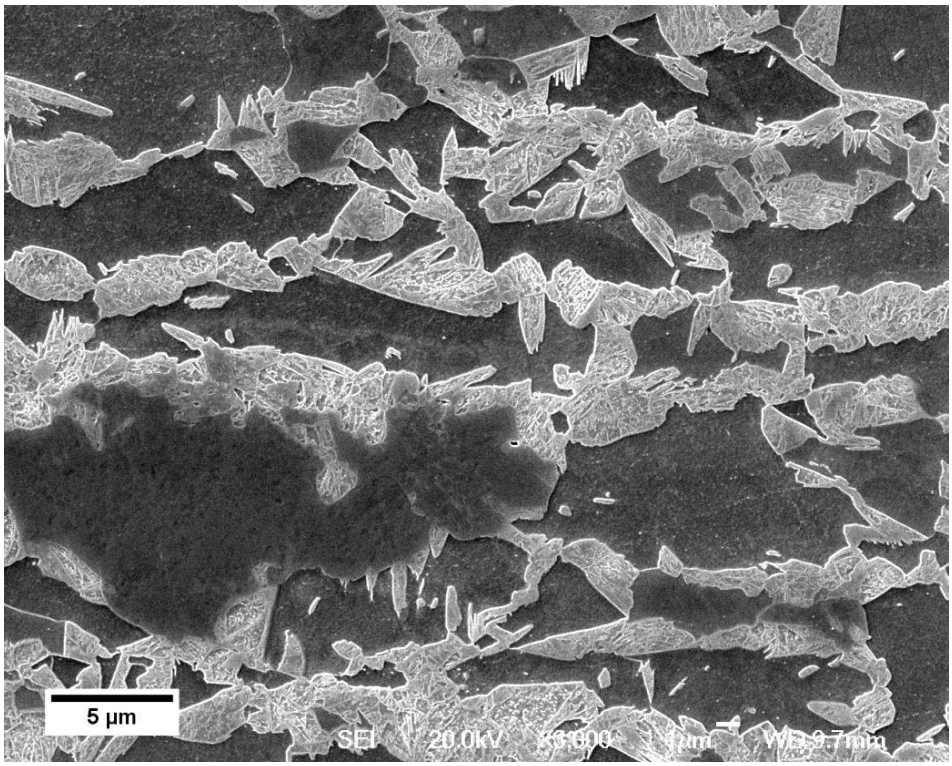

Figure 7.24: Typical SEM image of the DP1000B samples

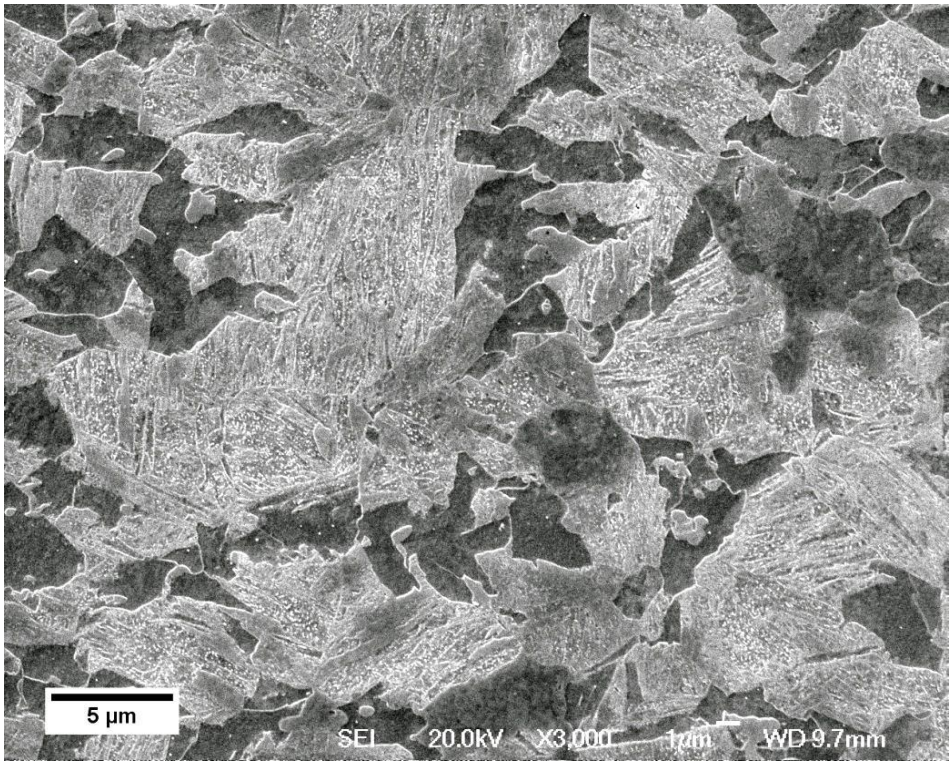

Figure 7.25: Typical SEM image of the CP1000 samples

Table 7.3: Average phase fraction in the commercial DP and CP samples.

Sample	Ferrite %	Bainite + tempered martensite %	Martensite %
DP600	83.6±1.6	10.0±1.4	6.4±1.0
DP600GI	85.9±1.5	14.1±1.5	0.0±0
DP800	78.4±2.1	19.4±1.9	2.2±0.2
DP800GI	76.2±2.2	22.1±2.0	1.8±0.1
DP1000A	40.0±1.9	54.1±0.8	5.9±1.9
DP1000B	42.6±2.1	51.7±2.4	5.8±2.1
CP1000	24.0±3.8	58.6±3.6	17.5±7.0

7.3.3 Mechanical properties

The yield and tensile strength were measured, by Tata Steel, in the transverse direction for the DP600, DP600GI and DP1000B grades and the longitudinal direction for the DP800, DP800GI, DP1000A and CP1000 grades. A plot of the tensile strength against ferrite fraction is shown in Figure 7.26. The tensile strength increases with a decrease in the ferrite fraction. The trend does not follow a simple law of mixtures rule (linear relationship) since the amount of carbon in the second phase (and hence its strengthening contribution) drops significantly with the increase in the amount of second phase (as the overall carbon content does not change significantly between the grades, described in 4.1.3 in Chapter 4). In dual phase steels the strengthening effect of grain size is less significant than that in the low carbon steels sample, where ferrite is

the dominate phase. Also the difference in hardness is far larger between ferrite and second phase than between types of the second phase (i.e. bainite/tempered martensite/martensite). A clear relationship between the ferrite fraction and tensile strength for the DP grades can still be seen in Figure 7.26. The relationship between the ferrite fraction and yield strength is shown in Figure 7.27. It can be seen that, in general, the yield strength increases with a decreasing ferrite fraction, although a higher yield strength of the DP600 grade compared to the DP800 grade can be seen, which is believed to be due to the DP600 grade sample was heavily temper rolled which raises the yield strength.

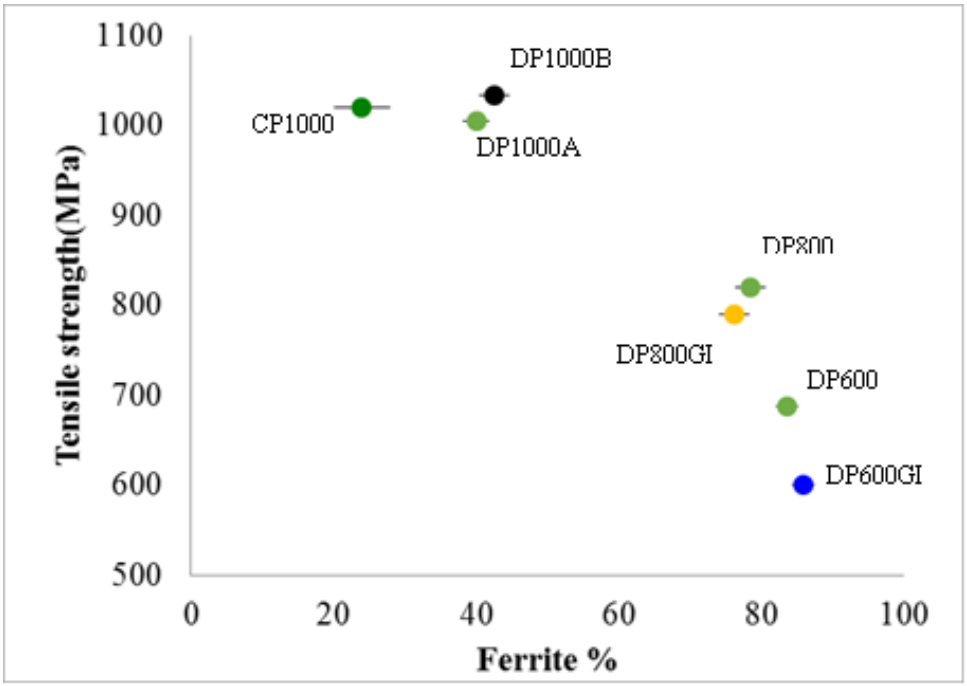

Figure 7.26: Plot of tensile strength against ferrite fraction for the commercial DP/CP steel samples.

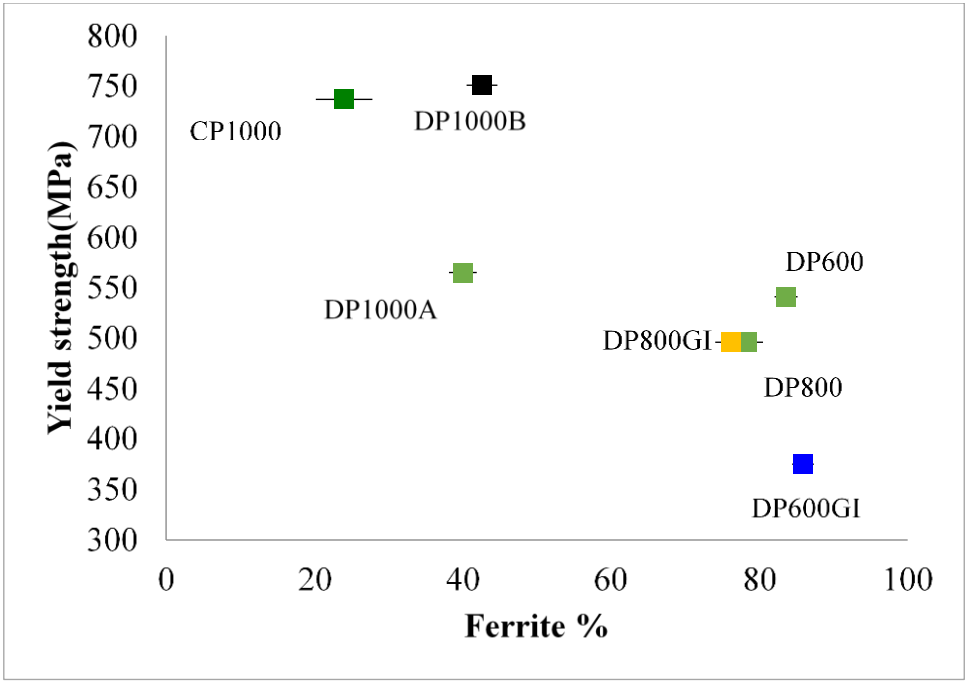

Figure 7.27: Plot of tensile strength against ferrite fraction for the commercial DP/CP steel samples.

7.3.4 EM sensor measurements

The real inductance at 100Hz, measured by placing the sensor both parallel and perpendicular to the steel strip rolling direction, are plotted against ferrite fraction in Figures 7.28 and 7.29 respectively. The low frequency (100 Hz) real inductance values, which are dominated by differences in the relative permeability between the samples, increase with an increasing amount of ferrite as this has a much higher relative permeability than martensite, bainite and tempered martensite. It can be seen that the real inductance values at 100Hz measured by placing the sensor perpendicular to the rolling direction are consistently slightly lower than the ones measured parallel to the rolling direction. This is because ferrite grains are elongated and the second phase is banded in the rolling direction meaning that the magnetic flux lines are less impeded parallel to the rolling direction. A full discussion on the role of banded structures in

ferrite + austenite microstructures on the EM signal has been reported previously [8]. An increase of relative permeability from 36.5 to 51.5 was seen for a ferrite aspect ratio change from 1 to 2.25 in modelled ferrite + austenite microstructures with 54% ferrite. Such increase in relative permeability was reported to be equivalent to 6.4% change in ferrite fraction [8]. The effect of banded structure on relative permeability value in the ferrite + austenite microstructures is expected to be larger than in ferrite + martensite/tempered martensite microstructures, due to the smaller difference of relative permeability value in the latter phase combination. However, there will still be an effect on these DP steels.

The real inductance values for the non-galvanised and galvanised samples are generally similar, which is expected based on the similar ferrite fraction in these samples. The difference in microstructure (reduction of martensite in preference to tempered martensite) does not have a strong effect on the relative permeability of the samples because, similar to the strength properties, the difference in relative permeability is larger between ferrite and second phase than between types of the second phase (i.e. bainite/tempered martensite/martensite). This suggests that the thin (50 μm) galvanized layer has little effect on the EM signal. This is expected since zinc is paramagnetic and therefore does not affect the relative permeability of the sample significantly. The exception are the results for the DP800 and DP800GI samples measured parallel to the rolling direction (shown in Figure 7.28), This is due to the fact that the unlike the DP800GI, where the ferrite grains are mostly equiaxed (shown in Figure 7.22), the DP800 sample has a heavily banded microstructure (shown in Figure 7.21), when the sensor was measured along the rolling direction, it is expected that the magnetic flux can be more easily penetrated through the banded ferrite grains.

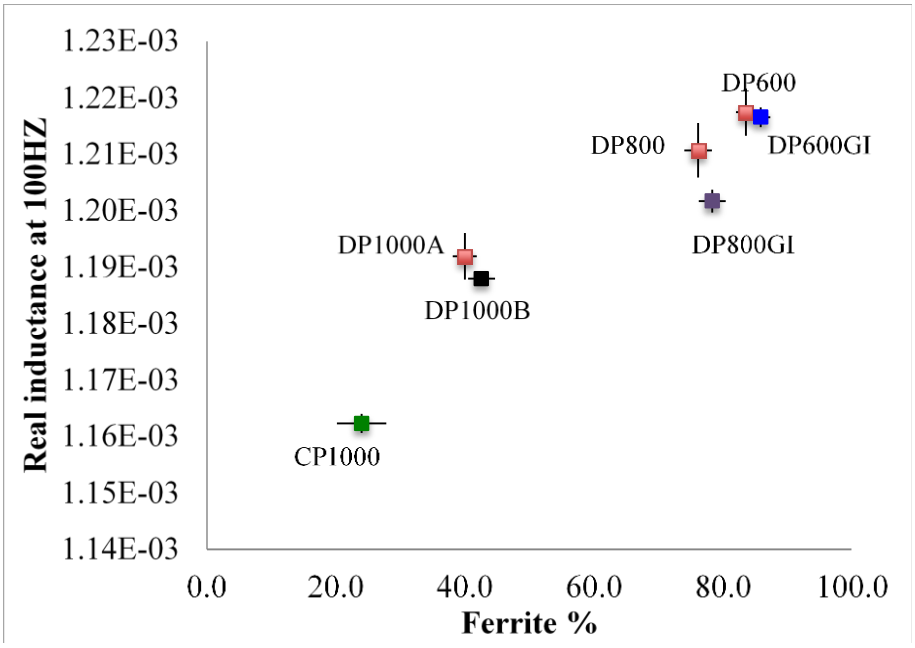

Figure 7.28: Real inductance at 100Hz measured by placing the sensor parallel to the rolling direction; plotted against ferrite fraction.

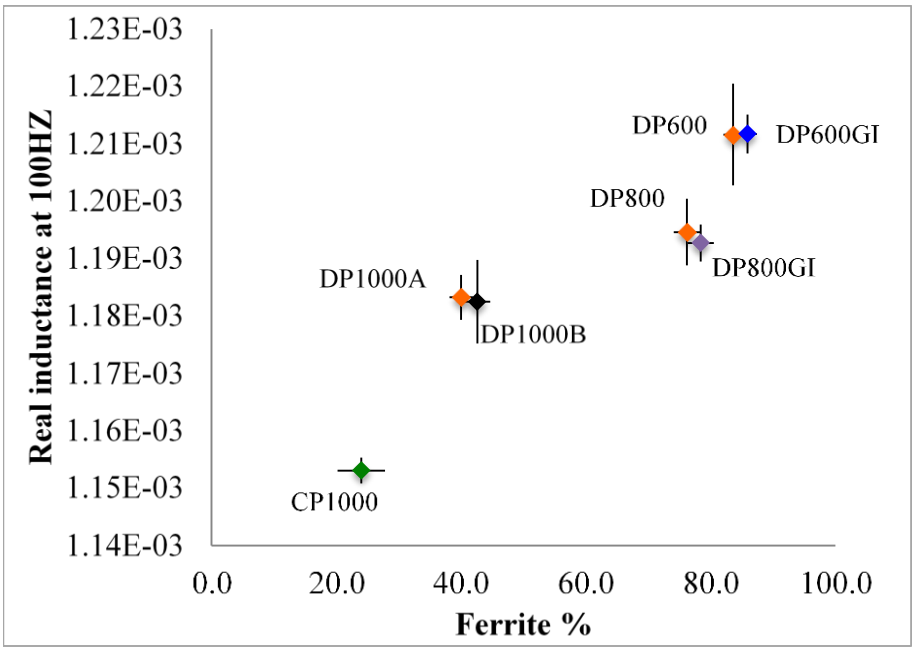

Figure 7.29: Real inductance at 100Hz measured by placing the sensor perpendicular to the rolling direction; plotted against ferrite fraction.

The real inductance values at 100Hz (measured parallel and perpendicular to the rolling direction) plotted against tensile strength are shown in Figure 3.30 and 3.31. There was only one tensile strength value for each sample supplied, hence no standard deviations are given. The real inductance values show a strong correlation with the tensile strength for the DP grades (an approximately linear decrease in real inductance with higher tensile strength), however the CP1000 grade does not follow the trend. This is due to the CP1000 grade having a different phase balance, and hence EM signal, to the DP1000 grade but similar tensile strength. It can be seen from Figure 3.31 that the galvanised and non-galvanised samples have similar real inductance values but different tensile strength values, this is due to their having a similar phase balance (ferrite + other phases), which controls the EM signal, but different tensile strengths due to the process conditions employed.

Figures 7.32 and 7.33 show the real inductance values at 100Hz measured by placing the sensor parallel and perpendicular respectively to the rolling direction plotted against yield strength. The correlation between inductance and yield strength is not as good as for tensile strength (R^2 value of 0.58 compared to 0.93), which is also reflected in the plot of yield strength against ferrite fraction, Figure 7.27.

In summary, the results show that the EM sensor could be used to determine the tensile strength of DP grades (R^2 value of 0.97). If the galvanised grades are considered alongside the standard DP grades, the correlation is less accurate (R^2 value of 0.93) but may still be sufficient for industrial quality control. Based on the data provided for yield strength the correlation between the EM sensor signal and yield strength is not strong (R^2 value of 0.58 for all the DP grades). It has also been shown that separate predictions

(or calibration curves) would be required for CP grades as the results do not follow the trends for the DP grades.

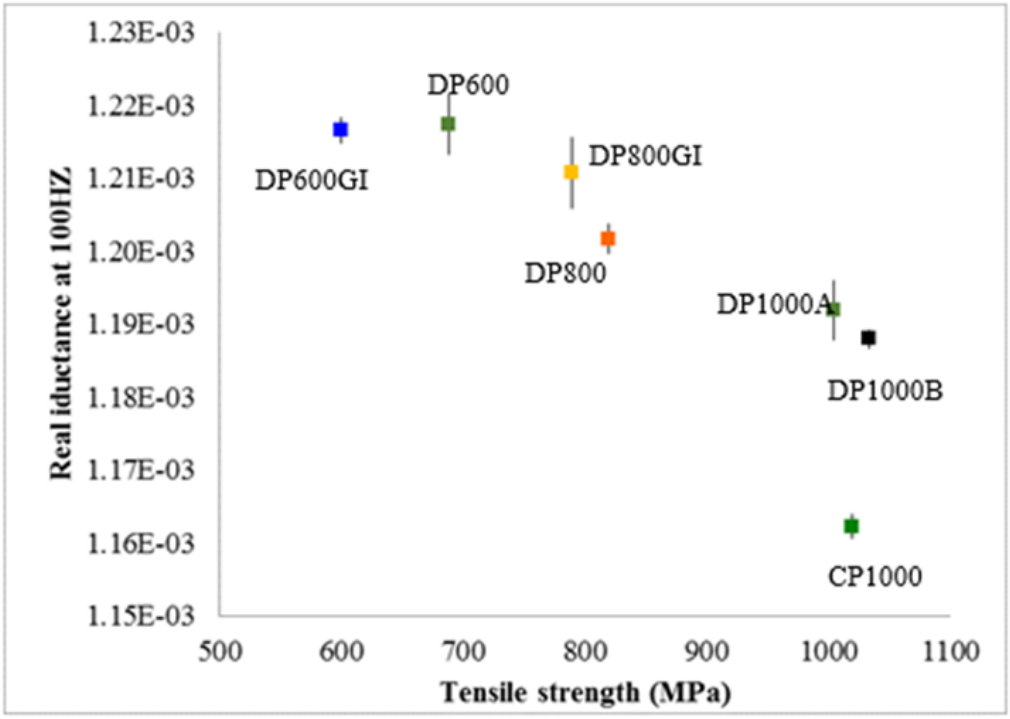

Figure 7.30: Real inductance at 100Hz measured by placing the sensor parallel to the rolling direction; plotted against tensile strength

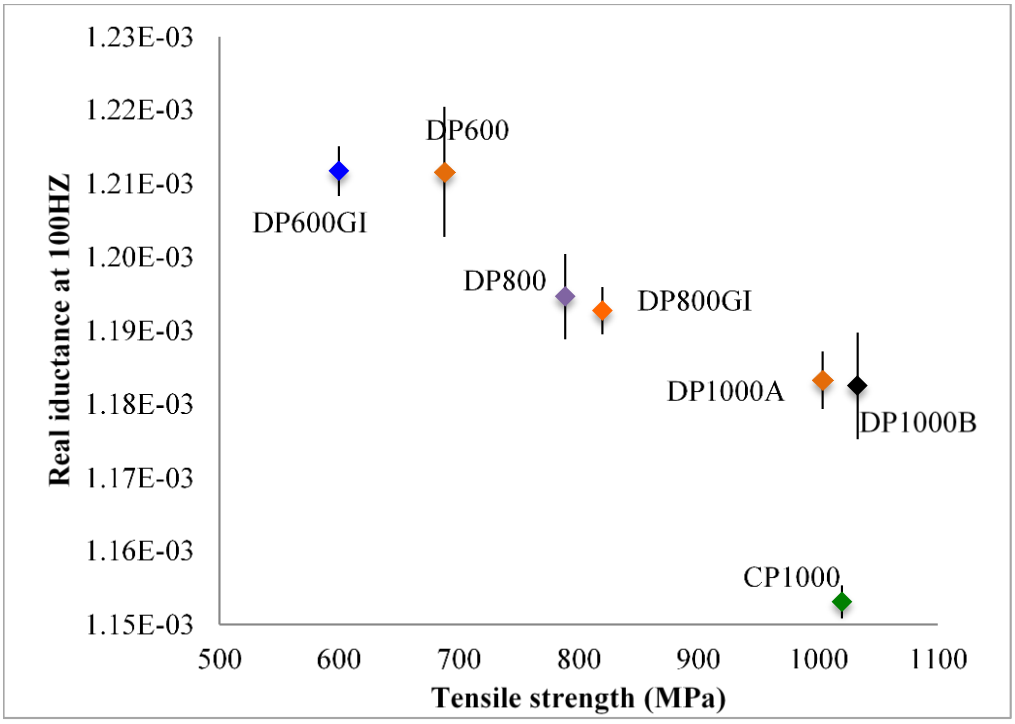

Figure 7.31: Real inductance at 100Hz measured by placing the sensor perpendicular to the rolling direction; plotted against tensile strength

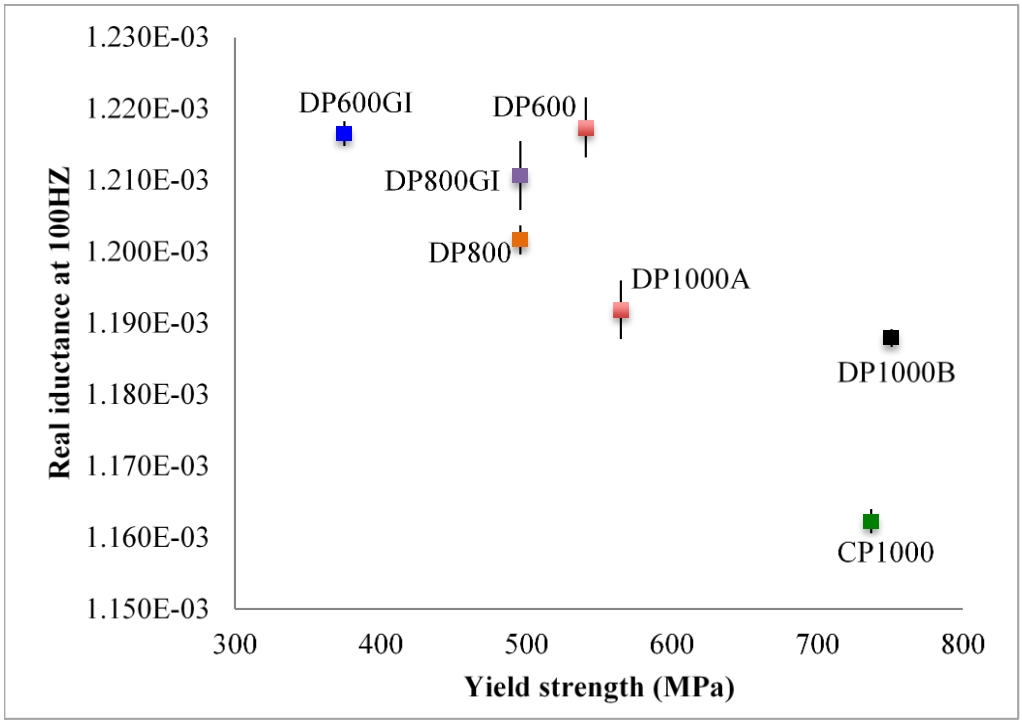

Figure 7.32: Real inductance at 100Hz measured by placing the sensor parallel to the rolling direction; plotted against yield strength.

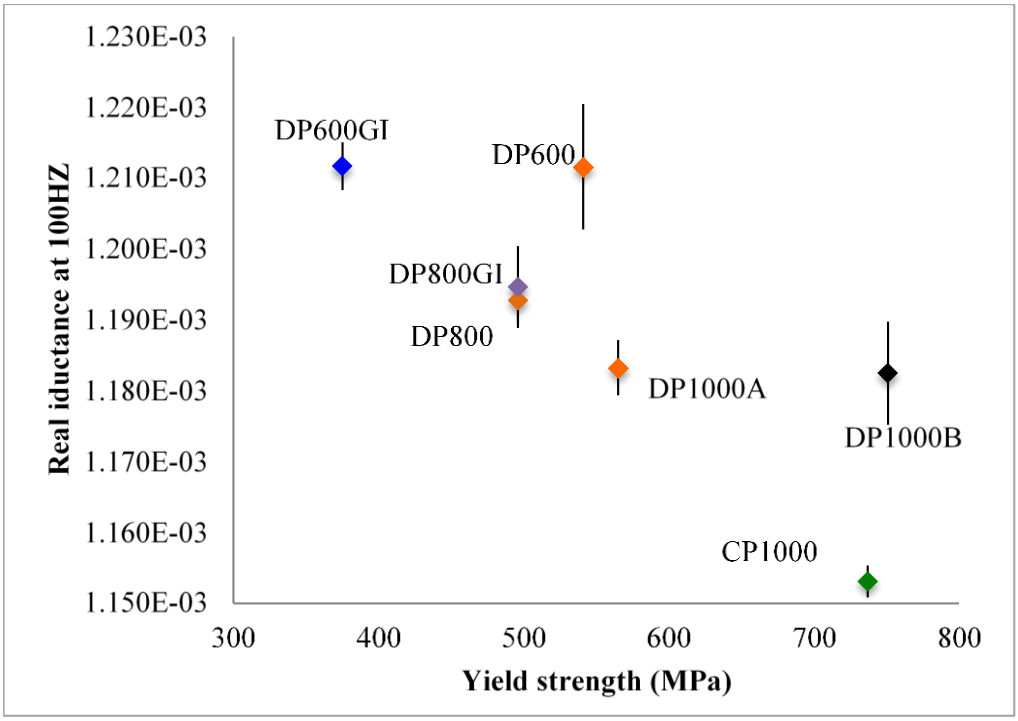

Figure 7.33: Real inductance at 100Hz measured by placing the sensorperpendicular to the rolling direction; plotted against yield strength.

7.3.5 Modelling the relative permeability and hence inductance values

The micrographs used in the FE microstructure model described in section 4.6 in Chapter 4 were taken with the sample sectioned transversely. Therefore, the FE modelled relative permeability results from the EM sensor-microstructure model should represent the sensor placed perpendicular to the rolling direction. The relative permeability of ferrite, martensite and tempered martensite was set as 330, 55 and 97 (the relative permeability for bainite was set the same as tempered martensite) respectively. The predicted relative permeability results for the DP and CP steels are given in Figure 7.34 and show large differences in values (from 138 to 285) due to the different fractions of ferrite present (24 to 84%). The EM sensor real inductance values at 100Hz plotted against the ferrite fraction are also shown in Figure 7.34. An

approximately linear increase in relative permeability, or inductance value, with increasing ferrite fraction is seen. Therefore the model could be used to predict the relative permeability, hence EM inductance value, and then tensile strength, for DP steels with real microstructures. The potential for this approach is being considered in a future PhD project and is discussed in the future work Chapter.

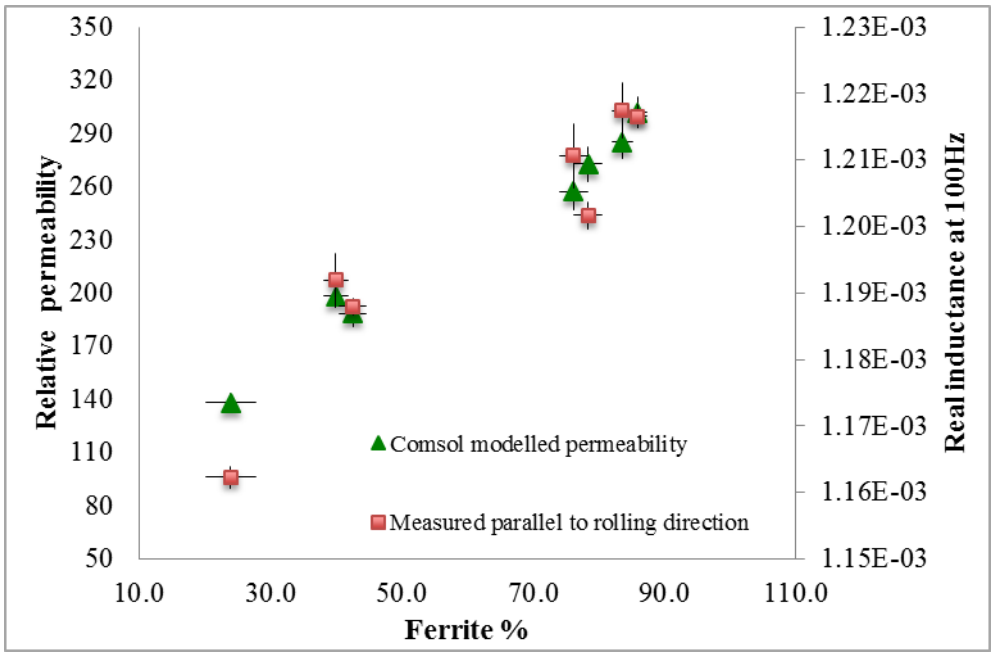

Figure 7.34: Predicted relative permeability values (from Comsol modeling) for the DP and CP microstructures compared to the measured inductance value (from EM sensor testing) plotted against ferrite fraction.

7.3.6 Summary

The relative permeability values of the DP and CP steels, and hence the measured inductance at 100Hz, increases approximately linearly with an increase in ferrite fraction, due to the higher relative permeability of ferrite. The results presented indicate that the EM sensor can be used to distinguish between the different commercial DP and CP steel grades due to their different phase fractions.

There is a clear increase in the tensile strength with a decrease in ferrite fraction for the DP grades, however the CP grade shows a different phase balance to the DP1000 grade but similar tensile strength. There is an approximately linear decreasing relationship between the EM sensor inductance value and increasing tensile strength for the DP grades (R^2 value of 0.97). Again, the CP grade does not fit this trend, due to the different phase balance and strength relationship. Therefore the EM sensor could be used to determine the tensile strength of DP grades. As the galvanised (GI) grades show a decreased tensile strength compared to the corresponding non-galvanised grades greater accuracy in prediction of tensile strength from the EM signal would be obtained by considering galvanised and non-galvanised grades separately. Separate predictions (or calibration curves) would be required for CP grades as the results do not follow the trends for the DP grades.

A Comsol model to predict the relative permeability values for different DP microstructures was used. There is an approximately linear trend between the relative permeability values and ferrite fraction, which agrees with the trend between the measured EM sensor inductance value and ferrite fraction. Therefore the model could be used to predict the relative permeability, and hence EM inductance value, and then tensile strength, for DP microstructures.

8 Conclusions

Electromagnetic (EM) sensors can be used to non-destructively characterise steel microstructures, as the EM signal is sensitive to both changes in magnetic relative permeability (dominant effect) and electrical resistivity. The influence of key microstructural parameters, including ferrite grain size, pearlite interlamellar spacing, carbon content in as-quenched martensite, tempering temperature for tempered martensite, ferrite-pearlite and ferrite-martensite phase balance, on the magnetic relative permeability and hence EM sensor signal has been studied in this work. In order to determine the relative permeability values both experimental and modelling studies have been carried out. The main conclusions from the research are as following:

In the area of modelling of the EM sensor output:

- The EM sensor output was modelled using a Finite Element (FE) based commercial software package; COMSOL MultiPhysics. A sensitivity study of the EM sensor output (real inductance) to changes in relative permeability and electrical resistivity suggested the latter has a much lower influence on the signal due to the narrow range of electrical resistivity values of structural steels.

- The model results for the EM sensor output show that any changes in resistivity can be ignored if the plateau low frequency inductance value is considered, where changes in relative permeability result in different low frequency inductance values. Therefore, in order to determine the effect of different

microstructures on the relative permeability of steel, the low frequency inductance value in the plateau region can be measured.

- A method was developed, for a cylindrical shaped EM sensor, to determine the relative permeability values of a steel sample by fitting the modelled real inductance value with the experimentally measured value through Comsol LiveLink for Matlab. It has been found that the relative permeability determined for steel samples using the EM sensor is very similar to the initial permeability value obtained from hysteresis loop measurements, reported in the literature, due to the very low field applied by the sensors. Therefore the EM sensor can be used to determine the relative permeability values of different steel microstructures, which can be compared with the results measured by other methods and are independent of sensor design.

In the area of the effect of single microstructure parameters on the relative permeability and hence the EM sensor signal:

1. *Effect of ferrite grain size*

- The relative permeability value, and hence the low frequency inductance value in the plateau region of the EM sensor output, increases with an increase in ferrite grain size from 13 to 64 μm in a 0.17 wt% C steel. A Hall–Petch type relationship (relative permeability varying linearly with the inverse square root of grain size) between the relative permeability values and the ferrite grain size was shown.

- Magnetic domain structures, obtained using the Bitter method, were related to the ferrite grain size in the 0.17 wt% C steel, with closure domains being observed near the grain boundaries. The observations were used to explain the phenomenon of the grain boundaries effective pinning magnetic domain movement, when the small magnetic field generated by the EM sensor was applied, and hence the Hall–Petch type relationship between the grain size and relative permeability.

- Results obtained for a pure iron sample with much larger ferrite grain sizes showed that the relative permeability did not increase further when the grain size becomes very large (increasing from 155 to 223 μm). Therefore the Hall-Petch type relationship was not obeyed for these large grain sizes. The magnetic domain structure observations suggested that this may have been due to the largest grain size sample showing a multi-magnetic domain structure per ferrite grain compared to a single domain per grain for the smaller grain sized samples.

2. *Effect of pearlite interlamellar spacing*

- The relative permeability, and hence the low frequency (plateau region) real inductance value, increased almost linearly with pearlite interlamellar spacing in the range of 52-106 nm in 0.81 wt%C pearlitic steel wire samples. This is believed to be mainly due to the reduced pinning effect on the magnetic domain wall movement in the samples with a larger pearlite interlamellar spacing.

- A case study of EM sensor measurement of pearlite interlamellar spacing in commercial tyre bead steel wire samples (fully pearlitic microstructures) shown

the linear trend between the low frequency (plateau region) real inductance and pearlite interlamellar spacing also held in the pearlite interlamellar spacing range of 142-202 nm. The EM sensor technique therefore shows potential to be used as a non-destructive charaterisation technique for determining the pearlite interlamellar spacing of tyre wire steels.

3. *Effect of carbon content in the as quenched martensite and tempering temperature in tempered martensite*

- Martensitic steel microstructures were also assessed in C-Mn steel samples, with a range of carbon contents from 0.17 to 0.80 wt%, and it was found that the relative permeability values, and hence the low frequency (plateau region) real inductance, decreased with an increase in carbon content in the as quenched martensite microstructure. This is believed to be due to the increase in dislocation density and reduction in martensite lath size in the higher carbon content samples, which in turn decreased the size of mean free path for domain wall motion and hence the relative permeability values.

- After tempering the martensitic structures, the relative permeability values increased due to the effect of decreased dislocation density. The precipitation of carbides, which would be expected to decrease the permeability values (due to providing pinning sites for domain wall movement) was a less dominant effect. The relative permeability increased with an increasing tempering temperature (for the same tempering time) due to the coarsening and

spheroidisation of carbides, which further increases the mean free path length for domain wall motion.

In the area of effect of phase balance detection using EM sensor:

- The effect of ferrite-pearlite phase balance on the relative permeability, and hence the EM sensor output, was studied using C-Mn steels (ferrite + pearlite) with different carbon contents. The results shows that the relative permeability, and hence inductance value, decreases with an increase in pearlite content (0-90%), due to the low permeability of pearlite compared with ferrite.

- A 2D FE COMSOL model for the sample and EM sensing coils that also allowed the steel microstructures to be included within the sample, was used to predict the relative permeability of the two phase microstructures. In the model the relative permeability of the separate phases (i.e. 100% ferrite and 100% pearlite, determined through experiment from suitable steels) was used as input and then any real or simulated microstrucutral phase distribution could be simulated. The results from the model showed good agreement with the experimental results for the ferrite + pearlite microstructures. These results indicated that the EM approach can be potentially used to non-destructively measure the ferrite fraction in ferrite – second phase microstructures.

- Measurements of ferrite-martensite phase balance in laboratory heat-treated dual phase (DP) steels were carried out using a U-shaped sensor to indicate how the approach could be used for more industrially interesting steel grades. The

low frequency (plateau region) real inductance value increased almost linearly with the ferrite fraction in the range of 35-72% in the DP steels.

- Finally, the research outcomes were applied to investigate the possibility of using the U-shaped EM sensor to predict the microstructure, and hence strength (as there is a known relationship between microstructure and strength), of commercial DP steel grades. The low frequency (plateau region) real inductance value was found to be able to distinguish between each of the grades, showing an approximately linear trend of increasing low frequency inductance value with increasing ferrite content. There is also a trend of decreasing low frequency inductance value with increasing tensile strength for the DP samples. Therefore, it has been shown that the EM sensor has great potential for use as a non-destructive technique for characterising the phase balance, and hence tensile strength, of DP steels.

9 Future works

Following the work carried out in this research, to further develop EM sensor characterisation of steel microstructures the following areas are suggested for further study:

In the area of EM sensor output modelling:

- 3D FE modelling of cylindrical and H-shaped sensors, to extend the approach from the 2D modelling carried out in this work. This would allow relative permeability prediction for strip/plate steels samples rather than cylindrical samples. This would have the advantage of more rapid assessment of commercial steel products. Optimisation of sensor designs for particular products (to ensure appropriate sampling of microstructures in steels with non-uniform structures) could also be carried out.

- Following from the point above then a study of the influences of EM sensor design parameters (e.g. number of turns of the coils, coil diameter, coil separation distance, ferrite core shape and material etc.) should be carried out for different steel microstructures (i.e. different relative permeability values) and products. Therefore the best sensor design can be selected for different microstructure parameters according to their relative permeability values range.

In the area of effect of microstructure parameters on relative permeability hence the EM sensor signal:

- Effect of each crystallographic texture component and fraction of texture component in commercial structural steels on their relative permeability values and hence the EM sensor signal. Whilst a great deal of work has been done on the effect of crystallographic texture on magnetic parameters for electrical steel [36, 116-134], there is little available in the literature for structural steels and for initial / relative permeability.

- Effect of elastic and plastic strain on relative permeability values and hence the EM sensor signal for steels with different starting (zero strain) relative permeability. Again, there is some data available in the literature of the effect of strain, but much of the work about elastic strain has focussed on pure iron [85, 91, 92, 98, 135].

- Effect of temperature on relative permeability values – this is an important area if EM sensors are to be used for in-situ monitoring (e.g. for phase transformations) at elevated temperatures.

- Effect of the morphology and distribution (e.g. the degree of banding) of the second phase in dual/multi-phase microstructures on relative permeability values and hence the EM sensor signal. In particular, to determine the effect of microstructural variations on the EM signal compared to industrial operational variability (changes in sample surface finish, lift off effects etc).

- Apply the FE microstructure model to predict the relative permeability, and hence EM inductance values, and then tensile strength, for DP steels for a much wider range and number of steel grades. This will allow the potential for the EM characterisation approach demonstrated in this thesis to be developed further towards a potential commercial application. This idea is being taken forward in a future PhD project.

10 References

[1] C.L.Davis. Overview of non-destructive evaluation of steel microstructures using multifrequency electromagnetic sensors. Ironmaking and Steelmaking. 2011;38.

[2] Dickinson SJ, Binns R, Yin W, Davis C, Peyton AJ. The Development of a Multifrequency Electromagnetic Instrument for Monitoring the Phase Transformation of Hot Strip Steel. IEEE Transations on instrumentation and measurement. 2007;56.

[3] Haldane R, Yin W, Strangwood M, Peyton A, Davis C. Multi-frequency electromagnetic sensor measurement of ferrite/austenite phase fraction—Experiment and theory. Scripta Materialia. 2006;54:1761-5.

[4] Papaelias M, Strangwood M, Peyton A, Davis C. Measurement and modeling of the electromagnetic response to phase transformation in steels. Metallurgical and Materials Transactions A. 2004;35:965-72.

[5] A.J.Peyton, C.L.Davis, F.D.Van den Berg, B Smith. EM Inspection of microstructure during hot processing: The journey from first principles to plant. Iron & Steel Technology magazine 2014

[6] Hao X, Yin W, Strangwood M, Peyton A, Morris P, Davis C. Off-line measurement of decarburization of steels using a multifrequency electromagnetic sensor. Scripta Materialia. 2008;58:1033-6.

[7] Hao XJ, Yin W, Strangwood M, Peyton AJ, Morris PF, Davis CL. Characterization of Decarburization of Steels Using a Multifrequency Electromagnetic Sensor: Experiment and Modeling. Metallurgical and Materials Transactions A. 2009;40:745-56.

[8] Hao XJ, Yin W, Strangwood M, Peyton AJ, Morris PF, Davis CL. Modelling the electromagnetic response of two-phase steel microstructures. NDT & E International. 2010;43:305-15.

[9] William D. Callister J. Materials Science and Engineering An Introduction. 7th ed2008.

[10] Apfel A, Moysan J, Corneloup G, Fouquet T, Chassignole B. Coupling an ultrasonic propagation code with a model of the heterogeneity of multipass welds to simulate ultrasonic testing. Ultrasonics. 2005;43:447-56.

[11] Bregliozzi G, Schino AD, Ahmed SIU, Kenny JM, Haefke H. Cavitation wear behaviour of austenitic stainless steels with different grain sizes. Wear. 2005;258:503-10.

[12] V.K.Bafna, P.U.Haribhakti. IN-SITU METALLOGRAPHY FOR THE PLANT HEALTH ASSESSMENT STUDY AND

FAILURE INVESTIGATION 4th Middle East NDT Conference and Exhibition. Kingdom of Bahrain2007.

[13] Nondestructive Evaluation and Quality Control. ASM Handbook: ASM internaltionl. p. 52-6.

[14] Peter.J.Goodhew. Electron microscopy and analysis2001.

[15] Khursheed A, Nelliyan K, Ding Y. Nanoscale imaging with a portable field emission scanning electron microscope. Microelectronic Engineering. 2006;83:762-6.

[16] Ramachandran VS, Paroli RM, Beaudoin JJ, Delgado AH. Handbook of Thermal Analysis of Construction Materials. William Andrew Publishing/Noyes; 2002.

[17] San Mart ń D, Rivera-D áz-del-Castillo PEJ, Garc á-de-Andr és C. In situ study of austenite formation by dilatometry in a low carbon microalloyed steel. Scripta Materialia. 2008;58:926-9.

[18] Gomez M, Medina SF, Caruana G. Modelling of Phase Transformation Kinetics by Correction of Dilatometry Results for a Ferritic Nb-microalloyed Steel. ISIJ International. 2003;43:1228-37.

[19] Kop TA, Sietsma J, Van Der Zwaag S. Dilatometric analysis of phase transformations in hypo-eutectoid steels. Journal of Materials Science. 2001;36:519-26.

[20] Yang JR, Bhadeshia HKDH. Continuous heating transformation of bainite to austenite. Materials Science and Engineering: A. 1991;131:99-113.

[21] Takahashi M, Bhadeshia HKDH. The Interpretation of Dilatometric Data for Transformations in Steels. Journal of Materials Science Letters. 1989;8:477-8.

[22] Reed RC, Akbay T, Shen Z, Robinson JM, Root JH. Determination of reaustenitisation kinetics in a Fe–0.4C steel using using dilatometry and neutron diffraction. Materials Science and Engineering: A. 1998;256:152-65.

[23] Zhang M, Li L, Fu RY, Krizan D, De Cooman BC. Continuous cooling transformation diagrams and properties of micro-alloyed TRIP steels. Materials Science and Engineering: A. 2006;438–440:296-9.

[24] van Bohemen SMC, Sietsma J. The kinetics of bainite and martensite formation in steels during cooling. Materials Science and Engineering: A. 2010;527:6672-6.

[25] Olasolo M, Uranga P, Rodriguez-Ibabe JM, López B. Effect of austenite microstructure and cooling rate on transformation characteristics in a low carbon Nb–V microalloyed steel. Materials Science and Engineering: A. 2011;528:2559-69.

[26] Raju S, Jeya Ganesh B, Rai AK, Mythili R, Saroja S, Raj B. A study on martensitic phase transformation in 9Cr–1W–0.23V–0.063Ta–0.56Mn–0.09C–0.02N (wt.%) reduced activation steel using differential scanning calorimetry. Journal of Nuclear Materials. 2010;405:59-69.

[27] Shi W, Li L, De Cooman BC, Wollants P, Yang C-x. Thermal Stability of Retained Austenite in TRIP Steel After Different Treatments. Journal of Iron and Steel Research, International. 2008;15:61-4.

[28] Raju S, Ganesh BJ, Banerjee A, Mohandas E. Characterisation of thermal stability and phase transformation energetics in tempered 9Cr–1Mo steel using drop and differential scanning calorimetry. Materials Science and Engineering: A. 2007;465:29-37.

[29] Ren L, Zhu J, Nan L, Yang K. Differential scanning calorimetry analysis on Cu precipitation in a high Cu austenitic stainless steel. Materials & Design. 2011;32:3980-5.

[30] Wasnik DN, Dey GK, Kain V, Samajdar I. Precipitation stages in a 316L austenitic stainless steel. Scripta Materialia. 2003;49:135-41.

[31] Primig S, Leitner H. Transformation from continuous-to-isothermal aging applied on a maraging steel. Materials Science and Engineering: A. 2010;527:4399-405.

[32] Primig S, Leitner H. Separation of overlapping retained austenite decomposition and cementite precipitation reactions during tempering of martensitic steel by means of thermal analysis. Thermochimica Acta. 2011;526:111-7.

[33] Hutchinson B, Jonsson S, Ryde L. On the kinetics of recrystallisation in cold worked metals. Scripta Metallurgica. 1989;23:671-6.

[34] Hazra SS, Gazder AA, Pereloma EV. Stored energy of a severely deformed interstitial free steel. Materials Science and Engineering: A. 2009;524:158-67.

[35] Ghosh SK, Haldar A, Chattopadhyay PP. Effect of ageing on the mechanical properties of directly quenched copper bearing microalloyed steels. Materials Chemistry and Physics. 2010;119:436-41.

[36] PremKumar R, Samajdar I, Viswanathan NN, Singal V, Seshadri V. Relative effect(s) of texture and grain size on magnetic properties in a low silicon non-grain oriented electrical steel. Journal of Magnetism and Magnetic Materials. 2003;264:75-85.

[37] Habibi Bajguirani HR. The effect of ageing upon the microstructure and mechanical properties of type 15-5 PH stainless steel. Materials Science and Engineering: A. 2002;338:142-59.

[38] B én éteau A, Aeby-Gautier E, Geandier G, Weisbecker P, Redja ïmia A, Appolaire B. Tempering of a martensitic stainless steel: Investigation by in situ synchrotron X-ray diffraction. Acta Materialia. 2014;81:30-40.

[39] Geandier G, Aeby-Gautier E, Settefrati A, Dehmas M, Appolaire B. Study of diffusive transformations by high energy X-ray diffraction. Comptes Rendus Physique. 2012;13:257-67.

[40] Shin J-H, Jeong J, Lee J-W. Microstructural evolution and the variation of tensile behavior after aging heat treatment of precipitation hardened martensitic steel. Materials Characterization. 2015;99:230-7.

[41] Yongtao Z, Haibo H, Lede M, Hanqian Z, Jinfu L. Quantitative carbide analysis using the Rietveld method for 2.25Cr–1Mo–0.25V steel. Materials Characterization. 2009;60:953-6.

[42] Haušild P, Davydov V, Drahokoupil J, Landa M, Pilvin P. Characterization of strain-induced martensitic transformation in a metastable austenitic stainless steel. Materials & Design. 2010;31:1821-7.

[43] Cakmak E, Choo H, An K, Ren Y. A synchrotron X-ray diffraction study on the phase transformation kinetics and texture evolution of a TRIP steel subjected to torsional loading. Acta Materialia. 2012;60:6703-13.

[44] Fu B, Yang WY, Wang YD, Li LF, Sun ZQ, Ren Y. Micromechanical behavior of TRIP-assisted multiphase steels studied with in situ high-energy X-ray diffraction. Acta Materialia. 2014;76:342-54.

[45] Ribeiro Miranda MA, Sasaki JM, Tavares SSM, de Abreu HFG, Neto JM. The use of X-ray diffraction, microscopy, and magnetic measurements for analysing microstructural features of a duplex stainless steel. Materials Characterization. 2005;54:387-93.

[46] Solano-Alvarez W, Abreu HFG, da Silva MR, Peet MJ. Phase quantification in nanobainite via magnetic measurements and X-ray diffraction. Journal of Magnetism and Magnetic Materials. 2015;378:200-5.

[47] Tolchard JR, Sømme A, Solberg JK, Solheim KG. On the measurement of austenite in supermartensitic stainless steel by X-ray diffraction. Materials Characterization. 2015;99:238-42.

[48] Wießner M, Leisch M, Emminger H, Kulmburg A. Phase transformation study of a high speed steel powder by high temperature X-ray diffraction. Materials Characterization. 2008;59:937-43.

[49] Xu Y, Zhang SH, Cheng M, Song HW. In situ X-ray diffraction study of martensitic transformation in austenitic stainless steel during cyclic tensile loading and unloading. Scripta Materialia. 2012;67:771-4.

[50] Suwanpinij P, Stark A, Li X, Römer F, Herrmann K, Lippmann T, et al. In Situ High Energy X-Ray Diffraction for Investigating the Phase Transformation in Hot Rolled TRIP-Aided Steels. Advanced Engineering Materials. 2014;16:1044-51.

[51] Kopineck H-J, Löffel R, Otten H-B. Industrial on-line texture determination in rolled steel strips. Journal of Nondestructive Evaluation. 1993;12:13-9.

[52] Bunge HJ. On-line determination of texture-dependent materials properties. Journal of Nondestructive Evaluation. 1993;12:3-11.

[53] J.Sull P. Nondestructive evaluation: Taylor & Francis; 2002.

[54] R.Halmshaw. Non-Destructive Testing. 2 ed: Edward Arnold; 1991.

[55] Blitz J, Simpson G. Ultrasonic methods of non-destructive testing: Champman & Hall; 1996.

[56] Gür CH, Tuncer BO. Characterization of microstructural phases of steels by sound velocity measurement. Materials Characterization. 2005;55:160-6.

[57] Freitas VLdA, Albuquerque VHCd, Silva EdM, Silva AA, Tavares JMRS. Nondestructive characterization of microstructures and determination of elastic properties in plain carbon steel using ultrasonic measurements. Materials Science and Engineering: A. 2010;527:4431-7.

[58] Vary A. CORRELATIONS BETWEEN ULTRASONIC AND FRACTURE TOUGHNESS FACTORS IN METALLIC MATERIALS. ASTM Special Technical Publication. 1979:563-78.

[59] Palanichamy P, Joseph A, Jayakumar T, Raj B. Ultrasonic velocity measurements for estimation of grain size in austenitic stainless steel. NDT & E International. 1995;28:179-85.

[60] Hirsekorn S. The scattering of ultrasonic waves by polycrystals. The Journal of the Acoustical Society of America. 1982;72:1021-31.

[61] Prasad R, Kumar S. Study of the influence of deformation and thermal treatment on the ultrasonic behaviour of steel. Journal of Materials Processing Technology. 1994;42:51-9.

[62] Vasudevan M, Palanichamy P. Assessment of microstructure stability of cold worked Ti-modified austenitic stainless steel during aging using ultrasonic velocity

measurements and correlation with mechanical properties. Journal of Nuclear Materials. 2003;312:181-90.

[63] Papaelias M. Detection and measurement of phase transformation in steel using electronmagnetic sensors: University of Birmingham; 2004.

[64] Dubois M, Moreau A, Militzer M, Bussière JF. Laser-ultrasonic monitoring of phase transformations in steels. Scripta Materialia. 1998;39:735-41.

[65] Duquennoy M, Ouaftouh M, Qian ML, Jenot F, Ourak M. Ultrasonic characterization of residual stresses in steel rods using a laser line source and piezoelectric transducers. NDT & E International. 2001;34:355-62.

[66] Green Jr RE. Non-contact ultrasonic techniques. Ultrasonics. 2004;42:9-16.

[67] Moreau A, Lord M, Lévesque D, Dubois M, Bussière JF. Laser–ultrasonic absorption measurements in low carbon steels. Journal of Alloys and Compounds. 2000;310:427-31.

[68] Hutchinson B, Lindh-Ulmgren E, Carlson L. Application of Laser Ultrasonics to Studies of Recrystallisation and Grain Growth in Metals. 1st International symposium on laser ultrasonics: science, technology and applicaions. Montreal, Canada2008.

[69] Pandey JC. Study of Recrystallization in Interstitial Free (IF) Steel by Ultrasonic Techniques. Materials and Manufacturing Processes. 2011;26:147-53.

[70] Kruger SE, Damm EB. Monitoring austenite decomposition by ultrasonic velocity. Materials Science and Engineering: A. 2006;425:238-43.

[71] Scruby CB, Moss BC. Non-contact ultrasonic measurements on steel at elevated temperatures. NDT & E International. 1993;26:177-88.

[72] Scruby CB, Smith RL, Moss BC. Microstructural monitoring by laser-ultrasonic attenuation and forward scattering. NDT International. 1986;19:307-13.

[73] Dubois M, Militzer M, Moreau A, Bussière JF. A new technique for the quantitative real-time monitoring of austenite grain growth in steel. Scripta Materialia. 2000;42:867-74.

[74] Hutchinson B, Moss B, Smith A, Astill A, Scruby C, Engberg G, et al. Online characterisation of steel structures in hot stripmill using laser ultrasonic measurements. Ironmaking and Steelmaking. 2002;29:77.

[75] Davis CL, Dickinson SJ, Peyton AJ. Impedance spectroscopy for remote analysis of steel microstructures. Ironmaking & Steelmaking. 2005;32:381-4.

[76] Zhou L, Liu J, Hao X, Strangwood M, Davis C. The role of microstructure such as phase balance and pearlite lamellar spacing to EM sensor signal. International conference on NDE of steel. Jamshedpur, India2011. p. 208-15.

[77] Liu J, Hao XJ, Zhou L, Strangwood M, Davis CL, Peyton AJ. Measurement of microstructure changes in 9Cr,Äì1Mo and 2.25Cr,Äì1Mo steels using an electromagnetic sensor. Scripta Materialia. 2012;66:367-70.

[78] Konoplyuk S. Estimation of pearlite fraction in ductile cast irons by eddy current method. NDT & E International. 2010;43:360-4.

[79] Balamurugan S, Bhattacharyya T, Gudhae D, Zhou L, Davis CL, Peyton AJ, et al. Prediction of interlamellar pearlite spacing of tyre bead wires after patenting using electromagnetic techniques. Insight - Non-Destructive Testing and Condition Monitoring. 2013;55:132-5.

[80] Ghanei S, Kashefi M, Mazinani M. Eddy current nondestructive evaluation of dual phase steel. Materials & Design. 2013;50:491-6.

[81] Mercier D, Lesage J, Decoopman X, Chicot D. Eddy currents and hardness testing for evaluation of steel decarburizing. NDT & E International. 2006;39:652-60.

[82] Uchimoto T. Eddy current evaluation of cast irons for material characterization. Journal of Magnetism and Magnetic Materials. 2003;258-259:493-6.

[83] Konoplyuk S, Abe T, Uchimoto T, Takagi T, Kurosawa M. Characterization of ductile cast iron by eddy current method. NDT & E International. 2005;38:623-6.

[84] Habermehl S, Jiles DC, Teller CM. Influence of heat treatment and chemical composition on the magnetic properties of ferromagnetic steels. Magnetics, IEEE Transactions on. 1985;21:1909-11.

[85] Thompson SM, Tanner BK. The magnetic properties of specially prepared pearlitic steels of varying carbon content as a function of plastic deformation. Journal of Magnetism and Magnetic Materials. 1994;132:71-88.

[86] Moorthy V, Vaidyanathan S, Jayakumar T, Raj B. Microstructural characterization of quenched and tempered 0.2% carbon steel using magnetic Barkhausen noise analysis. Journal of Magnetism and Magnetic Materials. 1997;171:179-89.

[87] Liu T, Kikuchi H, Kamada Y, Ara K, Kobayashi S, Takahashi S. Comprehensive analysis of Barkhausen noise properties in the cold rolled mild steel. Journal of Magnetism and Magnetic Materials. 2007;310:e989-e91.

[88] Kleber X, Vincent A. On the role of residual internal stresses and dislocations on Barkhausen noise in plastically deformed steel. NDT & E International. 2004;37:439-45.

[89] Pal'a J, Bydžovský J. Barkhausen noise as a function of grain size in non-oriented FeSi steel. Measurement. 2013;46:866-70.

[90] Yamaura S, Furuya Y, Watanabe T. The effect of grain boundary microstructure on Barkhausen noise in ferromagnetic materials. Acta Materialia. 2001;49:3019-27.

[91] Thompson SM, Tanner BK. The magnetic properties of pearlitic steels as a function of carbon content. Journal of Magnetism and Magnetic Materials. 1993;123:283-98.

[92] Thompson SM. The magnetic properties of plastically deformed steels: University of Durham; 1991.

[93] Saquet O, Chicois J, Vincent A. Barkhausen noise from plain carbon steels: analysis of the influence of microstructure. Materials Science and Engineering: A. 1999;269:73-82.

[94] Ghanei S, Saheb Alam A, Kashefi M, Mazinani M. Nondestructive characterization of microstructure and mechanical properties of intercritically annealed dual-phase steel by magnetic Barkhausen noise technique. Materials Science and Engineering: A. 2014;607:253-60.

[95] Titto S, Otala M, S‰yn‰j‰kangas S. Non-destructive magnetic measurement of steel grain size. Non-Destructive Testing. 1976;9:117-20.

[96] Gatelier-Rothea C, Chicois J, Fougeres R, Fleischmann P. Characterization of pure iron and (130 p.p.m.) carbon–iron binary alloy by Barkhausen noise measurements: study of the influence of stress and microstructure. Acta Materialia. 1998;46:4873-82.

[97] Gurruchaga K, Martinez-de-Guerenu A, Soto M, Arizti F. Magnetic Barkhausen Noise for Characterization of Recovery and Recrystallization. Magnetics, IEEE Transactions on. 2010;46:513-6.

[98] Bozorth RM. Ferromagnetism: Van Nostrand; 1965.

[99] Van Heuvelen A. Physics: A General Introduction. 2 ed: Harper Collins; 1986.

[100] B. D. Cullity, Graham CD. Introduction to Magnetic Materials, 2nd Edition.

[101] Bethe H, Handb D. Physik. 1938;24:595-8.

[102] S.Tian. Physical properties of materials2001.

[103] D.J.Craik;, R.S.Tebble. Ferromagnatism and ferromagnetic domains: North-Holland Publishing Co. - Amsterdam; 1965.

[104] Bitter F. On inhomogeneities in the magnetisation of ferromagnetic materials. Physical Review. 1931;38:1903-5.

[105] Ahns SJ, Yoon CS, Yoon SG, Kim CK, Byun TY, Hong KS. Domain structure of polycrystalline MnZn ferrites. Materials Science and Engineering B. 2001;84:146-54.

[106] Carey R, Isaac ED. Magnetic domains and techniques for their observation: The English universities press limited; 1966.

[107] Szmaja W. Studies of the surface domain structure of cobalt monocrystals by the SEM type-I magnetic contrast and Bitter colloid method. Journal of Magnetism and Magnetic Materials. 2000;219:281-93.

[108] Moses AJ, Williams PI, Hoshtanar OA. Real time dynamic domain observation in bulk materials. Journal of Magnetism and Magnetic Materials. 2006;304:150-4.

[109] Cha SY, Kim CG, Chang SK. Study of pinning conditions, magnetic domain structure and magnetic properties of laser-scribed 3%Si-steels. Journal of Magnetism and Magnetic Materials. 2002;242–245, Part 1:205-7.

[110] Batista L, Rabe U, Hirsekorn S. Magnetic micro- and nanostructures of unalloyed steels: Domain wall interactions with cementite precipitates observed by MFM. NDT & E International. 2013;57:58-68.

[111] Lo KH. Magnetic domain characterisation of duplex stainless steel after different treatments. Materials Characterization. 2012;72:46-52.

[112] Szmaja W, Grobelny J, Cichomski M, Makita K, Kozłowski W. Imaging domains of hard magnetic materials by SEM and MFM. Vacuum. 2007;81:1367-70.

[113] Hosemann P, Hawley M, Mori G, Li N, Maloy SA. AFM and MFM characterization of oxide layers grown on stainless steels in lead bismuth eutectic. Journal of Nuclear Materials. 2008;376:289-92.

[114] Guo LQ, Zhao XM, Li M, Zhang WJ, Bai Y, Qiao LJ. Annealing effects on the microstructure and magnetic domain structures of duplex stainless steel studied by in situ technique. Applied Surface Science. 2012;259:213-8.

[115] Michalak JT, Glenn RC. Transmission Electron Microscope Observations of Magnetic Domain Walls. Journal of Applied Physics. 1961;32:1261-5.

[116] Chaudhury A, Khatirkar R, Viswanathan NN, Singal V, Ingle A, Joshi S, et al. Low silicon non-grain-oriented electrical steel: Linking magnetic properties with metallurgical factors. Journal of Magnetism and Magnetic Materials. 2007;313:21-8.

[117] Hou C-K, Lee, Sanboh. Effect of rolling strain on the loss separation and permeability of lamination steels. IEEE Transactions on Magnetics 1993;30:212-6.

[118] Hou C-K. Effect of silicon on the loss separation and permeability of laminated steels. Journal of Magnetism and Magnetic Materials. 1996;162:280-90.

[119] Hou CK, Hu CT, Lee S. The effect of titanium and niobium on degradation of magnetic properties of lamination steels. Journal of Magnetism and Magnetic Materials. 1990;87:44-50.

[120] Hou CK, Hu CT, Lee S. Effect of residual aluminium on the microstructure and magnetic properties of low carbon electrical steels. Materials Science and Engineering: A. 1990;125:241-7.

[121] Chun-Kan H. The effects of grain size on the magnetic properties of fully processed, continuous-annealed low-carbon electrical steels. Magnetics, IEEE Transactions on. 1996;32:471-7.

[122] Baudouin P, Belhadj A, Houbaert Y. Effect of the rapid heating on the magnetic properties of non-oriented electrical steels. Journal of Magnetism and Magnetic Materials. 2002;238:221-5.

[123] Liu H-T, Liu Z-Y, Qiu Y-Q, Sun Y, Wang G-D. Microstructure, texture and magnetic properties of strip casting Fe–6.2 wt%Si steel sheet. Journal of Materials Processing Technology. 2012;212:1941-5.

[124] Zhang Y, Xu Y, Liu H, Li C, Cao G, Liu Z, et al. Microstructure, texture and magnetic properties of strip-cast 1.3% Si non-oriented electrical steels. Journal of Magnetism and Magnetic Materials. 2012;324:3328-33.

[125] Ghosh P, Chromik RR, Vaseghi B, Knight AM. Effect of crystallographic texture on the bulk magnetic properties of non-oriented electrical steels. Journal of Magnetism and Magnetic Materials. 2014;365:14-22.

[126] Ghosh P, Chromik RR, Knight AM, Wakade SG. Effect of metallurgical factors on the bulk magnetic properties of non-oriented electrical steels. Journal of Magnetism and Magnetic Materials. 2014;356:42-51.

[127] Gallaugher M, Brodusch N, Gauvin R, Chromik RR. Magnetic domain structure and crystallographic orientation of electrical steels revealed by a forescatter detector and electron backscatter diffraction. Ultramicroscopy. 2014;142:40-9.

[128] Jenkins K, Lindenmo M. Precipitates in electrical steels. Journal of Magnetism and Magnetic Materials. 2008;320:2423-9.

[129] Sidor JJ, Verbeken K, Gomes E, Schneider J, Calvillo PR, Kestens LAI. Through process texture evolution and magnetic properties of high Si non-oriented electrical steels. Materials Characterization. 2012;71:49-57.

[130] Chen S, Butler J, Melzer S. Effect of asymmetric hot rolling on texture, microstructure and magnetic properties in a non-grain oriented electrical steel. Journal of Magnetism and Magnetic Materials. 2014;368:342-52.

[131] Bian X, Zeng Y, Nan D, Wu M. The effect of copper precipitates on the recrystallization textures and magnetic properties of non-oriented electrical steels. Journal of Alloys and Compounds. 2014;588:108-13.

[132] Park J-T, Szpunar JA. Effect of initial grain size on texture evolution and magnetic properties in nonoriented electrical steels. Journal of Magnetism and Magnetic Materials. 2009;321:1928-32.

[133] Beckley P. Steels, Silicon Iron-based: Magnetic Properties. In: Veyssière KHJBWCCFIJKM, editor. Encyclopedia of Materials: Science and Technology (Second Edition). Oxford: Elsevier; 2001. p. 8847-51.

[134] ElBidweihy H, Burgy CD, Della Torre E. Stress-associated changes in the magnetic properties of high strength steels. Physica B: Condensed Matter. 2014;435:16-20.

[135] Thompson SM, Tanner BK. The magnetic properties of plastically deformed steels. Journal of Magnetism and Magnetic Materials. 1990;83:221-2.

[136] Tanner BK, Szpunar JA, Willcock SNM, Morgan LL, Mundell PA. Magnetic and metallurgical properties of high-tensile steels. Journal of Materials Science. 1988;23:4534-40.

[137] Willcock SNM, Tanner BK, Mundell PA. The magnetic properties of seamless steel pipe. Journal of Magnetism and Magnetic Materials. 1987;66:153-7.

[138] Liu J, Strangwood M, Davis C, Peyton A. Magnetic Evaluation of Microstructure Changes in 9Cr-1Mo and 2.25Cr-1Mo Steels Using Electromagnetic Sensors. Metallurgical and Materials Transactions A. 2013;44:5897-909.

[139] Yin W, Hao XJ, Peyton AJ, Strangwood M, Davis CL. Measurement of decarburisation of steel rods with an electromagnetic sensor using an analytical model. NDT & E International. 2010;43:667-70.

[140] Zhou L, Liu J, Hao XJ, Strangwood M, Peyton AJ, Davis CL. Quantification of the phase fraction in steel using an electromagnetic sensor. NDT & E International. 2014;67:31-5.

[141] Karimian N, Wilson JW, Peyton AJ, Yin W, Liu J, Davis CL. Differential permeability behaviour of P9 and T22 power station Steels. Journal of Magnetism and Magnetic Materials. 2014;352:81-90.

[142] Papaelias MP, Strangwood M, Peyton AJ, Davis CL. Effect of microstructural variations on smart inductive sensor measurements of phase transformation in steel. Scripta Materialia. 2004;51:379-83.

[143] Yin W, Karimian N, Liu J, Hao XJ, Zhou L, Peyton AJ, et al. Measurement of electromagnetic properties of power station steels. NDT & E International. 2012;51:135-41.

[144] Liu J, Hao XJ, Zhou L, Strangwood M, Davis CL, Peyton AJ. Measurement of microstructure changes in 9Cr–1Mo and 2.25Cr–1Mo steels using an electromagnetic sensor. Scripta Materialia. 2012;66:367-70.

[145] Wilson JW, Karimian N, Liu J, Yin W, Davis CL, Peyton AJ. Measurement of the magnetic properties of P9 and T22 steel taken from service in power station. Journal of Magnetism and Magnetic Materials. 2014;360:52-8.

[146] Hao XJ, Yin W, Strangwood M, Peyton AJ, Morris PF, Davis CL. Off-line measurement of decarburization of steels using a multifrequency electromagnetic sensor. Scripta Materialia. 2008;58:1033-6.

[147] Hetherington MG, Jakubovics JP, Szpunar JA, Tanner BK. High-voltage Lorentz electron microscopy studies of domain structures and magnetization processes in pearlitic steels. Philosophical Magazine Part B. 1987;56:561-77.

[148] Ranjan R, Jiles DC, Rastogi P. Magnetic properties of decarburized steels: An investigation of the effects of grain size and carbon content. Magnetics, IEEE Transactions on. 1987;23:1869-76.

[149] Beale AD, Jakubovics JP, Hetherington MG, Scruby CB, Lewis BA, Davies KJ. TEM studies of domains and micromagnetic processes in structural steels. Journal of Magnetism and Magnetic Materials. 1992;104–107, Part 1:365-7.

[150] Jiles DC. Magnetic properties and microstructure of AISI 1000 series carbon steels. Journal of Physics D: Applied Physics. 1988;21:1186.

[151] Yin W, Hao X, Peyton A, Strangwood M, Davis C. Measurement of permeability and ferrite/austenite phase fraction using a multi-frequency electromagnetic sensor. NDT & E International. 2009;42:64-8.

[152] Yin W, Peyton AJ, Strangwood M, Davis CL. Exploring the relationship between ferrite fraction and morphology and the electromagnetic properties of steel. Journal of Materials Science. 2007;42:6854-61.

[153] Looyenga H. Dielectric constants of heterogeneous mixtures. Physica. 1965;31:401-6.

[154] Birchak JR, Gardner LG, Hipp JW, Victor JM. Proceedings of the EEEEE. 1974;62:93-8.

[155] Ludwigso.Dc, Schwerer FC. EFFECT OF COMPOSITION ON RESISTIVITY OF CARBON STEEL SHEET. Metallurgical Transactions. 1971;2:3500-&.

[156] Norbury AL. JISI. 1920;101:627.

[157] ASM Handbook: Properties and Selection: Irons and Steels. 9 ed: American Society for Metals.

[158] Mohanty ON, Bhagat AN. Electrical Resistivity and Phase Transformation in Steels. Materialwissenschaft und Werkstofftechnik. 2003;34:96-101.

[159] Chaudhuri SP, Mahanti RK, Sivaramakrishnan CS, Singh MP. Physical properties of some thermomechanically processed microalloyed steels. Materials & Design. 2002;23:489-96.

[160] Park JS, Lee YK. Determination of Nb(C,N) dissolution temperature by electrical resistivity measurement in a low-carbon microalloyed steel. Scripta Materialia. 2007;56:225-8.

[161] Bhagat AN, Pabi SK, Ranganathan S, Mohanty ON. Study on copper precipitation during continuous heating and cooling of HSLA steels using electrical resistivity. Materials Science and Technology. 2007;23:158-64.

[162] Yin W, Hao XJ, Peyton AJ, Strangwood M, Davis CL. Measurement of permeability and ferrite/austenite phase fraction using a multi-frequency electromagnetic sensor. NDT & E International. 2009;42:64-8.

[163] ASM Handbook: Properties and Selection: Stainless Steels, Tool Materials and Special Purpose Metals

9ed: American Society for Metals.

[164] Elwazri AM, Wanjara P, Yue S. The effect of microstructural characteristics of pearlite on the mechanical properties of hypereutectoid steel. Materials Science and Engineering: A. 2005;404:91-8.

[165] Karlsson B, Lindén G. Plastic deformation of eutectoid steel with different cementite morphologies. Materials Science and Engineering. 1975;17:153-64.

[166] Gladman T, McIvor ID, Pickering FB. SOME ASPECTS OF THE STRUCTURE-PROPERTY RELATIONSHPS IN HIGH-CARBON FERRITE-PEARLITE STEELS. J Iron Steel Inst (London). 1972;210:916-30.

[167] Bhadeshia HKDH, Honeycombe SR. Steels - Microstructure and Properties. 3 ed. Oxford: Butterworth-Heinemann; 2006.

[168] Honeycombe RWK, Bhadeshia HKDH. Steels Microstructures and Properties1995.

[169] O'Donnelly BE, Reuben RL, Baker TN. QUANTITATIVE ASSESSMENT OF STRENGTHENING PARAMETERS IN FERRITE-PEARLITE STEELS FROM MICROSTRUCTURAL MEASUREMENTS. Metals Technology. 1984;11:45-51.

[170] He Y, Rao Q, Tan Y. Investigation on the morphology of martensite in carbon steels. J Cent South Univ Technol. 1996;3:122-34.

[171] Zhu W, Yin W, Peyton A, Ploegaert H. Modelling and experimental study of an electromagnetic sensor with an H-shaped ferrite core used for monitoring the hot transformation of steel in an industrial environment. NDT & E International. 2011;44:547-52.

[172] Chatterjee S, Verma AK, Sharma V. Direct-cast dual-phase steel. Scripta Materialia. 2008;58:191-4.

[173] Bag A, Ray KK, Dwarakadasa ES. Influence of martensite content and morphology on tensile and impact properties of high-martensite dual-phase steels. Metallurgical and Materials Transactions A. 1999;30:1193-202.

[174] Akbarpour MR, Ekrami A. Effect of ferrite volume fraction on work hardening behavior of high bainite dual phase (DP) steels. Materials Science and Engineering: A. 2008;477:306-10.

[175] Zhou L, Strangwood M, Davis CL, Peyton AJ, Parker SV, Smith AWF, et al. Non-destructive monitoring of phase fraction and tensile properties of dual-phase steels by an electro-magnetic sensor 9th International ROLLING Conference2013.